

**Time-dependent flows over textured or compliant surfaces
Turbulent drag reduction & compliant wall deformation**

Benschop, Henk

DOI

[10.4233/uuid:7482b78d-9daf-4760-b114-ec1ad338e66b](https://doi.org/10.4233/uuid:7482b78d-9daf-4760-b114-ec1ad338e66b)

Publication date

2018

Document Version

Final published version

Citation (APA)

Benschop, H. (2018). *Time-dependent flows over textured or compliant surfaces: Turbulent drag reduction & compliant wall deformation*. [Dissertation (TU Delft), Delft University of Technology].
<https://doi.org/10.4233/uuid:7482b78d-9daf-4760-b114-ec1ad338e66b>

Important note

To cite this publication, please use the final published version (if applicable).
Please check the document version above.

Copyright

Other than for strictly personal use, it is not permitted to download, forward or distribute the text or part of it, without the consent of the author(s) and/or copyright holder(s), unless the work is under an open content license such as Creative Commons.

Takedown policy

Please contact us and provide details if you believe this document breaches copyrights.
We will remove access to the work immediately and investigate your claim.

Time-dependent Flows over Textured or Compliant Surfaces

TURBULENT DRAG REDUCTION & COMPLIANT WALL
DEFORMATION

Time-dependent Flows over Textured or Compliant Surfaces

TURBULENT DRAG REDUCTION & COMPLIANT WALL DEFORMATION

Proefschrift

ter verkrijging van de graad van doctor
aan de Technische Universiteit Delft,
op gezag van de Rector Magnificus
prof. dr. ir. T. H. J. J. van der Hagen,
voorzitter van het College voor Promoties,
in het openbaar te verdedigen op
donderdag 6 december 2018 om 12:30 uur

door

Hendrik Otto Gijsbertus BENSCHOP

ingenieur in de Technische Natuurkunde,
Technische Universiteit Delft, Nederland
geboren te Gorinchem, Nederland

Dit proefschrift is goedgekeurd door de promotoren.

Samenstelling promotiecommissie:

Rector Magnificus,	voorzitter
Prof. dr. ir. J. Westerweel,	Technische Universiteit Delft, promotor
Dr. ir. W.-P. Breugem,	Technische Universiteit Delft, promotor

Onafhankelijke leden:

Prof. dr. M. Quadrio,	Politecnico di Milano
Prof. dr. S. Hickel,	Technische Universiteit Delft
Prof. dr. ir. J. H. Snoeijer,	Universiteit Twente
Prof. dr. ir. E. H. van Brummelen,	Technische Universiteit Eindhoven
Prof. dr. ir. B. J. Boersma,	Technische Universiteit Delft

Dr. ir. W.-P. Breugem heeft als begeleider in belangrijke mate aan de totstandkoming van het proefschrift bijgedragen.



The research leading to this thesis was carried out in the Laboratory for Aero- & Hydrodynamics of the faculty of Mechanical, Maritime & Materials Engineering (3mE) at the Delft University of Technology. It has received funding from the European Union Seventh Framework Programme (FP7) in the SEAFRONT project under grant agreement nr. 614034. The parallel computations were performed on the Dutch national supercomputer Cartesius at SURFsara, Amsterdam. This work was sponsored by NWO Physical Sciences for the use of supercomputer facilities.

Cover: Contours of the instantaneous wall shear stress in a turbulent plane channel flow (cf. figure 3.8)

Printed by: Gildeprint - Enschede

Copyright © 2018 by H. O. G. Benschop

ISBN 978-94-6366-100-3

An electronic version of this dissertation is available at <http://repository.tudelft.nl/>.

If any of you lack wisdom, let him ask of God, That giveth to all men liberally, and upbraideth not; and it shall be given him. (James 1:5)

En indien iemand van u wijsheid ontbreekt, dat hij ze van God begere, Die een iegelijk mildelijk geeft, en niet verwijt; en zij zal hem gegeven worden. (Jakobus 1:5)

Summary

A significant part of the fuel used for transportation results from the drag in turbulent flows. Techniques for turbulent drag reduction yield associated reductions of the fuel consumption and greenhouse gas emissions, which is desirable from both economic and environmental perspectives (cf. chapter 1). This thesis investigates two passive techniques that could be exploited for the reduction of frictional drag in turbulent flows, namely textured and compliant surfaces. Correspondingly, the aim of the thesis is twofold, namely to explore the drag-reducing potential of riblet-textured surfaces, and to characterize the interaction between time-dependent (possibly turbulent) flows and a compliant wall. The work presented in this thesis was performed as part of the European project SEAFRONT, which aimed at the development of environmentally benign antifouling and drag-reducing technologies for the maritime sector.

For a favourable use of riblets in the marine environment, it is essential that they possess antifouling properties. This motivated the investigation of a drag-reducing riblet texture with fouling-release properties (cf. chapter 2). Such a texture was manufactured by two partners within the SEAFRONT project, namely Fraunhofer IFAM and AkzoNobel. With use of a Taylor-Couette setup at TU Delft, we have measured an optimum drag reduction of 6%, like for the riblet texture without fouling-release properties.

While a conventional riblet geometry was employed in the experiments, alternative textures could be investigated as well to find out whether more drag reduction is achievable. We investigated a bird-feather-inspired texture (cf. chapter 3), since a recent study claimed that it would have drag-reducing properties. The texture consists of thin rectangular-shaped riblets in a converging/diverging or herringbone pattern. We performed direct numerical simulations of turbulent flow through a channel with textured walls. An extension of the Fukagata-Iwamoto-Kasagi identity for drag decomposition was used to study the drag change mechanisms. A strong drag increase was found, which was attributed to the secondary flow that forms over regions of riblet convergence/divergence. Hence, the employment of convergent/divergent riblets in the texture seems to be detrimental to turbulent drag reduction.

The second aim of this thesis is to characterize the interaction between time-dependent (possibly turbulent) flows and a compliant wall. Since the interaction can be quite complex, a relatively simple problem was investigated first, namely an oscillatory pressure-driven laminar flow coupled to a compliant viscoelastic layer on a rigid base (cf. chapter 4). The influence of all nine physical parameters in the analytical solution was systematically investigated. The interface velocity approaches zero for heavy, stiff and/or thin solids, such that the classical Womersley flow is recovered. When the forcing frequency, coating softness and coating thickness are sufficiently large, the interface velocity exhibits multiple resonances that are especially strong for purely elastic solids. The lowest resonance frequency is obtained for viscous, heavy fluids and/or lightweight, soft, thick solids. Except near resonances, the one-way coupling yields a quite accurate estimate of the coating deformation.

As a next step, the deformation of a compliant coating in a turbulent flow was investigated using the one-way coupling method (cf. chapter 5). The deformation was computed analytically as the response to a spectrum of stress waves. The influence of five coating properties on the surface displacement was examined. The modelled surface displacement was compared with recent measurements on the deformation of three different coatings in a turbulent boundary-layer flow. The model predicts the order of magnitude of the surface displacement. It also accurately captures the increase of the coating displacement with the Reynolds number and the coating softness. Finally, a scaling was proposed that collapses all the experimental data for the root-mean-square of the vertical surface displacement onto a single curve.

Although the analytical model is promising, it cannot be used to predict how the coating deformation affects the turbulent drag. That requires a two-way coupling approach, e.g. by using direct numerical simulations of turbulent flow coupled to a compliant wall. We provide some literature, theory and simple examples to guide future work on the implementation of such simulations (cf. chapter 6). Possible techniques for the numerical computation of a deforming viscoelastic solid are demonstrated for a compliant coating forced by either a spanwise-homogeneous impulse forcing or a spanwise-homogeneous streamwise-travelling stress wave. The stable integration of a coupled problem is illustrated for an oscillatory flow over a compliant coating.

Finally, we present some ideas for further research in the area of turbulent drag reduction by textured or compliant surfaces (cf. chapter 7). For the drag-reducing riblets with fouling-release properties, a next important step for commercialization is to investigate fouling and wear under in-service conditions. In addition, the search for alternative textured surfaces can continue, e.g. by using a more general immersed boundary method for numerical simulations or rapid prototyping to manufacture unconventional textures for experimental studies in a relatively quick and cheap way. An important recommendation for compliant surfaces is to extend the present research to the two-way coupling regime, such that the influence of the coating deformation on the turbulent drag can be quantified.

Samenvatting

Een significant deel van de brandstof die wordt gebruikt voor transport wordt veroorzaakt door de weerstand in turbulente stroming. Technieken voor vermindering van de turbulente weerstand resulteren in bijbehorende reducties van het brandstofverbruik en broeikasgasemissies, wat wenselijk is zowel vanuit het economisch als het milieu-perspectief (zie hoofdstuk 1). Dit proefschrift onderzoekt twee passieve technieken die kunnen worden geëxploiteerd voor de reductie van wrijvingsweerstand in turbulente stromingen, namelijk getextureerde en vervormbare oppervlaktes. Het doel van het proefschrift is dienovereenkomstig tweërlei, namelijk om het weerstandsverminderende potentieel van geribbelde oppervlaktes te verkennen en om de interactie tussen een tijdsafhankelijke (mogelijk turbulente) stroming en een vervormbare wand te karakteriseren. Het werk dat in dit proefschrift wordt gepresenteerd, is uitgevoerd als onderdeel van het Europese project SEAFRONT, wat als doel had om milieuvriendelijke aangroeiwerende en weerstandsverminderende technologieën voor de maritieme sector te ontwikkelen.

Voor een gunstig gebruik van ribbels in de mariene omgeving is het essentieel dat deze aangroeiwerende eigenschappen bezitten. Dit motiveerde het onderzoek naar een weerstandsverminderende geribbelde textuur met aangroeiwerende eigenschappen (zie hoofdstuk 2). Zo'n textuur is vervaardigd door twee partners uit het SEAFRONT project, namelijk Fraunhofer IFAM en AkzoNobel. Met behulp van een Taylor-Couette opstelling aan de TU Delft hebben we een optimum weerstandsvermindering van 6% gemeten, evenals voor een geribbelde textuur zonder aangroeiwerende eigenschappen.

Terwijl een conventionele ribbelgeometrie is gebruikt in de experimenten, kunnen alternatieve texturen ook worden onderzocht om na te gaan of meer weerstandsvermindering haalbaar is. Wij hebben een textuur die is geïnspireerd door vogelveren onderzocht (zie hoofdstuk 3), aangezien een recente studie claimde dat deze weerstandsverminderende eigenschappen zou bezitten. De textuur bestaat uit dunne, rechthoekvormige ribbels in een convergerend/divergerend of visgraat-patroon. We hebben directe numerieke simulaties van een turbulente stroming door een kanaal met getextureerde wanden uitgevoerd. Een uitbreiding van de Fukagata-Iwamoto-Kasagi-identiteit voor weerstandsdecompositie is

gebruikt om de mechanismen voor weerstandsverandering te bestuderen. Een sterke weerstandstoename is gevonden, wat werd toegeschreven aan de secundaire stroming die ontstaat boven ribbelconvergentie/divergentie. De toepassing van convergerende/divergerende ribbels in de textuur lijkt dus nadelig te zijn voor vermindering van de turbulente weerstand.

Het tweede doel van dit proefschrift is om de interactie tussen tijdsafhankelijke (mogelijk turbulente) stromingen en een vervormbare wand te karakteriseren. Aangezien de interactie behoorlijk complex kan zijn, is een relatief eenvoudig probleem eerst onderzocht, namelijk een oscillerende, drukgedreven, laminaire stroming gekoppeld aan een vervormbare viscoelastische laag op een rigide basis (zie hoofdstuk 4). De invloed van negen fysische parameters in de analytische oplossing is systematisch onderzocht. De grensvlaksnelheid nadert naar nul voor zware, stijve en/of dunne vaste stoffen, zodat de klassieke Womersley-stroming wordt herkreten. Wanneer de frequentie van de forcering, de zachtheid van de coating en de dikte van de coating voldoende groot zijn, dan vertoont de grensvlaksnelheid meerdere resonanties die vooral sterk zijn voor puur elastische vaste stoffen. De laagste resonantiefrequentie wordt verkregen voor viskeuze, zware vloeistoffen en/of lichte, zachte, dikke vaste stoffen. Behalve nabij resonanties geeft de enkelzijdige koppeling een behoorlijk nauwkeurige schatting van de vervorming van de coating.

Vervolgens is de deformatie van een vervormbare coating in een turbulente stroming onderzocht met behulp van de methode van enkelzijdige koppeling (zie hoofdstuk 5). De deformatie is analytisch berekend als de respons op een spectrum van golven van mechanische spanning. De invloed van vijf coatingeigenschappen op de oppervlakverplaatsing is getest. De gemodelleerde oppervlakverplaatsing is vergeleken met recente metingen aan de deformatie van drie verschillende coatings in een turbulente grenslaagstroming. Het model voorspelt de orde van grootte van de oppervlakverplaatsing. Ook beschrijft het nauwkeurig de toename van de coatingverplaatsing met het Reynoldsgetal en de zachtheid van de coating. Tenslotte is een schaling voorgesteld die de experimentele data van de effectieve waarde (rms) van de verticale oppervlakverplaatsing laat samenvallen op een enkele curve.

Hoewel het analytische model veelbelovend is, kan het niet voorspellen hoe de coatingvervorming de turbulente weerstand beïnvloedt. Dat vereist een aanpak van dubbelzijdige koppeling, bijvoorbeeld met behulp van directe numerieke simulaties van een turbulente stroming gekoppeld aan een vervormbare wand. Wij verstrekken enige literatuur, theorie en eenvoudige voorbeelden om toekomstig werk aan de implementatie van zulke simulaties te sturen (zie hoofdstuk 6). Mogelijke technieken voor de numerieke berekening van een vervormende viscoelastische vaste stof worden gedemonstreerd voor een vervormbare coating geforceerd door een in de spanwijdte homogene stoot of een in de spanwijdte homogene stroomafwaartsreizende golf van mechanische spanning. De stabiele integratie van een gekoppeld probleem wordt geïllustreerd voor een oscillerende stroming over een vervormbare coating.

Tenslotte presenteren we een aantal ideeën voor verder onderzoek in het vakgebied van turbulente weerstandsvermindering door getextureerde en vervormbare oppervlaktes (zie hoofdstuk 7). Voor de weerstandsverminderende ribbels met aangroeiwerende eigenschappen is een belangrijke volgende stap voor commercialisatie om aangroei en slijtage tijdens bedrijf te onderzoeken. Verder kan de zoektocht naar alternatieve getextureerde oppervlaktes doorgaan, bijvoorbeeld door gebruik te maken van een meer generieke ‘immersed boundary’ methode voor numerieke simulaties of rapid prototyping om onconventionele texturen voor experimentele studies op een relatief snelle en goedkope manier te vervaardigen. Een belangrijke aanbeveling voor vervormbare oppervlaktes is om het huidige onderzoek uit te breiden naar het regime van dubbelzijdige koppeling zodat de invloed van de coatingvervorming op de turbulente weerstand kan worden gekwantificeerd.

Contents

Summary	vii
Samenvatting	ix
1 Introduction	1
1.1 Biofouling and hydrodynamic drag	1
1.2 Drag reduction benefits	3
1.3 Drag reduction technologies	3
1.4 Aim of the thesis	6
1.5 Outline of the thesis	6
2 Drag-reducing riblets with fouling-release properties	9
2.1 Rationale	9
2.2 Development and testing	11
2.3 Taylor-Couette setup and measurements	11
2.4 Drag computation	14
2.5 Coatings tested	20
2.6 Results	25
2.7 Conclusions and recommendations	35
3 Drag reduction by herringbone riblet texture	37
3.1 Abstract	37
3.2 Introduction	37
3.3 Numerical methods	40
3.4 Drag reduction quantification	43
3.5 Validation	44
3.6 Herringbone riblets	48
3.7 Drag change decomposition	62
3.8 Discussion	70
3.9 Conclusions and outlook	72

4	Oscillatory flow over a compliant layer	75
4.1	Abstract	75
4.2	Introduction	76
4.3	Theory	78
4.4	Analytical solution	80
4.5	Dynamics	86
4.6	Interface velocity	90
4.7	Resonances	94
4.8	Compliant coatings in practice	96
4.9	Conclusions & Perspectives	97
5	Deformation of a compliant wall in a turbulent flow	101
5.1	Abstract	101
5.2	Introduction	102
5.3	One-way coupling model	105
5.4	Coating deformation for a single surface stress wave	109
5.5	Coating deformation in turbulent channel flow	115
5.6	Coating deformation in turbulent boundary-layer flow	129
5.7	Conclusions and perspectives	143
6	Numerical simulations of a deforming compliant layer	147
6.1	Introduction	147
6.2	Literature	148
6.3	Theory	151
6.4	Numerical methods	162
6.5	Spanwise-homogeneous impulse forcing on compliant coating	170
6.6	Deformation of a compliant wall by a travelling stress wave	172
6.7	Oscillatory flow coupled to a compliant wall	174
6.8	Conclusions and recommendations	178
7	Conclusions and perspectives	181
7.1	Textured surfaces	181
7.2	Compliant surfaces	183
A	Direct Numerical Simulations	185
A.1	Time advancement at fixed bulk velocity	185
A.2	Immersed boundary method for blade riblet textures	186
A.3	Simulation parameters	190
B	Coating deformation by oscillatory flow	193
B.1	Deformation of a compressible solid due to surface stresses	193
B.2	Interaction parameters in limiting cases	194

C Coating deformation by turbulent flow	195
C.1 Coating deformation by single travelling stress wave	195
C.2 Wavevector spectrum of measured surface displacement	198
C.3 Travelling waves and point spectra	200
Bibliography	203
Curriculum Vitae	225
Scientific contributions	227
Acknowledgements / Dankwoord	231

Chapter 1

Introduction

This chapter provides the introduction to this thesis. Section 1.1 describes the context in which our research was performed, namely a European project that aimed at the development of environmentally benign antifouling and drag-reducing coatings for maritime applications. Section 1.2 clarifies the drag reduction benefits, also for non-maritime industries. An overview of several drag reduction technologies is provided in section 1.3. Finally, the aim and outline of the thesis are disclosed in sections 1.4 and 1.5.

1.1 Biofouling and hydrodynamic drag

Marine biofouling, the undesired colonization of marine organisms on surfaces immersed in seawater (cf. figure 1.1), has a dramatic impact on several marine-based industries, such as fishery, renewable energy and marine transport. Some of these problematic consequences are: increased fuel consumption and operational costs, additional greenhouse gas emissions, spread of non-native marine species, increase of structural weight, provision of sites for corrosion, increased frequency of maintenance and cleaning.¹ For instance, severe fouling of a ship hull can increase fuel consumption by 40% at cruising speed and can escalate overall voyage costs by 77% (Schultz, 2007).

International shipping is one of the largest consumers of fossil fuels on earth. The scale of the problem is clear from the size of the global trading fleet – 58,000 vessels at the end of 2016 (Department for Transport UK, 2017) – and the significant fuel consumption of a single vessel, e.g. 100 tonnes (i.e. metric tons) of bunker fuel per day for a very large crude carrier. Metrics for the period 2007-2012 suggest that the average annual fuel consumption for all shipping ranged between approximately 247 million and 325 million tonnes (Mt) of fuel with the

¹FP7-OCEAN-2013, Innovative antifouling materials for maritime applications, Part B: Synergistic Fouling Control Technologies (ACRONYM: SEAFRONT).



FIGURE 1.1: Two examples of biofouling: fouled ship hull (*left*)², and fouling close-up (*right*)³.

associated average annual emission of carbon dioxide between 739 and 1135 Mt (Third IMO GHG Study 2014).

Marine biofouling in the shipping industry is typically prevented or reduced with use of antifouling or fouling-release coatings, which have been in use for several decades already. These coatings combat fouling, thereby minimizing hull roughness and the associated hydrodynamic drag, such that fuel consumption and emissions are reduced. While such coatings have primarily been based on biocide-containing paints, environmental awareness and legislation have motivated the development of non-biocidal fouling-release solutions (Yebra et al., 2004; Finnie and Williams, 2010; Callow and Callow, 2011; Lejars et al., 2012).

The need for continuous improvement was the principal motivating factor for the research that was performed within the SEAFRONT project. More specifically, that European Union project aimed at the development of environmentally benign antifouling and drag-reducing coatings for mobile and stationary maritime applications. The project ran from January 2014 till December 2017, and it consisted of 19 partners, namely 5 universities (7 groups), 2 research institutes, 4 large enterprises and 8 small and medium enterprises. More information about the project and its contributing partners can be found on the project's website: <http://seafont-project.eu>.

The research presented in this thesis was performed within the context of the SEAFRONT project, with a specific focus on drag-reducing technologies. Suppose that marine biofouling could completely be eliminated, a next significant challenge to researchers in this field would then be to incorporate technologies that offer hydrodynamic benefits beyond those that are achievable from a smooth surface.

²Ship hull showing extensive fouling by barnacles, International Paint, Akzo Nobel NV, accessed 23 July 2018, <http://www.european-coatings.com/Homepage-news/Nanotechnology-and-anti-fouling>.

³Marine Eco Analytics (MEA-nl), accessed 23 July 2018, <https://www.mea-nl.com/en/expertise/hull-fouling>.

1.2 Drag reduction benefits

The previous section already highlighted the benefits of drag reduction in the maritime context. The concepts of drag and drag reduction, however, are not restricted to the maritime industry. Drag is defined as ‘the retarding force acting on a body (such as an airplane) moving through a fluid (such as air) parallel and opposite to the direction of motion.’⁴ Energy is required to overcome the drag and sustain the motion of moving bodies, such as vehicles (airplanes, automobiles, ships), transported fluids (oil in pipelines) or renewable energy devices (power from tides, waves, wind). For fuel-consuming engines, drag reduction implies also a reduction of the fuel consumption, which is desirable from several viewpoints:

- Cheaper (use less fuel)
- Healthier (less pollutant emissions)
- Fairer (preserve fuel for growing global human population)
- More sustainable (use less from limited fossil fuel supplies)
- More ecological (less greenhouse gas emissions and global warming)

It should be noted, however, that the reduction of fluid drag does not translate into an equally large reduction in the fuel consumption, since not all fuel is used to overcome the fluid drag. It might be of value to illustrate this with an example. For ground vehicles, most of the usable energy from the engine is used to overcome the aerodynamic drag (53%); the rest is attributed to rolling resistance (32%), auxiliary equipment (9%) and the drive-train (6%) (Sudin et al., 2014).

1.3 Drag reduction technologies

Table 1.1 provides an overview of several passive and active drag-reducing methods. In passive methods, drag reduction is obtained in a permanent way: the flow is permanently changed such that drag reduction is always achieved. In contrast, active methods require continual addition of energy for the drag-reducing mechanism to work. Below, we very briefly discuss each drag-reducing method. More detailed theory and/or literature will be provided in the chapters that follow.

Surface shape: drag reduction can be obtained by shape optimization of airship bodies (Lutz and Wagner, 1998). An example from the maritime industry is the use of bulbous bows to reduce the wave-making resistance (Kracht, 1978).

Surface texture: the drag of a sphere can be reduced by delaying the main separation, for example by using a trip wire (Son et al., 2011) or dimples as on a golf ball (Bearman and Harvey, 1976). A texture can also be used to reduce the (turbulent) drag on flat surfaces, for instance by using riblets aligned with the mean flow (Bechert et al., 1997). Riblets impede the turbulent transport of momentum towards the surface, thereby reducing the drag.

Surface elasticity: compliant coatings have been studied as a means to delay transition in laminar flows, to reduce drag in turbulent flows, and to suppress vibrations or noise (Gad-el Hak, 2002). There are some indications that compliant

⁴Merriam-Webster.com, accessed 9 January 2018, <https://www.merriam-webster.com>.

TABLE 1.1: Passive and active methods to obtain fluid drag reduction.

<i>Type</i>	<i>Method</i>	<i>Example(s)</i>
Passive	Surface shape	Shape of airfoil or ship hull
	Surface texture	Riblets (shark skin), dimples
	Surface elasticity	Compliant walls (dolphin skin)
	Surface chemistry	Superhydrophobicity (lotus leaf)
	Surface add-on devices	Vortex generators
Active	Wall mass transfer	Blowing/suction, opposition control
	Fluid injection	Gas bubbles, lubricated transport
	Additive means	Polymers, surfactants
	Wall motion	Wall oscillation or deformation
	Wall cooling or heating	Atmospheric turbulent boundary layer
	Electromagnetic forcing	Steady or time-oscillating Lorentz force

walls can reduce drag in turbulent flows (Lee et al., 1993; Choi et al., 1997); other studies, however, reported a drag increase (Greidanus et al., 2017; Ivanov et al., 2017). Suggested drag-reducing mechanisms include energy dissipation inside the coating, and Reynolds stress reduction due to the coating surface velocity (Kulik, 2012).

Surface chemistry: superhydrophobic surfaces have unique water-repellent properties (like the lotus leaf), which typically results from the combination of surface chemistry with micro- or nanoscale surface roughness (Rothstein, 2010). As a consequence, air pockets can be sustained within the corrugations. The flow partially ‘slips’ over the surface, which yields drag reduction in both laminar and turbulent flows.

Surface add-on devices: vortex generators can be used for drag reduction in two ways, either by delaying boundary-layer flow separation (Lin, 2002) or by delaying the transition from laminar to turbulent flow (Shahinfar et al., 2012). Vehicle aerodynamics can be improved with the addition of vortex generators, spoilers, diffusers, deflectors, etc. (Sudin et al., 2014).

Wall mass transfer: uniform blowing at the wall in a spatially developing turbulent boundary layer enhances turbulence, but the thickening of the boundary layer still yields a net drag reduction (Kametani and Fukagata, 2011). Another control strategy combines suction and blowing - as in oscillatory or synthetic jets with zero net mass flux - to influence the aerodynamics of bluff bodies or to control the lift and drag on airfoils (Glezer and Amitay, 2002). An example of a closed-loop or feedback method is opposition control, in which blowing/suction is adapted to the instantaneous near-wall flow velocity (Choi et al., 1994).

Fluid injection: fluid injection is distinguished from wall mass transfer in that a fluid with different properties is injected into the flow. Two injection regimes can be identified, namely the dispersed and the stratified regime. In the dispersed phase, the fluid flow contains separate pockets or bubbles of a different

fluid. The drag reductions obtained by injecting gas bubbles (Murai, 2014) can be attributed to density reduction as well as bubble interactions with the turbulent flow (Ceccio, 2010). The stratified phase is characterized by a sustainable fluid layer between the object and the surrounding fluid. Examples include the use of gas layers or cavities (Murai, 2014), and water-lubricated transport of heavy oil (Ghosh et al., 2009).

Additive means: drag can also be reduced through the addition of drag reducing agents (DRAs) which are usually high-mass polymers or surfactants (surface active agents). The most notable application of polymer drag-reducing additives is in the Trans-Alaska Pipeline System, where polymer injection has been responsible for a 50% increase of oil flow (White, 2003). The drag-reducing mechanism involves the interaction between polymers and the near-wall turbulence regeneration cycle (White and Mungal, 2008).

Wall motion: two types of wall motion can be distinguished, namely wall oscillation (in-plane wall motion, Quadrio (2011)) and wall deformation (out-of-plane wall motion, Tomiyama and Fukagata (2013)). The motion can be spatially uniform, or a travelling wave in the streamwise or spanwise direction. For wall oscillation, the drag-reducing mechanism is identified as the control of the near-wall longitudinal vortices and the corresponding suppression of the instability of the low-speed streaks (Karniadakis and Choi, 2003). Complete relaminarization has been obtained with a travelling wave-like wall deformation (i.e. peristalsis) in turbulent channel flow (Nakanishi et al., 2012). Two mechanisms may play a role here, namely modification of the near-wall turbulence structures, and additional pumping from the wall (Kim, 2011; Nakanishi et al., 2012).

Wall cooling or heating: wall cooling can stabilize or eventually extinguish turbulence, thereby reducing turbulent drag significantly (Wilkinson et al., 1988; Kametani and Fukagata, 2012). This typically happens in the atmospheric boundary layer at the end of a sunny day (Stull, 2012). Wall heating is another possibility: substantial drag reduction can be realized with a heated sphere during free fall in water when a Leidenfrost vapour layer forms on the surface (Vakarelski et al., 2014). Drag reduction was also obtained numerically with a periodic array of heating and cooling strips in a gravitational field; the drag reduction was attributed to the oscillatory fluid motion induced by the buoyancy forces (Yoon et al., 2006).

Electromagnetic forcing: the turbulent flow can also be manipulated with the electromagnetic Lorentz force. Drag reductions were obtained with both steady and time-oscillating forces (Shatrov and Gerbeth, 2007). Turbulence can even be completely destroyed with strong uniform magnetic fields (Lee and Choi, 2001).

From table 1.1 it is clear that many different ways exist by which turbulent drag can be reduced. This might be due to the fact that the turbulent boundary layer is sensitive to many factors. Bushnell and McGinley (1989) mention several parameters that have a first-order influence upon the two-dimensional turbulent boundary layer structure. Their list is reproduced here for convenience:

- Pressure gradient
- Coriolis forces
- Wall curvature
- Wall roughness
- Compliant walls (wall motion)
- Energy release / chemical reaction
- Proximity to transition / Reynolds number
- Shock interaction
- Density stratification (e.g. buoyancy problem)
- Additives (polymers, fibers, surfactants)
- Compressibility (density variation)
- Two-phase flow
- Electrohydrodynamic (EHD) and magnetohydrodynamic (MHD) forces
- Stream oscillations
- Wall permeability / microgeometry
- Wall mass transfer

Note that they distinguish wall roughness and wall curvature: small geometry variations (scale $< \mathcal{O}(\delta_{bl})$ with boundary-layer thickness δ_{bl}) are termed ‘roughness’, whereas flow changes due to large-scale geometric non-uniformities (scale $> \mathcal{O}(\delta_{bl})$) are termed ‘curvature’ effects.

1.4 Aim of the thesis

The present thesis investigates two passive techniques that can possibly be used for drag reduction in turbulent flows, namely textured surfaces and compliant surfaces. Correspondingly, the aim of this thesis is twofold:

1. Explore the drag-reducing potential of alternative riblet-textured surfaces.
2. Characterize the interaction between time-dependent (possibly turbulent) flows and a compliant wall.

Although turbulent drag reduction is the ultimate goal, the interaction between a turbulent flow and a compliant wall is so complex that this thesis starts with a characterization of that interaction. More details are provided in the next section.

1.5 Outline of the thesis

The thesis follows the two main objectives that have been stated in the previous section. The first aim is considered in the chapters 2 and 3, while the second aim is addressed in the chapters 4, 5 and 6.

Chapter 2 summarizes the drag measurements in a Taylor-Couette setup that were performed on several textured and untextured coatings. The main focus is on the drag-reducing riblets with fouling-release properties that were manufactured as a result of the collaboration between two project partners, namely Fraunhofer IFAM and AkzoNobel. The riblet-textured surfaces have a conventional geometry, namely streamwise-homogeneous riblets aligned with

the mean flow. The drag reduction of the antifouling riblet texture is compared with a similar riblet texture without fouling-control properties.

While chapter 2 considers the conventional riblet texture, chapter 3 investigates the drag-reducing performance of an alternative texture that consists of riblets in a herringbone pattern. The aim is to quantify the drag change for this texture as compared to a smooth wall and to study the underlying mechanisms. To that purpose, direct numerical simulations of turbulent channel flow over a herringbone riblet geometry were performed. Flow statistics and a drag decomposition are used to elucidate the influence of the texture on the flow and the drag.

Chapter 4 is the first chapter that addresses the second thesis objective. It presents an analytical study of oscillatory pressure-driven laminar flow two-way coupled to a compliant viscoelastic layer on a rigid base. The coating deforms in the streamwise direction only, and the deformation solely depends on time and the wall-normal coordinate. Although the flow is not turbulent, this relatively simple problem facilitates the understanding of the interaction between a time-dependent flow and a compliant wall. An analytical solution for the fluid and solid velocity is obtained and the influence of the problem parameters is systematically investigated. Except near resonances, the one-way coupling approach yields a quite accurate estimate of the coating deformation.

While chapter 4 is limited to laminar flows, chapter 5 considers the deformation of a compliant coating in a turbulent flow, using the one-way coupling approach. The analytically calculated coating deformation now depends on the temporal, the streamwise and the wall-normal coordinate. The influence of five coating properties on the surface deformation is investigated. The modelled surface displacement is also compared with recent measurements on the deformation of three different coatings in a turbulent boundary-layer flow.

Although the analytical model from chapter 5 yields promising results, it nevertheless relies on many assumptions. A better approximation of an actual turbulent flow coupled to a compliant layer can be obtained with numerical simulations. The purpose of chapter 6 is to provide some literature, theory and simple examples to guide future work on the implementation of such simulations. We demonstrate possible techniques for the numerical computation of a deforming viscoelastic solid, and for the stable integration of coupled problems. The coating deformation is computed for three types of surface stresses, namely a spanwise-homogeneous impulse forcing, a spanwise-homogeneous streamwise-travelling stress wave, and the shear stress from an oscillatory flow.

Finally, chapter 7 summarizes the conclusions of this thesis in relation to the two objectives from the previous section. It also presents an outlook for further research in the area of turbulent drag reduction by textured or compliant surfaces.

Chapter 2

Drag-reducing riblets with fouling-release properties

This chapter describes the measurements that were performed to quantify the influence of different coatings on the skin frictional drag. (The terms skin frictional drag, skin friction and drag are all used interchangeably in this chapter to refer to the tangential force acting on the surface due to flow.) The main purpose is to assess the drag-reducing performance of a riblet coating with fouling-release properties.

This chapter is organized as follows: section 2.1 elucidates the rationale for a drag-reducing and foul-releasing coating, while section 2.2 summarizes the development and testing of such a coating. The remainder of this chapter is devoted to the hydrodynamic tests with the Taylor-Couette setup. Section 2.3 describes the setup and the measurement procedure, whereas section 2.4 explains the data postprocessing to compute the drag. Section 2.5 gives an overview of the coatings that were tested, followed by the measurement results in section 2.6 and the conclusions in section 2.7.

2.1 Rationale¹

Chapter 1 already motivated the need for fouling-controlling surfaces in the maritime industry. A next significant challenge to researchers in this field is to design and formulate coating systems that maintain the desired fouling-control performance whilst additionally offering hydrodynamic benefits beyond those which are achievable from a smooth surface. For instance, the hydrodynamic drag in a turbulent flow can be reduced with use of a riblet texture. This

¹Adapted from the introduction of H. O. G. Benschop, A. J. Guerin, A. Brinkmann, M. L. Dale, A. A. Finnie, W.-P. Breugem, A. S. Clare, D. Stübing, C. Price, and K. J. Reynolds. Drag-reducing riblets with fouling-release properties: development and testing. *Biofouling*, pages 1–13, 2018.

texture has been found on the scales of some shark skins and consists of ridges or riblets aligned with the mean flow direction (Dean and Bhushan, 2010). A drag reduction of 8.2% has been obtained with a simplified geometry of trapezoidal grooves with wedge-like ribs (Bechert et al., 1997). Researchers from Fraunhofer IFAM developed a simultaneous embossing-curing technology to produce riblet-textured paints denoted as Dual-cure Riblets. Maximum drag reductions of 5.2% and 6.2% were measured in water and air, respectively (Stenzel et al., 2011).

The utility of these riblet paints in under-water applications is however compromised by the absence of fouling-control properties. Investigations showed that micro-textured surfaces, including similar riblet designs, may reduce colonization by certain biofouling organisms, such as barnacle cyprids (Ring, 2000; Berntsson et al., 2000). However, many other fouling taxa are not deterred by surface topographies in the micrometre range. Organisms settling on the riblet-textured surface will have a detrimental effect on its drag-reducing performance; hence the need for fouling-controlling riblet textures. Addition of biocides to the non-eroding dual-cure paint formulation only provided limited protection against biofouling. After 12 months of static immersion the tested surfaces were overgrown with macrofouling since the biocide concentration in the near-surface coating layers was too low to maintain the antifouling effect (Stenzel et al., 2016).

One solution would be to produce a riblet coating using a material or surface that is already known to have good anti-fouling or fouling-release properties. This has motivated the design, synthesis and testing of a single synthetically engineered solution which effectively combines the fouling-control properties of the commercial fouling-release product Intersleek[®] 1100SR with the drag-reducing properties of the riblet texture.

Several partners of the SEAFRONT project were involved in the development and testing of such a drag-reducing and fouling-releasing coating. Two partners developed the coating, namely Fraunhofer IFAM (Institute for Manufacturing Technology and Advanced Materials, D. Stübing, A. Brinkmann and coworkers) and AkzoNobel (International Paint Ltd., K. J. Reynolds, C. Price, A. A. Finnie, M. Dale and colleagues); Fraunhofer IFAM contributed with the embossing-curing technology and AkzoNobel provided the Intersleek[®] 1100SR system². The hydrodynamic performance was assessed at Delft University of Technology (section Fluid Mechanics, W.-P. Breugem, H. O. G. Benschop and collaborators) with use of the Taylor-Couette setup for drag measurements. The antifouling properties were characterized by Newcastle University (school of Natural and Environmental Sciences, A. S. Clare, A. J. Guerin and colleagues) and AkzoNobel; Newcastle University used barnacle settlement, and diatom adhesion and ease-of-removal assays; AkzoNobel performed biofilm growth and release, and field immersion testing. The next section provides a summary of this development and testing; more information can be found in Benschop et al. (2018). Subsequent sections will focus on the hydrodynamic assays.

²Advanced fluoropolymer foul release coating for the control of slime, one of the marine coatings that belong to AkzoNobel's International[®] brand, see also <https://www.international-marine.com/product/intersleek-1100sr>, accessed 24 July 2018.

2.2 Development and testing³

The manufacture and preliminary testing of a drag-reducing riblet texture with fouling-control properties is presented. The commercial fouling-release product Intersleek[®] 1100SR was modified to make it compatible with an embossing technology that is used to manufacture riblet-textured coatings. The drag-reducing and fouling-release performance was assessed using various techniques. Hydrodynamic drag measurements in a Taylor-Couette setup showed that the Modified Intersleek[®] Riblets reduce drag by up to 6% as compared to a smooth uncoated surface. Barnacle settlement assays demonstrated that the riblet pattern does not substantially reduce the ability of Intersleek[®] 1100SR to prevent fouling by *Balanus amphitrite* cyprids. Diatom adhesion tests revealed significantly higher attachment of diatoms on the riblet surface as compared to smooth Intersleek[®] 1100SR. However, after exposure to flow, the final cell density was very similar to the smooth surface. Statically immersed panels in natural seawater showed an increase of biofilm cover due to the riblet texture. However, the release of semi-natural biofilms grown in a multi-species biofilm culturing reactor (slime farm) was largely unaffected by the presence of a riblet texture. Future research could consider the use of Modified Intersleek[®] Riblets on moving vessels.

2.3 Taylor-Couette setup and measurements⁴

The hydrodynamic drag of coated cylinders was measured with a Taylor-Couette facility, which is depicted in figure 2.1. It consists of two concentric cylinders of acrylic glass (Plexiglas, PMMA): an inner cylinder and an uncoated outer cylinder. The curved outer surface of the inner cylinder was either coated or uncoated; the bottom and top lids or end plates were uncoated. Ball bearings at bottom and top were used for stabilization. The height of the outer cylinder was $L_o = 22.0$ cm; the height of the inner cylinder (including bottom and top lids) varied between $L_i = 21.65$ cm and 21.71 cm for different cylinders. Small gaps, so-called Von Kármán (VK) gaps, of about 1.5 mm were present between the bottom and top end plates of the two cylinders. The radius of the inner surface of the outer cylinder was $r_o = 12.0$ cm. The radius of the outer surface of the inner cylinder varied between $r_i = 11.00$ cm and 11.09 cm, depending on the radius of the uncoated cylinder and the thickness of the applied coating. The radial gap in between the cylinders, which is called the Taylor-Couette (TC) gap, had thus a width $d = r_o - r_i$ between 0.91 and 1.0 cm. The Taylor-Couette gap and both Von Kármán gaps (bottom and top) were filled with demineralised water. The curvature of the flow geometry can be quantified with two dimensionless

³Adapted from the abstract of H. O. G. Benschop, A. J. Guerin, A. Brinkmann, M. L. Dale, A. A. Finnie, W.-P. Breugem, A. S. Clare, D. Stübing, C. Price, and K. J. Reynolds. Drag-reducing riblets with fouling-release properties: development and testing. *Biofouling*, pages 1–13, 2018.

⁴A large part of this work is based on the research reported in A. Greidanus, R. Delfos, S. Tokgoz, and J. Westerweel. Turbulent Taylor–Couette flow over riblets: drag reduction and the effect of bulk fluid rotation. *Experiments in Fluids*, 56(5):107, 2015.

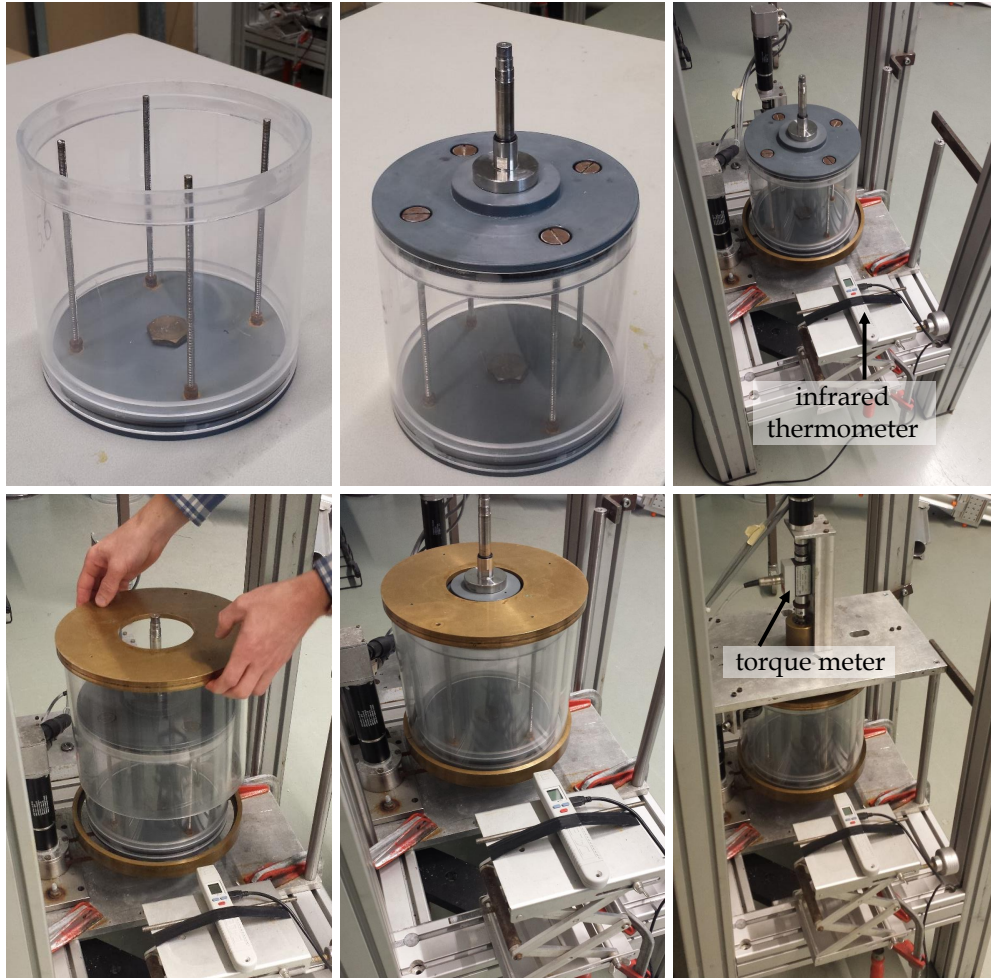


FIGURE 2.1: Mounting of the Taylor-Couette setup for hydrodynamic drag measurements. From left to right and top to bottom: bottom plate of the inner cylinder with an uncoated PMMA cylinder; inner cylinder with bottom and top end plates; inner cylinder placed on the brass bottom plate of the outer cylinder; mounting of the uncoated PMMA outer cylinder and the attached brass top plate; mounted inner and outer cylinder; completely mounted Taylor-Couette setup, where the metal construction on top contains the ball bearings and the torque meter for the axis of the inner cylinder.

numbers (Greidanus et al., 2015), namely the gap ratio $\eta = r_i/r_o$ (between 0.917 and 0.924) and the curvature number $R_C = (1 - \eta)/\sqrt{\eta}$ (between 0.087 and 0.079).

The outer cylinder rotates with an angular frequency ω_o , such that the corresponding azimuthal velocity of the inner surface is $U_o = \omega_o r_o$. Similarly, the inner cylinder has an angular frequency ω_i and an outer-surface velocity $U_i = \omega_i r_i$. The

sign of the frequencies and velocities indicates the rotation direction, with a positive sign for the rotation direction of the outer cylinder. Using the velocities U_i and U_o , several dimensionless numbers can be defined:

$$Re_i = \frac{U_i d}{\nu}, \quad (2.1a)$$

$$Re_o = \frac{U_o d}{\nu}, \quad (2.1b)$$

$$Re_s = \frac{2}{1 + \eta} |\eta Re_o - Re_i| \equiv \frac{U_{sh} d}{\nu}, \quad (2.1c)$$

$$R_\Omega = (1 - \eta) \frac{Re_i + Re_o}{\eta Re_o - Re_i}, \quad (2.1d)$$

where d is the radial gap width, ν the kinematic fluid viscosity and η the gap ratio. Re_i and Re_o are the inner- and outer-cylinder Reynolds numbers. The shear Reynolds number Re_s is based on the shear rate between the two cylinders; a shear velocity U_{sh} is introduced for convenience. The rotation number R_Ω quantifies the mean fluid rotation relative to the shear. The measurements presented in this thesis were performed in exact counter-rotation: the cylinders rotate in opposite directions with exactly the same surface speed, i.e. $U_i = -U_o$, such that $Re_i = -Re_o$ and $R_\Omega = 0$. In that specific case, the shear velocity as defined in equation 2.1c simply becomes the velocity difference between both cylinders, i.e. $U_{sh} = U_o - U_i = 2U_o$. Given that $d \approx 1.0$ cm and $\nu \approx 10^{-6}$ m²s⁻¹, the following relation between Re_s and U_{sh} can be used as a rule of thumb: $Re_s \approx 10^4 \cdot U_{sh}$.

Two quantities were measured, namely the drag of the inner cylinder and the water temperature. The drag of the inner cylinder was determined from the torque on the inner cylinder measured with a co-rotating torque meter in the shaft. The water temperature was measured to compute the fluid viscosity, which depends on temperature. During a typical experiment of approximately 78 minutes, the fluid temperature rose with 4 to 5 °C, which resulted in a decrease of the viscosity. The water temperature was measured with a thermocouple through an opening in the top end plate of the outer cylinder, just before and after each measurement series (stationary cylinders). When the cylinders were rotating, however, an infrared thermometer was used to measure the temperature of the outer wall of the outer cylinder.

A fixed measurement procedure was followed to allow a fair comparison between different coatings. Before a coated cylinder was measured, it had been soaked in demineralised water to reduce the possibility that coating compounds (e.g. residual solvent) would contaminate the water in the setup. After removal of the cylinder from the water, its dimensions (diameter and length) were measured with a vernier caliper. Next, the inner and outer cylinder were mounted in the setup (figure 2.1). The Taylor-Couette gap and both Von Kármán gaps (bottom and top) were filled with demineralised water. Care was taken to remove air bubbles that could be present in the setup. The fluid temperature was measured

with a thermocouple. A LabVIEW software program was used to execute the measurement series and for data acquisition of the measured torque, the angular velocity of the inner cylinder, and the temperature of the outer-cylinder wall. The speed of the cylinders was increased in 38 steps from 0 to about 4.6 m s^{-1} , such that the velocity difference (or shear velocity U_{sh}) between the surfaces of the two cylinders varied from 0 to 9.2 m s^{-1} . At each cylinder speed, torque measurements were taken at a sampling frequency of 2 kHz for 120 s. The average torque was determined from the last 100 s to ensure that the cylinders were moving at constant speed. A thermocouple was again used to measure the fluid temperature just after the measurement had finished.

There are several advantages of using the Taylor-Couette facility for skin friction measurements as compared to drag plate measurements in a water tunnel. *First*, the Taylor-Couette flow is a fully-developed turbulent flow. On the contrary, boundary-layer flow is developing flow in two respects: the boundary layer not only grows in thickness, but it also needs a certain entrance length to adapt to the possibly different coating properties (e.g. texture). *Second*, the Taylor-Couette setup can reach high wall shear stresses, comparable to values found for real ships. This is due to the fact that large differential velocities (on the order of 10 m s^{-1}) can be reached for a gap width as small as 1 cm in our case. *Third*, the Taylor-Couette facility is small as compared to a water tunnel: only a surface area of 0.15 m^2 needs to be coated, whereas the water tunnel plates used in the related research of Bezuijen (2017) have an area of 0.59 m^2 . In addition, the inner test cylinder can be easily replaced by one person, and one measurement series of the skin friction as function of the differential speed typically takes about 2 hours.

There are also a few issues that should be carefully considered when performing drag measurements with a Taylor-Couette setup. *First*, the turbulent flow created in between two rotating cylinders is slightly different from boundary-layer flow due to the presence of curvature and a second wall. The amount of drag reduction that can be realized in a Taylor-Couette facility might therefore be different from that in a boundary-layer flow. *Second*, the Von Kármán gaps deliver a considerable contribution to the measured torque on the inner cylinder. That contribution should be subtracted to obtain the drag that is solely due to the coating on the cylinder surface. *Third*, when the friction coefficient of the coated inner cylinder is different from that of an uncoated surface, the bulk fluid obtains a net rotation, which will affect the measured torque. The last two issues will be addressed in the next section.

2.4 Drag computation⁵

This section elaborates on the postprocessing of the obtained data. The first subsection describes the use of the temperature data to infer the fluid viscosity.

⁵A large part of this work is based on the research reported in A. Greidanus, R. Delfos, S. Tokgoz, and J. Westerweel. Turbulent Taylor–Couette flow over riblets: drag reduction and the effect of bulk fluid rotation. *Experiments in Fluids*, 56(5):107, 2015.

The second and third subsection elucidate how the drag of different cylinders was computed and compared. The goal of the Taylor-Couette measurements was to quantify how different coatings influence the drag. Specifically, we are interested in the change of the drag as compared to a smooth (uncoated) cylinder. The second subsection therefore quantifies how the reference drag of a smooth wall was determined, while the last subsection clarifies how the drag change was computed.

2.4.1 Fluid viscosity

The temperature of the fluid inside the setup was determined from the data of the infrared thermometer with help of a heat balance equation. The two thermocouple measurements were used to calibrate this computation. Finally, the water viscosity was determined from the thus computed water temperature using an empirical formula for the kinematic viscosity (Cheng, 2008).

2.4.2 Reference drag of a smooth wall

The torque M^{meas} measured by the torque meter depends on the shear velocity U_{sh} , and can be decomposed into two parts:

$$M^{\text{meas}} = M^{\text{tot}} + M^{\text{offset}}, \quad (2.2)$$

with M^{tot} the velocity-dependent total torque on the inner cylinder and M^{offset} the velocity-independent torque offset, which represents the nonzero torque for stationary cylinders. The latter was determined by extrapolating a polynomial fit of the time-averaged torques for the first nine cylinder speeds to zero velocity. The total torque on the inner cylinder is also decomposed:

$$M^{\text{tot}} = M^{\text{VK}} + M^{\text{TC}}. \quad (2.3)$$

The contribution of the Von Kármán gaps, M^{VK} , accounts for the torque that is exerted on the top and bottom end plates of the inner cylinder. The contribution of the Taylor-Couette gap, M^{TC} , accounts for the torque that is exerted on the cylindrical surface of the inner cylinder. The latter can be written as the product of the wall shear stress $\tau_{w,i}$ on the cylindrical wall, the surface area and the lever arm:

$$M^{\text{TC}} = \tau_{w,i} \cdot 2\pi r_i L_i \cdot r_i. \quad (2.4)$$

The friction coefficient is obtained when $\tau_{w,i}$ is normalized with $(1/2)\rho U_{sh}^2$, which yields:

$$c_{f0}^{\text{TC}} = \frac{\tau_{w,i}}{(1/2)\rho U_{sh}^2} = \frac{M^{\text{TC}}}{\pi r_i^2 L_i \rho U_{sh}^2}, \quad (2.5)$$

with fluid mass density ρ . The subscript 0 is used to denote a smooth (uncoated) cylinder. When equation 2.3 is normalized in the same way (using the same

factor), the following relation is obtained:

$$c_{f0}^{\text{tot}} = c_{f0}^{\text{VK}} + c_{f0}^{\text{TC}}. \quad (2.6)$$

In the context of drag reduction, we are interested in the change of the wall shear stress on the cylindrical surface of the inner cylinder, so c_{f0}^{TC} is the quantity of particular interest. However, only c_{f0}^{tot} can be derived directly from the measurements. Knowledge of c_{f0}^{VK} is required to obtain c_{f0}^{TC} . It is assumed that the VK contribution is a certain fraction of the total torque:

$$c_{f0}^{\text{VK}} = \gamma_{\text{cor}} c_{f0}^{\text{tot}}. \quad (2.7)$$

The fraction γ_{cor} depends on Re_s . Greidanus et al. (2015) proposed the dependence that is plotted in figure 2.2. For most Reynolds numbers, about 30% of the total torque is attributed to the VK gaps.

To quantify the drag change of coated cylinders, first the reference drag of a smooth cylinder should be determined. The use of a single dataset as a reference is not desirable, because the scatter of that data then also appears when the drag change is computed. Instead, several measurements on smooth cylinders were performed to compute a baseline or reference line. The procedure is as follows:

1. For each measurement of a smooth cylinder, compute:

- (a) c_{f0}^{tot} ,
- (b) $c_{f0}^{\text{VK}} = \gamma_{\text{cor}} c_{f0}^{\text{tot}}$,
- (c) $c_{f0}^{\text{TC}} = c_{f0}^{\text{tot}} - c_{f0}^{\text{VK}}$.

2. Fit a power law through all the data c_{f0}^{TC} to obtain the baseline $c_{f,b}^{\text{TC}}$.

3. Determine the baseline also for the other contributions:

- (a) $c_{f,b}^{\text{tot}} = \frac{1}{1-\gamma_{\text{cor}}} c_{f,b}^{\text{TC}}$, total contribution;
- (b) $c_{f,b}^{\text{VK}} = \frac{\gamma_{\text{cor}}}{1-\gamma_{\text{cor}}} c_{f,b}^{\text{TC}}$, VK contribution.

Note that the subscript b is used to denote the baseline. The actual measurements and the baseline will be shown in section 2.6.

2.4.3 Drag change relative to a smooth wall

For coated cylinders, the total torque can again be decomposed as $M^{\text{tot}} = M^{\text{VK}} + M^{\text{TC}}$. However, this time M^{TC} is decomposed as well:

$$M^{\text{TC}} = M_0^{\text{TC}} + \Delta M^{\text{rot}} + \Delta M^{\text{surf}}, \quad (2.8)$$

where M_0^{TC} is the contribution for a smooth cylindrical wall. The second contribution, ΔM^{rot} , represents the change of the torque that results from the effect

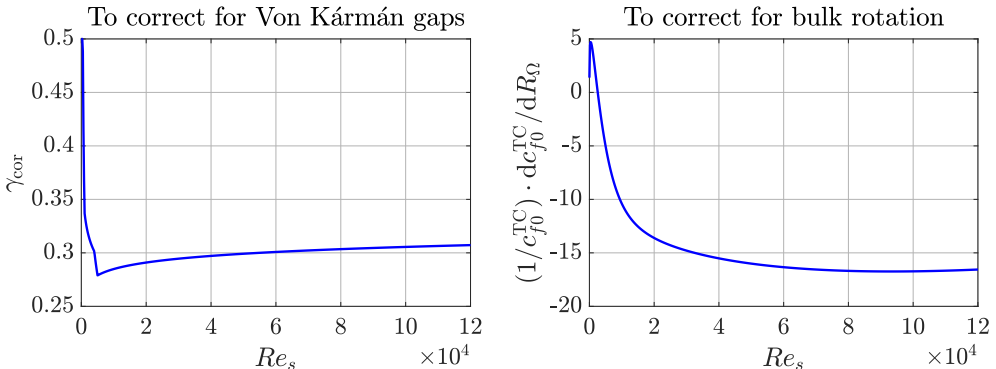


FIGURE 2.2: Two functions that were used to correct the measured torque. *Left*: function to correct for the contribution of the VK gaps. *Right*: function to correct for the effect of bulk fluid rotation.

of bulk fluid rotation, as will be explained below. Finally, the third contribution, ΔM^{surf} , represents the change of the torque that results from the coated surface of the inner cylinder. Using the same normalization as for smooth walls, the latter equation can be rewritten in dimensionless form:

$$c_f^{\text{TC}} = c_f^{\text{tot}} - c_f^{\text{VK}} = c_{f0}^{\text{TC}} + \Delta c_f^{\text{rot}} + \Delta c_f^{\text{surf}}. \quad (2.9)$$

This relation can be used to introduce the drag change:

$$\begin{aligned} \frac{c_f^{\text{TC}} - c_{f0}^{\text{TC}}}{c_{f0}^{\text{TC}}} &= \frac{\Delta c_f^{\text{rot}}}{c_{f0}^{\text{TC}}} + \frac{\Delta c_f^{\text{surf}}}{c_{f0}^{\text{TC}}}, \\ DC^{\text{TC}} &= DC^{\text{rot}} + DC^{\text{surf}} \end{aligned} \quad (2.10)$$

The second equation introduces symbols that represent the fractions that appear in the first equation. The drag in the TC gap thus changes for two reasons, namely due to bulk fluid rotation and due to the coating.

The quantity of particular interest is $DC^{\text{surf}} \equiv DC$; the superscript ‘surf’ is dropped for convenience. The drag change DC can be computed from c_f^{tot} as soon as three other parameters are also known, namely c_f^{VK} , c_{f0}^{TC} and Δc_f^{rot} . It is assumed that the VK contribution is the same as for a smooth wall, i.e. $c_f^{\text{VK}} = c_{f,b}^{\text{VK}}$. The TC contribution for a smooth cylinder is also obtained from the baseline: $c_{f0}^{\text{TC}} = c_{f,b}^{\text{TC}}$. The next paragraph explains how Δc_f^{rot} is computed.

Bulk fluid rotation effect The contribution Δc_f^{rot} is computed using the procedure that is outlined in Greidanus et al. (2015). Instead of repeating the whole derivation, some of the key results are summarized here. When the friction coefficient of the inner cylinder has changed, the bulk fluid will co-rotate slightly with either the inner or the outer cylinder. In other words, the bulk velocity U_b

will be nonzero. The new bulk velocity can be estimated from:

$$\delta_b \equiv \frac{U_b}{U_o} = \frac{1 - \sqrt{c_f^{\text{TC}}/c_{f0}^{\text{TC}}}}{1 + \sqrt{c_f^{\text{TC}}/c_{f0}^{\text{TC}}}}. \quad (2.11)$$

When there is no drag change, $c_f^{\text{TC}}/c_{f0}^{\text{TC}} = 1$ and $U_b = 0$. When the drag of the inner cylinder wall increases, $c_f^{\text{TC}}/c_{f0}^{\text{TC}} > 1$ and $U_b < 0$, which means that the fluid slightly co-rotates with the inner cylinder. When the drag reduces, $c_f^{\text{TC}}/c_{f0}^{\text{TC}} < 1$ and $U_b > 0$, which indicates that the bulk flow co-rotates with the outer cylinder. The non-zero bulk velocity can also be quantified with an apparent rotation number \widehat{R}_Ω , which is computed as follows:

$$\widehat{R}_\Omega = \frac{2\delta_b(1 - \eta)}{1 + \eta - \delta_b(1 - \eta)}. \quad (2.12)$$

All measurements were performed at exact counter-rotation, so $R_\Omega = 0$. In reality, the rotation number for smooth cylinders is close to zero: $R_\Omega \lesssim 10^{-4}$ for $Re_s \gtrsim 10^4$. When the inner cylinder is coated with drag-reducing riblets, the apparent rotation number $\widehat{R}_\Omega = O(10^{-3})$, which seems small. However, the friction coefficient strongly depends on the rotation number. In an elaborate measurement campaign, Greidanus et al. (2015) determined c_{f0}^{TC} for several rotation numbers slightly different from zero. Data was obtained for two smooth cylinders and for Reynolds numbers $Re_s = 4 \cdot 10^3$ to 10^5 . Based on that data, the dependence on the rotation number was quantified with the slope $dc_{f0}^{\text{TC}}/dR_\Omega$ and the following fit was obtained:

$$\frac{dc_{f0}^{\text{TC}}}{dR_\Omega} = 4 \cdot 10^{-3} \cdot \left(11 \cdot e^{-Re_s/3500} + Re_s/90000 - 5.3 \right). \quad (2.13)$$

When this slope is multiplied with the apparent rotation number, an estimate for the change of c_f^{TC} due to rotation is obtained: $\Delta c_f^{\text{rot}} = \left(dc_{f0}^{\text{TC}}/dR_\Omega \right) \cdot \widehat{R}_\Omega$ and therefore:

$$DC^{\text{rot}} = \frac{1}{c_{f0}^{\text{TC}}} \frac{dc_{f0}^{\text{TC}}}{dR_\Omega} \widehat{R}_\Omega. \quad (2.14)$$

Figure 2.2 shows $(1/c_{f0}^{\text{TC}}) \cdot dc_{f0}^{\text{TC}}/dR_\Omega$ as function of Re_s .

Summary of corrections Till now, two corrections have been proposed, namely the first to correct for the contribution from the VK gaps and the second to correct for bulk flow rotation. Using the uncorrected or the corrected data, four drag

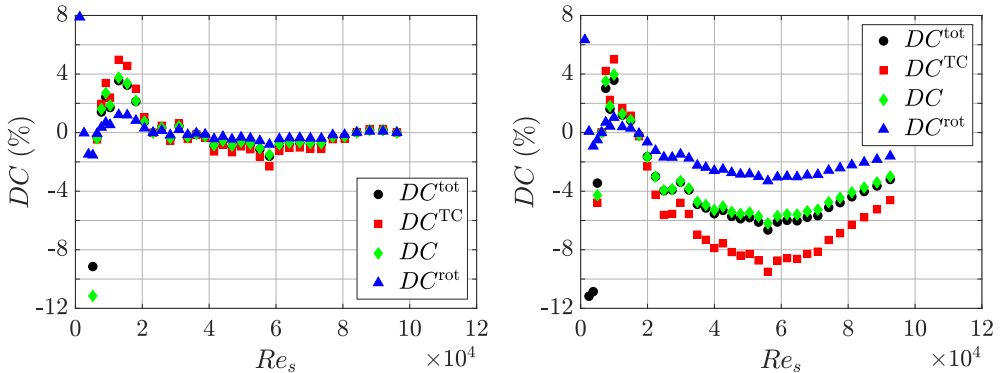


FIGURE 2.3: Several possible definitions for the drag change. DC^{tot} uses the uncorrected data, DC^{TC} is based on the data corrected for the VK gaps and DC is derived from the data corrected for both the VK gaps and bulk rotation. DC^{rot} is the contribution to DC^{TC} that is attributed to bulk rotation. *Left*: Smooth (c2), an uncoated cylinder. *Right*: Modified Intersleek[®] Riblets (a2), a riblet-coated cylinder.

changes can be defined:

$$\begin{aligned}
 DC^{\text{tot}} &= \frac{c_f^{\text{tot}} - c_{f0}^{\text{tot}}}{c_{f0}^{\text{tot}}}, & DC^{\text{TC}} &= \frac{c_f^{\text{TC}} - c_{f0}^{\text{TC}}}{c_{f0}^{\text{TC}}}, \\
 DC^{\text{rot}} &= \frac{\Delta c_f^{\text{rot}}}{c_{f0}^{\text{TC}}}, & DC &= \frac{\Delta c_f^{\text{surf}}}{c_{f0}^{\text{TC}}},
 \end{aligned}
 \tag{2.15}$$

where DC^{tot} uses the uncorrected data, DC^{TC} is based on the data corrected for the VK gaps and DC is derived from the data corrected for both the VK gaps and bulk rotation. Note that DC^{TC} , DC^{rot} and DC have already appeared in equation 2.10. These four quantities were computed for all cylinders, including the uncoated ones. The data analysis can thus be summarized as follows:

1. For each measurement of an arbitrary cylinder, compute:

- (a) c_f^{tot} ,
- (b) $c_f^{\text{VK}} = c_{f,b}^{\text{VK}}$ from the baseline,
- (c) $c_f^{\text{TC}} = c_f^{\text{tot}} - c_f^{\text{VK}}$,
- (d) $c_{f0}^{\text{tot}} = c_{f,b}^{\text{tot}}$ and $c_{f0}^{\text{TC}} = c_{f,b}^{\text{TC}}$ from the baseline,
- (e) DC^{tot} and DC^{TC} ,
- (f) DC^{rot} ,
- (g) $DC = DC^{\text{TC}} - DC^{\text{rot}}$.

Figure 2.3 plots the four drag changes that appear in equation 2.15 for two different cylinders: an uncoated cylinder and a riblet-coated cylinder. The measurements are qualified with a letter and a number, as will be explained in section

2.6. The figure shows that the corrections do not alter the trend of the drag curve; only the magnitude changes. For the smooth cylinder, the drag is close to the baseline and the correction for net bulk flow is very small. Quantitatively, the bulk flow has a local maximum around $Re_s = 5.8 \cdot 10^4$ with $\delta_b = 0.0058$, $\hat{R}_\Omega = 4.9 \cdot 10^{-4}$ and $DC^{\text{rot}} = -0.8\%$. In contrast, the riblet cylinder has a large rotation effect. At $Re_s = 5.6 \cdot 10^4$, the drag change attributed to rotation is $DC^{\text{rot}} = -3.3\%$, which corresponds with $\delta_b = 0.025$ and $\hat{R}_\Omega = 2.0 \cdot 10^{-3}$.

Interestingly, the correction for the VK gaps and the one for bulk rotation approximately cancel each other, which is a coincidence for the present setup. To show that, approximate relations between DC^{tot} , DC and DC^{TC} are derived below. Using the assumption that $c_f^{\text{VK}} = c_{f0}^{\text{VK}}$, one can show that $DC^{\text{tot}} = (1 - \gamma_{\text{cor}})DC^{\text{TC}}$. Given that $\gamma_{\text{cor}} \approx 0.30$ for $Re_s \gtrsim 10^4$ (figure 2.2), it follows that $DC^{\text{tot}} \approx 0.70DC^{\text{TC}}$. The rotation correction can be simplified using an asymptotic analysis. The square roots of $c_f^{\text{TC}}/c_{f0}^{\text{TC}} = 1 + DC^{\text{TC}}$ simplify when DC^{TC} is assumed to be small: $\sqrt{1 + DC^{\text{TC}}} \approx 1 + (1/2)DC^{\text{TC}}$. One can then derive that $\delta_b \approx -0.25DC^{\text{TC}}$, which yields $\hat{R}_\Omega \approx -0.021DC^{\text{TC}}$ for $\eta \approx 0.92$. Figure 2.2 shows that $(1/c_{f0}^{\text{TC}}) \cdot dc_{f0}^{\text{TC}}/dR_\Omega \approx -16$ for the higher Reynolds numbers, such that $DC^{\text{rot}} \approx 0.34DC^{\text{TC}}$ and $DC = DC^{\text{TC}} - DC^{\text{rot}} \approx 0.66DC^{\text{TC}}$. The relations $DC^{\text{tot}} \approx 0.70DC^{\text{TC}}$ and $DC \approx 0.66DC^{\text{TC}}$ show that DC^{tot} and DC are very similar, with a slightly larger magnitude for DC^{tot} , in agreement with figure 2.3.

2.5 Coatings tested⁶

Table 2.1 presents an overview of all the coatings that were tested, see also figure 2.4. The following abbreviations are used in the coating names: FH = Fraunhofer IFAM, AN = AkzoNobel, SR = slime release, LPP = linear polishing polymer, LM-LSE = low modulus, low surface energy. The indices (a), (b), etc. refer to different cylinders with the same coating type. The table presents a short description of the different coatings; a more extensive description is given below.

Dual-cure Riblets All riblet coatings were produced by Fraunhofer IFAM with use of a moulding technique. The manufacturing of Dual-cure Riblets utilizes a solvent-free, UV-curable polyurethane for in-mould cure. The mould (or embossing tool) of transparent silicone bears the negative riblet texture. The coating is applied to the mould, the mould is placed on the substrate, and the sample is cured with ultraviolet (UV) light. This whole procedure can be performed with an automated riblet applicator (Stenzel et al., 2011; Kordy, 2015) or manually with a hand-held UV lamp. The application of the riblet texture directly to the cylinders had proven to be difficult. Therefore, the riblet coating was applied to an adhesive foil first, which was then affixed to the cylinders.

⁶Adapted from the methods section of H. O. G. Benschop, A. J. Guerin, A. Brinkmann, M. L. Dale, A. A. Finnie, W.-P. Breugem, A. S. Clare, D. Stübing, C. Price, and K. J. Reynolds. Drag-reducing riblets with fouling-release properties: development and testing. *Biofouling*, pages 1–13, 2018.

TABLE 2.1: An overview of all the coated cylinders that were tested in the Taylor-Couette facility. All cylinders were received from Fraunhofer IFAM, unless stated otherwise. The best-performing Dual-cure and Modified Intersleek[®] Riblet coatings are marked in boldface.

<i>Coating qualifier</i>	<i>Cylinder numbers</i>	<i>Coating description</i>	<i>First time measured</i>
Substandard Dual-cure Riblets / SDCR	2.1 (a), 2.4 (b)	UV-curable polyurethane riblets of substandard quality	June 2015
Modified Intersleek [®] Riblets / MISR	2.2 (a) , 2.3 (b)	Modification of Intersleek [®] 1100SR applied as a riblet-textured coating	June 2015
Intersleek [®] 1100SR [FH]	3.3 (a), 3.5 (b)	Commercial fouling-release coating, doctor-blade applied	November 2015
Modified Intersleek [®] / MIS	3.1 (a), 3.8 (b)	Modification of Intersleek [®] 1100SR to make it compatible with the riblet manufacturing process, doctor-blade applied	November 2015
Intercept [®] 8000 LPP	3.6 (a), 3.7 (b)	Commercial biocidal antifouling coating, spray applied Received from AkzoNobel	December 2015
Intersleek [®] 1100SR [AN]	3.2 (a), 3.4 (b)	Commercial fouling-release coating, spray applied Received from AkzoNobel	December 2015
Substandard Dual-cure Riblets / SDCR	4.2 (c), 4.8 (d)	See above	July 2016
Modified Intersleek [®] Riblets / MISR	4.6 (c), 4.7 (d)	See above	July 2016
Fluoropolymer Riblets / FPR	4.1 (a), 4.4 (b)	Cross-linked fluoropolymer riblets	October 2016
LM-LSE Intersleek [®] Riblets / LM-LSE ISR	4.5 (a), 4.9 (b)	Low-modulus and low-surface-energy modification of Intersleek [®] 1100SR applied as a riblet-textured coating	October 2016
Dual-cure Riblets / DCR	2.1 (a), 2.4 (b), 4.2 (c), 4.8 (d)	UV-curable polyurethane riblets of good quality	December 2016

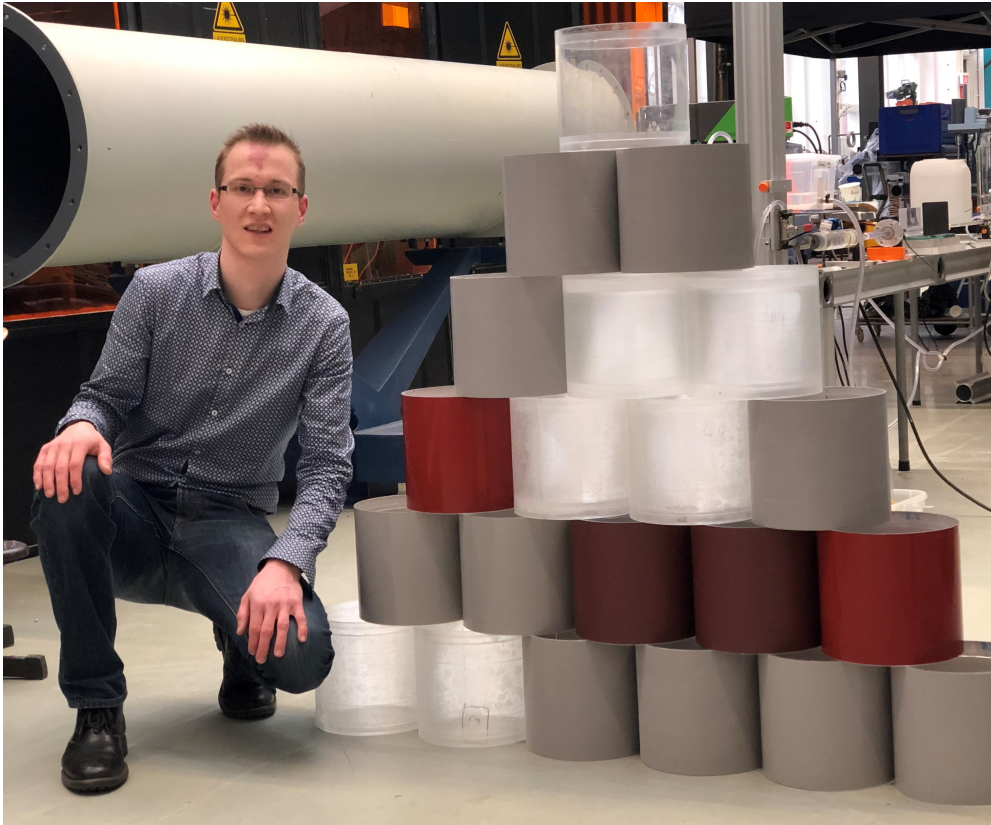


FIGURE 2.4: All coated cylinders whose drag was measured in the Taylor-Couette setup. The 20 cylinders are ordered from left to right and bottom to top in the same order in which they first appear in table 2.1. The top cylinder is uncoated.

The texture characteristics had not been checked initially, as confocal microscopy could not be used because of the transparency of the coating. However, the Taylor-Couette measurements showed that the drag-reducing performance of the Dual-cure Riblets was less than what had been expected (section 2.6). Therefore, Fraunhofer IFAM checked the riblet quality of all the Dual-cure Riblet coatings (cylinders 2.1, 2.4, 4.2, 4.8) around October 2016. Casts were taken from four patches on the cylinders, two in the middle and two at the edges. Fraunhofer IFAM discovered that the Dual-cure Riblets were of substandard quality, i.e. with rounded bottoms and reduced height ($\approx 37 \mu\text{m}$), see figure 2.5. This seemed to be more or less consistent over the whole area of the cylinders and for all four cylinders. Hence, these riblet textures are denoted as ‘Substandard Dual-cure Riblets’. For completeness, measurements with this texture have been included in the remainder of this chapter.

Because of the substandard quality of the Dual-Cure Riblet coatings, Fraunhofer IFAM recoated cylinders 2.1, 2.4, 4.2, 4.8 in November 2016. The reduced quality was probably due to insufficient or slow curing by the hand-held UV lamp.

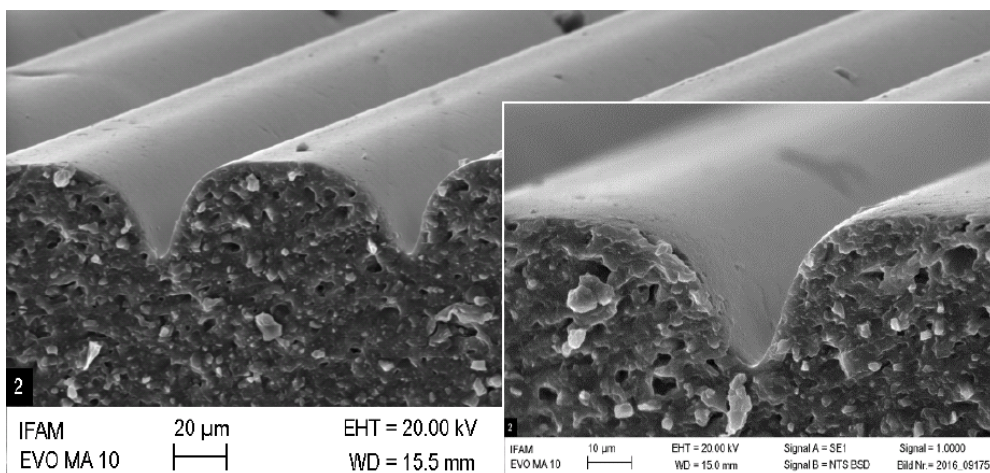


FIGURE 2.5: Substandard quality of the Substandard Dual-cure Riblet texture, visualized with a SEM image of a cast taken from the riblet foil, i.e. bearing the negative structure. The riblets have reduced heights and rounded tips. Source: D. Stübing, Fraunhofer IFAM, personal communication, 10 November 2016.

Hence, the UV lamp of the riblet applicator was used in order to achieve fast and intensive curing. The texture characteristics were measured with light microscopy and scanning electron microscopy (SEM). A SEM image of the texture (figure 2.6 (left)) shows that the riblet tips are sharp. The riblet characteristics, defined in figure 2.6 and measured by SEM, are its spacing $s = 91.7 \pm 1.3 \mu\text{m}$, its height $h = 42.4 \pm 0.5 \mu\text{m}$ and its tip angle $\theta = 41.5 \pm 0.9^\circ$. The mechanical coating properties were measured by a tensile test, and are specified with an elastic modulus of 125 MPa and a tensile strength of 8.5 MPa. While the original riblet coatings are marked as ‘Substandard Dual-cure Riblets’, the new coatings are simply denoted as ‘Dual-cure Riblets’.

Modified Intersleek[®] Riblets Intersleek[®] 1100SR, developed by AkzoNobel / International Paint Ltd., is an advanced fluoropolymer fouling-release coating that is free of biocides. It is primarily intended for commercial marine vessels and is designed to release marine biofilms even at low speeds. The technology provides a smooth, low-energy surface to which fouling organisms either cannot attach, or to which they adhere only loosely and can therefore be easily removed. Intersleek[®] 1100SR is a three-pack, chemically cured coating. Its rheological properties have been optimised to make it compatible with airless spray, which is by far the most common method used in marine shipyards for application of paint to large areas.

Initial attempts of Fraunhofer IFAM to prepare riblet surfaces from Intersleek[®] 1100SR produced articles with poor fidelity. The existing paint formulation was unsuitable for the moulding technique, because the moderate solvent content caused defects, and the low viscosity resulted in flow and levelling

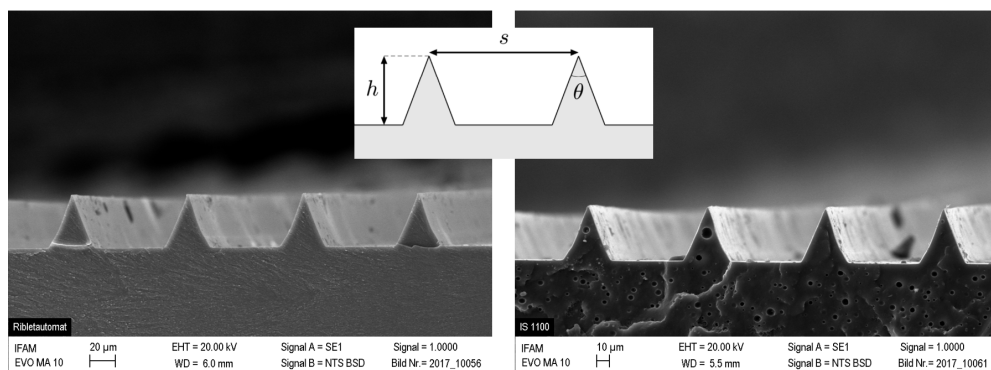


FIGURE 2.6: SEM images of two different riblet-textured coating systems: Dual-cure Riblets (*left*) and Modified Intersleek[®] Riblets (*right*). The inset defines three riblet characteristics, namely spacing s , height h and tip angle θ . Source: D. Stübing, Fraunhofer IFAM, see also Benschop et al. (2018).

of the riblet structure prior to full cure. Therefore, AkzoNobel modified the Intersleek[®] 1100SR system: most of the solvent was removed and the viscosity was increased. The thus obtained coating is described as medium-viscosity solvent-free Intersleek[®] 1100SR, or simply Modified Intersleek[®]. Its mechanical properties were measured with a tensile tester, and are specified with an elastic modulus of 0.87 MPa and a tensile strength of 0.84 MPa.

The Modified Intersleek[®] formulation was used by Fraunhofer IFAM to manufacture riblet-textured coatings. Embossing was performed with the same silicone moulds as for the Dual-cure Riblets. Because Intersleek[®] 1100SR adhered strongly to the mould, the latter was subjected to a plasma treatment. The coatings were conventionally cured at room temperature for 24 hours before the mould was removed. The resulting textured coating is denoted as Modified Intersleek[®] Riblets. The quality of the riblet structure was investigated by scanning electron microscopy. Figure 2.6 (right) shows a SEM image of the texture. The riblet characteristics, defined in figure 2.6 and measured by SEM, are its spacing $s = 92.7 \pm 0.7 \mu\text{m}$, its height $h = 42.4 \pm 0.5 \mu\text{m}$ and its tip angle $\theta = 41.7 \pm 1.2^\circ$.

Fluoropolymer Riblets A new paint formulation to manufacture compliant coatings, based on cross-linked fluoropolymer, was developed at Eindhoven University of Technology (TU/e, section Functional Organic Materials and Devices) by A. S. Kommeren, C. W. M. Bastiaansen and coworkers (Kommeren, 2017). They combined their formulation with the riblet manufacturing technique of Fraunhofer IFAM. Fluoropolymer Riblets were produced with the automated riblet applicator. Because of limited manufacturing and measuring capacity, only one type of riblet coating was tested. The material had a storage modulus of 6.2 MPa and a loss modulus of 0.6 MPa at 25 °C (Kommeren, 2017). Figure 2.7 shows SEM pictures of the texture.

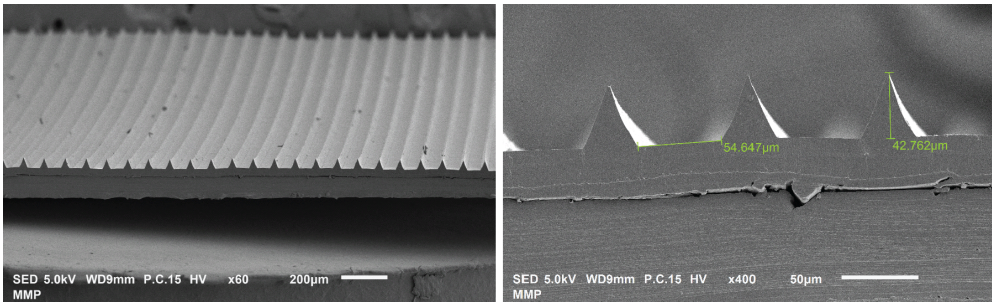


FIGURE 2.7: SEM images of the Fluoropolymer Riblet coatings developed as part of a collaboration between Eindhoven University of Technology (TU/e) and Fraunhofer IFAM. Source: A. S. Kommeren, TU/e, see also Kommeren (2017).

LM-LSE Intersleek[®] Riblets Intersleek[®] 1100SR was also modified to manufacture a low-modulus and low-surface-energy riblet coating. The resulting texture has unfortunately not been characterized, however.

Untextured coatings Besides the riblet coatings, some untextured coatings were tested as well. Fraunhofer IFAM provided four cylinders with untextured coatings, namely two with standard Intersleek[®] 1100SR and two with Modified Intersleek[®]. These coatings were first applied with a doctor blade to adhesive foils and then affixed to the cylinders. AkzoNobel provided four cylinders with spray-applied commercial antifouling coatings: two cylinders with a biocidal coating (Intercept[®] 8000 LPP) and two with a fouling-release coating (Intersleek[®] 1100SR).

2.6 Results⁷

This section describes the measurement results. The qualifiers from table 2.1 are used to denote the different cylinders. A number has been added within the parentheses in case a cylinder was measured more than once. For instance, ‘Modified Intersleek[®] Riblets (a2)’ indicates the second measurement of cylinder (a) with a Modified Intersleek[®] Riblet coating. The subsections below present the measurement data for smooth reference cylinders (2.6.1), riblet-textured coatings (2.6.2) and untextured coatings (2.6.3).

2.6.1 Smooth reference

Measurements were performed with several uncoated PMMA cylinders to check reproducibility of the results, to determine a baseline for the reference drag of a smooth surface, and to compare with previous experiments by Greidanus et al.

⁷Adapted from the public deliverable of the SEAFRONT project: H. O. G. Benschop. Deliverable 1.15: Report on hydrodynamic performance of provided specimens of WP1.1, August 2017. URL http://seafont-project.eu/images/Deliverable_SEAFRONT_1.15.pdf.

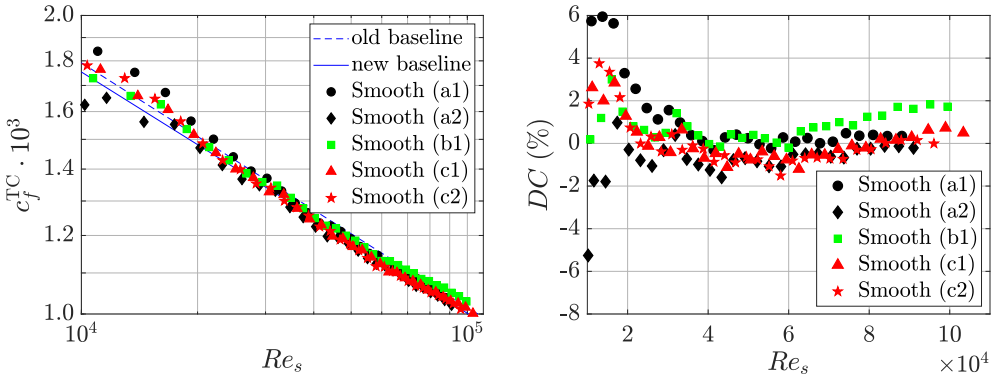


FIGURE 2.8: Drag data of smooth cylinders to determine the reference. *Left*: Experimentally determined skin friction coefficient as function of the shear Reynolds number. The symbols represent the data of 3 different uncoated PMMA cylinders (a,b,c) and different measurement series for these cylinders (as indicated by the numbers). The old baseline is a fit through previously reported experiments by Greidanus et al. (2015). The new baseline is a fit through the present data. *Right*: The same data as in the left figure, but now plotted as the drag change relative to the (new) baseline from the left figure.

(2015) in the same setup. Figure 2.8 depicts the drag coefficient of smooth cylinders as function of the shear Reynolds number. The measurements were performed on three smooth cylinders and at different times of the year (so at different water temperatures); some cylinders were measured twice. The drag data for the different cylinders and different measurement series are very similar.

The reference drag of smooth cylinders is determined from a fit through the data, which yields the baseline:

$$c_{f,b}^{\text{TC}} = 0.0165 Re_s^{-0.243}. \quad (2.16)$$

The Reynolds-number dependence is close to $c_f \propto Re_s^{-1/4}$, which is the same dependence as for ordinary boundary-layer flow along a hydraulically-smooth flat plate. The figure also shows the old baseline $c_{f,b}^{\text{TC}} = 0.0174 Re_s^{-0.247}$, which belongs to previously reported experiments of Greidanus et al. (2015). The setup was slightly modified after their experiments, which presumably explains the small difference between both baselines.

Figure 2.8 also presents the drag change DC for all measurements on smooth cylinders. DC was computed using the procedure outlined in section 2.4.3. Drag increase corresponds with a positive DC , while drag is reduced when DC is negative. The data in figure 2.8 is indicative for the natural variability in drag for different measurements on several cylinders of the same type. Variation in the data can be due to several factors such as: (a) uncertainty in the torque measurements (especially for low shear Reynolds number for which the torque is very small), (b) slight variations in the cylinder geometries, surface smoothness

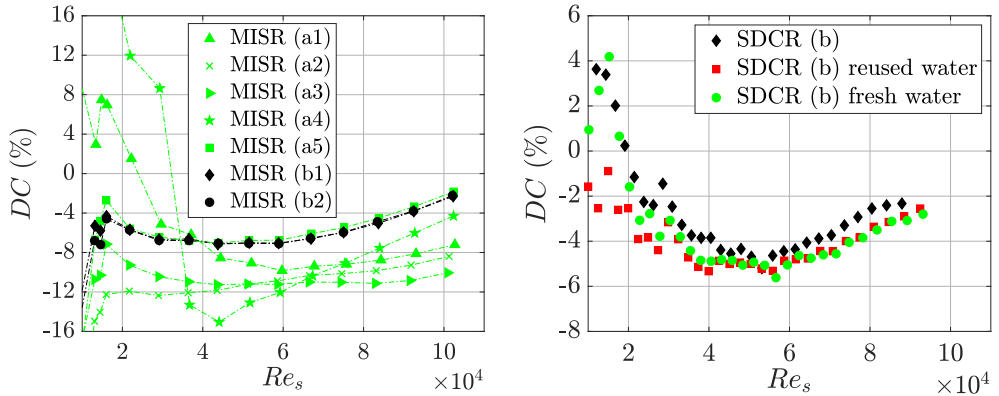


FIGURE 2.9: Anomalous drag measurements on Modified Intersleek® Riblets. *Left:* Repeated measurements (in the original setup) on one Modified Intersleek® Riblet coating were initially not reproducible. The water in the setup was replaced after the fourth measurement series. *Right:* Three measurements (in a slightly updated setup) on a Substandard Dual-cure Riblet coating. The first and third measurement series used fresh water, whereas the second series used water which came from a measurement on a Modified Intersleek® coating (cylinder 3.8).

and coating thickness (the latter is only relevant for coated cylinders), (c) slight differences in alignment of the cylinders in the setup, in particular slight variations in the heights of the Von Kármán gaps. Based on these observations, the uncertainty of the drag measurements for $Re_s > 3 \cdot 10^4$ is estimated to be around $\pm 1\%$.

2.6.2 Riblet-textured coatings

The focus of this subsection will be on the comparison between the Dual-cure and Modified Intersleek® Riblet coatings. Benschop et al. (2018) only present the final comparison between these two coating types. In contrast, this subsection also shows preliminary results in order to convey some of the important lessons that have been learned in the course of time. As a consequence, some figures display measurement results for the Dual-cure Riblets that were denoted ‘substandard’ in retrospect.

Anomalous drag reduction of Modified Intersleek® Riblet coatings Initial measurements on one of the Modified Intersleek® Riblet coatings were not reproducible, see figure 2.9. Five measurement series were performed in total. Interestingly, when changing the water in the setup after the fourth measurement series, the results for the fifth measurement series appeared very similar to the results for the other Modified Intersleek® Riblet coating. The reason for these anomalous results is not completely clear. It is perhaps due to some compounds of the coating (e.g. solvents) that dissolved into the water, which could have

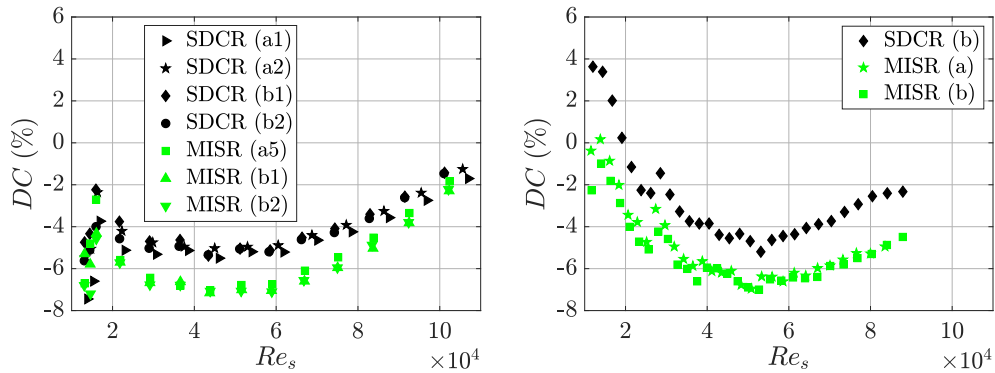


FIGURE 2.10: Drag change for Substandard Dual-cure Riblet and Modified Intersleek[®] Riblet coatings in two slightly different Taylor-Couette setups. The drag change was computed using the corresponding baseline of that setup. *Left*: measurement series in the original setup. *Right*: measurement series in the slightly updated setup.

changed the drag for two reasons. First, some polymers are known to be drag-reducing in a turbulent flow (Owolabi et al., 2017). Second, the rheology (e.g. viscosity) of the water could have changed.

To investigate whether the water content could have significantly affected the drag, some additional measurements (in the slightly updated setup) were performed in December 2015. First, one experiment with a (smooth) Modified Intersleek[®] coating was executed (cylinder 3.8). The water of that experiment, which likely contained some chemicals, was reused for a measurement with a Substandard Dual-cure Riblet coating. Finally, the water was replaced by fresh water, without unmounting the cylinder, and a last experiment was performed. As the figure shows, the drag of the riblet foil seems independent of the use of fresh or reused water. Therefore, an influence of chemicals in the water on the drag could not be confirmed.

The latter experiments, however, cannot exclude the possibility that chemicals in the water altered the frictional drag. Cylinder 3.8 was already used in an earlier experiment, so it had soaked for at least 24 hours and a drag measurement had been performed. Most chemicals had presumably been released when the second measurement was conducted. The unusual drag data presented in figure 2.9 still suggest an important influence of contaminated water. Therefore, cylinders were soaked in demineralised water prior to the experiments. Cylinders whose number starts with 3 were soaked for at least 24 hours, and since the start of 2016 the soaking time has been at least two weeks.

Influence of setup After the first measurements on riblet coatings, the Taylor-Couette setup was slightly updated. Specifically, the bottom plate of the outer cylinder was replaced because it was slightly deformed. Figure 2.10 shows the drag change of four riblet coatings as measured in the original and the updated

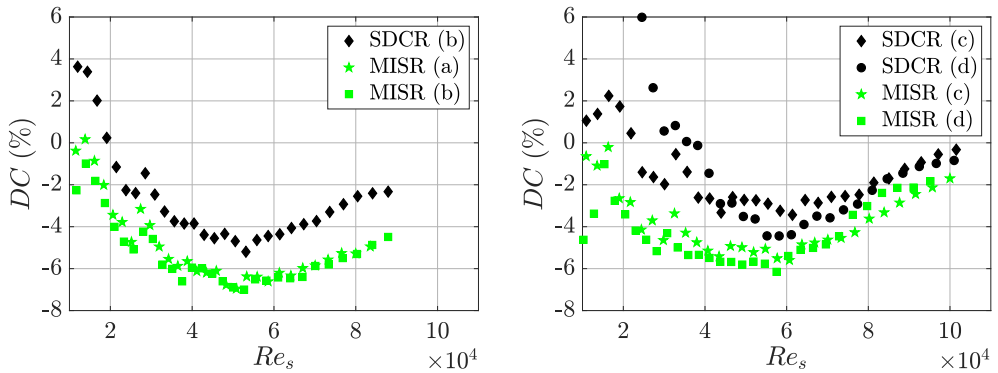


FIGURE 2.11: Drag change for Substandard Dual-cure Riblet and Modified Intersleek[®] Riblet coatings in two different cylinder batches. *Left*: first batch. *Right*: second batch.

setup. The drag change was computed using the corresponding baseline of that setup.

In the original setup, all riblet coatings were measured at least twice, without unmounting of the cylinders in between subsequent measurement series. Apart from the initial measurements on the Modified Intersleek[®] Riblet (a) coating (see figure 2.9), the drag data were very reproducible. When the cylinders would have been unmounted before a second measurement was performed, the drag variations would have been larger. The drag differences between two cylinders with the same coating type were small. The same applies also to the data for the new setup. No data are presented for the Substandard Dual-cure Riblet (a) coating. The riblet foil detached at the seam from the cylinder during the initial stage of the measurement series. That became apparent from a much higher torque than usual, and water that was spilled from the setup at the top.

Both subfigures prove that the riblet coatings can reduce drag in a turbulent flow. The maximum drag reduction is obtained somewhere between $Re_s = 5 \cdot 10^4$ and $6 \cdot 10^4$. Although the trend of the drag curves differs slightly among the two setups, the magnitude of the maximum drag reduction is the same. The Modified Intersleek[®] Riblet coatings show consistently about 2 percentage points more drag reduction as compared to the Substandard Dual-cure Riblets. Most of the research that followed was triggered by this difference. The updated setup was used to obtain the data that will be presented from now on.

Comparison of two batches To see whether the differences between the two types of riblet coatings were reproducible, a new batch of coated cylinders was manufactured by Fraunhofer IFAM. The results of the drag measurements are presented in figure 2.11. Note that the tests of the two batches do not cover the same Reynolds-number range, although the velocity range is exactly the same. This is due to the temperature-dependent viscosity of water. The first batch was measured in June 2015 in the old setup and in November 2015 in the new

setup. For the latter measurements, the final water temperature varied between 19.2 and 21.5 °C. The second batch was measured in July 2016, with the final temperature varying between 26.3 and 27.7 °C. The kinematic viscosity of water decreases from $1.0 \cdot 10^{-6}$ at 20 °C to $0.86 \cdot 10^{-6}$ at 27 °C. This results in an increase of the Reynolds number by about 16%, which is indeed what figure 2.11 shows.

The second batch shows about 1 percentage point less drag reduction as compared to the first batch. Also, the Substandard Dual-cure Riblets of the new batch show somewhat unexpected behaviour for $Re_s < 6 \cdot 10^4$, namely large drag differences for the same type of coating. The Modified Intersleek® Riblet coatings demonstrate better reproducibility, with drag differences less than 1% for most Reynolds numbers.

Despite the differences between the two batches, the overall conclusion still seems to be that the Modified Intersleek® Riblets outperform the Substandard Dual-cure Riblets. Since the substandard quality of the Dual-cure Riblets was yet unknown at that time, we hypothesized that the drag differences between the two riblet types could be attributed to some of the following factors:

1. Release of chemicals from the coating. This was expected to be relevant in particular for the Modified Intersleek® Riblet coatings. When they were removed from the water after soaking, they had a strong smell, and foam appeared on the surface of the discharged water. Also, the anomalous drag data reported in figure 2.9 are most likely due to contaminated water. The chemicals might act as drag-reducing agents (like e.g. some polymers, Owolabi et al. (2017)) or adjust the rheological properties of the fluid.
2. Sharpness of the riblet tips. As the two types of riblet coatings were manufactured in a different way, the quality of the riblet tips could be different. Blunt tips yield less drag reduction (Stenzel et al., 2011).
3. Compliancy of the coating. The Modified Intersleek® Riblet coating with an elastic modulus of approximately 0.87 MPa is relatively soft as compared to the Dual-cure Riblet coating with an elastic modulus of 125 MPa (Benschop et al., 2018). There are indications that compliant coatings can reduce drag in turbulent flows (Choi et al., 1997).
4. Surface energy of the coating. The Modified Intersleek® Riblet coating is amphiphilic, so it has both hydrophilic and hydrophobic (or lipophilic) properties. As a result, air layers could form in the riblet valleys, stabilized by the hydrophobic domains, although the distance between the riblets is possibly too large for these air pockets to be stable in a turbulent flow. If air nevertheless stays in between the riblets, air lubrication can yield drag reduction (Jung et al., 2016).

Influence of riblet quality The quality of the Dual-cure Riblets turned out to be substandard (see section 2.5). A new batch of four riblet coatings with

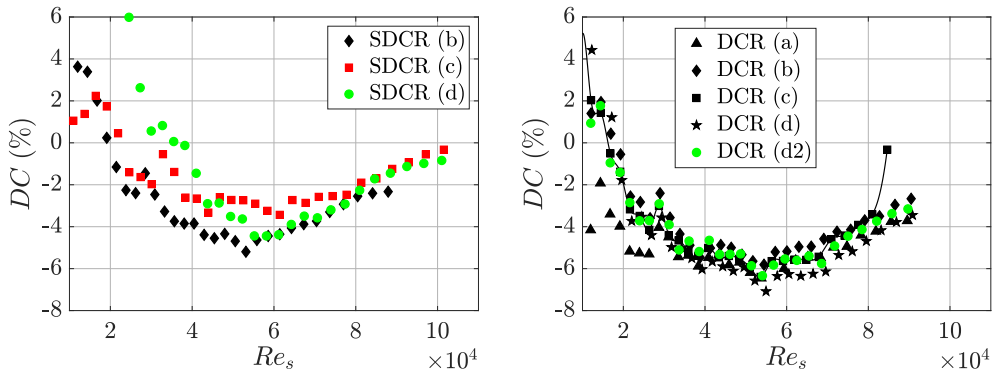


FIGURE 2.12: Drag change for several Dual-cure Riblet coatings of different quality. *Left*: the Dual-cure Riblets of substandard quality. *Right*: the Dual-cure Riblets of good quality.

improved quality was manufactured by Fraunhofer IFAM and was tested in our Taylor-Couette facility. The results are presented in figure 2.12: the left subfigure shows the drag change for the Substandard Dual-cure Riblets (these data have already been presented in figure 2.11), whereas the right subfigure shows the drag change for the Dual-cure Riblet coatings of good quality. The results for the latter are quite reproducible, with a natural variability around the average of about ± 1 percentage point. Coating (c) detached partly at the seam of the foil at the penultimate rotation rate, as is apparent from the sudden drag increase.

The riblets with the improved quality indeed yield more drag reduction. An optimum drag reduction of 6.4% on average is obtained, with a peak value of 7.1% for coating (d). The substandard riblets have a maximum drag reduction of 4.4% on average, with an overall optimum of 5.2% for coating (b). Hence, the performance of the new Dual-cure Riblets improved significantly as compared to the old Dual-cure Riblets. This confirms that the optimum drag reduction depends quite heavily on the quality and height of the riblet tips, in accordance with the study of Stenzel et al. (2011).

Final comparison between Dual-cure and Modified Intersleek[®] Riblets

Because the optimum drag reduction of the Dual-cure Riblets improved, the comparison between the Dual-cure and Modified Intersleek[®] Riblets will also change. To select the best-performing coating of each type, several riblet coatings were measured again within one week. Because the Dual-cure Riblet coatings had been measured recently, only the best-performing (namely (d)) was repeated. Figure 2.12 shows that the corresponding curve represents quite well the average trend of all Dual-cure Riblet coatings.

Three Modified Intersleek[®] Riblet coatings were measured again. Figure 2.13 (left) presents the data of both the original and the repeated tests. Coating (c) reproduces very well, while coatings (a) and (b) of the first batch yield less drag reduction as compared to the first measurements. Specifically, the maximum drag

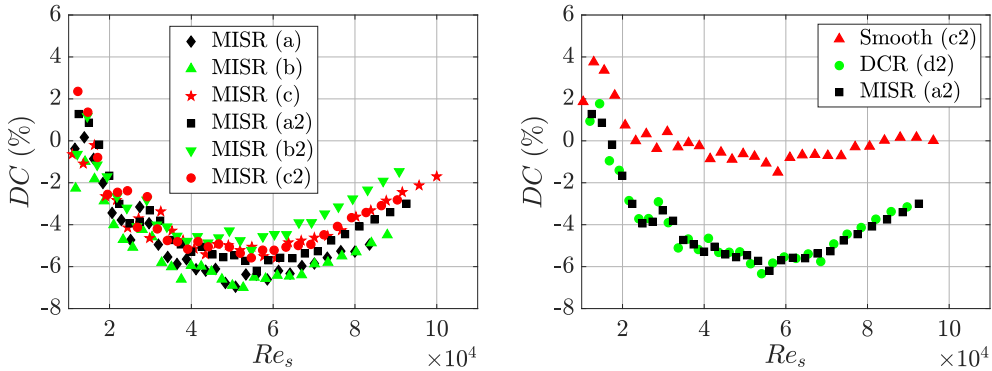


FIGURE 2.13: Final comparison between Dual-cure and Modified Intersleek[®] Riblets. *Left*: Repeated measurements to select the best-performing Modified Intersleek[®] Riblet coating. *Right*: Comparison of the best-performing Dual-cure and Modified Intersleek[®] Riblet coatings.

reduction diminished from 7.0% to 6.2% for coating (a), and from 7.0% to 5.2% for coating (b). These changes were initially unexpected. On second thoughts, however, we realize that the Modified Intersleek[®] Riblet coatings (a) and (b) were among the first coatings that were tested. At that time, the importance of soaking was not yet fully realized. As a result, tests were performed with little soaking in advance, which presumably explains why the original results were not reproduced.

The new tests show that cylinder (b) has about 1% more drag than cylinder (a). This is ascribed to the poor quality of coating (b): it exhibits quite a number of small imperfections, whereas no visual imperfections were found on coating (a).

The final comparison between the Dual-cure and Modified Intersleek[®] Riblet coatings is presented in the right part of figure 2.13. The best-performing coatings of each type were selected from the repeated measurements in one week. A smooth dataset, obtained in the same week, is included. The figure shows an almost perfect match between the two types of riblet coatings. The maximum drag reduction is 6.3% for the Dual-cure Riblets and 6.2% for the Modified Intersleek[®] Riblets. The differences in figures 2.10 and 2.11 have disappeared for two reasons. First, the Dual-cure Riblets had initially a substandard quality of the riblet tips. Second, the initial measurements on the Modified Intersleek[®] Riblets were not reproducible, presumably due to insufficient soaking in advance of the first measurements.

In summary, the Dual-cure and Modified Intersleek[®] Riblets have the same drag-reducing performance within the experimental uncertainty of ± 1 percentage point. Hence, the use of Modified Intersleek[®] to manufacture riblet coatings did not significantly compromise the drag-reducing potential of such textured coatings. Although the Modified Intersleek[®] Riblet texture is much softer as compared to the Dual-cure Riblets, it is presumably stiff enough such that it does not significantly deform in the turbulent Taylor-Couette flow. The maximum

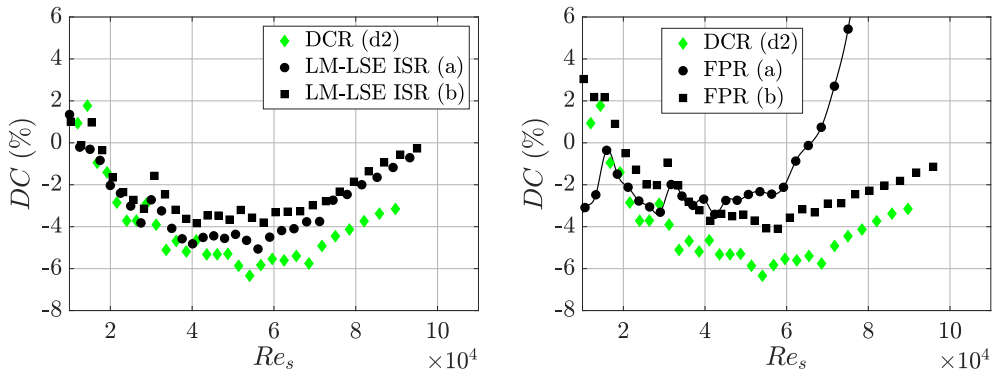


FIGURE 2.14: Drag change for two other riblet-textured coatings. *Left*: Intersleek[®] Riblets with low modulus and low surface energy. *Right*: Fluoropolymer Riblets.

drag reduction is about 6%, which is less than 7.8% obtained by Bechert et al. (1997) for comparable riblets with a tip angle of 45° . This is possibly due to the curved flow geometry in the Taylor-Couette setup, which is different from the plane flow geometry in Bechert's work. The figure of 6% drag reduction is thus subject to scrutiny, e.g. by further testing using a flat plate.

Other riblet-textured coatings Figure 2.14 shows the drag change for two other riblet coatings. The left subfigure shows the data for Intersleek[®] Riblets with low modulus and low surface energy (LM-LSE). The two coatings exhibit a very similar trend, but their performance is slightly less than the optimized Dual-cure Riblets.

The right subfigure presents the results for the Fluoropolymer Riblets. For low Reynolds numbers, both coatings behave similarly, showing a drag reduction of around 3.5%. However, coating (a) detached at higher velocities, resulting in the relatively sudden drag increase around $Re_s = 6 \cdot 10^4$. This demonstrates an adhesion problem, like for some other coatings that were tested previously. Coating (b) shows a better performance with an optimum drag reduction of 4.1%.

Both the LM-LSE Intersleek[®] and Fluoropolymer Riblets exhibit a somewhat reduced performance as compared to the optimized Dual-cure Riblets. Further research would be required to reveal the reason for this difference. Possible reasons include substandard quality of the riblet tips or the use of another material.

Drag reduction optimum Till now the drag change has been shown as a function of the Reynolds number Re_s , which is common to both textured and untextured coatings. In the literature, however, the drag change is typically plotted as function of the dimensionless riblet spacing $s^+ = su_\tau/\nu$, where $+$ denotes normalization in viscous units and u_τ is the wall-shear velocity. The latter is determined from $u_\tau = \sqrt{\tau_w/\rho}$, where τ_w represents the wall shear stress for an uncoated reference cylinder exposed to identical flow conditions. The

dimensionless spacing can be computed from three other dimensionless numbers:

$$s^+ = \frac{su_\tau}{\nu} = \frac{u_\tau}{U_{sh}} \frac{U_{sh}d}{\nu} \frac{s}{d}. \quad (2.17)$$

The first dimensionless number can be obtained from the definition of the skin-friction coefficient (equation 2.5) and the baseline (equation 2.16):

$$c_f^{\text{TC}} = 2 \left(\frac{u_\tau}{U_{sh}} \right)^2 = 0.0165 Re_s^{-0.243}. \quad (2.18)$$

The second dimensionless number is the shear Reynolds number Re_s , and s/d is the ratio between the riblet spacing and the radial gap width.

The optimum drag reduction is typically obtained around $Re_s = 5.5 \cdot 10^4$ (see e.g. figure 2.13), which yields $c_f^{\text{TC}} = 0.0012$ and $u_\tau/U_{sh} = 0.024$. The riblet spacing is $s \approx 92 \mu\text{m}$, whereas the radial gap width is typically $d = 0.95 \text{ cm}$. All together, the drag reduction optimum is attained for $s^+ \approx 13$. Bechert et al. (1997) obtained an optimum at a slightly higher value of $s^+ \approx 17$ for a comparable texture in the Berlin oil channel. Greidanus et al. (2015) performed measurements on a sawtooth riblet texture in the same Taylor-Couette facility; they reported an optimum around $s^+ \approx 13$ versus $s^+ \approx 16$ for Bechert et al. (1997). Hence, it seems that the optimum drag reduction for Taylor-Couette flow occurs at a slightly lower value of s^+ as compared to channel flow.

2.6.3 Untextured coatings

Figure 2.15 presents the drag change for four types of untextured coatings, together with data of smooth cylinders as reference. All coatings were soaked in water at least 24 hours in advance of the measurements. Intercept[®] 8000 LPP shows a slight drag increase (about 1 to 2%) at high flow speeds, possibly due to coating roughness, although the drag is not much higher than that of the worst-performing smooth cylinder. The Intersleek[®] 1100SR coatings of AkzoNobel [AN] and Fraunhofer IFAM [FH] do not exhibit a clear indication of drag reduction or increase. The spray-applied coatings of AkzoNobel seem to have slightly more drag than the doctor-blade-applied coatings of Fraunhofer IFAM; the doctor blade presumably yields smoother coatings as compared to spray. The first two measurements of the Modified Intersleek[®] coatings suggest a slight drag reduction (about 2%), although they exhibit somewhat strange behaviour at the lower Reynolds numbers. The last measurement (numbered (b2)) was performed to obtain the water that was used for the tests reported in figure 2.9 (right). Therefore, it was soaked for only 5 minutes, which presumably explains its anomalous behaviour in figure 2.15. Again, soaking appears to be essential for reproducible experiments.

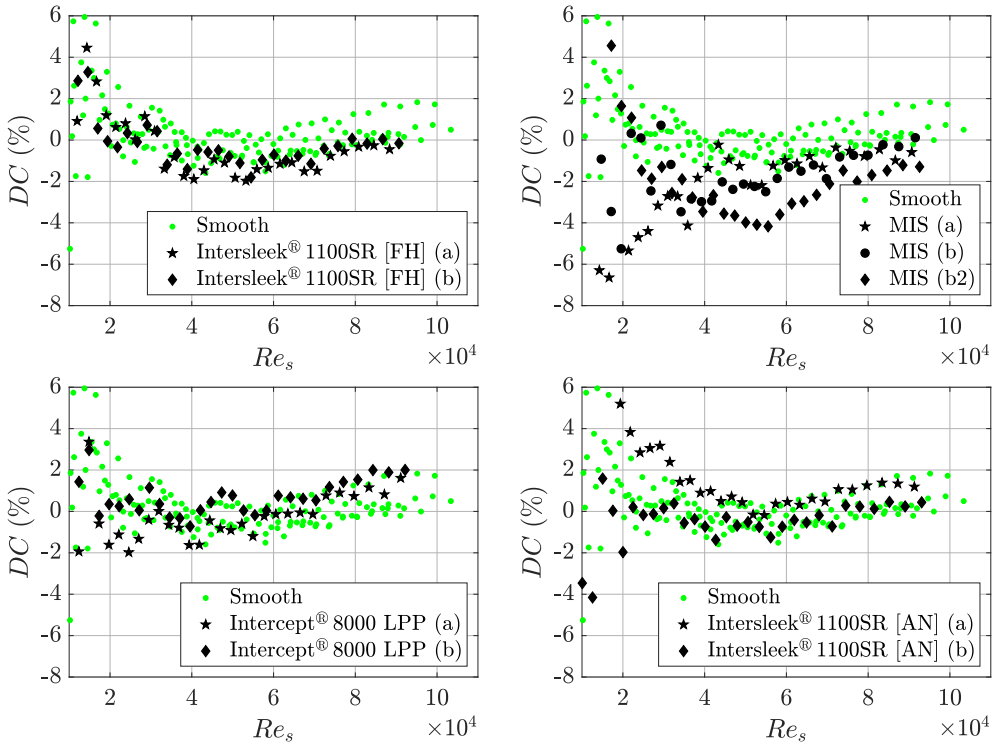


FIGURE 2.15: Drag change for four types of untextured coatings. *Top left*: Intersleek[®] 1100SR, doctor-blade-applied by Fraunhofer IFAM. *Top right*: Modified Intersleek[®], doctor-blade-applied by Fraunhofer IFAM. *Bottom left*: Intercept[®] 8000 LPP, spray-applied by AkzoNobel. *Bottom right*: Intersleek[®] 1100SR, spray-applied by AkzoNobel.

2.7 Conclusions and recommendations

A summary of the development and testing of the Modified Intersleek[®] Riblet coating has already been provided in section 2.2. This section summarizes the main conclusions for the drag measurements in the Taylor-Couette facility:

- The Taylor-Couette setup is a useful tool to measure drag changes larger than 1% relatively quickly.
- Soaking of coated cylinders in water prior to a measurement series is essential for reproducibility of the drag measurements.
- Sufficient adhesion of the coatings to the cylinders is crucial. Three coatings partially detached from the cylinders during the measurements, as was apparent from a significant and sudden drag increase. A measurement should be aborted when this happens, because the high torques can destroy the expensive torque meter in the worst case.

- Sharpness of the riblet tips is important to achieve optimum drag reduction. The drag difference between riblet coatings of optimal and substandard quality was found to be about 2%.
- A riblet-textured coating can be augmented with fouling-release properties without compromising its drag-reducing performance. Indeed, the Dual-cure and Modified Intersleek[®] Riblet coatings showed the same drag-reducing performance, with an optimum drag reduction of about 6%.

For many coatings that were measured in the Taylor-Couette setup, relatively little was known about the coating properties, e.g. the exact surface topography, the elastic modulus and the surface energy. For instance, the surface texture of the Dual-cure Riblets was initially not visualized. This explains why it took more than a year before it was realized that the substandard riblet quality caused the reduced performance. As a second example, there was barely any information available regarding the Fluoropolymer Riblets and the LM-LSE Intersleek[®] Riblets. Hence, the reason for the disappointing drag reduction was not revealed. For future experiments, a surface characterization will facilitate the interpretation of the measurement results.

Chapter 3

Drag reduction by herringbone riblet texture¹

3.1 Abstract

A bird-feather-inspired herringbone riblet texture was investigated for turbulent drag reduction. The texture consists of blade riblets in a converging/diverging or herringbone pattern with spanwise wavelength Λ_f . The aim is to quantify the drag change for this texture as compared to a smooth wall and to study the underlying mechanisms. To that purpose, Direct Numerical Simulations of turbulent flow in a channel with height L_z were performed. The Fukagata-Iwamoto-Kasagi identity for drag decomposition was extended to textured walls and was used to study the drag change mechanisms. For $\Lambda_f/L_z \gtrsim O(10)$, the herringbone texture behaves similarly to a conventional parallel-riblet texture in yaw: the suppression of turbulent advective transport results in a slight drag reduction of 2%. For $\Lambda_f/L_z \lesssim O(1)$, the drag increases strongly with a maximum of 73%. This is attributed to enhanced mean and turbulent advection, which results from the strong secondary flow that forms over regions of riblet convergence/divergence. Hence, the employment of convergent/divergent riblets in the texture seems to be detrimental to turbulent drag reduction.

3.2 Introduction

Drag-reducing techniques can be of great value for fuel consumption reduction, as a significant part of the fuel used for transportation arises from drag in turbulent flows. Drag reduction (DR) in fluid flows can be obtained by active and passive

¹This chapter has been published as H. O. G. Benschop and W.-P. Breugem. Drag reduction by herringbone riblet texture in direct numerical simulations of turbulent channel flow. *Journal of Turbulence*, 18(8):717–759, 2017.

methods. Active methods include the use of additives (White and Mungal, 2008), gas injection (Ceccio, 2010), wall mass transfer (Kametani and Fukagata, 2011), wall cooling or heating (Yoon et al., 2006; Kametani and Fukagata, 2012; Vakarelski et al., 2014), wall motion (Quadrio, 2011), wall deformation (Tomiyama and Fukagata, 2013) and electromagnetic forcing (Shatrov and Gerbeth, 2007). Passive methods include the change of surface chemistry (e.g. superhydrophobicity (Rothstein, 2010)), elasticity (e.g. compliant walls (Choi et al., 1997)), shape (e.g. airfoil or ship hull shape) and texture (e.g. riblets (Dean and Bhushan, 2010)). Surface roughness and surface textures have been successfully used for DR by transition delay in laminar flow (Fransson et al., 2006), separation delay in turbulent flow over curved surfaces (Choi et al., 2006; Son et al., 2011) and turbulence modification in turbulent flow over flat surfaces.

Of the investigated flat plate textures – such as sifted sand grains (Abe et al., 1990), transverse square grooves (Wahidi et al., 2005), dimples (Abdulbari et al., 2013) and V-shaped protrusions (Sagong et al., 2008) – the well-studied riblet texture seems most promising for turbulent DR. This texture has been found on the scales of some fast-shark skins (Díez et al., 2015) and consists of ridges or riblets aligned with the mean flow direction. With a simplified riblet geometry, a maximum DR of almost 10% has been obtained (Bechert et al., 1997). In the search for even higher values of DR, many variations on the standard riblet geometries have been investigated (Dean and Bhushan, 2010), such as hierarchical or compound riblets (Wilkinson et al., 1988), riblets on a spanwise travelling surface wave (Li et al., 2015), oscillating riblets (Wassen et al., June 23–26, 2008; Grüneberger et al., 2013; Vodop'yanov et al., 2013), riblets in a wave-like pattern (either in phase (Grüneberger et al., 2012) or out of phase (Sasamori et al., 2014)) and riblets combined with drag-reducing polymers (Chen et al., 2015). The rationale behind these alternatives is to further reduce drag by somehow incorporating other drag-reducing methods, such as oscillating walls or polymer addition.

A little-studied alternative to the standard riblets is the herringbone riblet texture that has been found on bird flight feathers. Feathers serve several functions, including flight, thermal insulation, waterproofing and colouration (e.g. for camouflage or visual signals). The following description of the feather morphology is derived from Chen et al. (2013, 2014a,b). A feather consists of two vanes (anterior and posterior), separated by a central supporting shaft. Each vane consists of parallel barbs attached obliquely to the shaft. The barbs are linked together by a set of finer barbs, called barbules. A microgroove is formed between neighbouring barbs. The angle between shaft and barbs is typically $\alpha \approx 30^\circ$. The groove spacing s remains approximately constant with $s^+ \approx 20$. The groove depth decreases gradually away from the shaft. A wing is formed when several feathers are positioned next to each other with almost parallel shafts. The feather shafts are approximately parallel to the flying direction for steady forward glide.

The study of Chen et al. (2014a) is one of the first to investigate the herringbone riblet texture for turbulent drag reduction. Inspired by bird flight feathers, they designed a riblet texture with two typical features that differ from the shark-skin riblets. First, the riblets were arranged in a converging/diverging or herringbone pattern. Second, the riblet height or groove depth changed gradually. Using laser engraving and replica moulding, the researchers manufactured such bio-inspired herringbone-riblet skins. They covered the inner wall of a test pipe with these skins and measured a DR of up to 20%, twice that of optimal standard riblets. Although this seems promising, it has not been reproduced yet, and it is unclear for which texture and flow parameters drag is maximally reduced.

Sagong et al. (2008) investigated a rather comparable geometry, namely the V-shaped protrusions that were found on the sailfish skin. In a comprehensive experimental and numerical study, they found a few cases for which drag was decreased slightly ($\sim 1\%$), although within the experimental uncertainty. The herringbone riblet texture also resembles the vortex generators that have been used to reduce drag by flow-separation delay (Lin, 2002) or transition delay (Shahinfar et al., 2012). Furthermore, several studies confirm that roughness on a bird wing contributes to separation control (Bushnell and Moore, 1991; Lilley, 1998; van Bokhorst et al., 2015).

Herringbone riblet textures have been studied for several other reasons, such as for heat-transfer enhancement (Gao and Sunden, 2001; Fang et al., 2015) and mixing of laminar flows in microchannels (Stroock et al., 2002). The hot-wire study by Koeltzsch et al. (2002) was initiated by the observation of convergent and divergent riblet patterns on the shark skin near sensory organs, possibly used for local flow-noise reduction. Nugroho et al. (2013) revisited the same texture and conducted a parametric study using the hot-wire technique. They were motivated by the potential use for passive flow control and disruption of large-scale coherent motions. They proposed that the herringbone riblets induce large-scale counter-rotating vortices, giving rise to large-scale spanwise periodicity in the boundary layer. The suggested streamwise counter-rotating vortices have recently been visualised in a flat-plate laminar boundary layer over convergent riblets (Nadesan et al., 2014). So, the motivation for herringbone riblet studies has been drag reduction, heat-transfer enhancement, mixing improvement, flow control and large-scale flow structures manipulation.

The study by Nugroho et al. (2013) is a manifestation of the recent interest in surfaces that manipulate the whole boundary layer. There is much evidence that DR techniques that rely on near-wall flow manipulation are less effective at higher Reynolds numbers: DR degrades with increasing Re (Iwamoto et al., 2002, 2005; Spalart and McLean, 2011; Gatti and Quadrio, 2013). That has partially motivated the study of rough or textured surfaces that also impact the outer part of the turbulent boundary layer by means of large-scale secondary flows. These secondary flows have been observed over spanwise-varying longitudinal bedforms (Wang and Cheng, 2006), a regular array of cubes (Reynolds et al., 2007), a bed with two parallel lanes of different roughnesses (Vermaas et al.,

2011), the irregular surface of a replica of a damaged turbine blade (Barros and Christensen, 2014), streamwise strips of elevated roughness (Vanderwel and Ganapathisubramani, 2015) and the aforementioned herringbone riblet texture (Koeltzsch et al., 2002; Nugroho et al., 2013). Interestingly, Schoppa and Hussain (1998) obtained 20% DR in Direct Numerical Simulations of turbulent channel flow with imposed large-scale counter-rotating streamwise vortices.

The aim of this paper is to quantify how and why drag is changed by a herringbone texture as compared to a smooth wall, using Direct Numerical Simulations (DNSs). The numerical methods are described in section 3.3. Section 3.4 explains how drag reduction is quantified. Section 3.5 validates the simulated drag of smooth walls, parallel riblets aligned with the mean flow, and parallel riblets in yaw. Section 3.6 examines the herringbone texture with use of a parametric study. A drag decomposition is derived and applied in section 3.7. A discussion of the results is presented in section 3.8, followed by the main conclusions and an outlook in section 3.9.

3.3 Numerical methods

In this study, Direct Numerical Simulations (DNSs) of incompressible turbulent flow were performed. An overview of all simulations with the corresponding parameters can be found in appendix A.3. This section outlines the method that was used, describing successively the notation conventions, flow domain, texture, grid, numerical code and averaging.

In what follows, dimensional variables are denoted by an asterisk *. Variables without that asterisk are nondimensionalised using the domain height L_z^* and the bulk velocity U_b^* , such that $L_z = 1$ and $U_b = 1$. Note that U_b^* is a constant, as simulations were performed at fixed mass flow rate. The constant bulk Reynolds number is defined as $Re_b = U_b^* L_z^* / \nu^*$, with kinematic viscosity ν^* . The superscript $+$ is used for nondimensionalisation with ν and $u_\tau = \sqrt{\tau_w / \rho}$, with wall shear stress τ_w and fluid density ρ . Nondimensionalisation for textured walls uses the viscous wall units derived from the smooth-wall simulation with the same Re_b .

The flow domain is a plane channel, bounded by two horizontal walls. At the channel walls, no-penetration and no-slip boundary conditions are applied, whereas periodic boundary conditions are used in the streamwise and spanwise directions. The streamwise, spanwise and wall-normal coordinates are denoted by x , y and z with the corresponding velocity components u , v and w .

The domain is specified by its length L_x , width L_y and height L_z . For a good comparison, the domain size should ideally be the same for all simulations. However, slight size variation was needed to fit an integer number of texture periods in the streamwise and spanwise directions, or to ensure that the number of grid cells complies with the parallel-computing algorithm. In general, all domains are approximately of size $(4.0 \times 2.5 \times 1)$, which is considered to be large enough to obtain reliable statistics for several reasons. First, it is comparable to the domain size used by other researchers (Moser et al., 1999; Breugem and Boersma, 2005;

Orlandi et al., 2006; Vreman and Kuerten, 2014b). In addition, it is full-span, as opposed to the recently reconsidered minimal-span channels (Chung et al., 2015). Finally, it is larger than the moderate box of size $(\pi \times \pi/2 \times 1)$ that is large enough to reproduce the one-point statistics of larger boxes (Lozano-Durán and Jiménez, 2014).

Textures are applied to the inside of both channel walls to enforce symmetry in the mean flow (García-Mayoral and Jiménez, 2011b). Unless stated otherwise, the top wall texture is the bottom wall texture mirrored in the centreline plane. To simulate flow over a non-smooth surface, two methods can be adopted: coordinate transformation or the Immersed Boundary Method (IBM) (Orlandi et al., 2006). Both methods have been applied to simulate turbulent flow over riblet walls (Choi et al., 1993; Goldstein et al., 1995). We used an IBM similar to the one employed by Breugem and Boersma (2005) and Pourquie et al. (2009), which is based on Fadlun et al. (2000). The IBM forcing is direct, i.e. a forcing term is added to the discretised equations. Appendix A.2 provides case-specific details.

The chosen IBM allows the use of a simple staggered Cartesian grid. The number of grid cells in the three Cartesian directions is denoted by N_x , N_y and N_z . The grid is uniform in the horizontal directions, so the grid spacings Δx and Δy are constant. In the wall-normal direction, three zones are distinguished, namely the roughness regions near the two walls and the remaining part of the channel. In the roughness region, which extends from the wall to one grid cell above the maximum texture height, the vertical grid spacing Δz_w is constant. In the remaining part of the channel, grid stretching is applied using a cosine function that is symmetrical with respect to the channel centreline. The maximum vertical grid spacing occurs at the centreline and is called Δz_c .

The grid-cell size is important to correctly resolve small-scale fluid motions. The recommendations of Vreman and Kuerten (2014a) for finite difference codes were followed, namely $\Delta x^+ = 4.4$, $\Delta y^+ = 2.9$, $\Delta z_w^+ = 0.49$ and $\Delta z_c^+ = 2.2$ as maximum grid spacings for smooth-wall turbulent flows. For textured walls, the spanwise grid spacing was reduced to $\Delta y^+ \approx 1.0$. For all investigated textures, one simulation at a double spanwise and/or streamwise resolution was performed. Particular attention was paid to the resulting drag change, which was marginal in all cases. As only one simulation at a higher resolution was performed for each texture, grid independence of the results cannot be claimed. However, as the grid resolution is relatively high and about the same in all cases, comparison of results is still justified.

The incompressible Navier–Stokes equations and continuity equation were solved at fixed bulk velocity:

$$\frac{\partial u_i}{\partial t} + \frac{\partial u_i u_j}{\partial x_j} = -\frac{\partial p}{\partial x_i} + \frac{1}{Re_b} \frac{\partial^2 u_i}{\partial x_j^2} + \gamma_f f^{\text{driving}} \delta_{i1} + f_i^{\text{IBM}}, \quad (3.1)$$

$$\frac{\partial u_j}{\partial x_j} = 0, \quad (3.2)$$

where the Einstein summation convention for repeated indices is used. Here u_i

represents one component of the velocity vector, t time, x_j a spatial coordinate, p the pressure and f^{driving} the spatially uniform forcing term to obtain a constant bulk velocity. The phase-indicator function γ_f is defined at grid points of the streamwise velocity. It equals 1 in fluid and 0 in solid obstacle volume to ensure that only fluid experiences the bulk forcing that drives the flow. The Kronecker-delta function δ_{i1} guarantees that fluid is driven in the streamwise direction with $i = 1$. Appendix A.1 describes how f^{driving} is calculated. The IBM forcing f_i^{IBM} is a body force that models the (drag) force that the texture exerts on the flow (see appendix A.2 for more details).

These equations are discretised using the finite-volume method combined with a pressure-correction scheme (Ferziger and Perić, 2002). Fluxes or stresses at the cell faces are evaluated using linear interpolation, i.e. a central-differencing scheme is used. Time-integration is performed using a fractional-step method that consists of three steps. For the pressure, which is staggered in time with respect to the velocities, a Crank–Nicolson scheme is used. All other terms are advanced in time using a three-step Runge–Kutta method (Wesseling, 2001). This discretisation procedure yields a Poisson equation, which is solved using a non-iterative solver based on Fast Fourier Transforms (FFTs). Specifically, FFTs are applied to the horizontal directions and the resulting tridiagonal system is solved using Gaussian elimination. More details about the time advancement at fixed bulk velocity can be found in appendix A.1.

For computation of flow statistics, a unit-cell average was stored each 100 timesteps. Like in crystallography, a unit cell is the smallest unit of volume that builds up the entire texture by translation. It extends vertically from bottom to top wall. For smooth walls, its size in grid cells is $1 \times 1 \times N_z$. In a unit-cell average, the data of all unit cells are reduced to an average in one unit cell. In addition to this unit-cell average during the computations, temporal and spatial averages were performed afterwards. Let $\phi = \phi(x, y, z, t)$ represent an arbitrary flow variable. The following averages were used:

$$\bar{\phi} = \frac{1}{T} \int_{t_{\text{stat}}}^{t_{\text{stat}}+T} \phi \, dt, \quad (3.3a)$$

$$\langle \phi \rangle_{x_i} = \frac{1}{L_{x_i}} \int_0^{L_{x_i}} \phi \, dx_i, \quad (3.3b)$$

$$\langle \phi \rangle_V = \frac{1}{V} \int_V \phi \, dV. \quad (3.3c)$$

Here, $\bar{\phi}$ is a time average over the statistically stationary part of the signal ϕ (which starts at t_{stat} and has duration T). An average over one spatial coordinate is denoted by $\langle \phi \rangle_{x_i}$. For instance, $\langle \phi \rangle_x$ is a streamwise average. A similar notation is adopted for an average over two spatial coordinates. For example, $\langle \phi \rangle_{xy}$ is a streamwise and spanwise average. Finally, $\langle \phi \rangle_V$ represents an average over the entire volume $V = L_x L_y L_z$. For instance, the bulk velocity is defined by $U_b = \langle u \rangle_V$.

3.4 Drag reduction quantification

This section describes the quantification of drag reduction. It explains under what conditions the smooth- and textured-wall flows are compared, with special attention for flow generation, the definition of a reference case and the formulation of the benefit of DR.

In general, channel flow is generated by either a constant flow rate (CFR), a constant pressure gradient (CPG) or a constant power input (CPI) (Frohnapfel et al., 2012). The obtained DR depends slightly on the choice of CFR, CPG or CPI. In this study, the flow was generated by CFR.

The quantification of DR requires the definition of a reference case compared to which drag is reduced or increased. Special attention should be paid to the Reynolds number and channel height, as drag depends heavily on both of them. Conceptually, this study compares two channels with the same fluid, the same flow rate per unit of spanwise width and the same outer dimension L_z^* . With $U_b^* L_z^*$ being the volumetric flow rate per unit width, the first two conditions imply that Re_b is the same for both flows. The third condition guarantees that both channels are geometrically identical, apart from the texture that is applied to the inside of the channel walls in one case. It implies that the wall location is not adjusted to compensate for the texture volume. The fluid volume for the case with textured walls is thus slightly less than that of the smooth-wall case. This is a conservative choice: DR cannot result from an increased fluid volume or a locally increased channel height (Daschiel et al., 2012; Mohammadi and Floryan, 2013).

This paper uses the drag change DC as a quantifying parameter. To account for possible differences in domain width and length, DC was computed from the time-averaged drag force per unit volume. As the driving term balances the total drag, the instantaneous drag force per unit volume $f_d^* = \rho^* (U_b^*)^2 (L_z^*)^{-1} V^{-1} \int_V \gamma_f f^{\text{driving}} dV$. Since the dimensional prefactor is equal for the smooth- and textured-wall channel flows, the drag change is given by

$$\begin{aligned}
 DC &= \frac{\overline{\langle \gamma_f f^{\text{driving}} \rangle_V} \Big|_{\text{textured}}}{\overline{\langle \gamma_f f^{\text{driving}} \rangle_V} \Big|_{\text{smooth}}} - 1 \\
 &\equiv \frac{d_{\text{textured}}^{\text{tot}}}{d_{\text{smooth}}^{\text{tot}}} - 1.
 \end{aligned} \tag{3.4}$$

It measures the increase of the driving force that is required to maintain a given flow rate. The drag reduction $DR = -DC$, so drag is reduced in case DC is negative.

The thus computed drag change is supplemented by a 95% confidence interval. The error in DC can be attributed to the uncertainty in the drag computed for both the textured and smooth wall. For ease of notation, define $d_t \equiv d_{\text{textured}}^{\text{tot}}$ and $d_s \equiv d_{\text{smooth}}^{\text{tot}}$. Let u_ϕ for now denote the uncertainty in ϕ . Given the independence of d_t and d_s , the uncertainty in DC follows from the law of error

TABLE 3.1: Validation of drag and flow statistics of smooth-wall simulations. The relative deviation of Re_τ from that predicted by Pope’s relation is given by $\Delta Re_\tau^{\text{Pope}}$ (equation 3.6). Statistics of U , u_{rms} , v_{rms} , w_{rms} and p_{rms} are compared with simulations by Vreman and Kuerten (2014a,b) at $Re_\tau^{\text{ref}} = 180$ and 590. The relative difference between current and reference flow statistic Q is measured with the root-mean-square relative deviation δQ (equation 3.7).

Re_b	Re_τ	$\Delta Re_\tau^{\text{Pope}}$ (%)	Re_τ^{ref}	δU (%)	δu_{rms} (%)	δv_{rms} (%)	δw_{rms} (%)	δp_{rms} (%)
5500	175.0	-0.6	180	0.58	1.09	1.39	1.52	3.98
11000	320.9	-1.0	-	-	-	-	-	-
22000	587.4	-1.5	590	0.55	1.85	0.82	0.88	0.94

propagation:

$$u_{DC}^2 = \left(\frac{u_{d_t}}{d_s} \right)^2 + \left(\frac{d_t u_{d_s}}{d_s^2} \right)^2. \quad (3.5)$$

The uncertainties in d_t and d_s were computed using the method outlined by Hoyas and Jiménez (2008). It accounts for correlation in the drag time signal. The thus obtained error bar only results from the finite simulation time. Errors of other origins (e.g. discretisation errors) were not considered.

3.5 Validation

The numerical methods were validated with simulations of smooth walls, parallel riblets, and parallel riblets in yaw, as described in the following subsections.

3.5.1 Smooth wall

Smooth-wall DNSs were performed at three bulk Reynolds numbers, namely 5500, 11000 and 22000. Table 3.1 shows the corresponding friction Reynolds number $Re_\tau = u_\tau \delta / \nu$, where $\delta = L_z / 2$ is the half-channel height. Compared to recent DNSs reaching $Re_\tau = 4000$ (Bernardini et al., 2014), $Re_\tau \approx 4200$ (Lozano-Durán and Jiménez, 2014) and $Re_\tau \approx 5200$ (Lee and Moser, 2015), the simulations in this study are considered to be standard. Therefore, this subsection suffices to validate drag and flow statistics.

Drag is validated by comparing Re_τ with the value predicted by an approximate relation $Re_\tau^{\text{Pope}} = 0.09 Re_b^{0.88}$ (Pope, 2000). The deviation of Re_τ from Re_τ^{Pope} is quantified using

$$\Delta Re_\tau^{\text{Pope}} = \frac{Re_\tau}{Re_\tau^{\text{Pope}}} - 1. \quad (3.6)$$

Table 3.1 lists $\Delta Re_\tau^{\text{Pope}}$ for all smooth-wall simulations. Although the relation for Re_τ^{Pope} is approximate, good agreement is obtained for all Re_b .

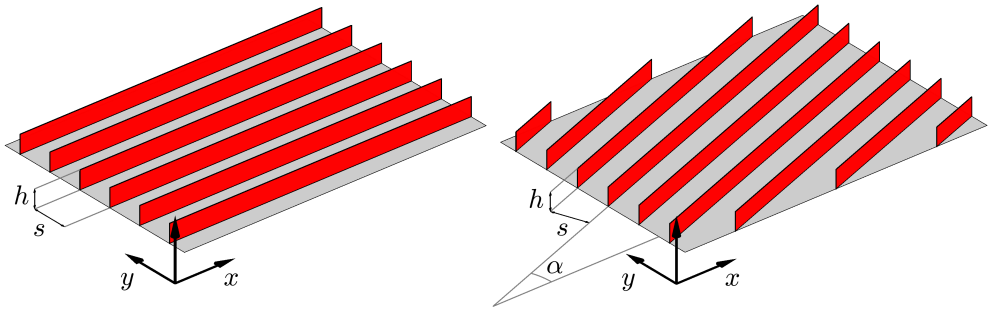


FIGURE 3.1: Parallel blade riblet texture. *Left*: Bird's-eye view of the texture aligned with the mean flow, showing six unit cells in the spanwise direction. *Right*: Bird's-eye view of the texture in yaw with yaw angle α , showing six unit cells in the spanwise and three in the streamwise direction.

Flow statistics of U , u_{rms} , v_{rms} , w_{rms} and p_{rms} were compared with simulations at $Re_\tau = 180$ (Vreman and Kuerten, 2014a) and $Re_\tau = 590$ (Vreman and Kuerten, 2014b). Here, $U = \langle \bar{u} \rangle_{xy}$, $u_{\text{rms}} = (\langle \bar{u}^2 \rangle_{xy} - \langle \bar{u} \rangle_{xy}^2)^{1/2}$ and similarly for the other root-mean-square quantities. Let $Q(z)$ be one of these statistics, then the root-mean-square relative deviation

$$\delta Q = \sqrt{\left\langle \left(\frac{Q(z) - Q^{\text{ref}}(z)}{Q^{\text{ref}}(z)} \right)^2 \right\rangle_z} \quad (3.7)$$

is used to quantify the difference between Q (current) and Q^{ref} (reference). It was computed after piecewise cubic spline interpolation of Q and Q^{ref} to a uniform grid, $z^+(k) = k$ for integers $1 \leq k \leq k_{\text{max}}$, with $k_{\text{max}} = 175$ at the lowest and $k_{\text{max}} = 587$ at the highest Re_b . Table 3.1 shows δQ for the five flow quantities. The root-mean-square relative deviation is smaller than 1% for the mean velocity and smaller than 2% for the root-mean-square fluctuations. The somewhat larger value for p_{rms} at the lowest Re_b is attributed to the difference between Re_τ and Re_τ^{ref} .

3.5.2 Parallel riblets

A parallel riblet texture consists of riblets aligned with the mean flow direction and can reduce turbulent drag up to almost 10% (Bechert et al., 1997). An overview of previous research can be found elsewhere (Dean and Bhushan, 2010). A thorough DNS study has been performed quite recently (García-Mayoral and Jiménez, 2011a,b, 2012).

This paper investigates the blade riblet texture (see figure 3.1). The blades have zero thickness, spacing s and height h with $h/s = 0.5$. In a small parametric study, mainly s^+ and Re_b were varied (see also table A.1). The grid resolution (specified in wall units) is about the same for all cases.

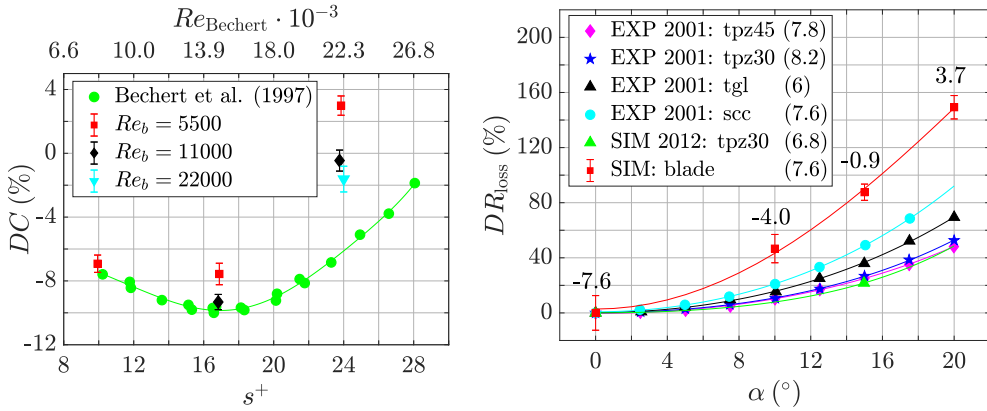


FIGURE 3.2: Validation of drag change for the parallel blade riblet texture. *Left*: Drag change as function of riblet spacing in wall units (no yaw). Numerical results at three different Reynolds numbers are compared with experimental data of Bechert et al. (1997). The experimental bulk Reynolds number is denoted by Re_{Bechert} . *Right*: Drag reduction loss (equation 3.8) as function of yaw angle for different riblet geometries at $s^+ = 17$. EXP 2001 are experiments by Hage et al. (2001) at $Re_b \approx 14900$. SIM 2012 are DNSs by Grüneberger et al. (2012) at $Re_b = 5750$. SIM are the current simulations. The riblet cross-sections are trapezoidal with a tip angle of either 30° (tpz30) or 45° (tpz45), triangular (tgl), semicircular (scc) or rectangular (blade). The numbers in parentheses in the legend represent the maximum drag reduction DR_{max} in percent. The numbers in the figure represent the drag change DC in percent for the simulated blade riblet geometry.

Figure 3.2 (left) compares the simulated drag change as function of s^+ with experiments performed by Bechert et al. (1997). The top axis shows the experimental bulk Reynolds number Re_{Bechert} , which is based on the horizontal channel width and the average velocity between the test plates. In the experiments only the Reynolds number was varied, whereas in the present numerical study both the Reynolds number and the riblet spacing were varied.

The drag change varies slightly with Reynolds number for fixed s^+ : the drag at $Re_b = 5500$ is higher than at $Re_b = 11000$ and 22000 . The approximate overlap of the data points at the two highest Reynolds numbers (for $s^+ = 24$) suggests a low-Reynolds-number effect, which is underpinned by the observation that DR data below $Re_{\text{Bechert}} \approx 10000$ deviated more and more from previous high-Reynolds-number data (Bechert et al., 1997). The deviation of DC at $Re_b = 5500$ from that at higher Reynolds numbers is also larger at larger s^+ , which might be explained by riblet height increase. For $Re_b = 5500$, an increase of s^+ from 10 to 24 is accompanied by a decrease of δ/h from 35 to 15. The blades protrude farther into the channel, which is presumably detrimental to DR. This is supported by the finding that, for $\delta/h \lesssim 50$, the effect of roughness extends across the boundary layer and the original wall flow dynamics is changed significantly (Jiménez, 2004).

The simulations capture the experimental trend quite well when Re_b is close to Re_{Bechert} . Especially good agreement is obtained around and below the optimum spacing. At $s^+ = 17$, a maximum DR of 9.3% is achieved, which is very close to the 9.9% of the experiments. The difference is slightly larger at $s^+ = 24$: there the total drag is reproduced within 5%. A higher reproduction accuracy probably requires a combined experimental/numerical study, a more extensive grid resolution study, the incorporation of blade thickness and an analytical correction of momentum fluxes near the riblet tips to resolve the high gradients there. However, the accuracy demonstrated here is sufficient for the herringbone riblet simulations, as drag differences for these were found to be much larger than 5%.

3.5.3 Parallel riblets in yaw

Among other factors, the performance of riblets deteriorates in yaw, i.e. when they are not aligned with the mean flow direction. An overview of past research is given by Koeltzsch et al. (2002). The study of Hage et al. (2001) shows the significant influence of riblet geometry and spacing s^+ . Simulations of turbulent flow over parallel riblet textures in yaw are rare in the literature. Grüneberger et al. (2012) have performed DNSs at $Re_b = 5750$ ($Re_\tau = 180$) for trapezoidal grooves. The driving pressure gradient was rotated such that the streamwise direction no longer coincides with the x -direction. Good agreement with experimental data was obtained.

This paper investigates the blade riblet texture in yaw (see figure 3.1) with $h/s = 0.5$ and $s^+ = 17$. The yaw angle α was varied for fixed $Re_b = 5500$. The horizontal grid resolution was comparable to that used for aligned parallel riblets: $\Delta x^+ \leq 4.1$ and $\Delta y^+ \leq 1.1$ for all cases. As the trick of driving-pressure-gradient rotation cannot be applied for herringbone-riblets simulations, the parallel riblet texture was rotated with respect to the grid. That required a different Immersed Boundary Method (IBM), as the blades are not anymore aligned with the Cartesian directions (see appendix A.2 for details).

Figure 3.2 (right) shows DC as function of α (indicated by the numbers in the figure). Clearly, the DR diminishes with increasing yaw angle, as is expected from the literature. Unfortunately, to the best of the authors' knowledge, no experimental data of blade riblets in yaw is available. For comparison of the simulated results with experimental data for other riblet geometries, the drag reduction loss DR_{loss} is introduced (Hage et al., 2001):

$$DR_{\text{loss}}(\alpha, s^+) = \frac{DR_{\text{max}} - DR(\alpha, s^+)}{DR_{\text{max}}}, \quad (3.8)$$

where $DR = -DC$, and DR_{max} is the maximum DR that can be obtained with a given geometry: $DR_{\text{max}} = DR(\alpha = 0, s^+ = s_{\text{opt}}^+)$. It was assumed that $DR_{\text{max}} = DR(\alpha = 0, s^+ = 17)$ for the simulations.

Figure 3.2 shows the drag reduction losses as function of yaw angle for different riblet geometries at $s^+ = 17$. The experimental data of Hage et al. (2001) (at

$Re_b \approx 14900$) and the numerical data of Grüneberger et al. (2012) (at $Re_b = 5750$) are included. The values of h/s are geometry dependent, namely $h/s = 0.5$ for the trapezoidal and blade, $h/s = 0.7$ for the semicircular, and $h/s = 1$ for the triangular geometries.

The dependence of DR_{loss} on α is different for each geometry, which might be explained by differences in h/s and riblet shape (Hage et al., 2001). Of the two trapezoidal geometries, the one with the sharpest tip (30°) is slightly more sensitive to misalignment. The triangular geometry has the largest tip angle of about 54° , but its DR loss is nevertheless larger than for the trapezoidal geometries, presumably because of its larger height ($h/s = 1$). Of the experimental data, the semicircular geometry is most sensitive to yaw, likely because of its larger height ($h/s = 0.7$) and sharp tip.

The simulation results suggest that the blade riblet geometry is more susceptible to yaw than any of the other geometries. This is likely not a low-Reynolds-number effect, as the simulations at $Re_b = 5750$ by Grüneberger et al. (2012) reproduced well the experimental data (see the figure). Instead, it might be ascribed to the sharper riblet tips (and the associated pressure drag increase) and the broader riblet valleys (and the associated increase of sloshing) (Hage et al., 2001).

3.6 Herringbone riblets

3.6.1 Texture description

The feather texture (described in section 3.2) is modelled as shown in figure 3.3, fairly similar to the spatial three-dimensional (s-3D) texture proposed in Chen et al. (2014a). It consists of N_{feather} feathers placed in parallel such that their edges touch. The modelled feather has no physical shaft, although the term ‘shaft’ is employed to denote the symmetry axis of a feather. The barbs are modelled as blade riblets with zero thickness. As opposed to the s-3D texture that consists of sawtooth riblets, the present study uses blades because of their superior drag-reducing performance in the conventional riblet texture. The angle between the positive x -direction and the blades is called α , which is restricted to $0 \leq \alpha < 180^\circ$. The shortest distance between the blades is s . Between two neighbouring blades a groove forms, which has spanwise blade spacing $s_y = s/\cos(\alpha)$. N_{groove} is the integer number of spanwise blade spacings s_y that fits in one feather half-width (see also figure 3.3). The feather width or spanwise texture wavelength $\Lambda_f = 2N_{\text{groove}}s_y$. The riblet height h_r decreases linearly with distance to the shaft. Let h represent the riblet height at the shaft and y_s the y -coordinate of the shaft, then h_r is given by

$$\frac{h_r(y)}{h} = 1 - \left| \frac{y - y_s}{\Lambda_f/2} \right|, \quad \text{for } -\frac{1}{2} \leq \frac{y - y_s}{\Lambda_f} \leq \frac{1}{2}. \quad (3.9)$$

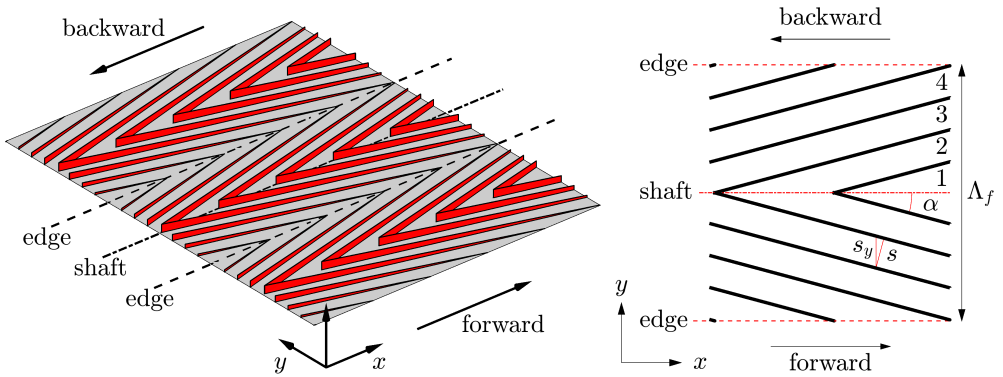


FIGURE 3.3: Herringbone blade riblet texture with 4 grooves per feather half ($N_{\text{groove}} = 4$), and angle between shaft and riblets of 15 degrees ($\alpha = 15^\circ$). *Left*: Bird’s-eye view of the texture, showing five unit cells in the streamwise and three unit cells (or feathers) in the spanwise direction. The edges and shaft of the middle feather are shown. Backward flow over this texture is equivalent to forward flow over a texture with $\alpha = 165^\circ$. *Right*: Top view of the texture, showing two unit cells in the streamwise and one unit cell in the spanwise direction. The feather width is Λ_f . Four grooves on one feather half are numbered.

Note that Koeltzsch et al. (2002) and Nugroho et al. (2013) used herringbone riblets of constant height. The texture was implemented using the same IBM that was used for blade riblets in yaw; only the texture indicator functions were different.

As figure 3.3 shows, a difference is made between forward and backward flow. ‘Forward’ is used for bulk flow in the positive, ‘backward’ indicates flow in the negative x -direction. Forward flow over a texture with angle α is the same as backward flow over a texture with angle $\alpha_{\text{backward}} = 180^\circ - \alpha$. Using this trick, textures with angle α and α_{backward} can be compared to study the influence of mean flow direction on drag.

In addition to the standard herringbone texture, two texture variations were considered. The first variation is called ‘shifted’. It differs from the standard herringbone texture by a spanwise shift of the top wall texture by half a spanwise texture wavelength as compared to the bottom wall (see figure 3.4). This shifted texture was investigated for its ability to generate the drag-reducing secondary flow that is described by Schoppa and Hussain (1998), namely one that extends from the bottom to the top wall. The second variation is a riblet texture with $\alpha = 0^\circ$ (see figure 3.4), which results in a parallel blade riblet geometry with blade height variation in the spanwise direction given by equation 3.9. This texture does not suffer from yaw and the resulting pressure drag, but it still might give rise to secondary flows.

The herringbone texture and its variations have been subjected to a parametric study (see also table A.1). According to Chen et al. (2014a), bird-feather parameters are typically $s^+ \approx 20$, $h/s \approx 0.5$ and $\alpha \approx 30^\circ$. Values for N_{groove} or

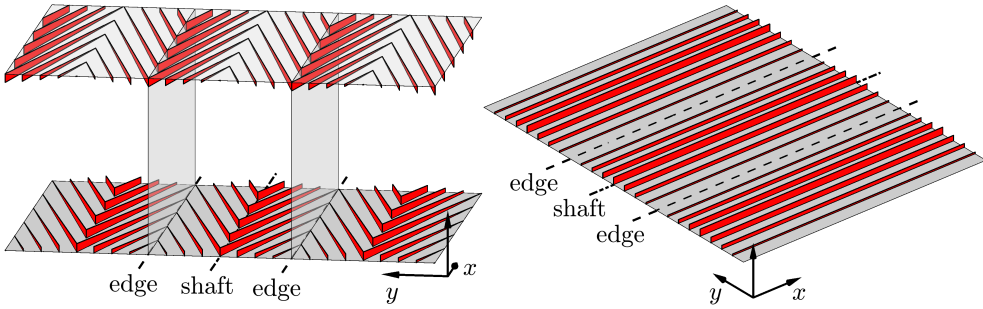


FIGURE 3.4: Herringbone riblet texture variations. *Left*: Bird's-eye view of a shifted texture variation with $N_{\text{groove}} = 4$ and $\alpha = 15^\circ$. ‘Shifted’ refers to the spanwise shift of the top wall texture by half a spanwise texture wavelength as compared to the bottom wall. The two vertical planes demarcate the middle unit cell. Note that the distance between bottom and top wall is not to scale. *Right*: Bird's-eye view of a parallel texture variation with $N_{\text{groove}} = 4$ and $\alpha = 0^\circ$, showing three unit cells (or feathers) in the spanwise direction.

Λ_f were not given. Their SEM-pictures show that the feather barbs are comparable to blades with finite thickness and rounded tips. Although the present study was inspired by the bird-feather texture, it did not attempt to exactly reproduce that texture. Instead, texture parameters were chosen to allow a close comparison with the parallel-riblet studies described in Subsections 3.5.2 and 3.5.3. Specifically, ridge spacing and maximum blade height were fixed at $s^+ = 17$ and $h/s = 0.5$. Mainly two parameters were varied, namely α and N_{groove} . The angle α was either 15° or 165° , which permits the direct comparison with the conventional riblet texture in 15 degrees yaw. Larger angles (e.g. $\alpha = 30^\circ$ or $\alpha = 150^\circ$) were not considered, as figure 3.2 suggests that such angles will result in a drag increase. The number of grooves N_{groove} was varied between 1 and 128, which resulted in a feather-width change from $\Lambda_f = 0.10$ to 12.9 in outer units or $\Lambda_f^+ = 35$ to 4506 in wall units.

Apart from texture parameters, the other simulation parameters were (almost) the same for all herringbone simulations, which facilitates a fair comparison. Specifically, table A.1 shows that domain size, grid resolution, Reynolds number and simulation time do not change much among the simulations. In addition, these parameters are also close to the ones for parallel-riblet (without/in yaw) simulations. All herringbone simulations were performed at $Re_b = 5500$. Based on the validation of blade-riblet simulations (see section 3.5.2), a low-Reynolds-number effect can be anticipated. However, as all simulations were performed at the same Re_b , a proper comparison can still be made. The number of grid cells per groove $N_{cg} = 16$, so 16 grid cells span the groove width.

To substantiate the accuracy of the used numerical methods, two issues have to be addressed. The first issue relates to the boundary conditions at the texture surface. Appendix A.2.4 shows that the no-slip and no-penetration conditions are sufficiently satisfied. The second issue relates to the flow around the blade tip.

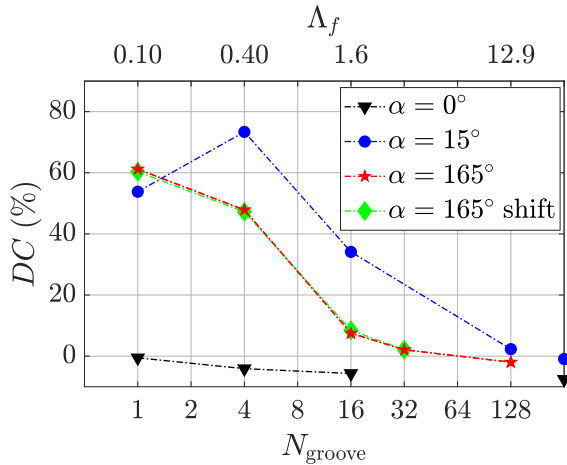


FIGURE 3.5: Drag change as function of feather width for the herringbone riblet geometry, including results for the parallel ($\alpha = 0^\circ$) and shifted variants (see figure 3.4). The shown values of Λ_f apply to the textures with $\alpha = 15^\circ$ or 165° , and are approximate for $\alpha = 0^\circ$ textures. The corresponding values of Λ_f^+ are 35, 141, 563 and 4506. The data points on the right vertical axis belong to conventional parallel riblets with yaw angle $\alpha = 0^\circ$ and $\alpha = 15^\circ$.

The exact solution is singular there, which might introduce errors in the numerical solution. The improvement of the numerical accuracy for problems involving singularities is a research in itself (Shi et al., 2004), but it is not the focus of the current study. For the present purpose, the used IBM is sufficiently accurate. Very similar IBMs have been used in DNSs of flow around other obstacles with sharp corners, such as cubes (Breugem and Boersma, 2005; Orlandi and Leonardi, 2006), square and triangular elements (Orlandi et al., 2006), and a flat plate normal to the free stream (Saha, 2007; Narasimhamurthy and Andersson, 2009). The penultimate example shows that the IBM can deal with obstacles that are not aligned with the Cartesian grid, whereas the last example demonstrates that the IBM can also accurately capture separating flows at sharp corners.

3.6.2 Drag reduction

Figure 3.5 shows the drag change as function of feather width for the herringbone riblet geometry. Drag changes significantly with the spanwise texture wavelength or feather width. For the texture with $\alpha = 165^\circ$, the drag increases by 61% for very narrow feathers, while the drag decreases by 2% for very wide feathers. In general, wider feathers experience less drag. Only the texture with $\alpha = 15^\circ$ and $N_{\text{groove}} = 1$ does not comply with this trend. DR was only obtained when the texture approaches the parallel riblet texture in yaw, i.e. in the limit of very wide feathers. Only 2% reduction was found in that limit, which is indeed comparable to the 0.9% reduction that was obtained for parallel riblets at yaw angle $\alpha = 15^\circ$. It is significantly less than the 7.6% reduction for parallel riblets aligned with the mean flow.

There is a clear drag difference between textures with $\alpha = 15^\circ$ (forward flow) and $\alpha = 165^\circ$ (backward flow). For example, at $N_{\text{groove}} = 16$ drag increases by 34% for $\alpha = 15^\circ$, and only by 7.5% for $\alpha = 165^\circ$. This shows that mean-flow reversal has a considerable effect on drag, in agreement with Chen et al.

(2014a). Here, forward flow experiences more drag than backward flow, except for the $N_{\text{groove}} = 1$ texture. The drag difference between forward and backward flow decreases for increasingly wide feathers, as can be expected. The textures with $\alpha = 15^\circ$ and 165° differ only because of riblet convergence or divergence in the feather shaft or feather edge regions. When $\Lambda_f \rightarrow \infty$, only a very small portion of the complete texture consists of converging or diverging riblets, so their contribution to the total drag becomes negligible.

Figure 3.5 also shows the drag for the shifted and parallel riblet ($\alpha = 0^\circ$) variations. The drag of textures with and without shift is about the same for all feather widths. Hence, shifting of the top wall texture has almost no effect on drag, although the next subsection will explain that the mean flow is different for some cases.

In contrast with most herringbone textures, the parallel riblet texture with spanwise riblet height variation is able to reduce drag. The DR is the least for $N_{\text{groove}} = 1$, namely 0.5%. The texture with $N_{\text{groove}} = 1$ and $\alpha = 0^\circ$ is the conventional parallel-riblet geometry with $s^+ = 17$, but with every second blade removed. It is known that this geometry is not optimal for DR. When N_{groove} increases, DR increases as well. In the limit of very large N_{groove} , the texture approaches the standard parallel-riblet geometry, apart from a very slight spanwise height variation. Therefore, in that limit one might expect the DR to be close to that for standard riblets.

3.6.3 Flow description

To understand the drag-reduction results presented in the previous subsection, a detailed flow analysis is indispensable. Figure 3.6 shows three cross sections of the instantaneous streamwise velocity. The V-shaped contours in the horizontal cross section reveal the presence of the herringbone texture. The plumes that appear in the yz -plane represent up- or downdrafts that result from the converging/diverging riblets in the texture.

Figure 3.7 shows part of the mean streamwise-averaged flow fields for textures with $\alpha = 165^\circ$ and $N_{\text{groove}} = 1, 4, 16$. Because of flow symmetry, the figures show only one feather half. The feather shaft is located at the left side and the feather edge at the right side of the figures. For textures with $\alpha = 165^\circ$, the flow near the shaft converges, a local updraft of fluid results, and an approximately square vortex appears. The vortex does not reach the channel centreline, probably because of the small misalignment of the riblets with the mean flow ($\alpha = 165^\circ$ is relatively close to 180°). For $N_{\text{groove}} \geq 4$, it is limited in vertical extent to approximately $z = 0.2$, as can be seen for $N_{\text{groove}} = 4$ and 16 in the figure. Because of spanwise confinement, for small feather widths the vortex decreases in size. For $N_{\text{groove}} = 1$, it only reaches $z = 0.05$. Secondary flow is thus suppressed for small spanwise roughness spacings. This accords with the experimental finding that secondary flow disappears for decreasing spanwise spacing of roughness elements (Vanderwel and Ganapathisubramani, 2015).

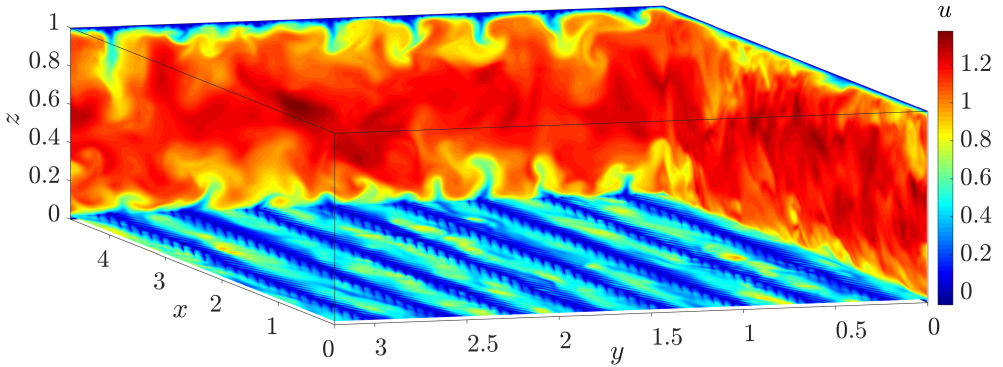


FIGURE 3.6: Three cross sections of the instantaneous streamwise velocity in the simulation domain that belongs to the herringbone texture with $N_{\text{groove}} = 4$, $\alpha = 165^\circ$. The horizontal plane is located at $z = 0.016$ or $z/h = 0.68$.

While mainly one vortex constitutes the secondary flow for $N_{\text{groove}} = 1$ and 4, tertiary flows appear for larger feather widths. For example, the mean flow for $N_{\text{groove}} = 16$ (see figure 3.7) shows a counterclockwise-rotating flow that extends to the channel centreline. Less pronounced is the small clockwise-rotating vortex near the feather edge. Several tertiary flows were also observed for even wider feathers ($N_{\text{groove}} = 32, 128$). This agrees with the experimental finding that tertiary flows appear when the spanwise spacing of roughness elements increases above the boundary layer thickness (Vanderwel and Ganapathisubramani, 2015). These tertiary flows are likely similar to the secondary flows that form over streamwise-aligned roughness strips (Anderson et al., 2015). The latter are stress-induced (i.e. Prandtl’s secondary flows of the second kind), as opposed to the flow-curvature-induced secondary flows (i.e. Prandtl’s secondary flows of the first kind).

Reversing the flow direction from backward to forward also changes the secondary flow direction. For textures with $\alpha = 15^\circ$, riblets near the shaft diverge, resulting in a local downdraft of fluid and the appearance of a counterclockwise-rotating secondary flow to the right of the shaft. A tertiary flow again appears for $N_{\text{groove}} \geq 16$. However, this time it is less well-defined, as its rotation direction is also counterclockwise. So, the most dominant tertiary flow does not change rotation direction by flow reversal.

Shifting of the top-wall textures changes the mean-flow patterns only slightly. For all cases, the dominant vortex near the top wall shifts in the spanwise direction. As this vortex does not reach the channel centreline, it has no noticeable effect on the mean flow in the bottom channel half. For $N_{\text{groove}} = 1$ and 4, this spanwise shift is the only change of the mean flow. For $N_{\text{groove}} = 16$, however, the pronounced counterclockwise-rotating tertiary flow is also modified. It reaches the centreline for the not-shifted texture (see figure 3.7), but it occupies the whole channel for the shifted variant. It is almost square, as for $N_{\text{groove}} = 16$ the feather half-width ($\Lambda_f/2 = 0.80$) approximately equals the channel height

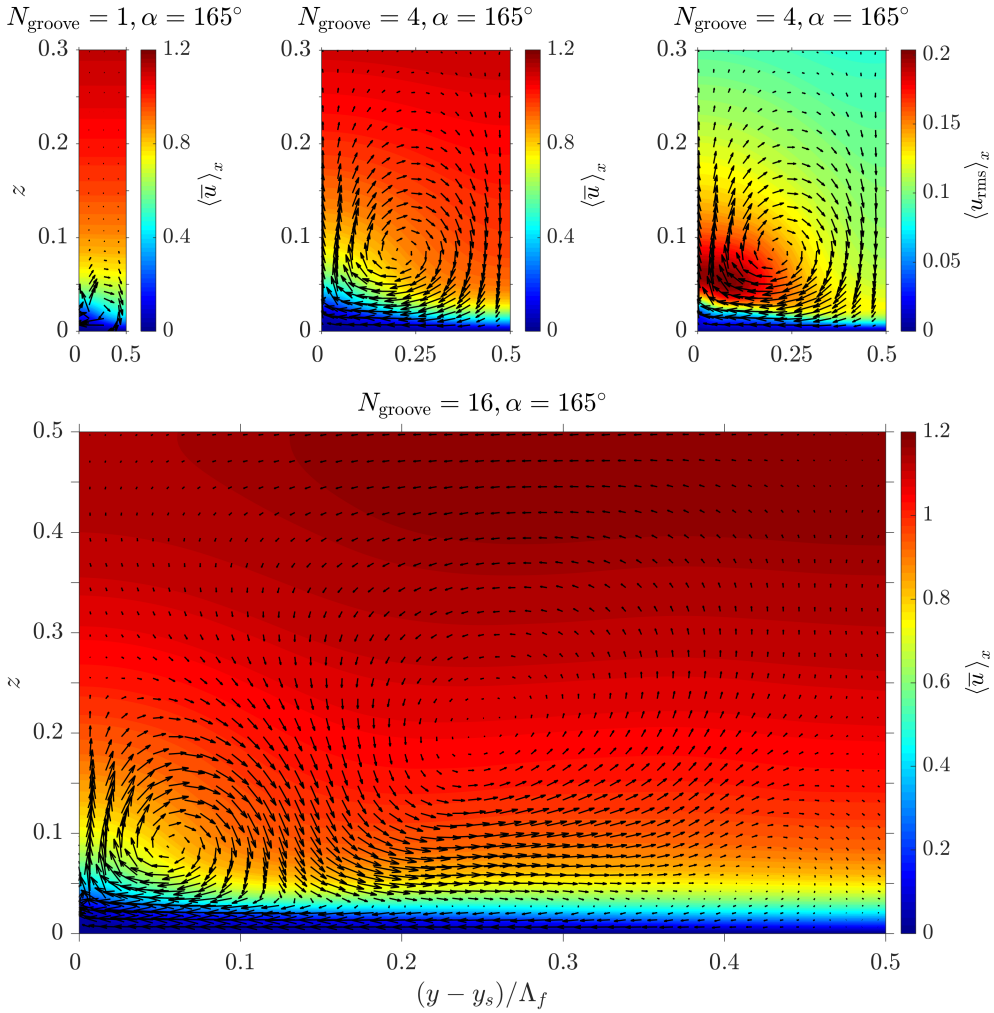


FIGURE 3.7: Streamwise-averaged mean flow in a plane perpendicular to the streamwise direction for herringbone textures with $\alpha = 165^\circ$ and $N_{\text{groove}} = 1$ (top left), 4 (top centre and right), 16 (bottom). Vectors exhibit in-plane secondary flow. Contours represent streamwise velocity (top left, top centre, bottom) or streamwise velocity fluctuations (top right, $u_{\text{rms}} = (\overline{u^2} - \bar{u}^2)^{1/2}$).

($L_z = 1$). Tertiary flow for $N_{\text{groove}} = 32$ also extends from bottom to top wall. However, these modified tertiary flows apparently have not much influence on drag (considering figure 3.5).

The strong secondary-flow vortex near the shaft causes a spanwise modulation of the boundary layer, as is clear from the streamwise-velocity contours in figure 3.7. Regions of updrafts (downdrafts) are characterised by low (high) streamwise velocity. The trend for streamwise velocity fluctuations is opposite,

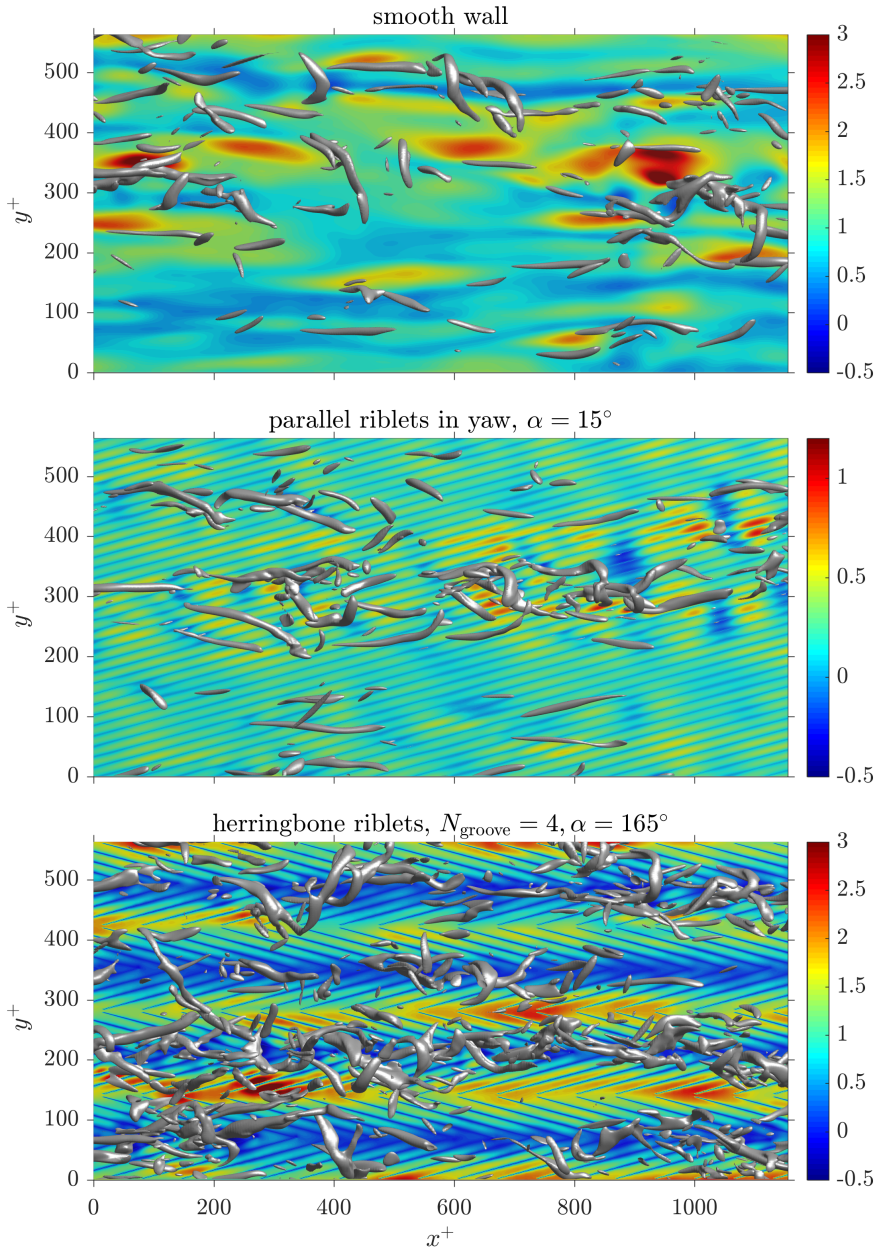


FIGURE 3.8: Instantaneous vortical structures and wall shear in a part of the bottom channel half. Vortical structures are iso-surfaces of the second invariant of the velocity gradient tensor with $Q^+ = 0.03$. The coloured contours represent the wall shear stress τ_w^+ on the bottom wall. Three cases are shown (from *top* to *bottom*): smooth walls; parallel riblets in yaw of $\alpha = 15^\circ$; herringbone riblets with $N_{\text{groove}} = 4, \alpha = 165^\circ$. $Re_b = 5500$ for all cases and $s^+ = 17$ for all textures.

as the top-right subfigure shows: updrafts (downdrafts) are associated with increased (decreased) fluctuations. The same was found in experimental studies of convergent/divergent riblets (Koeltzsch et al., 2002; Nugroho et al., 2013) and in DNSs of turbulent boundary layers with uniform blowing/suction (Kametani and Fukagata, 2011).

Figure 3.8 shows the instantaneous vortical structures and wall shear for three cases, namely smooth walls, parallel riblets in yaw and herringbone riblets. The vortical structures are iso-surfaces of the second invariant of the velocity gradient tensor (the Q -criterion, see e.g. Dubief and Delcayre (2000)). The contours represent the shear stress τ_w^+ on the bottom wall. The smooth-wall plot shows some well-known features, such as low-speed streaks and hairpin-type vortical structures. The streaks are much less apparent in the second plot, which is attributed to the parallel riblets that adjust the turbulence. The streaks are more evident in the flow above the riblets. The vortices are comparable to the ones for the smooth wall. The plot for parallel riblets without yaw is not shown, as it is very similar to the one for parallel riblets in yaw.

The herringbone riblet texture exhibits the largest changes in vortical structures and shear. High shear is associated with diverging riblets, and low shear with converging riblets. The vortices seem to be ordered as well: they are abundant over regions with updrafts, but almost absent over regions with downdrafts. The same trend was again found for blowing/suction: vortices are enhanced by blowing in spite of the reduced wall shear stress, while vortices are suppressed by suction despite the increase of wall shear stress Kametani and Fukagata (2011).

3.6.4 Secondary flow strength

To quantify the strengths of the secondary flows described in the previous subsection, the secondary flow strength Γ_s is introduced:

$$\Gamma_s = \sqrt{v^2 + w^2} = \sqrt{\Gamma_m^2 + \Gamma_t^2}, \quad (3.10a)$$

$$\Gamma_m = \sqrt{\bar{v}^2 + \bar{w}^2}, \quad (3.10b)$$

$$\Gamma_t = \sqrt{(\overline{v'})^2 + (\overline{w'})^2}, \quad (3.10c)$$

with $v' = v - \bar{v}$ and $w' = w - \bar{w}$. The secondary flow strength is decomposed into the mean-secondary-flow strength Γ_m and the turbulent-secondary-flow strength Γ_t . These variables still depend on the spatial coordinates. A volume- and xz -average of Γ_m and Γ_t is shown in figure 3.9.

Figure 3.9 (left part) shows that both mean and turbulent secondary flow become stronger with decreasing feather width. This is attributed to the converging or diverging riblets that trigger updrafts and downdrafts. When the feather width decreases, the spanwise density of these texture-generated secondary flows increases. In other words, the secondary flows that are created near the feather shaft and edges cover a relatively larger portion of the total fluid volume. This yields a stronger volume-averaged secondary flow for smaller feather widths.

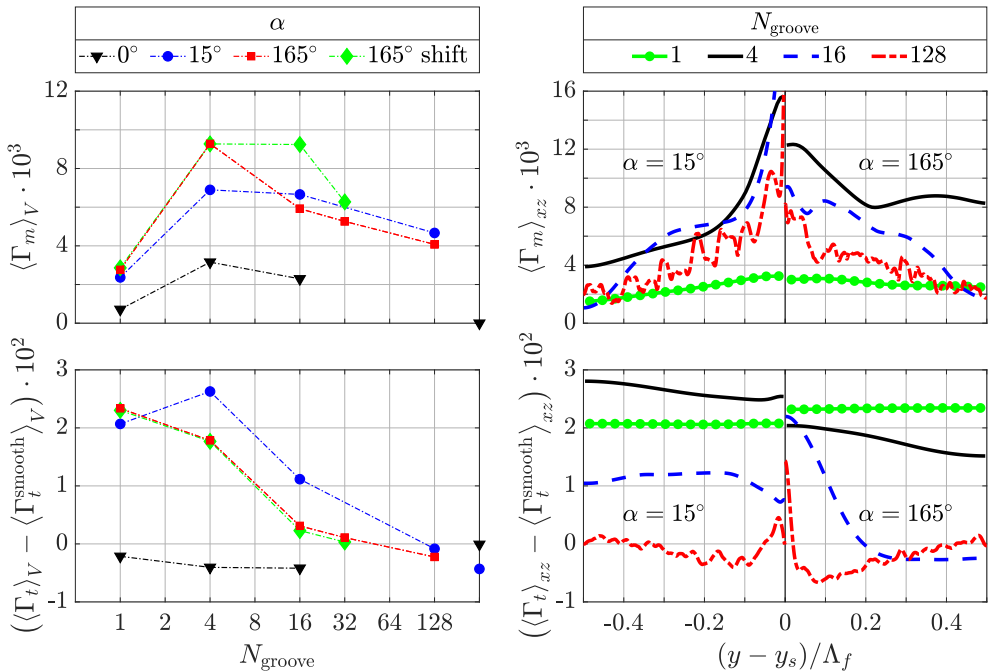


FIGURE 3.9: Strength of mean and turbulent secondary flow for the herringbone riblet geometry. *Top left*: Volume-averaged mean-secondary-flow-strength as function of feather width (specified by N_{groove}). The data points on the right vertical axis represent the conventional parallel blade riblets with yaw angle $\alpha = 0^\circ$ and $\alpha = 15^\circ$ (not visible with $\langle \Gamma_m \rangle_V = 0.027$). *Top right*: Streamwise- and wall-normal-averaged mean-secondary-flow-strength as function of spanwise distance for textures with $\alpha = 15^\circ$ (left part) and $\alpha = 165^\circ$ (right part). *Bottom left*: turbulent-secondary-flow-strength plotted as in top-left subfigure. *Bottom right*: turbulent-secondary-flow-strength plotted as in top-right subfigure. In the bottom figures, the turbulent-secondary-flow-strength of the smooth wall $\langle \Gamma_t^{\text{smooth}} \rangle_V = \langle \Gamma_t^{\text{smooth}} \rangle_{xz} = 0.069$ is subtracted.

The mean- and turbulent-secondary-flow strengths follow the same trend for most textures (namely an increase with a decrease of Λ_f). For all N_{groove} , the converging or diverging riblets near the shaft trigger updrafts and downdrafts. As figure 3.6 demonstrates, these are not steady flow patterns. Instead, they can be considered as fluctuating ejections and sweeps that are generated by the texture. The resulting instantaneous secondary flow ($v^2 + w^2$) projects both onto Γ_m and Γ_t (see equation 3.10). A stronger instantaneous secondary flow yields in general an increase of both the mean and turbulent secondary flow. That explains why the mean and turbulent strength follow the same trend for $N_{\text{groove}} \geq 4$. The results for $N_{\text{groove}} = 1$, however, deviate in this respect: $\langle \Gamma_m \rangle_V$ more than halves as compared to $N_{\text{groove}} = 4$. This suppression of mean secondary flow is due to spanwise confinement (see previous subsection). However, the fluctuating updrafts and downdrafts are not suppressed, so the turbulent secondary flow

remains strong.

Figure 3.9 (top right) shows how Γ_m varies with spanwise distance. The mean secondary flow is clearly strongest near the shaft, which is due to the counter-rotating vortices that form there. Such vortices are also generated near the feather edges, but the riblets have a small height there, which yields only a relatively weak secondary flow. Compared to $\alpha = 165^\circ$, textures with $\alpha = 15^\circ$ have a stronger mean secondary flow at the shaft, which is probably due to the downdraft of high-momentum fluid there.

Figure 3.9 (bottom right) shows how Γ_t varies with spanwise distance. The relatively uniform turbulence for the textures with $N_{\text{groove}} = 1, 4$ shows that the flow is well-mixed. In contrast, the turbulence changes with y for the other textures. When approaching the shaft, turbulence reduces when $\alpha = 15^\circ$ and increases when $\alpha = 165^\circ$. The same was observed for the streamwise velocity fluctuations in the previous subsection. When compared with the smooth wall, however, the turbulence at the shaft is increased for all textures. Away from the shaft, three textures exhibit local turbulence reductions.

Figure 3.9 also shows the volume-averaged secondary flow strength for the shifted texture variation. The turbulent contribution is practically the same as for the not-shifted texture. The same applies to the mean contribution for $N_{\text{groove}} = 1$ and 4. This agrees with the observation that, apart from the spanwise shift of the main vortex near the top wall, the mean secondary flow does not change. For $N_{\text{groove}} = 16$ and 32, however, the mean secondary flow is stronger for the shifted texture, which is ascribed to the formation of a tertiary flow that extends from bottom to top wall.

The secondary flow for the texture variation with $\alpha = 0^\circ$ is much weaker than for the herringbone riblet geometries, which is attributed to alignment of the riblets with the mean flow. Both $\langle \Gamma_m \rangle_V$ and $\langle \Gamma_t \rangle_V$ are still larger than the values for the parallel riblet geometry with constant blade height, although they seem to approach those values in the limit of large N_{groove} . The figure shows that parallel riblet geometries can reduce turbulence.

3.6.5 Spanwise transport of streamwise momentum

To confirm that advective transport is most important around the shaft, this subsection considers the streamwise momentum balance as function of spanwise distance. The Navier–Stokes equation for streamwise momentum (see equation 3.1) is rewritten as $\partial u / \partial t = \sum f$, where f is one of the terms in that equation. A time, streamwise and wall-normal average (denoted by $\langle \bar{f} \rangle_{xz}$) is applied to this equation. Assuming statistical stationarity and using the boundary conditions, the balance becomes:

$$0 = - \underbrace{\left\langle \frac{\partial \bar{u} \bar{v}}{\partial y} \right\rangle_{xz}}_{\text{adv } y} + \underbrace{\left\langle \frac{1}{Re_b} \frac{\partial^2 \bar{u}}{\partial y^2} \right\rangle_{xz}}_{\text{dif } y} + \underbrace{\left\langle \frac{1}{Re_b} \frac{\partial^2 \bar{u}}{\partial z^2} \right\rangle_{xz}}_{\text{shear}} + \underbrace{\left\langle \gamma_f \overline{f^{\text{driving}}} \right\rangle_{xz}}_{\text{driving}} + \underbrace{\left\langle \overline{f_x^{\text{IBM}}} \right\rangle_{xz}}_{\text{IBM}}. \quad (3.11)$$

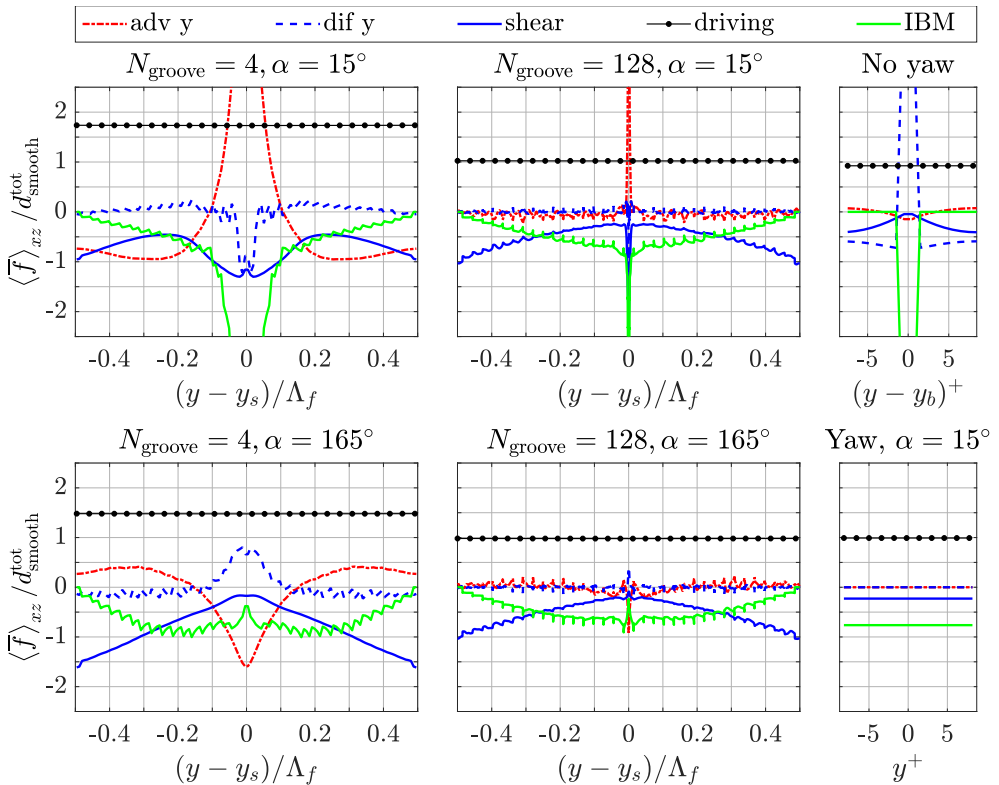


FIGURE 3.10: Streamwise momentum balance as function of the spanwise coordinate (equation 3.11). Six textures are shown: narrow herringbone feathers ($N_{\text{groove}} = 4$) for $\alpha = 15^\circ$ (top left) and $\alpha = 165^\circ$ (bottom left); wide herringbone feathers ($N_{\text{groove}} = 128$) for $\alpha = 15^\circ$ (top centre) and $\alpha = 165^\circ$ (bottom centre); parallel riblets aligned with the mean flow (top right) and in yaw of $\alpha = 15^\circ$ (bottom right). The blade location is denoted by y_b . For all cases, $Re_b = 5500$ and $s^+ = 17$.

The terms in this equation only depend on the spanwise coordinate y . The third term is called ‘shear’, since it equals the sum of bottom and top-wall shear as a result of the wall-normal integration. All terms are divided by $d_{\text{smooth}}^{\text{tot}}$ and shown in figure 3.10 for four herringbone textures. The abscissa represents the spanwise distance to the feather shaft. Most curves exhibit approximately equidistant wiggles that result from staircasing: the riblet height increases in 17 steps of size Δz_w from 0 at the feather edges to h at the shaft.

Before the differences between $N_{\text{groove}} = 4$ and 128 are highlighted, the general behaviour of the different terms is clarified. The driving term is almost constant with y , because γ_f changes only marginally from the feather shaft to the edges. For $N_{\text{groove}} = 4$, this term is clearly larger than 1, indicating a significant drag increase.

The shear term is negative, as it tends to decelerate the fluid. Its magnitude

quantifies how the flat-wall streamwise shear changes with the spanwise coordinate. When moving from the feather edges towards the shaft, the wall-shear term first decreases (in magnitude), which is attributed to shielding of the flat wall by blades which increase in height. This trend continues for textures with $\alpha = 165^\circ$. However, the shear magnitude peaks near the shaft for $\alpha = 15^\circ$, which is ascribed to the local downdraft that transports high momentum towards the wall. For very wide feathers ($N_{\text{groove}} = 128$), the shear term equals -1 at the feather edges. There the blade height is zero and the smooth-wall result is recovered.

The IBM term represents the streamwise drag force on the riblets. It is negative, as it is responsible for a velocity decrease (like the shear term). It equals zero at the feather edges, because the riblets have no height there. When approaching the feather shaft from the edges, the IBM-force magnitude first increases, which is due to riblet-height increase. Near the shaft, it has a local minimum for $\alpha = 165^\circ$. In contrast, it is very large there for $\alpha = 15^\circ$, likely due to the downdraft of high-speed fluid.

The balance for $N_{\text{groove}} = 4$ shows significant contributions from spanwise advective and diffusive transport, especially near the shaft. For $\alpha = 15^\circ$, advection is on average responsible for an increase of streamwise momentum near the shaft. This is attributed to the secondary-flow vortex that transports low momentum away from the shaft (near the wall) and high momentum towards the shaft (closer to the channel centreline). In contrast, diffusion transports high momentum away from the shaft. These trends are opposite to that of textures with $\alpha = 165^\circ$, for which spanwise advection causes a streamwise momentum decrease and diffusion an increase near the shaft.

Compared to $N_{\text{groove}} = 4$, the relative importance of the terms in equation 3.11 is very different for $N_{\text{groove}} = 128$. The prominent peaks near the shaft are very narrow. Spanwise transport by advection and diffusion is close to zero for the largest part of the feather. Away from the shaft, the texture behaves as parallel riblets in yaw with a local balance between the driving force on the one hand, and the IBM and wall-shear force on the other hand.

3.6.6 Wall-normal transport of streamwise momentum

The previous subsections show that drag increase is accompanied by a strong secondary flow, which suggests that enhanced advection is responsible for the drag augmentation. To underpin this suggestion, this subsection considers the streamwise momentum balance as function of the wall-normal coordinate. A time, streamwise, and spanwise average (denoted by $\langle \bar{f} \rangle_{xy}$) is applied to the Navier–Stokes equation $\partial u / \partial t = \sum f$. Assuming statistical stationarity and using the boundary conditions, the balance reads:

$$0 = - \underbrace{\left\langle \frac{\partial \bar{u} \bar{w}}{\partial z} \right\rangle_{xy}}_{\text{adv } z} + \underbrace{\left\langle \frac{1}{Re_b} \frac{\partial^2 \bar{u}}{\partial z^2} \right\rangle_{xy}}_{\text{dif } z} + \underbrace{\left\langle \gamma_f \bar{f}^{\text{driving}} \right\rangle_{xy}}_{\text{driving}} + \underbrace{\left\langle \bar{f}_x^{\text{IBM}} \right\rangle_{xy}}_{\text{IBM}}. \quad (3.12)$$

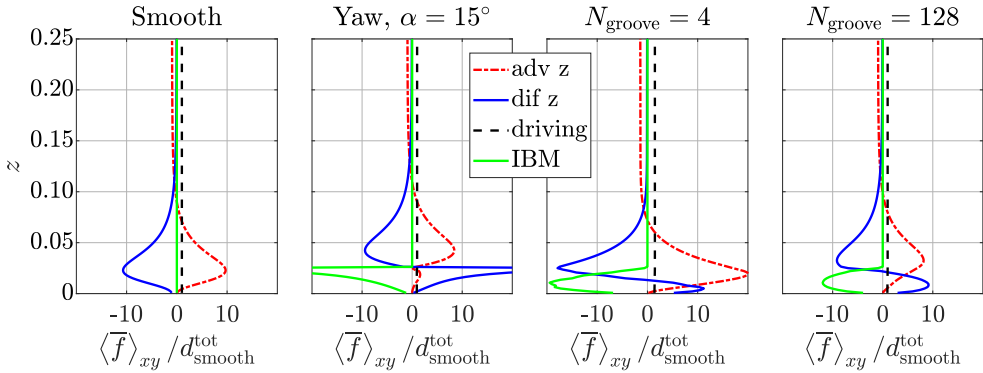


FIGURE 3.11: Streamwise momentum balance as function of the wall-normal coordinate (equation 3.12). Four cases are shown (from *left to right*): smooth walls; parallel riblets in yaw of $\alpha = 15^\circ$; narrow herringbone feathers ($N_{\text{groove}} = 4$) for $\alpha = 165^\circ$; wide herringbone feathers ($N_{\text{groove}} = 128$) for $\alpha = 165^\circ$. $Re_b = 5500$ for all cases and $s^+ = 17$ for all textures.

The terms in this equation only depend on the wall-normal coordinate z . All terms are divided by $d_{\text{smooth}}^{\text{tot}}$ and displayed in figure 3.11 for four cases. The profiles for parallel riblets without yaw (not shown) are very similar to that for riblets in yaw. In addition, the profiles for herringbone textures with $\alpha = 15^\circ$ (not shown) are similar to the ones for $\alpha = 165^\circ$. The behaviour of the different terms is clarified below. The driving term is almost constant, as before.

The IBM term represents the drag force on the texture, so it is only present near the wall and it is responsible for a velocity decrease. The drag force is especially large near the blade tips. That explains the peak at blade height for riblets in yaw, for which all blades have the same height. The large IBM force near the blade tips is in figure 3.11 not evident for herringbone textures. Instead, the peak is smeared out due to the spanwise blade-height variation between 0 and h (see equation 3.9). For the two herringbone textures shown in the figure, the narrower feather clearly experiences a larger IBM force than the wider feather.

Diffusive transport is especially important near the wall. It has a negative tendency for smooth walls, but for textured walls it becomes positive in between the riblets. The latter is associated with an inflection point in the mean streamwise-velocity profile.

Advective transport is significant throughout the whole channel. Near the channel centreline, it balances the driving force (for all cases). Near the wall, turbulent advective transport is responsible for a velocity increase and the associated drag augmentation. Parallel riblets suppress turbulent advection, as is clear from the second sub-figure. Compared to smooth walls, the peak of advection shifts upwards and shrinks. The herringbone case with $N_{\text{groove}} = 128$ shows the same trend, although the upward shift is less pronounced. Turbulent transport below $z = h$ is less suppressed as compared to parallel riblets in yaw, which is ascribed to the blade height decrease with spanwise distance to the shaft. Still,

weakening and lifting of advective transport is quite apparent. In contrast, advective transport is much stronger for $N_{\text{groove}} = 4$ as compared to a smooth wall. This reinforces the suggestion that drag augmentation is caused by enhanced advection, which will be confirmed in the next section with a quantitative analysis.

3.7 Drag change decomposition

3.7.1 Previous research

Fukagata et al. (2002) derived an equation (called FIK-identity) that decomposes the frictional-drag coefficient into contributions from different dynamical effects. They distinguished four contributions, namely laminar (or bulk), turbulent, inhomogeneous and transient. For homogeneous and steady plane channel flow, the FIK-identity reads (in our notation):

$$\frac{1}{12} \overline{f^{\text{driving}}} = \frac{1}{Re_b} + \int_0^1 \left(\frac{1}{2} - z \right) \langle -\overline{u'w'} \rangle_{xy} dz, \quad (3.13)$$

where it is used that the domain height $L_z = 1$. Note that the skin-friction coefficient $C_f \equiv 2\overline{\tau_w^*} / (\rho^* U_b^{*2}) = \overline{f^{\text{driving}}}$ for smooth-wall channel flow.

This relation has been extended to geometrically more complex surfaces by Peet and Sagaut (2009). They derived analytical relations for streamwise-, spanwise- and quasistreamwise-homogeneous surfaces. To our knowledge, however, these relations cannot be used for the herringbone textures. That asks for a second extension of the FIK-identity.

3.7.2 Derivation of extended FIK-identity

The extended FIK-identity is derived from the slab-averaged streamwise momentum balance (equation 3.12). For ease of notation, that equation is written as $0 = \sum_l f^{(l)} \Big|_z$, where $f^{(l)}$ represents one of the terms in that equation. The subscript z expresses that $f^{(l)}$ only depends on the wall-normal coordinate. In what follows, the global drag balance is needed. It follows from a single integration of equation 3.12: $0 = \sum_l \int_0^1 f^{(l)} \Big|_z dz$ or

$$\begin{aligned} d^{\text{tot}} &= \left\langle \gamma_f \overline{f^{\text{driving}}} \right\rangle_V \\ &= \left\langle \frac{1}{Re_b} \frac{\partial \bar{u}}{\partial z} \Big|_{z=0} \right\rangle_{xy} - \left\langle \frac{1}{Re_b} \frac{\partial \bar{u}}{\partial z} \Big|_{z=1} \right\rangle_{xy} - \left\langle \overline{f_x^{\text{IBM}}} \right\rangle_V. \end{aligned} \quad (3.14)$$

Next, equation 3.12 is rewritten as $0 = \sum_l (1/2) \left(f^{(l)} \Big|_z + f^{(l)} \Big|_{1-z} \right)$ to explicitly account for symmetry in the mean flow. Triple integration is applied to this equation, such that the extended FIK-identity in condensed form reads:

$$0 = \sum_l \int_0^1 \int_0^z \int_0^{\tilde{z}} \frac{1}{2} \left(f^{(l)} \Big|_{\tilde{z}} + f^{(l)} \Big|_{1-\tilde{z}} \right) d\tilde{z} dz. \quad (3.15)$$

Using the boundary conditions at the channel walls, the definition of the bulk velocity (i.e. $\int_0^1 \langle \bar{u} \rangle_{xy} dz = 1$), integration by parts to transform multiple to single integrations, and the global drag balance (i.e. equation 3.14), the last equation becomes:

$$\begin{aligned} \overline{f^{\text{driving}}} \left[\int_0^1 \left\{ \frac{1}{2} z (1-z) \right\} \langle \gamma_f \rangle_{xy} dz \right] = \\ \frac{1}{Re_b} + \int_0^1 \left\{ \frac{1}{2} - z \right\} \langle -\overline{uw} \rangle_{xy} dz + \int_0^1 \left\{ \frac{1}{2} z (1-z) \right\} \langle -\overline{f_x^{\text{IBM}}} \rangle_{xy} dz. \end{aligned} \quad (3.16)$$

To arrive at an equation for $d^{\text{tot}} = \langle \gamma_f \overline{f^{\text{driving}}} \rangle_V = \overline{f^{\text{driving}}} \int_0^1 \langle \gamma_f \rangle_{xy} dz$, equation 3.16 is divided by the prefactor in square brackets and multiplied by $\int_0^1 \langle \gamma_f \rangle_{xy} dz$, which yields the final extended FIK-identity:

$$\begin{aligned} d^{\text{tot}} &= d^{\text{bulk}} + d^{\text{mean advection}} + d^{\text{turbulent advection}} + d^{\text{IBM}} \\ &= \sum_l d^{(l)}. \end{aligned} \quad (3.17)$$

Notice that the total advection term is split up into contributions from mean and turbulent flow, using that $\overline{uw} = \bar{u}\bar{w} + \overline{u'w'}$. The symmetry or antisymmetry with respect to the channel centreline at $z = 1/2$ is evident from the factors in braces in equation 3.16. As the multiplier of $\overline{f^{\text{driving}}}$ in that equation depends on γ_f , the bulk term d^{bulk} is slightly texture dependent, as was also found by Peet and Sagaut (2009). For smooth walls, $\gamma_f = 1$ and that multiplier equals $1/12$, such that equation 3.13 is recovered.

As equation 3.17 applies to both smooth and textured walls, the drag change can be decomposed in a similar way:

$$\begin{aligned} DC &= \frac{d^{\text{tot}} - d_{\text{smooth}}^{\text{tot}}}{d_{\text{smooth}}^{\text{tot}}} \\ &= \sum_l \left\{ \frac{d^{(l)} - d_{\text{smooth}}^{(l)}}{d_{\text{smooth}}^{\text{tot}}} \right\} \equiv \sum_l dc^{(l)}. \end{aligned} \quad (3.18)$$

The term within braces is abbreviated as $dc^{(l)}$. It represents the change of a certain term for textured walls as compared to that term for smooth walls. This decomposition quantifies which terms contribute to drag reduction or increase.

The identity presented here is somewhat different from the one derived by Peet and Sagaut (2009). First, their decomposition only applies to skin friction, whereas the drag decomposition in equation 3.17 also includes the pressure drag.

TABLE 3.2: Contributions to the total skin friction for smooth-wall turbulent channel flow. The terms are as given in equation 3.17 and divided by d^{tot} . The rest term equalises the left-hand and right-hand side of that equation.

Re_b	d^{tot} (%)	d^{bulk} (%)	$d^{\text{mean advection}}$ (%)	$d^{\text{turbulent advection}}$ (%)	d^{IBM} (%)	d^{rest} (%)
5500	100	26.9	$4.3 \cdot 10^{-17}$	73.1	0	-0.013
11000	100	16.0	$1.7 \cdot 10^{-17}$	83.9	0	0.086
22000	100	9.6	$1.4 \cdot 10^{-16}$	90.3	0	0.10

Second, the IBM-term is not present in their identity. They used a body-fitted coordinate system in their derivation. As a result, the shear stress on the texture directly derives from integration of the viscous diffusion term. That approach has the added advantage that the skin-friction coefficient for simple textures in a laminar flow can be computed exactly based on purely geometrical considerations without performing the flow calculations (Peet and Sagaut, 2009). However, their relation applies to quasi-homogeneous surfaces only and adopts a more complicated integration using a body-fitted grid. In contrast, the Cartesian integration that is employed here is not restricted to certain geometries.

The extended FIK-identity (equation 3.17) is not only useful when an Immersed Boundary Method (IBM) is used. In the present work, f_i^{IBM} is a body force that models the shear and pressure forces that the texture exerts on the flow. However, the FIK-identity applies to any body force. Furthermore, the current drag decomposition is also applicable to body-fitted calculations. In that case, the obstacles should be considered as part of the domain, because the identity is based on integration over the entire rectangular channel volume. Three steps are required for a successful use of the decomposition in this situation. (1) The geometry should be translated into a three-dimensional phase-indicator function γ_f . (2) A zero-flow condition should be used for the obstacle volume. (3) The drag force on the obstacle surface should be translated into a three-dimensional body force or IBM force.

In view of the factors between braces in equation 3.16, advection and the IBM force contribute differently to the total drag. The weighing factor for advection is largest near the wall, so significant advective transport near the wall contributes most to drag augmentation. In contrast, the weighing factor for the IBM force is largest near the channel centreline. Obstructing the flow there is for two reasons more detrimental than an obstruction near the wall: drag increases due to a larger flow velocity (so a larger IBM force) and a larger weighing factor.

3.7.3 Smooth walls

Table 3.2 shows the decomposition of the total drag into the different contributions for smooth-wall turbulent channel flow. The results for three Reynolds numbers are shown. The total drag is taken as a reference. The rest term equalises the left-hand and right-hand side of equation 3.17. It results from the

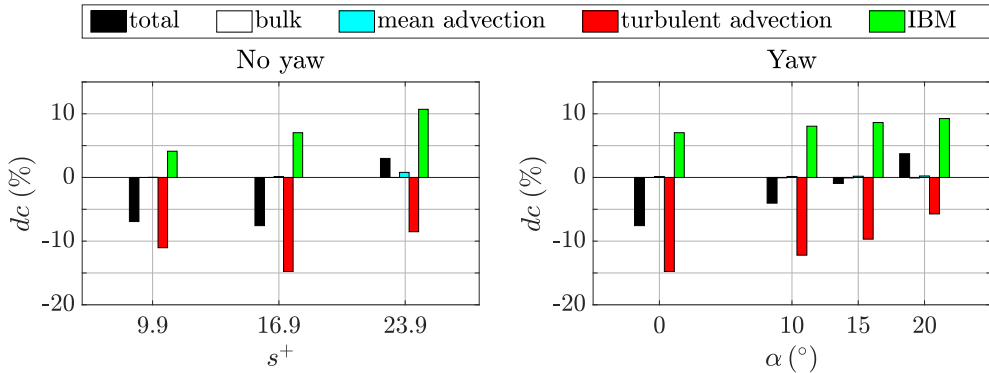


FIGURE 3.12: Different contributions to the total drag change (equation 3.18) for parallel blade riblets. Note that five bars belong to only one abscissa. *Left*: Decomposition as function of riblet spacing in wall units for riblets aligned with the mean flow ($\alpha = 0^\circ$). *Right*: Decomposition as function of yaw angle for fixed riblet spacing $s^+ = 17$.

finite simulation time. It becomes slightly larger for higher Re_b , which is attributed to a relatively shorter simulation time. Its magnitude is typical for all the other simulations.

As the table shows, only bulk transport and turbulent advection contribute to the total drag in smooth-wall channel flows. The mean advection term is zero to machine precision, and $d^{\text{IBM}} = 0$. At $Re_b = 5500$, the total drag comes for 27% from the bulk and for 73% from the turbulent advection term. These numbers are close to the 26% and 74% reported previously for $Re_b = 5460$ (Peet and Sagaut, 2009). As the Reynolds number increases, the relative contribution of turbulence to the total drag increases. This stresses once more the need for reduction of turbulent drag in high-Reynolds-number flows.

3.7.4 Parallel riblets

Using equation 3.18, the drag change for parallel riblets is decomposed into contributions from the bulk, mean advection, turbulent advection and IBM terms. Figure 3.12 exhibits this decomposition as function of s^+ and α in a bar graph. The total term equals the total drag change, which was shown already in figure 3.2. The bulk term is in both graphs not visible, as it is very close to zero. The IBM term, which represents the drag force on the blades, is responsible for an increase of the total drag. Apart from being positive, it also increases with s^+ . When the riblet spacing increases, the riblet height increases as well ($h/s = 0.5$ is fixed), but the total blade area per unit spanwise width remains constant. Therefore, the increase of the IBM term with s^+ cannot be due to an increased wetted area, but it is ascribed to blades that further protrude into the flow.

Although it remains small as compared to the other terms, the contribution from mean advection also increases with blade spacing. That is attributed to a

stronger mean secondary flow for larger s^+ (not shown here, see also e.g. (Choi et al., 1993; Goldstein and Tuan, 1998)). Finally, the turbulent drag contribution is negative, which indicates suppression of turbulent streamwise momentum transport. For the three s^+ values shown here, the maximum turbulent-drag suppression is almost 15% at $s^+ = 17$. The figure demonstrates that the optimum s^+ is a trade-off between an additional drag force on the blades and reduced turbulent transport because of the blades.

Figure 3.12 shows a similar decomposition for parallel riblets in yaw at fixed $s^+ = 17$. The IBM term increases for increasing yaw angle α , which might be due to the additional pressure drag. The change in the mean advection term is very small. The contribution from turbulent advection is increasingly less negative when α increases. The figure thus indicates that deterioration of riblets in yaw is both due to an increased drag force on the blades and reduced suppression of turbulent transport.

3.7.5 Herringbone riblets

Figure 3.13 shows the decomposition of the total drag change into its contributions from the IBM force, turbulent advection and mean advection. The bulk and rest terms are not presented. They never exceed 0.04% (bulk) and 0.08% (rest) in magnitude. The top left graph is the same as figure 3.5 and is shown here again for ease of comparison. Apart from the bulk contribution, the IBM term is the least important term for most textures. In the worst case, it causes an 8.1% increase of drag, which is comparable to results for standard parallel riblets (7.0% for $\alpha = 0^\circ$, 8.6% for $\alpha = 15^\circ$). Advection by the mean flow can be a significant contribution to drag increase, up to 28% for $N_{\text{groove}} = 4$, $\alpha = 165^\circ$. The turbulent advection term exhibits the largest changes: it varies between a 6% reduction and a 50% increase.

The variation of the mean and turbulent drag contributions with feather width very much resembles that of the mean and turbulent secondary flow strengths (compare figures 3.13 and 3.9). It thus appears that advection and secondary flow go hand in hand. The same can be observed from the instantaneous flow field in figure 3.14, which shows both contours of advection and vectors of secondary flow. Regions with strong secondary flow (in particular strong w) are also regions with strong advection. Both secondary flow and the advective flux are split into mean and turbulent contributions in view of $\Gamma_s^2 = \Gamma_m^2 + \Gamma_t^2$ and $\overline{uw} = \overline{u}\overline{w} + \overline{u'w'}$, respectively. In summary, the results clearly indicate an intimate connection between increased advective transport and stronger secondary flow.

Given the close correspondence between secondary flow and advection, the change of the secondary flow strength with feather width as clarified in section 3.6.4 also explains the trend of the advective drag contributions. In particular, the increased advective drag for smaller feather widths is due to the higher spanwise density of the converging or diverging riblets that generate the secondary flows. Also, reduction of the mean advective drag for $N_{\text{groove}} = 1$ is ascribed to a weaker mean secondary flow due to spanwise confinement. There is, however, one major

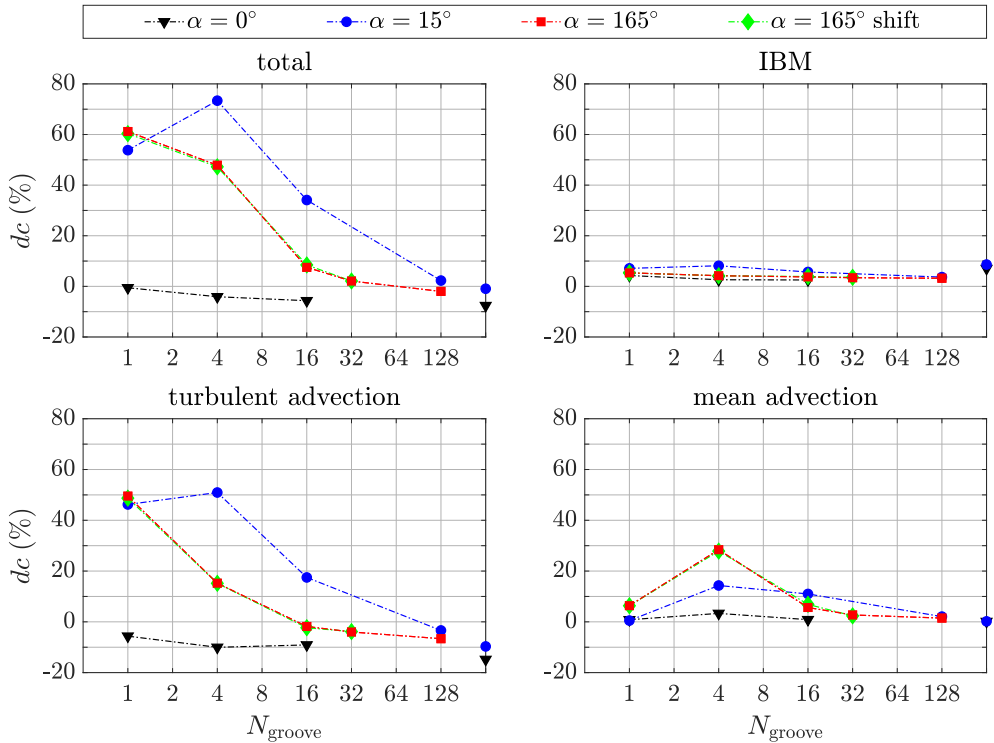


FIGURE 3.13: Decomposition of the total drag change (*top left*) for herringbone riblets in contributions from the IBM-force (*top right*), turbulent advection (*bottom left*) and mean advection (*bottom right*) according to equation 3.18. All figures show the contribution change relative to a smooth wall as function of feather width. The data points on the right vertical axes represent the conventional parallel blade riblets with yaw angle $\alpha = 0^\circ$ and $\alpha = 15^\circ$.

difference between figures 3.13 and 3.9, namely the effect of shifting of the top-wall texture. For 16 and 32 grooves, the mean secondary flow for the shifted textures is clearly stronger than for the not-shifted textures. In contrast, the drag due to mean advection is about the same, independent of the shift. This is explained by the fact that a stronger secondary flow near the channel centreline does not contribute much to drag because of the factor $(1/2 - z)$ in equation 3.16. This demonstrates that mean-secondary-flow strength is a good indicator for the contribution of mean advection to drag, provided that the mean secondary flow near the centreline is weak.

Figure 3.13 shows that drag reductions are possible in the limit of large N_{groove} . Like for the conventional riblet texture, these reductions originate from weakened turbulent advective transport. To reveal the origin of this weakening, the spanwise dependence of the advective FIK-terms is investigated with a spanwise decomposition. Let $\langle \bar{f} \rangle_{xy}$ be one term in equation 3.12 and $d^{(l)}$ the corresponding drag contribution. The calculation of this FIK-term can be rewritten

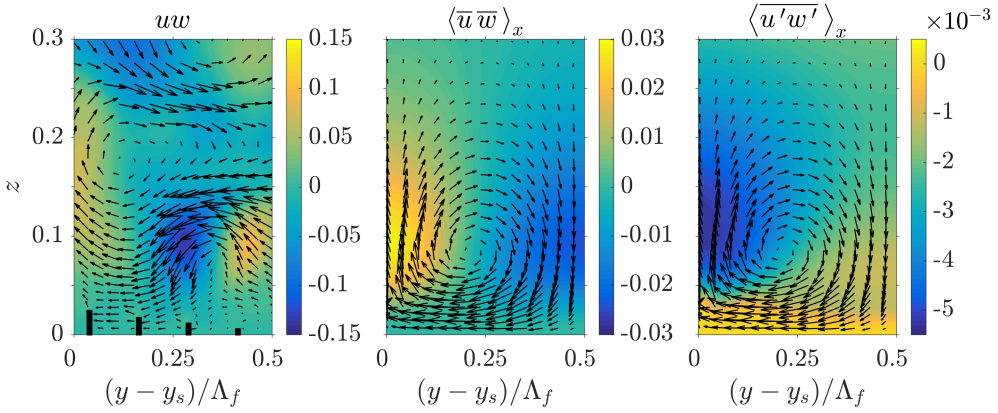


FIGURE 3.14: Advective transport in a plane perpendicular to the streamwise direction for the herringbone texture with $N_{\text{groove}} = 4$, $\alpha = 165^\circ$. Contours represent the instantaneous advection uw (left), the averaged mean advection (centre) or the averaged turbulent advection (right). Vectors depict the instantaneous (left) or averaged (centre, right) in-plane flow velocity.

as:

$$\begin{aligned}
 d^{(l)} &= \int_0^1 g \langle \bar{f} \rangle_{xy} dz \\
 &= \left\langle \int_0^1 g \langle \bar{f} \rangle_x dz \right\rangle_y \equiv \langle d_{sp}^{(l)} \rangle_y.
 \end{aligned} \tag{3.19}$$

The function $g = g(z)$ results from conversion of a triple to a single integral, and normalisation. The function $d_{sp}^{(l)} = d_{sp}^{(l)}(y)$ represents the spanwise decomposition of the FIK-term, as indicated by the subscript sp . The drag change contribution $dc^{(l)}$ can be decomposed in a similar way:

$$\begin{aligned}
 dc^{(l)} &= \frac{d^{(l)} - d_{\text{smooth}}^{(l)}}{d_{\text{smooth}}^{\text{tot}}} \\
 &= \left\langle \frac{d_{sp}^{(l)} - d_{\text{smooth}}^{(l)}}{d_{\text{smooth}}^{\text{tot}}} \right\rangle_y \equiv \langle dc_{sp}^{(l)} \rangle_y,
 \end{aligned} \tag{3.20}$$

where $dc_{sp}^{(l)}$ quantifies how the drag change depends on the spanwise coordinate. Note that $d_{sp}^{(l)}$ and $dc_{sp}^{(l)}$ have a spanwise dependence, whereas $d_{\text{smooth}}^{(l)}$ and $d_{\text{smooth}}^{\text{tot}}$ have not. The spanwise decomposition of the mean and turbulent advective terms is shown in figure 3.15 for $\alpha = 15^\circ$ and 165° , and four feather widths. Small asymmetries with respect to $y = y_s$ are attributed to slow convergence of weak secondary flows. The small oscillations in the curves for $N_{\text{groove}} = 128$ probably appear for the same reason.

The effect of convergent/divergent riblets can be isolated from that of parallel riblets in yaw for the textures with $N_{\text{groove}} = 128$. The parallel riblets dominate

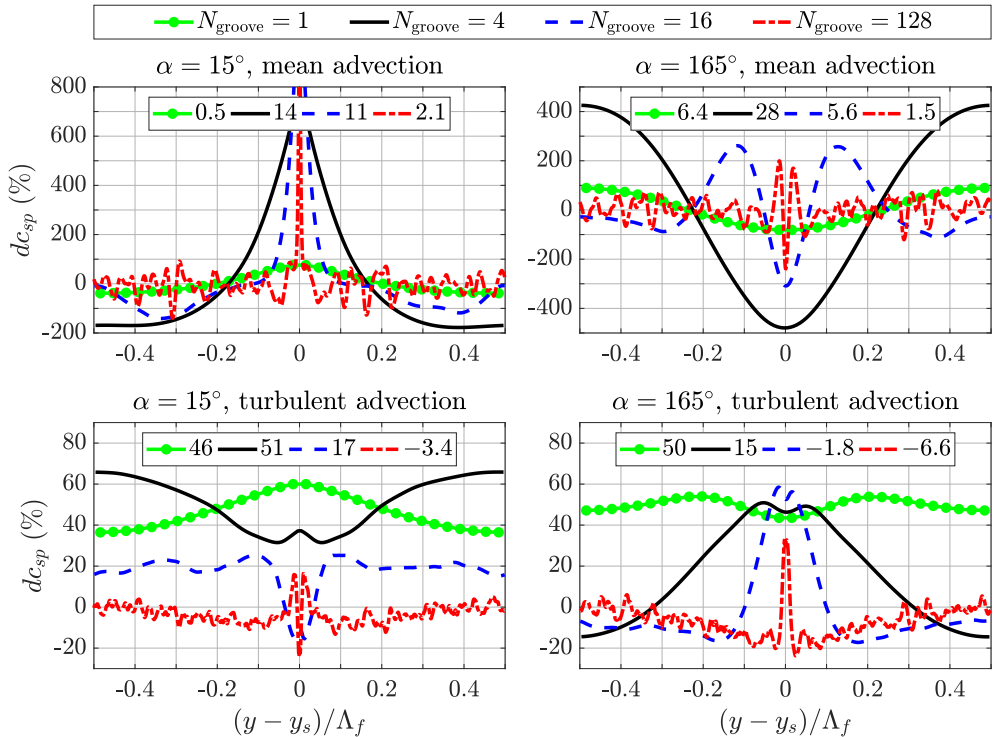


FIGURE 3.15: Spanwise decomposition of advective contributions to the total drag change (equation 3.20). The total advection term is split into a mean (*top*) and turbulent (*bottom*) part. Results for herringbone textures with $\alpha = 15^\circ$ (*left*) and $\alpha = 165^\circ$ (*right*) are shown. The number in the legend quantifies dc (in %), the spanwise average of each curve (equation 3.20), which was shown already in figure 3.13.

the flow in a region sufficiently far away from the shaft. In that region, the mean advection term fluctuates around zero. The turbulent term is zero at the feather edges. Riblets have no height there and the smooth-wall result is recovered. Away from the edges, the term decreases more or less linearly, which is attributed to riblet-height increase and the associated suppression of turbulent transport. It approaches approximately -10% , which belongs to full-height parallel riblets with yaw angle $\alpha = 15^\circ$ or 165° . These favourable trends of mean and turbulent advective drag stop near the shaft because of the strong secondary flow there.

The converging/diverging riblets dominate the flow in a region around the shaft. That is especially evident from the drag change due to mean advection, which shows a clear signature of the mean flow described before, in particular the strong secondary-flow vortices near the shaft. For $\alpha = 165^\circ$ and any N_{groove} , the updraft of fluid around the shaft results in a local DR, as is apparent from the dip in dc_{sp} at $y = y_s$. The peak next to this dip is associated with that part of the vortex that transports momentum towards the wall. For $N_{\text{groove}} = 16$, a

second dip appears, which is ascribed to the tertiary flow shown in figure 3.7. The central dip is narrower for larger N_{groove} , because the secondary-flow vortex near the shaft is smaller compared to the total feather width. A similar (but opposite) description applies to textures with $\alpha = 15^\circ$.

Local turbulent DR can be obtained by diverging riblets. For $\alpha = 15^\circ$ and $N_{\text{groove}} \geq 16$, the strong wall-directed mean flow is accompanied by reduced turbulent transport. The reverse is true for $\alpha = 165^\circ$, namely that the strong wall-leaving mean flow is accompanied by increased wall-directed turbulent transport, as can also be seen from figure 3.14. These observations fully agree with the findings for uniform blowing or suction. In DNSs, it has been found that uniform blowing reduces mean advective drag and enhances turbulent drag, while uniform suction enhances mean advective drag and reduces turbulent drag (Kametani and Fukagata, 2011).

The local contribution of advection to drag might be very different from its global (or volume-averaged) contribution. For instance, mean advection might seem much more important than turbulent advection in view of the scales of figures 3.14 and 3.15. However, the volume-averaged turbulent term is often at least as important as the mean term. As a second example, the texture with $\alpha = 165^\circ$ and $N_{\text{groove}} = 4$ exhibits locally a DR as high as 400% due to a strong wall-leaving flow. However, one should realise that the favourable updraft of low-momentum fluid is compensated by an adverse downdraft of high-momentum fluid. The influence of the whole vortex on the drag should be considered. In the case of $\alpha = 165^\circ$ and $N_{\text{groove}} = 4$, the vortex covers one feather half. The corresponding spanwise-averaged mean advective drag is 28%, which establishes again an unfavourable effect of the vortices near the shaft on the drag. Therefore, one should be careful to judge the performance of this (or any) texture based on a local drag determination. The mean or turbulent advective drag might be reduced locally. However, when the flow is dominated by strong advection (such as near the shaft), the volume-averaged drag generally increases due to an overall increase of both the mean and turbulent advective contributions.

In summary, the present study confirms two effects of the herringbone riblet texture on the turbulent drag. The first effect relates to the texture-generated secondary flows around the shaft. Although turbulent drag might be reduced locally due to a wall-directed mean flow, the overall trend is an increased turbulent drag because of the fluctuating secondary flows that are generated by the converging/diverging riblets near the shaft. The second effect relates to the parallel riblets sufficiently far away from the shaft. Those riblets suppress turbulent transport, which results in turbulent drag reduction.

3.8 Discussion

The results presented in this paper clarify the influence of the herringbone riblets on the drag. The drag increase for $\Lambda_f/L_z \lesssim O(1)$ is attributed to an increase of advective transport (figure 3.13), which in turn is associated with the secondary-flow vortex near the shaft (figure 3.15). Although the vortex might

locally be responsible for a drag reduction, as a whole it is responsible for a drag increase. That vortex originates from the herringbone riblets near the shaft (figures 3.7, 3.9, 3.10). That strongly suggests that these converging/diverging riblets are detrimental to DR. That is confirmed by the finding that $\Lambda_f \rightarrow \infty$ is most beneficial for DR (figure 3.5). In that limit, the herringbone texture approaches the conventional parallel-riblet texture in yaw. Hence, the presence of convergent/divergent riblets in the texture seems unfavourable for DR.

Research on the drag-reducing spanwise forcing further underpins the detrimental effect of the herringbone riblets on the drag. The spanwise travelling wave of spanwise body force is described by $f_y = A(z) \sin\{(2\pi/\Lambda_f)y - \omega t\}$. Here, f_y represents the spanwise body force, $A(z)$ the forcing amplitude (only nonzero in the vicinity of the wall), Λ_f the spanwise wavelength of the forcing, and ω the angular frequency of the forcing. The herringbone texture is similar to this forcing with respect to its spanwise periodicity, though the texture is static ($\omega = 0$). Research shows that the best-performing spanwise travelling wave (in terms of DR or net energy saving) is the one with infinite wavelength, i.e. the spanwise wall oscillation (Du et al., 2002; Quadrio and Xie, August 25–28, 2015). In other words, $\Lambda_f \rightarrow \infty$ is most beneficial for DR, like for the herringbone texture. Hence, the addition of spanwise periodicity seems detrimental to the drag-reducing performance of both the spanwise forcing and the riblet texture in yaw.

As the herringbone texture with a spanwise variation of the forcing appears to be unprofitable for DR, a streamwise variation of the forcing might be more advantageous. Indeed, streamwise travelling waves of spanwise forcing are superior to spanwise travelling waves of spanwise forcing, presumably because of the unaltered wall-normal gradient of the wall-normal velocity component at the wall (Quadrio and Xie, August 25–28, 2015). Both experimentally and numerically, DR has been obtained with a stationary streamwise variation of *spanwise* forcing (Viotti et al., 2009; Grüneberger et al., 2012). DR by streamwise variation of *wall-normal* forcing (e.g. suction and blowing) has been reported as well, although the net energy saving has been small (Quadrio et al., 2007; Mamori and Fukagata, 2014). The drag increasing/reducing trends in the current study are similar to what has been found for uniform suction/blowing (figures 3.8, 3.15), but a net drag-reducing effect could not be confirmed. It is difficult (if not impossible) to eliminate the unfavourable effects of downdrafts, as mass conservation dictates that updrafts need to be compensated by downdrafts. Also, textures with converging/diverging riblets are not fully comparable to uniform blowing/suction. For instance, uniform blowing originates from a nonzero mass flux through the wall, in contrast to the texture-generated updrafts. Still, textures with streamwise variation of the forcing seem more promising than the herringbone texture.

The conclusion that the herringbone texture seems detrimental to turbulent DR apparently contrasts with the experimental study of Chen et al. (2014a). Although it has not been the aim of the present study to reproduce their experiments numerically, a comparison might still be illuminating. Chen et al.

(2014a) obtained DR in forward flow for $\Lambda_f/D \lesssim 1$ (D being the pipe diameter), with a maximum of 20%. In contrast, the present study only achieved DR for $\Lambda_f/L_z > 10$, with a maximum of 2% in backward flow. These contrasting results might be ascribed to differences in riblet texture and Reynolds number.

First, the textures were different, particularly the riblet shape and angle. The feather width might have been different too, but it is unclear what value for N_{groove} was used in the experiments. The experimental texture consisted of sawtooth riblets at an angle of 30° with the flow direction. The numerical texture was composed of blades at an angle of 15° . Although blades seem to be more sensitive to yaw (see figure 3.2), they were studied at a smaller yaw angle. Therefore, there is currently no clear indication that the use of blade riblets in the numerical study contributed to a lesser drag-reducing performance of the herringbone texture.

Second, the Reynolds numbers differed significantly. The 20% DR was obtained at $Re_b \approx 2.6 \cdot 10^5$ (based on pipe diameter and bulk velocity), while the numerical study was performed at $Re_b = 5500$. For DR techniques that rely on near-wall flow manipulation, the attainable DR is approximately independent of the Reynolds number (although not fully (Iwamoto et al., 2002, 2005; Spalart and McLean, 2011; Gatti and Quadrio, 2013)) when near-wall scaling is applied. However, herringbone riblets (in contrast to conventional riblets) cannot be regarded as viscous-region modifiers, because they generate a secondary flow throughout a large part of the channel (figure 3.7). Therefore, viscous scaling is probably inappropriate in this case. Because of the unknown scaling and the Reynolds number difference, the texture parameters (e.g. Λ_f) and the drag-reduction results of the experiments and the simulations cannot be directly compared.

3.9 Conclusions and outlook

The drag-reducing performance of a herringbone riblet texture was studied with Direct Numerical Simulations (DNSs) of turbulent flow in a channel with height L_z . The FIK-identity for drag decomposition was extended to textured walls and was used to study the underlying drag change mechanisms. For validation, simulations with smooth walls, parallel blade riblets and parallel blade riblets in yaw were performed, which showed good agreement with literature. The parallel-riblet simulations exhibited an expected but small low-Reynolds-number effect. A maximum drag reduction (DR) of 9.3% was obtained, close to the 9.9% that has been found experimentally (Bechert et al., 1997).

The herringbone texture can both increase or reduce the drag, depending on the spanwise texture wavelength Λ_f . For $\Lambda_f/L_z \lesssim O(1)$ (i.e. narrow feathers), the drag increases with a maximum of 73% for $\Lambda_f/L_z = 0.4$. This increase is ascribed to the convergent/divergent riblets. They generate a fluctuating secondary flow, which on average consists of two counter-rotating vortices centred above the regions of riblet convergence/divergence. The strong secondary flow increases both mean and turbulent advective transport, which in turn results in the significant drag increase.

A slight DR of 2% was found for $\Lambda_f/L_z \gtrsim O(10)$ (wide feathers). Due to the large feather width, the secondary flow generated by the converging/diverging riblets now influences only a relatively small part of the whole texture. Its drag-increasing contribution is therefore small. The largest part of the texture behaves similarly to a conventional parallel-riblet texture in yaw. Specifically, suppression of turbulent advective transport is responsible for the small DR that was obtained.

As was found by other researchers for spanwise travelling waves of spanwise forcing, the current study confirms that $\Lambda_f \rightarrow \infty$ is most beneficial for DR. In that limit, the texture approaches the conventional parallel-riblet texture in yaw. Therefore, the presence of convergent/divergent riblets in the texture seems detrimental to turbulent drag reduction, which apparently contrasts with the experiments of Chen et al. (2014a). However, differences in Reynolds number and texture parameters (riblet shape, feather width, angle between riblets and flow direction) hindered a one-to-one comparison between the present simulations and the experiments.

More elaborate experiments and simulations are required to further investigate the drag-reducing potential of the herringbone texture. First, the maximum DR of 20% should be reproduced and the optimum texture parameters (Λ_f , s , h/s , α) should be determined. In numerical simulations, the more realistic sawtooth riblet geometry should be implemented. The Reynolds-number influence and the parameter scaling also need further attention. As the herringbone riblets generate a secondary flow throughout a large part of the channel, the scaling of DR with the texture and flow parameters is presumably non-trivial.

Whether feather riblets have an aerodynamic function remains an open question. Chen et al. (2014a) claimed that feather riblets greatly impact flight performance because of drag reduction. The DR was ascribed to suppression of turbulent momentum transport, but evidence has been inconclusive so far. One should realise that wings of birds are not flat and operate at a relatively low Reynolds number, so flow-separation delay seems a more plausible aerodynamic function of feather riblets. Indeed, several studies confirm that roughness on a bird wing contributes to separation control (Bushnell and Moore, 1991; Lilley, 1998; van Bokhorst et al., 2015). Furthermore, separation delay has been obtained with vortex generators that resemble the herringbone texture (Lin, 2002). So, future studies might investigate the potential of the herringbone texture for flow-separation control.

Acknowledgements

The research leading to these results has received funding from the European Union Seventh Framework Programme in the SEAFRONT project under grant agreement nr. 614034. The simulations were performed on the Dutch national supercomputer Cartesius at SURFsara, Amsterdam, The Netherlands. This work was sponsored by NWO Physical Sciences for the use of supercomputer facilities.

H.O.G.B. would like to thank his colleague Pedro Costa for his supercomputational support.

Chapter 4

Oscillatory flow over a compliant layer¹

4.1 Abstract

We present an analytical study of oscillatory pressure-driven laminar flow two-way coupled to a compliant viscoelastic layer on a rigid base, mainly motivated by oscillatory flows in soft microchannels. The layer (or coating) is considered incompressible and the flow is streamwise homogeneous, such that wall-normal coating deformation is negligible. The streamwise coating deformation results both from the streamwise pressure gradient and the shear stress on the coating surface as quantified by the complex, dimensionless interaction parameters χ_{pg} and χ_s , respectively. The interface velocity obtained with the one-way and two-way coupling approaches is the same when $|\chi_s| \ll 1$, which corresponds to lightweight, low-viscosity fluids in narrow channels and/or heavy, stiff, thin solids. The influence of all nine physical parameters in the analytical solution is systematically investigated. The interface velocity approaches zero for heavy, stiff and/or thin solids, such that the classical Womersley flow is recovered. When the forcing frequency, coating softness and coating thickness are sufficiently large, the interface velocity exhibits multiple resonances that are especially strong for purely elastic solids. The lowest resonance frequency is obtained for viscous, heavy fluids and/or lightweight, soft, thick solids. For typical microfluidic channels, the resonance frequencies are on the order of a few to a few hundred kHz. The presented solution can have a twofold use, namely to understand the underlying physics and to validate numerical fluid-structure-interaction solvers. Future work

¹This chapter is (nearly) identical to the manuscript H. O. G. Benschop and W.-P. Breugem. Oscillatory pressure-driven laminar flow coupled to a compliant viscoelastic layer on a rigid base. 2018c, to be submitted.

should include a stability analysis, for which the present work provides a useful description of the base flow.

4.2 Introduction

Fluid-structure interaction (FSI) is the mutual interaction between a deformable structure and a fluid flow. FSI appears in many engineering areas, such as aeronautical, biomedical and construction engineering. Some examples of FSI include aero-elastic flutter of aircraft wings (Kamakoti and Shyy, 2004), closure and re-opening of pulmonary airways (Heil and Hazel, 2011), fluid mechanics of heart valves (Sotiropoulos et al., 2016), flow-induced vibrations of pipes and cables (Nakamura and Kaneko, 2008), sloshing in partially-filled containers (Rebouillat and Liksonov, 2010), and self-sustained oscillations in musical instruments (Fabre et al., 2012).

Many of such FSI examples led to the investigation of fundamental FSI problems: simplified problems that retain important physics and help much in understanding. Examples of such classical problems are the flow past a freely vibrating cable (Newman and Karniadakis, 1997), the flow in collapsible tubes (Grotberg and Jensen, 2004), a flexible pipe conveying incompressible fluid (Xie et al., 2016), and lubrication of soft viscoelastic solids (Pandey et al., 2016). Another extensively-studied classical FSI problem is the stability of flow over compliant walls (Carpenter and Garrad, 1986; Kumaran, 1995), which has mainly been studied for two reasons: delay of transition to turbulence in laminar flows, and drag reduction in turbulent flows. Anisotropic, viscoelastic and permeable compliant walls have been investigated as well (Yeo, 1990; Hamadiche and Gad-el Hak, 2004; Pluvinage et al., 2014).

In this paper we investigate another fundamental FSI problem, namely the oscillatory pressure-driven laminar flow coupled to a compliant viscoelastic layer on a rigid base. The motivation for studying this problem is twofold. The first motivation comes from the field of physiological fluid mechanics, with hemodynamics (the dynamics of blood flow) in particular. There are at least three characteristics that distinguish blood flow from steady flow in rigid channels: pulsatility, distensibility and viscoelasticity. Cardiovascular flow is pulsatile: there is a periodically varying flow on top of the mean flow. Distensibility refers to the characteristic that an increase of the intravascular pressure results in swelling of the blood vessel, i.e. the vessel radius increases. Recent work shows that the axial (or longitudinal) displacement of arterial walls might be significant as well under certain conditions (Hodis and Zamir (2011) with references therein). Finally, blood vessels are viscoelastic, i.e. they exhibit both elastic and viscous behaviour (Bergel (1961) and Čanić et al. (2014) with references therein). The inclusion of viscoelasticity is important for predicting the correct hemodynamics (Valdez-Jasso et al., 2009).

A second and more important motivation comes from the recent interest in the deformation of channels in microfluidic flows. Microchannels are typically fabricated from polydimethylsiloxane (PDMS) because of its biocompatibility,

chemical stability, easy fabrication and optical transparency (Raj et al., 2017). PDMS is also easy to deform, which can be used advantageously in some situations (Pang et al., 2014). Some recent studies demonstrate the importance of deforming PDMS microchannels in pressure-driven flow (Gervais et al., 2006; Hardy et al., 2009; Roh et al., 2016; Raj et al., 2017). The deformation is largest near the channel inlet, and it decreases downstream due to the pressure drop. While most of the research has focused on wall deformations in steady flows, pulsatile flows are equally relevant in microfluidics. Some devices employed for microscale pumping (e.g. diaphragm pumps) typically yield pulsating flows (Iverson and Garimella, 2008). In addition, pulsatile flows can be used as a tool to determine the dynamic characteristics of microfluidic systems (Vedel et al., 2010). Finally, pulsatility has several microscale applications, e.g. for mixing enhancement (Glasgow et al., 2004), dynamic micro-rheometry (van der Burgt et al., 2014) and the design of a vortex flow meter (Ma and Kuo, 2017).

There has been quite some work on pulsating or oscillating flows in compliant tubes. Pulsatile flow has a mean component, while oscillatory flow has zero mean (Gundogdu and Carpinlioglu, 1999), although both terms are not always strictly used in this way. Womersley and co-workers derived the velocity profiles for oscillatory pressure-driven flows in rigid tubes (Womersley, 1955; Hale et al., 1955). Their work was later extended to include the effects of a thin-walled elastic tube (Womersley, 1957), a thick-walled viscoelastic tube (Cox, 1968) and wall compressibility (Cox, 1970). The fluid velocities and solid displacements are typically expressed as a series of travelling waves. Some of this work was summarized by Zamir (2000). More recent research considered oscillatory flow in microchannels and the computation of the impedance, the latter being the ratio of the pressure gradient and the (volumetric) flow rate (Morris and Forster, 2004). San and Staples (2012) investigated the effect of slip in thin-walled elastic tubes to greatly enhance the achievable flow rate. Torres Rojas et al. (2017) analysed pulsating flow in thin-walled elastic tubes; they showed that the interplay between fluid viscosity, wall elasticity and the characteristic size of confining media gives rise to rich dynamics that includes resonances. Finally, Hodis and Zamir (2011) noted that displacements and stresses within the arterial wall are highly significant, although these have been largely ignored in studies on thin-walled tubes. They also considered the effect of external tethering, namely a drastic restriction of radial (or wall-normal) displacements of the wall.

The stability of pulsatile or oscillatory flows in rigid channels or pipes has been investigated as well (Thomas et al., 2011; Pier and Schmid, 2017). Thomas et al. (2012) performed a linear stability analysis of the flow in a longitudinally oscillating pipe with wall velocity $U_w \cos(\omega t)$, U_w being the amplitude, ω the radial frequency and t the time. The stability was quantified in terms of a critical Reynolds number $Re_c = U_w / \sqrt{2\nu\omega}$ as function of $H = \sqrt{\omega R^2 / 2\nu}$, with kinematic viscosity ν and pipe radius R . The most unstable mode occurred at $H \approx 11$ with $Re_c \approx 560$, while $Re_c \approx 710$ for a planar Stokes layer ($H \rightarrow \infty$). In comparing different experimental studies, Gundogdu and Carpinlioglu (1999) defined $Re_c = U_m 2R / \nu = K \sqrt{\omega R^2 / \nu}$ as the critical Reynolds number at which turbulent bursts

first occur, with U_m the amplitude of the oscillatory component of the cross-sectional mean velocity. Their relation can be rewritten as $U_m/\sqrt{2\nu\omega} = K/\sqrt{8}$, where $K \approx 800$, although its precise value varied between different experiments. Only very few studies considered the stability of oscillatory flows past *compliant* surfaces. Thaokar and Kumaran (2004) studied oscillatory Couette flow over an incompressible viscoelastic gel. The interface velocity shows oscillatory behaviour for some parameters. Tsigklifis and Lucey (2017) investigated pulsatile Poiseuille flow through a channel with compliant walls modelled as thin spring-damper-supported plates. They showed that wall compliance is stabilizing the flow for the range of Womersley numbers considered, namely $5 \leq \text{Wo} = \sqrt{\omega h^2/\nu} \leq 50$ with half-channel height h .

The objective of the present study is to characterize the interaction between an oscillatory pressure-driven laminar flow and a compliant viscoelastic layer on a rigid base (i.e. tethered). The combination of soft channels with pulsatile flows seems largely unexplored for microfluidic flows. In addition, some previous studies reported rich dynamics resulting from the fluid-structure interaction (Thaokar and Kumaran, 2004; Torres Rojas et al., 2017), but it remained somewhat unclear where this dynamics comes from and how it is influenced by all physical parameters. Finally, most research in the context of hemodynamics and microfluidics has focused on the wall-normal or radial deformations, with little attention paid to tangential, axial or streamwise wall deformations.

The main novelties of this work are threefold. First, to the authors' knowledge it is the first time that the analytical solution to this problem is presented. Second, the present work focuses on the axial displacements, whereas related research is often concerned with wall-normal deformations. Third, the influence of nine physical parameters on the interaction is systematically investigated. The interaction is exemplified qualitatively with velocity profiles and quantitatively with the tangential interface velocity.

This paper is organized as follows. Section 4.3 describes the relevant theory, while section 4.4 introduces the specific FSI problem and derives the analytical solution. The dynamics of the coupled fluid-solid system is qualitatively considered in section 4.5. In section 4.6 we quantify how the interface velocity depends on the physical parameters. Section 4.7 investigates when resonance occurs, and section 4.8 applies the findings to some actual microfluidic flows. The paper closes with the conclusions and perspectives in section 4.9.

4.3 Theory

This section provides the relevant theory for the present FSI problem. The subsections below describe the fluid, solid and coupling equations that are applied to the present problem in section 4.4.

4.3.1 Fluid equations

The following equations describe the motion of an incompressible fluid:

$$\rho_f \frac{D u_i^f}{Dt} = \frac{\partial \sigma_{ij}^f}{\partial x_j} + \rho_f f_i^f, \quad (4.1)$$

$$\frac{\partial u_j^f}{\partial x_j} = 0, \quad (4.2)$$

with material (or total) time derivative $D/Dt = \partial/\partial t + u_j^f \partial/\partial x_j$, velocity u_i , time t , spatial coordinate x_j , density ρ , stress tensor σ_{ij} and body force f_i . The super- or subscripts f indicate the fluid phase. The Einstein summation convention for repeated indices is used. Equation 4.1 expresses momentum transport and equation 4.2 denotes mass conservation. The fluid is assumed to be incompressible and Newtonian, which gives the following constitutive relation for the fluid stress:

$$\sigma_{ij}^f = -p_f \delta_{ij} + \mu \left(\frac{\partial u_i^f}{\partial x_j} + \frac{\partial u_j^f}{\partial x_i} \right), \quad (4.3)$$

with dynamic viscosity μ and Kronecker delta function δ_{ij} .

4.3.2 Solid equations

The equation of motion for the solid is (Chung, 2007):

$$\rho_s \frac{\partial u_i^s}{\partial t} = \frac{\partial \sigma_{ij}^s}{\partial x_j} + \rho_s f_i^s. \quad (4.4)$$

The particle velocity $u_i^s = \partial \xi_i / \partial t$ is the time derivative of ξ_i , which is the displacement of a solid particle from its original position x_i . Assuming small displacements, the mass density is constant and nonlinear deformations can be neglected.

To close the structural equations, one needs a constitutive model that relates the stress tensor σ_{ij}^s to Cauchy's (infinitesimal) strain tensor ϵ_{ij} defined as:

$$\epsilon_{ij} = \frac{1}{2} \left(\frac{\partial \xi_i}{\partial x_j} + \frac{\partial \xi_j}{\partial x_i} \right). \quad (4.5)$$

For linear, time-translation-invariant, homogeneous, isotropic and viscoelastic media, the constitutive stress-strain relation can be written in integral form as (Robertsson et al., 1994; Carcione, 2015):

$$\sigma_{ij}^s = \dot{\psi}_\Lambda * \epsilon_{kk} \delta_{ij} + 2\dot{\psi}_G * \epsilon_{ij}, \quad (4.6)$$

where the dot denotes a time derivative and the asterisk symbolizes convolution:

$$f(t) * g(t) \equiv \int_{-\infty}^{\infty} f(\tau)g(t - \tau) d\tau. \quad (4.7)$$

The constitutive equation contains two relaxation functions, namely $\psi_{\Lambda}(t)$ for dilatation and $\psi_G(t)$ for shear. A relaxation function describes how stress decays as a function of time in response to a unit step in strain.

When the boundary conditions and body forces of a viscoelastic problem are steady-state harmonic functions of time, all field variables will have the same time dependence (Christensen, 1982). Suppose that all variables have a harmonic dependence of the form $e^{i\omega_0 t}$. Exponentials behave nicely under convolution:

$$f(t) * e^{i\omega_0 t} = F(\omega_0)e^{i\omega_0 t}, \quad (4.8)$$

where $F(\omega) = \mathcal{F}\{f(t)\}$ and $\mathcal{F}\{\}$ denotes the Fourier transform. Hence, the viscoelastic stress-strain relation (4.6) can be expressed as:

$$\sigma_{ij}^s = \Lambda(\omega_0)\epsilon_{kk}\delta_{ij} + 2G(\omega_0)\epsilon_{ij}, \quad (4.9)$$

where $\Lambda(\omega) = \mathcal{F}\{\dot{\psi}_{\Lambda}(t)\}$ and $G(\omega) = \mathcal{F}\{\dot{\psi}_G(t)\}$ are the complex dilatational and shear moduli (Tschoegl et al., 2002; Carcione, 2015). The viscoelastic stress for harmonic problems is the same as in linear elasticity, except for the use of complex moduli. A single viscoelastic wave equation can be obtained by combining equations 4.4, 4.5 and 4.9:

$$\rho_s \frac{\partial^2 \xi_i}{\partial t^2} = (\Pi - G) \frac{\partial}{\partial x_i} \left(\frac{\partial \xi_k}{\partial x_k} \right) + G \frac{\partial^2 \xi_i}{\partial x_j^2} + \rho_s f_i^s, \quad (4.10)$$

where the compressional-wave modulus $\Pi = \Lambda + 2G$ is used to replace the dilatational modulus Λ .

4.3.3 Coupling equations

The fluid and the solid phase are coupled at the interface by kinematic and dynamic boundary conditions, namely continuity of velocities and stresses:

$$u_i^f = u_i^s, \quad (4.11a)$$

$$\sigma_{ij}^f n_j = \sigma_{ij}^s n_j, \quad (4.11b)$$

where n_j is a unit vector normal to the interface. Effects of surface tension are neglected.

4.4 Analytical solution

This section applies the general theory from the previous section to an oscillatory pressure-driven flow over a viscoelastic coating, as sketched in figure 4.1. The

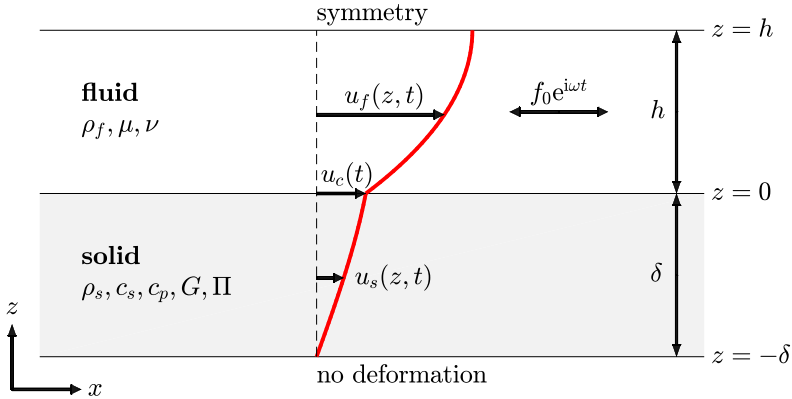


FIGURE 4.1: Sketch of the fluid-structure interaction problem. The fluid is indicated by a white and the solid by a light-grey background colour. A laminar, streamwise homogeneous flow is driven by an oscillatory pressure gradient. The normal and tangential stresses from the flow result in a deformation of the underlying viscoelastic coating. The thick solid line is a profile of the streamwise velocity in the fluid and the solid phase.

flow in a channel with half-height h is driven in the streamwise direction (x) by an oscillatory pressure gradient with angular frequency ω :

$$-\frac{1}{\rho_f} \frac{\partial p_f}{\partial x} = f_0 e^{i\omega t} = f_0 e^{i\phi}, \quad \phi = \omega t, \quad u_{ft} = \frac{f_0}{\omega}. \quad (4.12)$$

Note that the complex notation is used; physically relevant quantities are obtained by taking the real part, denoted as $\text{Re}\{\dots\}$. The forcing amplitude f_0 (in units $[\text{m s}^{-2}]$) is a real and positive constant, ϕ is the phase angle, and u_{ft} is a typical forcing velocity. The flow is assumed to be laminar, streamwise and spanwise homogeneous, and symmetric with respect to the channel centreline ($z = h$). Spanwise flow is absent, so the possibly nonzero flow velocities are u_f in the streamwise and w_f in the wall-normal direction. The fluid is incompressible, isotropic and Newtonian with mass density ρ_f , dynamic viscosity μ and kinematic viscosity $\nu = \mu/\rho_f$.

Stresses from the flow result in a deformation of the underlying coating. There is no spanwise deformation, so the relevant displacements are ξ in the streamwise and ζ in the wall-normal direction, with the corresponding velocities u_s and w_s . The coating of thickness δ is linear, time-translation-invariant, homogeneous, isotropic and viscoelastic. It is attached at the bottom to a rigid wall. It has density ρ_s , shear-wave speed c_s , shear modulus $G = \rho_s c_s^2$, compressional-wave speed c_p and compressional-wave modulus $\Pi = \rho_s c_p^2$. Note that the moduli are complex and frequency dependent (cf. section 4.3). As this paper considers only one forcing frequency, there is no need to describe the frequency dependence of the complex moduli. At the prescribed forcing frequency, the moduli and the

derived velocities are simply complex numbers with magnitude and phase:

$$G = |G|e^{i\phi_G} \quad \Rightarrow \quad c_s = |c_s|e^{i\phi_{c_s}}, \quad |c_s| = \sqrt{\frac{|G|}{\rho_s}}, \quad \phi_{c_s} = \frac{\phi_G}{2}, \quad (4.13)$$

and similarly for Π and c_p . The angle ϕ_G is the loss angle. It has been found empirically that it always lies between 0 and 90° (Pipkin, 1986). As a result, the loss tangent $0 \leq \tan(\phi_G) < \infty$. However, a loss tangent equal to one is considered outstandingly high (Chung, 2001). Therefore, the range $0 \leq \phi_G \leq 45^\circ$ might be more realistic.

The sketched problem allows an analytical solution, in which the following dimensionless parameters will appear:

$$\begin{aligned} \rho_r &= \frac{\rho_f}{\rho_s} = \frac{\text{fluid density}}{\text{solid density}}, \\ h_r &= \frac{h}{\delta} = \frac{\text{fluid geometrical length-scale}}{\text{solid geometrical length-scale}}, \\ \omega_{rf} &= \frac{\omega h^2}{\nu} = \frac{\text{forcing frequency}}{\text{frequency of viscous diffusion}}, \\ \omega_{rs} &= \frac{\omega \delta}{c_s} = \frac{\text{forcing frequency}}{\text{frequency of shear waves}}, \\ \omega_{rp} &= \frac{\omega \delta}{c_p} = \frac{\text{forcing frequency}}{\text{frequency of compressional waves}}, \end{aligned} \quad (4.14)$$

where ρ_r is the density ratio and h_r is a geometrical parameter. Note that there are three frequency-related dimensionless numbers: ω_{rf} is relative to a typical fluid frequency, ω_{rs} is relative to a typical shear-wave frequency and ω_{rp} is relative to a typical compressional-wave frequency. The parameter ω_{rf} relates to the Womersley number Wo according to $\omega_{rf} = Wo^2$ (Womersley, 1955). The parameter ω_{rs} is a reduced or dimensionless wave number, because it equals $\omega_{rs} = k_s \delta$ with wave number $k_s = \omega/c_s$ for shear waves. Note that ω_{rs} is a complex number: $\omega_{rs} = |\omega_{rs}| \exp i\phi_{\omega_{rs}}$, $|\omega_{rs}| = \omega \delta / |c_s|$, $\phi_{\omega_{rs}} = -\phi_{c_s} = -\phi_G/2$. Similar remarks also apply to ω_{rp} .

The problem is first solved analytically for the solid deformation that results from the oscillatory shear stress and streamwise pressure gradient on its surface. The normal fluid stress is $\sigma_{33}^f = -p_f + 2\mu \partial w_f / \partial z$ (cf. equation 4.3). Since the flow is homogeneous in the streamwise direction ($\partial u_f / \partial x = 0$) and using continuity ($\partial w_f / \partial z = -\partial u_f / \partial x$, cf. equation 4.2), the viscous part of the normal stress can be neglected: $\sigma_{33}^f = -p_f$. From equation 4.12, the surface pressure can be written as $p_c = -\rho_f f_0 x e^{i\omega t}$, for simplicity assuming that $p_c = 0$ at $x = 0$. Hence, the following boundary conditions for the solid deformation are obtained:

$$\begin{aligned} \xi|_{z=-\delta} &= 0, & \zeta|_{z=-\delta} &= 0, \\ \sigma_{tc} \equiv \sigma_{13}|_{z=0} &= \sigma_{tc0} e^{i\omega t}, & \sigma_{nc} \equiv \sigma_{33}|_{z=0} &= \rho_f f_0 x e^{i\omega t}, \end{aligned} \quad (4.15)$$

with subscripts t for tangential stress, n for normal stress and c for the interface. Because both fluid and solid behave linearly, all quantities have the same harmonic time dependence as the flow forcing. Given these boundary conditions, it is assumed that the solid displacements can be expressed in the following form:

$$\xi(z, t) = \xi_0(z)e^{i\omega t}, \quad \zeta(x, z, t) = \zeta_0(x, z)e^{i\omega t}, \quad (4.16)$$

where ξ is independent of x , while ζ depends linearly on x . In appendix B.1 we derive ξ_0 and ζ_0 for a compressible solid. In case the solid is close to incompressible ($|\omega_{rp}| \ll 1$), the vertical deformation simplifies to:

$$\frac{\zeta_0(x, z)}{\delta} = \frac{\rho_f f_0 x}{\Pi} \left(\frac{z + \delta}{\delta} \right). \quad (4.17)$$

This relation can be used - also for non-oscillatory channel flow - to estimate the significance of the vertical surface deformation for a given streamwise pressure gradient, channel length and compressional-wave modulus. Note that the relation between pressure and wall-normal deformation is linear, in agreement with Hardy et al. (2009).

For the remainder of this paper, we consider an incompressible solid ($|c_p| \rightarrow \infty$, $|\omega_{rp}| \rightarrow 0$), such that the displacements are (cf. appendix B.1):

$$\begin{aligned} \xi_0(z) &= \xi_1 \sin\left(\omega_{rs} \frac{z + \delta}{\delta}\right) + \xi_2 \left\{ \cos\left(\omega_{rs} \frac{z + \delta}{\delta}\right) - 1 \right\}, \\ \xi_1 &= \frac{f_0}{\omega^2} \left\{ \rho_r \tan(\omega_{rs}) + \frac{\rho_r h_r \omega_{rs} \sigma_{tc0}}{\cos(\omega_{rs}) \tau_{wt}} \right\}, \\ \xi_2 &= \frac{f_0}{\omega^2} \rho_r, \\ \zeta_0(x, z) &= 0. \end{aligned} \quad (4.18)$$

The second relation introduces τ_{wt} , which is defined as a typical wall shear stress for the quasi-static or viscous regime:

$$\tau_{wt} = \rho_f f_0 h = \mu \frac{f_0 h^2 / \nu}{h} = \sqrt{\omega_{rf}} \cdot \mu \frac{u_{ft}}{\sqrt{\nu/\omega}}. \quad (4.19)$$

The vertical deformation disappears completely ($\zeta = 0$). The horizontal interface velocity is $u_c \equiv u_{c0}e^{i\omega t}$ with $u_{c0} = i\omega\xi_0(z=0)$, such that:

$$\frac{u_{c0}}{u_{ft}} = i \frac{\rho_r (1 - \cos(\omega_{rs}))}{\cos(\omega_{rs})} + i \rho_r h_r \omega_{rs} \tan(\omega_{rs}) \frac{\sigma_{tc0}}{\tau_{wt}}. \quad (4.20)$$

The first term at the right-hand side results from the pressure gradient and the second term from the shear stress on the coating interface. The isotropic stress for an incompressible solid can be defined as the negative of a solid pressure p_s :

$$\lim_{|c_p| \rightarrow \infty} \Lambda \epsilon_{kk} \equiv -p_s = \rho_f f_0 x. \quad (4.21)$$

Hence, there is an oscillatory pressure gradient in both the fluid and the solid.

As a next step, a solution for the fluid velocity is derived. Using streamwise homogeneity of the flow ($\partial u_f / \partial x = 0$), mass conservation ($\partial w_f / \partial z = -\partial u_f / \partial x$) and the zero vertical interface velocity for an incompressible solid ($w_c = 0$), it follows that vertical flow is absent ($w_f = 0$). Hence, the only nonzero velocity is u_f , which satisfies the unsteady Stokes equation (cf. equations 4.1, 4.2, 4.3) with corresponding boundary conditions:

$$\frac{\partial u_f}{\partial t} = \nu \frac{\partial^2 u_f}{\partial z^2} - \frac{1}{\rho_f} \frac{\partial p_f}{\partial x}, \quad u_f|_{z=0} = u_c, \quad \frac{\partial u_f}{\partial z} \Big|_{z=h} = 0. \quad (4.22)$$

Using equation 4.12 for the pressure gradient, the solution is $u_f(z, t) = u_{f0}(z)e^{i\omega t}$ with:

$$\frac{u_{f0}(z)}{u_{ft}} = -i \left\{ 1 - \left(1 - i \frac{u_{c0}}{u_{ft}} \right) \frac{\cosh \left(\sqrt{i\omega_r f} \frac{z-h}{h} \right)}{\cosh \left(\sqrt{i\omega_r f} \right)} \right\}. \quad (4.23)$$

The shear stress at the interface is obtained from $\sigma_{tc} = \mu \partial u_f / \partial z|_{z=0} = \sigma_{tc0} e^{i\omega t}$, which yields:

$$\frac{\sigma_{tc0}}{\tau_{wt}} = \left(1 - i \frac{u_{c0}}{u_{ft}} \right) \frac{\tanh \left(\sqrt{i\omega_r f} \right)}{\sqrt{i\omega_r f}}. \quad (4.24)$$

For the two-way coupling approach, both the fluid and solid should satisfy the kinematic and dynamic boundary conditions at the interface, namely continuity of velocity and stress (cf. equations 4.11). Continuity of the normal velocity and stress is already guaranteed, since both fluid and (incompressible) solid satisfy $\sigma_{nc} = \rho_f f_0 x e^{i\omega t}$ and $w_c = 0$. Continuity of the tangential velocity and stress still needs to be enforced. The horizontal interface velocity as function of the interface shear stress has been obtained from the solid solution (equation 4.20), while an expression for the interface shear as function of the interface velocity has been calculated from the fluid solution (equation 4.24). One can solve both equations for u_{c0} to obtain:

$$\begin{aligned} \frac{u_{c0}}{u_{ft}} &= i \frac{\chi_{pg} + \chi_s}{1 - \chi_s}, \\ \chi_{pg} &= \frac{\rho_r (1 - \cos(\omega_{rs}))}{\cos(\omega_{rs})}, \\ \chi_s &= \rho_r h_r \omega_{rs} \tan(\omega_{rs}) \frac{\tanh \left(\sqrt{i\omega_r f} \right)}{\sqrt{i\omega_r f}} \\ &= \frac{\rho_f \omega h}{\rho_s c_s} \tan \left(\frac{\omega \delta}{c_s} \right) \frac{\tanh \left(\sqrt{i\omega h^2 / \nu} \right)}{\sqrt{i\omega h^2 / \nu}}. \end{aligned} \quad (4.25)$$

The parameters χ_{pg} and χ_s are denoted as interaction parameters, as they quantify the influence of the fluid-structure interaction on the interface velocity. Two

such parameters are introduced, one for the streamwise pressure gradient (subscript pg) and the other for the shear stress (subscript s) on the fluid/solid interface. Note that both χ_{pg} and χ_s are complex numbers in general. Appendix B.2 provides simplified expressions for the interaction parameters in the limits that $|\omega_{rs}|$ and ω_{rf} are small and/or large. The streamwise pressure gradient on the coating surface is independent of the channel height and the fluid viscosity, so h_r and ω_{rf} do not appear in χ_{pg} . For the remainder of this paper it might be convenient to express the normalized interface velocity in terms of the individual dimensionless numbers:

$$\frac{u_{c0}}{u_{ft}} = i \frac{\rho_r (1 - \cos(\omega_{rs})) + \rho_r h_r \omega_{rs} \sin(\omega_{rs}) \frac{\tanh(\sqrt{i\omega_{rf}})}{\sqrt{i\omega_{rf}}}}{\cos(\omega_{rs}) - \rho_r h_r \omega_{rs} \sin(\omega_{rs}) \frac{\tanh(\sqrt{i\omega_{rf}})}{\sqrt{i\omega_{rf}}}}. \quad (4.26)$$

Hence, the whole problem is governed by five real, dimensionless parameters, namely ρ_r , h_r , ω_{rf} , $|\omega_{rs}|$ and ϕ_G . Using the introduced interaction parameters, the solid solution can be simplified. Specifically, the solid velocity can be written as $u_s(z, t) = u_{s0}(z)e^{i\omega t}$ with amplitude $u_{s0} = i\omega\xi_0$:

$$\begin{aligned} \frac{u_{s0}(z)}{u_{ft}} = & \left\{ i\chi_{pg} \cos(\omega_{rs}) + \frac{u_{c0}}{u_{ft}} \right\} \frac{\sin\left(\omega_{rs} \frac{z+\delta}{\delta}\right)}{\sin(\omega_{rs})} \\ & - \left\{ i\chi_{pg} \cos(\omega_{rs}) \right\} \frac{1 - \cos\left(\omega_{rs} \frac{z+\delta}{\delta}\right)}{1 - \cos(\omega_{rs})}, \end{aligned} \quad (4.27)$$

which makes it easier to check the boundary conditions.

Although we focus on the two-way coupling approach, it is instructive to also calculate the interface quantities when the one-way coupling approach is used. In that case, the solid deforms due to the fluid stresses, but those stresses are not influenced by the solid deformation, such that the interface shear stress and streamwise velocity become:

$$\frac{\sigma_{tc0}}{\tau_{wt}} = \frac{\tanh(\sqrt{i\omega_{rf}})}{\sqrt{i\omega_{rf}}}, \quad (4.28a)$$

$$\frac{u_{c0}}{u_{ft}} = i(\chi_{pg} + \chi_s). \quad (4.28b)$$

The interface shear stress, which is obtained from equation 4.24 with $u_{c0}/u_{ft} = 0$, solely depends on forcing and fluid parameters. The interface velocity, obtained from equation 4.20, is the same as for the two-way coupling approach (equation 4.25), except for the absence of the denominator $1 - \chi_s$. Hence, the one-way coupling results are accurate when $|\chi_s| \ll 1$, which corresponds to lightweight, low-viscosity fluids in narrow channels and/or heavy, stiff, thin solids.

The dynamic response of the flow through a confining medium is typically quantified with the relation between flow rate and driving pressure gradient.

For instance, the impedance is defined as the ratio of complex amplitudes of pressure drop to volume flow rate (Morris and Forster, 2004), while the dynamic permeability represents the ratio between the averaged flow and the pressure gradient in the frequency domain (Torres Rojas et al., 2017). Here we define the oscillatory bulk velocity as:

$$U_b = U_{b0}e^{i\omega t}, \quad U_{b0} = \frac{1}{h} \int_0^h u_{f0}(z) dz. \quad (4.29)$$

Using equation 4.23, one obtains:

$$\frac{U_{b0}}{u_{ft}} = -i \underbrace{\left\{ 1 - \frac{\tanh(\sqrt{i\omega_{rf}})}{\sqrt{i\omega_{rf}}} \right\}}_{\text{rigid wall}} + \underbrace{\frac{u_{c0} \tanh(\sqrt{i\omega_{rf}})}{u_{ft} \sqrt{i\omega_{rf}}}}_{\text{compliant wall correction}}. \quad (4.30)$$

Note that U_{b0}/u_{ft} can be interpreted as a dimensionless number that quantifies the ratio between flow rate (proportional to U_{b0}) and pressure gradient (proportional to u_{ft}). The normalized flow rate has two contributions, one from a rigid wall and the other a correction for wall compliance. The flow rate increase (or decrease) is linearly proportional to the normalized interface velocity u_{c0}/u_{ft} .

4.5 Dynamics

In this section we consider the analytical solution that has been derived above. Specifically, velocity profiles in the fluid and the solid phase are used to qualitatively describe the dynamics away from the fluid/solid interface, since the next sections will focus on the interface velocity only. The first subsection analyses the dynamics in the flow, with specific attention paid to the parameter ω_{rf} . The second subsection describes the dynamics in the solid with the parameter ω_{rs} in particular.

4.5.1 Dynamics in fluid

The flow dynamics in the absence of a compliant structure is described by $\omega_{rf} = \omega h^2/\nu$, the related Womersley number $Wo = \sqrt{\omega h^2/\nu}$ or the Stokes number $\sqrt{\omega h^2/2\nu}$. The latter defines the characteristic length scale $l_S = \sqrt{2\nu/\omega}$, the Stokes layer thickness. Loosely speaking, l_S defines the extent of a near-wall region where viscous effects prevail over inertial effects. A second important dimensionless number is the Reynolds number, which quantifies when flow instabilities might arise (see section 4.2). The present paper considers laminar flow, so the Reynolds number should be sufficiently small.

The laminar-flow patterns can be classified into three types: quasi-steady ($Wo \lesssim 1.3$), intermediate ($1.3 \lesssim Wo \lesssim 28$) and inertia-dominated ($Wo \gtrsim 28$) (Gundogdu and Carpinlioglu, 1999). Figure 4.2 shows the profiles of fluid and

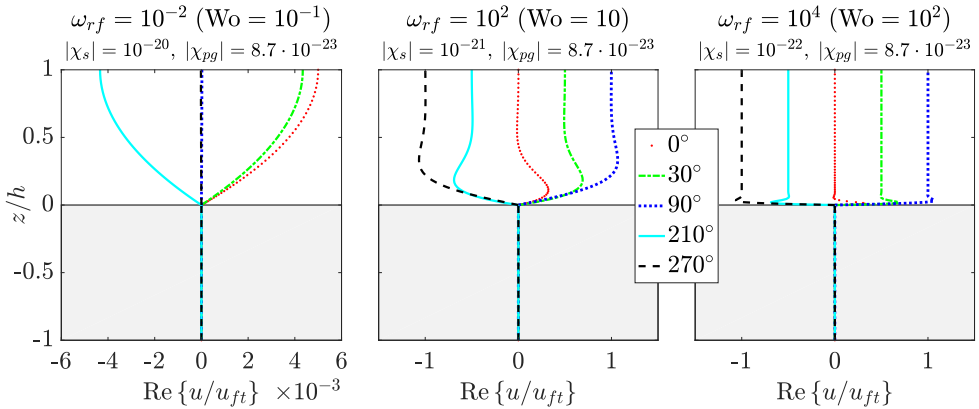


FIGURE 4.2: Profiles of the streamwise velocity in the fluid and the solid phase for flow over a rigid wall at three different values of the dimensionless frequency ω_{rf} . The other parameters are $\rho_r = 1$, $h_r = 1$, $|\omega_{rs}| = 10^{-10}$, $\phi_G = 1^\circ$. The situation is as sketched in figure 4.1, and the profiles are shown for five different phase angles $\phi = \omega t$.

solid velocity for flow over a rigid wall and for three different Womersley numbers, corresponding to the three different flow types.

At very low Womersley number, the flow is quasi-steady and dominated by viscous diffusion, so the Stokes layer thickness is much larger than the half-channel height. The unsteady Stokes equation (4.22) reduces to $\nu \partial^2 u_f / \partial z^2 + f_0 e^{i\omega t} = 0$. As a result, the velocity is parabolic and perfectly in phase with the flow forcing. A characteristic wall shear stress is $\tau_{wt} = \mu(f_0 h^2 / \nu) / h$ (cf. equations 4.19, 4.24), which is based on the relevant velocity scale $f_0 h^2 / \nu = u_{ft} \omega_{rf}$ and length scale h , independent of the frequency ω . This explains why $u_f / u_{ft} = O(\omega_{rf}) = O(10^{-2})$ in the left subfigure.

When the Womersley number is large (right subfigure), the viscous effects are confined to a thin layer near the wall. A characteristic wall shear stress is $\tau_{wt} / \sqrt{\omega_{rf}} = \mu u_{ft} / \sqrt{\nu / \omega}$ (cf. equations 4.19, 4.24), which is based on the relevant velocity scale u_{ft} and length scale $\sqrt{\nu / \omega}$ proportional to the Stokes layer thickness. The shear stress is determined by the oscillating Stokes layer near the surface, independent of the half-channel height h . Outside this layer, the flow velocity satisfies $\partial u_f / \partial t = f_0 e^{i\omega t}$, which yields a uniform velocity that is 90° out of phase with the forcing.

While figure 4.2 depicts the flow over a rigid wall, figure 4.3 shows an example of the flow over a deformable wall. The velocity profiles in solid and fluid are shown for five phase angles and three values of $\omega_{rf} = \text{Wo}^2$ (as in figure 4.2). Due to the deformation of the solid, the fluid has an apparent slip. For small ω_{rf} , viscous effects are strong, which results in an almost uniform velocity profile in the fluid. In addition, the flow is not any more in phase with the forcing because of the coupling to the solid. For large ω_{rf} , the shear forces are very small. The still significant interface velocity originates from the pressure gradient on the fluid/solid interface, which is also apparent from the interaction parameters:

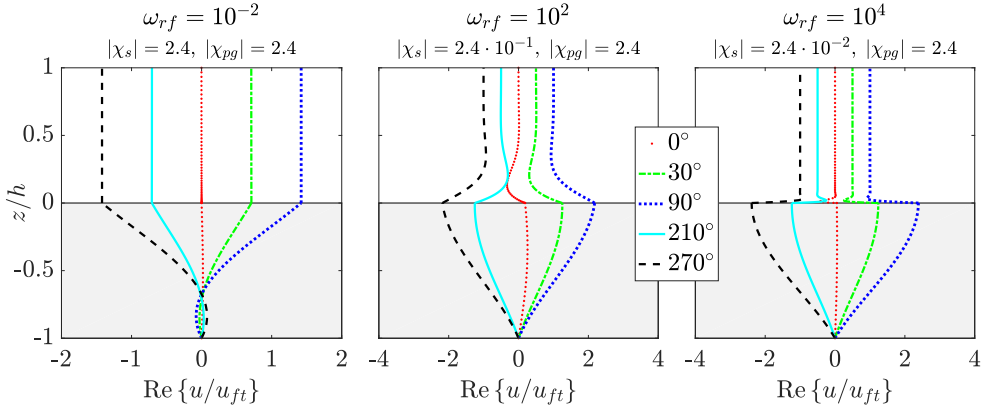


FIGURE 4.3: Profiles of the streamwise velocity for flow over a deformable wall at three different values of the dimensionless frequency ω_{rf} and five different phase angles. The other parameters are $\rho_r = 1$, $h_r = 1$, $|\omega_{rs}| = 3\pi/4$, $\phi_G = 1^\circ$.

$|\chi_{pg}| \gg |\chi_s|$. Like for a rigid wall (figure 4.2), the largest part of the flow is inertia-dominated, as is apparent from the flat velocity profile and the 90° phase delay.

4.5.2 Dynamics in solid

The solid dynamics is governed by travelling shear waves and pressure-driven uniform oscillation. This can be observed more easily when the solution for the solid velocity u_s is rewritten in terms of complex exponentials. First, the complex wave number $k_s = \omega/c_s$ is decomposed as follows:

$$k_s = \frac{\omega}{c_s} = k_{sp} - ik_{sa}, \quad k_{sp} = |k_s| \cos \phi_{c_s}, \quad k_{sa} = |k_s| \sin \phi_{c_s}, \quad \phi_{c_s} = \frac{\phi_G}{2}, \quad (4.31)$$

with a real part k_{sp} for propagation and an imaginary part k_{sa} for attenuation. One might call k_{sp} the (real) wave number and k_{sa} the attenuation factor (Carcione, 2015). Using these relations, the normalized solid velocity can be written as (using equation 4.27):

$$\frac{u_s(z, t)}{u_{ft}} = \underbrace{\alpha_1 e^{k_{sa}(z+\delta)} e^{ik_{sp}(z+\delta+c_{sp}t)}}_{\text{downward travelling wave}} + \underbrace{\alpha_2 e^{-k_{sa}(z+\delta)} e^{-ik_{sp}(z+\delta-c_{sp}t)}}_{\text{upward travelling wave}} - \underbrace{(\alpha_1 + \alpha_2) e^{i\omega t}}_{\text{uniform oscillation}}, \quad (4.32)$$

with $c_{sp} = \omega/k_{sp}$ the (real) propagation velocity or phase velocity. The parameters α_1 and α_2 are introduced for brevity; their sum $\alpha_1 + \alpha_2 = i\rho_r$.

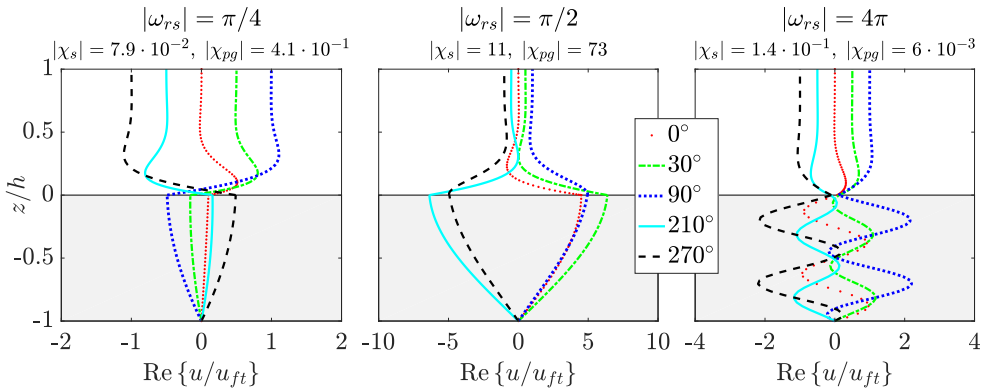


FIGURE 4.4: Profiles of the streamwise velocity for flow over a deformable wall at three different values of the dimensionless frequency $|\omega_{rs}|$ and five different phase angles. The other parameters are $\rho_r = 1$, $h_r = 1$, $\omega_{rf} = 10^2$, $\phi_G = 1^\circ$.

The first two terms in equation 4.32 represent a superposition of exponentially-decaying travelling shear-waves. The decay originates from the viscoelastic properties of the medium. One can define a characteristic decay length $l_{sa} = 1/k_{sa} = 1/(|k_s| \sin(\phi_G/2))$. When the loss angle ϕ_G increases, the waves decay over a shorter typical distance, in agreement with Kulik et al. (2008). The last term in equation 4.32 corresponds with the spatially uniform oscillation that results from the pressure gradient inside the solid (cf. equation 4.21). Indeed, one can solve equation 4.4 with $\sigma_{ij}^s = -p_s \delta_{ij}$ for ξ to obtain $u_s/u_{ft} = -i \rho_r e^{i\omega t}$.

Like with strings and pipes in acoustics, an *elastic* solid ($\phi_G = 0^\circ$) displays resonances at certain wavelengths or frequencies. The relevant parameter is ω_{rs} or $\lambda/\delta = 2\pi/\omega_{rs}$, where λ is the wavelength. Kulik et al. (2008) also recognized the importance of the parameter ω_{rs} , which they denoted as $\omega H/C_t$ with coating thickness H and shear-wave speed C_t . Resonances also occur for a *viscoelastic* solid, although they are less strong.

Figure 4.4 shows the velocity profiles for a slightly viscoelastic solid at three different values of $|\omega_{rs}|$. The left subfigure corresponds with a relatively stiff solid and an approximately quadratic dependence of the solid velocity on the vertical coordinate. The centre subfigure shows a resonance condition with an antinode at the coating interface: when $|\omega_{rs}| \approx \pi/2$, the coating thickness approximately equals one fourth of a wavelength and the surface velocity is relatively large (note the large values of $|\chi_{pg}|$ and $|\chi_s|$). The right subfigure corresponds with an even softer solid. Both the travelling waves and the uniform oscillation can be distinguished in the profiles of the solid velocity. The value of $|\omega_{rs}|$ is such that approximately two wavelengths fit in the coating thickness, which results in a node at the coating interface and a correspondingly small interface velocity (also apparent from the small values of $|\chi_{pg}|$ and $|\chi_s|$).

4.6 Interface velocity

Whereas the previous section has provided a qualitative description of the dynamics with use of velocity profiles, this section gives a more quantitative description. As compared to a rigid wall, the additional wall shear stress (equation 4.24) and bulk velocity (equation 4.30) for a compliant wall are linearly proportional to the normalized interface velocity u_{c0}/u_{ft} . The present section therefore investigates the influence of the problem parameters on the interface velocity. Instead of the five dimensionless numbers, we study the influence of the nine physical parameters, since some of them appear in more than one dimensionless number, which yields a non-trivial dependence. For brevity of presentation, the focus will be on the magnitude of the interface velocity.

4.6.1 Forcing parameters

There are two forcing parameters, namely the forcing amplitude f_0 and its frequency ω .

Forcing amplitude The influence of the forcing amplitude is simple: the surface velocity is linearly proportional to f_0 . A larger forcing yields larger velocities and deformations.

Forcing frequency Figure 4.5 (left) shows the influence of the forcing frequency on the interface velocity. The latter is normalized with $f_0 h^2 / \nu = u_{ft} \omega_{rf}$, which is a frequency-independent velocity scale (in contrast to u_{ft}). The frequency dependence is plotted for three values of $|c_s| h / \nu$, which is a dimensionless number that is proportional to the ratio of a characteristic solid frequency $|\omega_s| = |c_s| / \delta$ and fluid frequency $\omega_f = \nu / h^2$:

$$\frac{\omega_{rf}}{|\omega_{rs}|} = \frac{\omega / \omega_f}{\omega / |\omega_s|} = \frac{|\omega_s|}{\omega_f} = \frac{|c_s| / \delta}{\nu / h^2} = \frac{h}{\delta} \frac{|c_s| h}{\nu}. \quad (4.33)$$

In the limit of low frequency ($\omega, \omega_{rf}, |\omega_{rs}| \rightarrow 0$), the interface velocity becomes (cf. equations B.5, B.6):

$$\frac{u_{c0}}{u_{ft}} = i \left(\frac{1}{2} + h_r \right) \rho_r \omega_{rs}^2. \quad (4.34)$$

Since $u_{ft} = f_0 / \omega$, the interface velocity is linearly proportional to the frequency. While the interface velocity approaches zero in the low-frequency limit, the interface displacement stays finite:

$$\frac{\xi_c}{\delta} = \frac{1}{2} \frac{\rho_f f_0 \delta}{G} + \frac{\rho_f f_0 h}{G}. \quad (4.35)$$

The first term results from the pressure gradient, whereas the second term is the shear contribution. The displacement has the same sign as f_0 , so the coating

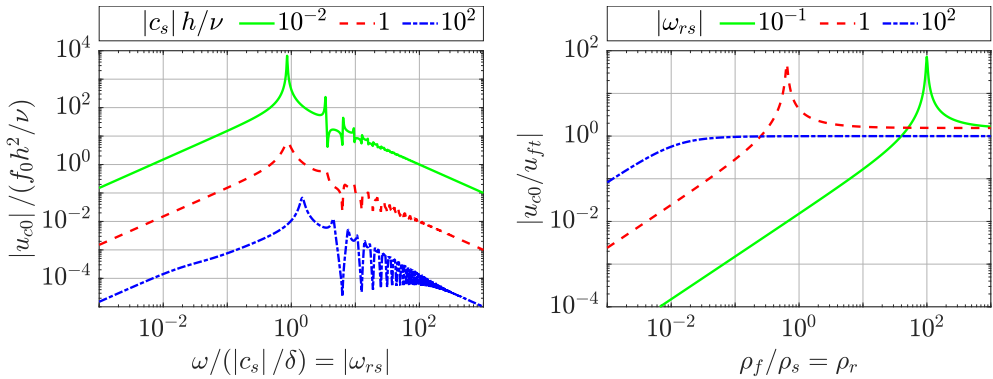


FIGURE 4.5: The magnitude of the interface velocity u_{c0} as function of the forcing frequency ω (left, $\rho_r = 1$) and density ratio ρ_r (right, $\omega_{rf} = 10^{-2}$) for $h_r = 1$, $\phi_G = 1^\circ$.

displaces in the direction of decreasing pressure. The factor 1/2 is associated with a parabolic profile. Specifically, the horizontal displacement as function of the vertical coordinate for steady flow ($\omega = 0$) is given by:

$$\frac{\xi(z)}{\delta} = \frac{1}{2} \frac{\rho_f f_0 \delta}{G} \left(1 - \left(\frac{z}{\delta}\right)^2\right) + \frac{\rho_f f_0 h}{G} \left(1 + \frac{z}{\delta}\right). \quad (4.36)$$

The pressure gradient yields a parabolic and the shear stress a linear displacement profile. For intermediate frequencies, the fluid-structure interaction can lead to resonances, which will be considered in section 4.7. For very high frequencies, the interface velocity is proportional to the inverse of the frequency ($u_{c0}/u_{ft} = -i$). Hence, the interface velocity approaches zero in both the low-frequency and the high-frequency limits.

4.6.2 Fluid parameters

There are three fluid parameters, namely density ρ_f , kinematic viscosity ν and half-channel height h .

Fluid density The interface velocity increases linearly with the density ratio when the latter is sufficiently small (figure 4.5 (right), cf. equation 4.25 with $|\chi_s| \ll 1$). Resonances can occur when the density ratio increases further, but the interface velocity will eventually be independent of ρ_r . The solid density is then so low that the corresponding inertia is irrelevant for the dynamics.

Fluid kinematic viscosity The influence of the kinematic viscosity is displayed in figure 4.6 (left). When the fluid has a very low viscosity ($\nu \rightarrow 0, \omega_{rf} \rightarrow \infty$), the shear approaches zero (cf. expression 4.24) and the solid deformation is solely due to the pressure gradient ($u_{c0}/u_{ft} = i\chi_{pg}$). The interface velocity also approaches a constant value when the viscosity is very high ($\nu \rightarrow \infty, \omega_{rf} \rightarrow 0$) since the

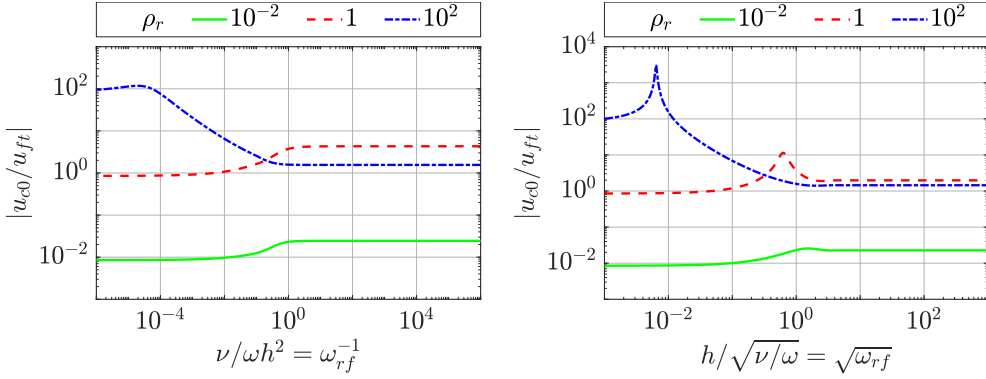


FIGURE 4.6: The magnitude of the interface velocity u_{c0} as function of the fluid kinematic viscosity ν (left, $h_r = 1$) and half-channel height h (right, $\omega\delta^2/\nu = 1$) for $|\omega_{rs}| = 1$, $\phi_G = 1^\circ$.

shear stress becomes independent of the kinematic viscosity for quasi-steady flow (cf. equation 4.24).

Half-channel height Figure 4.6 (right) shows the influence of the half-channel height. When it is very small ($h, h_r, \omega_{rf} \rightarrow 0$), the shear stress approaches zero (cf. equation 4.24) and the solid deformation is solely determined by the pressure gradient ($u_{c0}/u_{ft} = i\chi_{pg}$). When the channel height is very large ($h, h_r, \omega_{rf} \rightarrow \infty$), it is irrelevant for the interface dynamics and the interface velocity becomes constant. In that case, the interface dynamics is determined by the oscillating Stokes layer with the associated length scale $l_S = \sqrt{2\nu/\omega}$ and dimensionless number $\omega\delta^2/\nu$.

4.6.3 Solid parameters

There are four solid parameters, namely density ρ_s , stiffness $|c_s|$, thickness δ and loss angle ϕ_G .

Solid density The influence of the solid density through the density ratio has already been considered in the previous subsection.

Solid stiffness Figure 4.7 displays the influence of the coating softness $|c_s|^{-1}$ (the inverse of the stiffness), both on logarithmic and linear axes. For a very stiff solid ($|c_s| \rightarrow \infty, |\omega_{rs}| \rightarrow 0$), the interface velocity is given by (cf. equations B.5, B.6):

$$\frac{u_{c0}}{u_{ft}} = i\rho_r\omega_{rs}^2 \left\{ \frac{1}{2} + h_r \frac{\tanh(\sqrt{i\omega_{rf}})}{\sqrt{i\omega_{rf}}} \right\}, \quad (4.37a)$$

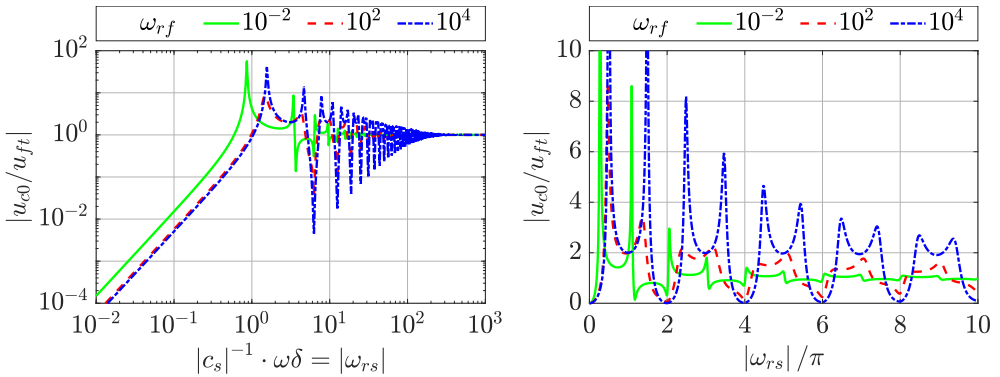


FIGURE 4.7: The magnitude of the interface velocity u_{c0} as function of the solid softness $|c_s|^{-1}$ on logarithmic axes (*left*) and linear axes (*right*) for $\rho_r = 1$, $h_r = 1$, $\phi_G = 1^\circ$.

$$= i \left(\frac{1}{2} + h_r \right) \rho_r \omega_{rs}^2, \quad \omega_{rf} \rightarrow 0, \quad (4.37b)$$

$$= i \frac{1}{2} \rho_r \omega_{rs}^2, \quad \omega_{rf} \rightarrow \infty. \quad (4.37c)$$

For flow with very low viscosity ($\omega_{rf} \rightarrow \infty$), the shear contribution (proportional to h_r) disappears. The ω_{rs}^2 dependence shows that the interface velocity and displacement are proportional to the inverse of the shear modulus (as in equation 4.35). Resonances again appear for intermediate values of the dimensionless stiffness.

For a very soft solid ($|c_s| \rightarrow 0$), the interface velocity eventually reaches $u_{c0}/u_{ft} = -i$. The resulting fluid velocity becomes uniform, independent of the vertical coordinate: $u_f = -i u_{ft} e^{i\omega t}$ (cf. equation 4.23). The interface dynamics is governed by the fluid, since it sets the interface velocity as if the solid is absent. Indeed, the unsteady Stokes equation (equation 4.22) in absence of boundaries reduces to $\partial u_f / \partial t = f_0 e^{i\omega t}$ with the same uniform fluid velocity as solution.

Solid thickness Figure 4.8 shows the influence of the coating thickness. The interface velocity for a thin solid is the same as for a stiff solid (cf. equation 4.37), except that $h_r \omega_{rs} = \omega h / c_s$ is independent of the coating thickness. Hence, for thin coatings both a linear dependence ($h_r \omega_{rs}^2 \propto \delta$) and a quadratic dependence ($\omega_{rs}^2 \propto \delta^2$) can be observed. For very thick coatings, the interface velocity is independent of the coating thickness. The relevant dimensionless parameter becomes $\omega h / c_s$, which is ω_{rs} with the coating thickness replaced by the half-channel height. In case the channel height is also very large ($\omega_{rf} \rightarrow \infty$), the characteristic length scale becomes ν / c_s with the corresponding dimensionless number $\omega \nu / c_s^2$ (cf. equation B.6).

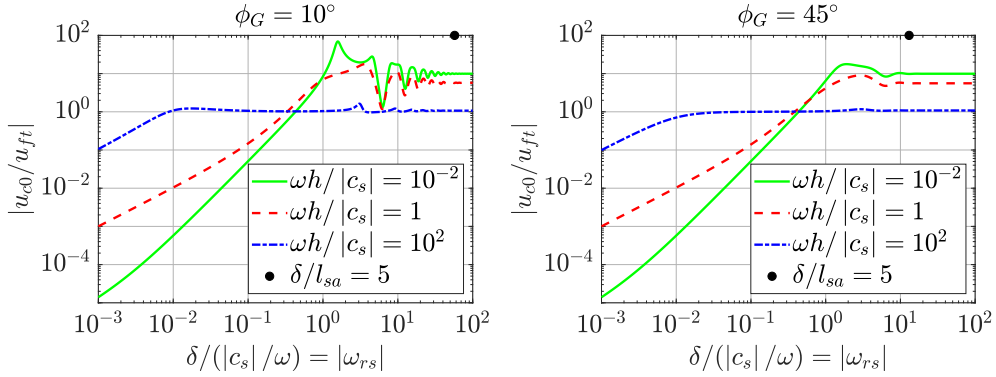


FIGURE 4.8: The magnitude of the interface velocity u_{c0} as function of the solid thickness δ for $\rho_r = 10$, $\omega_{rf} = 10^2$ and two solid loss angles, namely $\phi_G = 10^\circ$ (left, intermediate damping) and $\phi_G = 45^\circ$ (right, high damping).

Solid loss angle The viscoelastic coating properties are quantified with the loss angle ϕ_G . The two subfigures in figure 4.8 correspond with two different loss angles, one with intermediate damping ($\phi_G = 10^\circ$) and another with high damping ($\phi_G = 45^\circ$). The influence of ϕ_G is marginal, except when resonances are present in the coating response: the resonances are less strong when the loss angle increases, in agreement with Kulik et al. (2008). When the coating is sufficiently thick, the exponentially decaying coating deformation does not reach the rigid wall, such that the coating thickness becomes irrelevant for the interface dynamics. This observation can be quantified with the decay length $l_{sa} = 1/k_{sa}$ introduced below equation 4.32. The exponential function decays to less than 1% of its initial amplitude in 5 decay lengths. Hence, the interface velocity will be independent of the coating thickness when $\delta \gtrsim 5l_{sa}$ or $\delta/l_{sa} = |\omega_{rs}| \sin \phi_{cs} \gtrsim 5$, which is confirmed by figure 4.8.

4.7 Resonances

This section investigates resonances, which we define as local maxima in the magnitude of the normalized interface velocity $|u_{c0}/u_{ft}|$ as function of $|\omega_{rs}|$ (cf. figures 4.5, 4.7). Near resonances, the response of the fluid/solid system changes dramatically, as is also observed in other studies (Luhar et al., 2016). Previous figures have shown that multiple resonances can appear, and that their location changes with the physical parameters. This section focuses on the first resonance, i.e. the first local maximum in $|u_{c0}/u_{ft}|$ as function of $|\omega_{rs}|$, which corresponds to either the stiffest solid or the lowest frequency, depending on which other parameters are fixed. That resonance is typically the strongest (cf. figures 4.5, 4.7), and its location was determined numerically for a wide range of dimensionless numbers.

Figure 4.9 shows at what value of $|\omega_{rs}|$ the (first) resonance occurs. The left subfigure highlights the influence of ρ_r and ω_{rf} , while the right subfigure

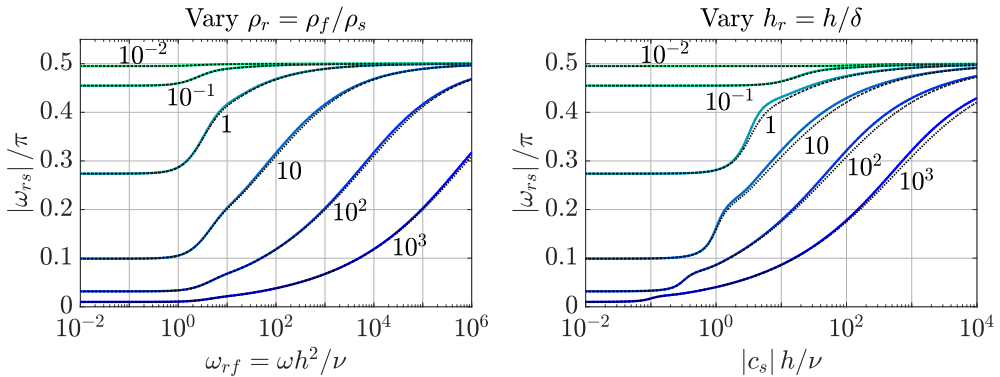


FIGURE 4.9: Dimensionless parameters corresponding to the first resonance, which is defined as the lowest value of $|\omega_{rs}|$ for which there is a local maximum in the magnitude of the normalized interface velocity $|u_{c0}/u_{ft}|$. The dotted lines belong to the first resonance when the pressure gradient is absent ($\chi_{pg} = 0$). *Left*: dependence on ω_{rf} for six values of ρ_r (several lines) and $h_r = 1$, $\phi_G = 1^\circ$. *Right*: dependence on $|c_s|h/\nu$ for six values of h_r (several lines) and $\rho_r = 1$, $\phi_G = 1^\circ$.

summarizes the dependence on h_r and $|c_s|h/\nu$. Both subfigures have the same loss angle ϕ_G , since there are not much qualitative changes when it varies. The dotted lines belong to the first resonance of the normalized interface velocity when the pressure gradient is absent ($\chi_{pg} = 0$), which shows that the pressure gradient has not much influence on the resonance frequency. Instead, the resonance is mainly determined by the shear interaction parameter χ_s as could have been anticipated because of the denominator $1 - \chi_s$ in the interface velocity (cf. equation 4.25).

In general, the resonance frequency depends on two frequency scales, namely a characteristic fluid frequency $\omega_f = \nu/h^2$ and a characteristic solid frequency $|\omega_s| = |c_s|/\delta$ (cf. left subfigure), which is also evident from the observation that χ_s depends on both ω_{rf} and ω_{rs} . It is not straightforward to collapse the different curves on a single line, since resonance typically occurs when $\tan(\omega_{rs})$ cannot be linearised. For very viscous fluids ($\omega_{rf} \lesssim 1$), the fluid frequency becomes irrelevant, such that the resonance frequency scales with the solid frequency $|c_s|/\delta$ and depends on $\rho_r h_r$ (cf. definition of χ_s , equation 4.25). There is no regime for which the resonance scales solely with the fluid frequency.

Both figures show that the maximum resonance frequency is obtained for $|\omega_{rs}| \approx 0.5\pi$, which corresponds with an antinode at the coating surface (cf. figure 4.4). This limit of $|\omega_{rs}| \approx 0.5\pi$ is reached for lightweight, low-viscosity fluids in narrow channels and/or heavy, stiff solids. These are typical conditions for which the one-way coupling approach should give reasonably accurate results too. Indeed, the resonance also occurs at $|\omega_{rs}| \approx 0.5\pi$ for the one-way coupling method, since $u_{c0}/u_{ft} \propto 1/\cos(\omega_{rs})$ (cf. equation 4.28). At conditions when the one-way coupling approach is not valid anymore, the resonance frequency can be significantly lower. It decreases for increasing fluid viscosity, density ratio, coating softness and coating thickness. The lowest resonance frequency is thus

TABLE 4.1: Typical dimensionless numbers and resonance frequencies for oscillatory flows in a microchannel with PDMS walls on a rigid base. The channel half-height is fixed at $h = 100 \mu\text{m}$, while the properties of the PDMS wall are $\rho_s = 970 \text{ kg m}^{-3}$, $|G| = 100 \text{ kPa}$ and $\phi_G = 0.05^\circ$. Three fluids (air, water and viscous oil) and two wall thicknesses (thin and thick) are considered.

Short name	ρ_f (kg m^{-3})	ν (m^2s^{-1})	δ (μm)	ρ_r	h_r	$ c_s h/\nu$	$ \omega_{rs} _{\text{res}}/\pi$	f_{res} (kHz)
Air, thin	1.2	$1.5 \cdot 10^{-5}$	10	0.0012	10	67	0.50	250
Air, thick	1.2	$1.5 \cdot 10^{-5}$	1000	0.0012	0.1	67	0.50	2.5
Water, thin	1000	$1.0 \cdot 10^{-6}$	10	1	10	1000	0.47	240
Water, thick	1000	$1.0 \cdot 10^{-6}$	1000	1	0.1	1000	0.50	2.5
Oil, thin	950	$3.0 \cdot 10^{-3}$	10	0.98	10	0.34	0.10	53
Oil, thick	950	$3.0 \cdot 10^{-3}$	1000	0.98	0.1	0.34	0.46	2.3

obtained for viscous, heavy fluids and/or lightweight, soft, thick solids.

4.8 Compliant coatings in practice

The purpose of this section is to apply the findings of the previous sections to some actual oscillatory flows in a microchannel with compliant walls of polydimethylsiloxane (PDMS) on a rigid base. PDMS is typically close to incompressible, its shear modulus can vary between 100 kPa and 3 MPa, and its loss tangent is very low ($\tan(\phi_G) < 0.001$) (Lötters et al., 1997). We consider a microchannel with half-height $h = 100 \mu\text{m}$, surrounded by PDMS walls with a shear modulus $|G| = 100 \text{ kPa}$ and a loss angle $\phi_G = 0.05^\circ$ (loss tangent $\tan(\phi_G) = 9 \cdot 10^{-4}$). Three different fluids and two different coating thicknesses are analysed, such that six possible combinations result (cf. table 4.1). The three fluids are air, water and a viscous oil, all at room temperature.

The resonance frequency is an important property of a given system, since it marks the conditions when the response becomes very large. In addition, the dynamics near resonance becomes less trivial, since a small change of parameters can yield a completely different response. Table 4.1 therefore shows some typical dimensionless numbers and corresponding resonance frequencies for the six combinations of fluids and solids. Resonance occurs around $|\omega_{rs}| \approx 0.5\pi$, except for the viscous oil with a thin wall (cf. figure 4.9). Since the wall stiffness is fixed ($|c_s| = 10 \text{ ms}^{-1}$), the resonance frequency $f_{\text{res}} = \omega_{\text{res}}/(2\pi)$ is predominantly determined by the coating thickness, with $f_{\text{res}} \approx 250 \text{ kHz}$ for two thin coatings and $f_{\text{res}} \approx 2.5 \text{ kHz}$ for the thick walls.

Next, we analyse the interface deformation for the same microfluidic oscillatory flows as in table 4.1 at a fixed forcing frequency $f = \omega/(2\pi) = 1 \text{ kHz}$, just below the lowest resonance frequency. The interaction is quantified with several

TABLE 4.2: Dimensionless numbers to quantify the interface velocity for the same microfluidic oscillatory flows as in table 4.1 at a fixed forcing frequency $f = \omega/(2\pi) = 1$ kHz. The subscript *owc* refers to the one-way coupling results from equation 4.28.

Short name	ω_{rf}	$ \omega_{rs} /\pi$	$ \chi_{pg} $	$ \chi_s $	$ u_{c0}/u_{ft} $	$ u_{c0}/u_{ft} _{owc}$
Air, thin	4.2	0.002	$2.4 \cdot 10^{-8}$	$2.6 \cdot 10^{-7}$	$2.8 \cdot 10^{-7}$	$2.8 \cdot 10^{-7}$
Air, thick	4.2	0.2	$2.8 \cdot 10^{-4}$	$3.0 \cdot 10^{-5}$	$3.0 \cdot 10^{-4}$	$3.0 \cdot 10^{-4}$
Water, thin	63	0.002	$2.0 \cdot 10^{-5}$	$5.0 \cdot 10^{-5}$	$6.5 \cdot 10^{-5}$	$6.5 \cdot 10^{-5}$
Water, thick	63	0.2	$2.3 \cdot 10^{-1}$	$5.7 \cdot 10^{-3}$	$2.4 \cdot 10^{-1}$	$2.4 \cdot 10^{-1}$
Oil, thin	$2.1 \cdot 10^{-2}$	0.002	$1.9 \cdot 10^{-5}$	$3.8 \cdot 10^{-4}$	$3.9 \cdot 10^{-4}$	$3.9 \cdot 10^{-4}$
Oil, thick	$2.1 \cdot 10^{-2}$	0.2	$2.2 \cdot 10^{-1}$	$4.3 \cdot 10^{-2}$	$2.8 \cdot 10^{-1}$	$2.7 \cdot 10^{-1}$

dimensionless numbers (cf. table 4.2), including the magnitudes of the two interaction parameters and the normalized interface velocity. An increase of $|\chi_{pg}|$, $|\chi_s|$ and $|u_{c0}/u_{ft}|$ indicates a more significant interaction between fluid and solid. Air has the smallest interaction, which is mainly due to its low density. Water, although it has a kinematic viscosity that is 15 times smaller than that of air, still yields a larger interface velocity due to its 1000 times larger density. By far the largest interaction is obtained with the viscous oil. Its density is comparable to that of water, but it is more viscous by a factor of 3000. The table also confirms that a thicker coating gives a larger interface velocity. Furthermore, the interface velocity according to the one-way coupling approach is quite accurate since $|\chi_s| \ll 1$ for all cases. In summary, the most significant interactions between a compliant coating and oscillatory pressure-driven flow are typically obtained for viscous, heavy fluids and soft, thick coatings.

4.9 Conclusions & Perspectives

This paper has investigated analytically a fundamental problem in fluid-structure interaction: the oscillatory pressure-driven laminar flow coupled to a compliant viscoelastic layer on a rigid base, mainly motivated by oscillatory flows in soft microchannels. The flow is assumed to be laminar and streamwise homogeneous, while the fluid is incompressible and Newtonian. The solid is attached at the bottom to a rigid wall and it is assumed to be linear, viscoelastic and incompressible. This problem is solved analytically using the two-way coupling approach, which requires equality of velocities and stresses at the fluid/solid interface. Vertical coating deformation and wall-normal flow are absent, since the coating is incompressible and the flow is streamwise homogeneous. The horizontal coating deformation can be decomposed into two contributions, one from the streamwise pressure gradient and another from the shear stress on the coating surface. These contributions can be quantified with two complex, dimensionless interaction parameters, namely χ_{pg} for the pressure gradient and χ_s for the shear stress. The interface velocity obtained with the one-way and two-way coupling approaches

is the same when $|\chi_s| \ll 1$, which corresponds to lightweight, low-viscosity fluids in narrow channels and/or heavy, stiff, thin solids.

The qualitative dynamics of the fluid/solid interaction has been described with use of profiles of the horizontal velocity inside the fluid and the solid phase. The flow dynamics is very similar to the Womersley flow, except that the horizontal velocity at the fluid/solid interface can be nonzero. The classical Womersley solutions are recovered when the solid does not deform, namely when it is heavy, stiff and/or thin. The solid dynamics is a combination of a uniform oscillation due to the pressure gradient inside the coating, and exponentially-decaying travelling shear waves. A characteristic decay length decreases when the loss angle increases.

The fluid-structure interaction has been quantified with the magnitude of the interface velocity, which depends on nine physical parameters and five real dimensionless numbers. The influence of all nine parameters has been investigated systematically and some findings are summarized here. The interface velocity increases linearly with the forcing amplitude. It is linearly proportional to the frequency for low frequencies, while inversely proportional to it for high frequencies. For steady flow, the interface displaces in the direction of decreasing pressure both due to the pressure gradient and the shear stress on the interface. The shear stress disappears for low-viscosity fluids and narrow channels, such that the solid deformation is mainly determined by the pressure gradient. The interface velocity approaches zero for heavy, stiff and/or thin solids. For very soft solids, the fluid velocity becomes spatially uniform as if the solid is absent. The interface velocity is independent of the coating thickness when the latter is larger than approximately five decay lengths.

When the forcing frequency, coating softness and coating thickness are sufficiently large, the interface velocity exhibits multiple resonances. This resonant behaviour is strongest when the solid is purely elastic. The frequency at which the first resonance occurs is an important characteristic of the combined fluid/solid system. The dependence of this resonance frequency on the dimensionless problem parameters has been investigated. For lightweight, low-viscosity fluids in narrow channels and/or heavy, stiff solids, the first resonance appears at $|\omega_{rs}| \approx 0.5\pi$, which corresponds with an antinode at the coating interface. The lowest resonance frequency is obtained for viscous, heavy fluids and/or lightweight, soft, thick solids. The resonance frequencies are typically on the order of a few to a few hundred kHz for microfluidic channels with PDMS walls on a rigid base.

The findings in this paper have a twofold use. First, they help to understand the fluid and solid dynamics for oscillatory pressure-driven flow over a compliant viscoelastic layer on a rigid base. Although the derivation is relatively simple and straightforward, the analytically obtained solution is very instructive. One can easily check the influence of several parameters on the interface velocity, as well as the conditions for which the one-way coupling method is appropriate. Second, the presented analytical solution is very useful for validation of numerical FSI solvers. The need for validation is clearly expressed by Gad-el Hak (2002):

“Without sufficient validation, any numerical result of the fluid-structure interaction problem is suspect at best and wrong at worst.” The current problem is relatively simple, which facilitates a quick first check.

The main limitation of the present study relates to stability. The derived analytical solution is only valid as long as the flow and the deformation are stable, which requires a sufficiently low Reynolds number and a sufficiently stiff coating. Above a critical Reynolds number (as discussed in the introduction), the laminar flow will become transitional and eventually turbulent, which involves more complex interactions. Regarding coating stiffness, the current work suggests that apparent slip of the fluid phase can be obtained with very soft coatings. However, soft coatings are also susceptible to flow-induced surface instabilities, such as travelling surface waves (Duncan et al., 1985; Gad-el Hak, 2002). A stability analysis, although beyond the scope of the current paper, is an important next step, since it will clarify when the interaction between fluid and solid becomes unstable. The present work is a first step in that direction, since a good understanding of the base flow will yield a more meaningful stability analysis.

Acknowledgements

The research leading to these results has received funding from the European Union Seventh Framework Programme in the SEAFRONT project under grant agreement nr. 614034.

Chapter 5

Deformation of a compliant wall in a turbulent flow¹

5.1 Abstract

We investigate the deformation of a linear viscoelastic compliant coating in a turbulent flow for a wide range of coating parameters. A one-way coupling model is proposed in which the turbulent surface stresses are expressed as a sum of streamwise-travelling waves with amplitudes determined from the stress spectra of the corresponding flow over a rigid wall. The analytically calculated coating deformation is analysed in terms of the root-mean-square (rms) surface displacement and the corresponding point frequency spectra. The present study systematically investigates the influence of five coating properties namely density, stiffness, thickness, viscoelasticity and compressibility. The surface displacements increase linearly with the fluid/solid density ratio. They are linearly proportional to the coating thickness for thin coatings, while they become independent of the thickness for thick coatings. Very soft coatings show resonant behaviour, but the displacement for stiffer coatings is proportional to the inverse of the shear modulus. The viscoelastic loss angle has only a significant influence when resonances occur in the coating response, while the Poisson's ratio has a minor effect for most cases. The modelled surface displacement is qualitatively compared with recent measurements on the deformation of three different coatings in a turbulent boundary-layer flow. The model predicts the order of magnitude of the surface displacement, and it captures the increase of the coating displacement with the

¹This chapter is (nearly) identical to the manuscript H. O. G. Benschop, A. J. Greidanus, R. Delfos, J. Westerweel, and W.-P. Breugem. Deformation of a linear viscoelastic compliant coating in a turbulent flow. *Journal of Fluid Mechanics*, 2018b, accepted. The experiments described in section 5.6 of this chapter were performed by Greidanus et al. (2017) and Delfos et al. (2017).

Reynolds number and the coating softness. Finally, we propose a scaling that collapses all the experimental data for the rms of the vertical surface displacement onto a single curve.

5.2 Introduction

The interaction of compliant coatings with laminar, transitional and turbulent flows has been the subject of much research for several decades. Early studies were triggered by the work of Kramer (1962), who reported substantial drag reduction with a compliant wall that modelled the dolphin skin. Follow-up research was motivated by the possible use of such compliant coatings to delay transition in laminar flows, to reduce drag in turbulent flows, and to suppress vibrations or noise (Gad-el Hak, 2002). Many researchers have investigated the instabilities that arise for flow along flexible boundaries (Benjamin, 1963; Carpenter and Garrad, 1986; Shankar and Kumaran, 1999), and overviews of compliant-coating research are provided by Bushnell et al. (1977), Riley et al. (1988) and Gad-el Hak (2002). Below we review some of the recent experimental, numerical and analytical work regarding the deformation of a compliant wall in a turbulent flow.

Several studies report measurements of the surface deformation of a compliant wall in a turbulent flow. Srinivas and Kumaran (2017) studied the flow in a channel with soft walls for three different values of the wall stiffness. Their Reynolds number Re , based on the bulk velocity and the channel height, ranged from about 300 to 4000. Both horizontal and vertical surface displacements were measured by tracking a glass bead close to the surface. The softest wall showed a hard-wall laminar-turbulent transition close to $Re = 1000$ and a soft-wall transition around $Re = 1400$. The latter was identified by a pronounced increase of the streamwise velocity fluctuations and the Reynolds stress, which suggests that turbulence was generated by the soft wall.

Zhang et al. (2017) investigated a compliant coating in a turbulent channel flow at $Re_\tau = 2300$. They report simultaneous measurements of the time-resolved, three-dimensional flow field (using Particle Image Velocimetry (PIV)) and the two-dimensional surface deformation (using Mach-Zehnder interferometry (Zhang et al., 2015)). Their compliant coating is relatively stiff: the root-mean-square (rms) values of the wall-normal surface displacement were much smaller than the viscous wall unit of the turbulent flow. By correlating the deformation with the flow pressure, they show that negative (positive) deformations or dimples are caused by positive (negative) pressure fluctuations.

Delfos et al. (2017) and Greidanus et al. (2017) studied the deformation of three compliant coatings with varying stiffness in a turbulent boundary-layer flow between $Re_\tau = 2100$ and 8500. Three quantities were measured, namely the flow velocity with planar Particle Image Velocimetry (PIV), the drag force on the plate with a force balance and the vertical coating displacement with high-speed Background Oriented Schlieren (BOS). The surface deformation increased with increasing Reynolds number and coating softness. The maximum rms of

the vertical surface displacement was 14, 1.0 and 0.31 wall units for the three different coatings. The two stiffest coatings had no influence on the drag, but the softest coating showed a drag increase when the surface displacement became approximately 2.4 wall units. There are some indications from other experiments that compliant walls can reduce drag in turbulent flows (Lee et al., 1993; Choi et al., 1997), though a drag increase was measured in recent experiments by Ivanov et al. (2017). Detailed, carefully conducted and independently verified experimental studies are very scarce in general.

Several numerical studies have appeared the past two decades. The resolvent formulation was used to consider the interactions between a compliant wall and turbulence (Luhar et al., 2015, 2016). Direct numerical simulations (DNSs) of turbulent flow over compliant walls have been performed as well (Endo and Himeno, 2002; Xu et al., 2003; Fukagata et al., 2008; Kim and Choi, 2014; Xia et al., 2017). The walls were modelled as spring-damper-supported plates or membranes and the surface motion was restricted to the vertical direction in most studies, although a viscoelastic layer is more appropriate to model the coatings that are typically used in experiments (Kulik et al., 2008). Kim and Choi (2014) showed that softer walls yield increased wall displacements, and very soft walls deformed as large-amplitude quasi-two-dimensional waves that travel in the downstream direction. Similar findings were reported by Luo and Bewley (2005) for their DNSs of turbulent flow over a compliant fabric. More recently, Rosti and Brandt (2017) performed DNSs of turbulent channel flow over an incompressible viscous hyper-elastic layer, which allowed them to use a one-continuum formulation. The skin friction monotonically increased when the elastic modulus decreased. Near-wall streaks were reduced, while the flow became more correlated in the spanwise direction, like for flows over rough and porous walls.

Analytical or semi-analytical studies have been performed as well. Some investigations describe dispersion relations for waves on (visco)elastic layers, either in absence of shear and pressure (Gad-el Hak et al., 1984; Kulik et al., 2008) or only in absence of shear (Duncan et al., 1985; Vedenev, 2016). The dispersion relation predicts the dominant speed(s) at which waves will travel when the coating is excited with a certain angular frequency or wavenumber, presuming that the propagation speed is not determined by the external forcing. The latter two studies have two important conclusions regarding the stability of coatings in a turbulent flow: (a) the most unstable waves are the shortest waves, and (b) two instabilities appear above a critical flow velocity, namely static divergence and flutter. Static divergence is a damping instability, caused by the viscous properties of the coating, that appears as an almost stationary wave pattern. Flutter is an elastic instability that appears as fast travelling waves, and it can be stabilized by damping. Duncan (1986) considered the response of a viscoelastic layer to travelling pressure pulses and the associated stability boundary.

Several researchers have studied the response of compliant layers to waves of shear stress and pressure. The propagation of waves on the surface of a semi-infinite solid has already been investigated more than a century ago

(Rayleigh, 1885; Lamb, 1904), while more recent studies have considered streamwise-travelling stress waves on a compliant layer of finite thickness (Chase, 1991; Kulik, 2012; Zhang et al., 2017). Chase (1991) focussed on the conversion of shear stress on the layer surface to normal stress within the layer and the associated influence on flow noise. Kulik (2012) employed a similar model to determine the surface displacements as function of several dimensionless parameters, such as the coating's loss tangent and Poisson's ratio. Finally, Zhang et al. (2017) used the model of Chase (1991) to elucidate many of their observations.

A systematic parameter study has not yet appeared in the literature. Experiments and numerical simulations have been very useful, but they are typically limited to a small parameter range. In addition, the numerical models that have been used are often quite simplistic: the walls are typically modelled as spring-damper-supported plates or membranes that only deform in the vertical direction. Kulik (2012) considered the influence of a few dimensionless parameters on the surface deformation, including wave properties such as wavelength, frequency and propagation speed. However, it remains unclear how these wave properties should be chosen such that the resulting waves represent the stresses in an actual turbulent flow.

The objective of the present study is to characterize the influence of several coating properties on its deformation in a turbulent flow, and the main novelties of this work are threefold. First, the response of a compliant coating to a whole spectrum of stress fluctuations is considered. We prescribe how the wave properties should be chosen such that the resulting waves represent the stresses in an actual turbulent flow. Second, this study systematically investigates the influence of five coating properties namely density, thickness, stiffness, viscoelasticity and compressibility. Third, the performance of the model is evaluated by direct comparison with experiments performed by Delfos et al. (2017) and Greidanus et al. (2017).

The approach in this study is analytical, using the one-way coupling method: turbulent flow stresses deform the compliant coating, but these coating deformations have negligible influence on the turbulent flow. The fluctuating stresses are obtained from stress spectra for turbulent flow over a rigid wall, and they are subsequently applied to a linear, viscoelastic layer on a rigid base. The resulting coating deformation is computed and the influence of the coating properties is investigated, including the behaviour in some limiting cases. The deformation is characterized with rms-values, point spectra and vector fields of displacements and velocities.

The paper is organized as follows: section 5.3 describes the one-way coupling model and its constituents, such as the concept of travelling waves of stress and deformation, the equations for viscoelastic deformation, and the coating model. The response of a viscoelastic coating to a single travelling stress wave is computed and discussed in section 5.4. In section 5.5, the one-way coupling model is applied to turbulent channel flow and the influence of the coating properties on the surface displacement and velocity is investigated. The model is applied

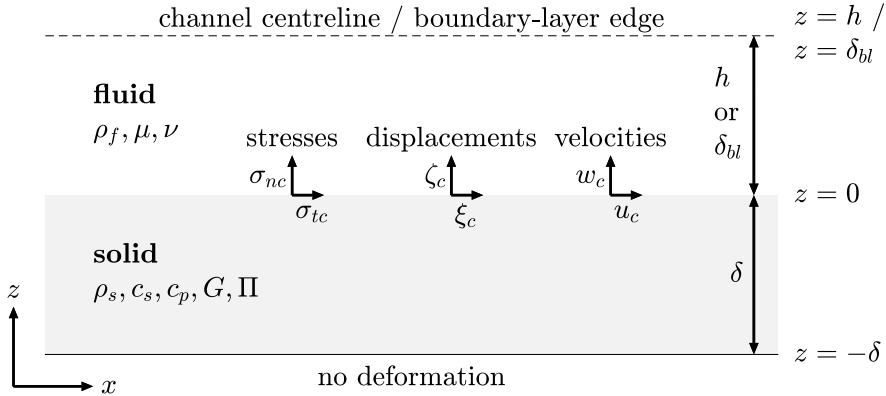


FIGURE 5.1: Sketch of the analytical problem. The grey layer represents a solid of thickness δ . A turbulent channel or boundary-layer flow exerts fluctuating tangential stresses σ_{tc} and normal stresses σ_{nc} on the coating surface. The stresses induce the surface displacements ξ_c and ζ_c , as well as the surface velocities u_c and w_c .

to turbulent boundary-layer flow in section 5.6, and the results are compared with recent measurements of wall deformation in such a flow. In section 5.7, the current study is summarized, the results are discussed and an outlook is presented.

5.3 One-way coupling model

5.3.1 Problem description

This study computes the deformation of a solid layer in a turbulent flow, as sketched in figure 5.1. A viscous and incompressible Newtonian fluid has mass density ρ_f , dynamic viscosity μ and kinematic viscosity $\nu = \mu/\rho_f$. The wall friction velocity u_τ is derived from $\tau_w = \rho_f u_\tau^2$ with τ_w the Reynolds-averaged wall shear stress for turbulent flow over a rigid wall. Because of the one-way coupling approach, the mean wall shear stress is not influenced by the fluctuating coating deformations. The Reynolds number is either $Re_\tau = hu_\tau/\nu$ for channel flow with half-height h , or $Re_\tau = \delta_{bl}u_\tau/\nu$ for boundary-layer flow with boundary-layer height δ_{bl} .

The problem is two-dimensional in space: only horizontal and vertical deformations, velocities and stresses are considered, as is motivated in section 5.5.2. The fluctuating fluid stresses at the coating interface are the tangential stress $\sigma_{tc}(x, t)$ and the normal stress $\sigma_{nc}(x, t)$, with the subscripts c for the interface, t for tangential stress and n for normal stress. These stresses, which vary with the streamwise coordinate x and with time t , result in a deformation of the underlying coating. The horizontal and vertical coating displacements are denoted by ξ and ζ , with the corresponding velocities u and w .

The coating of thickness δ is linear, time-translation-invariant, homogeneous, isotropic and viscoelastic. It is attached at the bottom to a rigid wall, and it has infinite length in the streamwise direction to neglect the influence of coating boundaries and the associated reflections. The coating has mass density ρ_s , shear-wave speed c_s , shear modulus $G = \rho_s c_s^2$, compressional-wave speed c_p and compressional-wave modulus $\Pi = \rho_s c_p^2$. These speeds and moduli are complex numbers, as explained below.

5.3.2 Surface stress and coating deformation as travelling waves

This subsection introduces the concept of travelling waves to describe the fluctuating surface stress and coating deformation. To simplify the analysis and to speed up the computations, four assumptions will be made regarding the surface stresses: (1) they are fully determined in space and time, thus ignoring any randomness, (2) the stresses can be considered as travelling waves, which excludes growing or decaying stress disturbances, (3) the set of frequencies is discrete and finite, and (4) each frequency corresponds with a single wavevector in the streamwise direction such that the spanwise dependence of the stresses can be neglected. Section 5.5.2 explains why the latter assumption is reasonable for turbulent flows. Given these assumptions, the fluctuating interface stresses can be expressed as a sum of N_m streamwise-travelling spanwise-homogeneous waves:

$$\boldsymbol{\sigma}_{\mathbf{c}}(x, t) = \sum_{m=1}^{N_m} \boldsymbol{\sigma}_{\mathbf{c},m} e^{-i(k_m x - \omega_m t)}, \quad (5.1)$$

with the two-dimensional stress vector $\boldsymbol{\sigma}_{\mathbf{c}} = [\sigma_{tc} \ \sigma_{nc}]^T$, where T denotes the transpose. Each travelling wave (or mode) has number m , complex amplitude $\boldsymbol{\sigma}_{\mathbf{c},m} = [\sigma_{tc,m} \ \sigma_{nc,m}]^T$, (streamwise) wave number k_m , angular frequency ω_m and wave speed $c_m = \omega_m/k_m$. This paper considers only the deformation by stress fluctuations, so ω_m is nonzero.

Assuming that the coating response is linear and stable, the coating deformation will have the same temporal and spatial dependence as the stresses. For example, the surface stress $\boldsymbol{\sigma}_{\mathbf{c},m} \exp\{-i(k_m x - \omega_m t)\}$ will generate the displacement $\boldsymbol{\xi}_{\mathbf{m}}(z) \exp\{-i(k_m x - \omega_m t)\}$, with $\boldsymbol{\xi}_{\mathbf{m}} = [\xi_m \ \zeta_m]^T$ the complex displacement amplitude of mode m . Because of linearity, the total response of the coating is simply a summation of the individual responses:

$$\begin{aligned} \boldsymbol{\xi}(x, z, t) &= \sum_{m=1}^{N_m} \boldsymbol{\xi}_{\mathbf{m}}(z) e^{-i(k_m x - \omega_m t)}, \\ \mathbf{u}(x, z, t) &= \sum_{m=1}^{N_m} \mathbf{u}_{\mathbf{m}}(z) e^{-i(k_m x - \omega_m t)}, \end{aligned} \quad (5.2)$$

where $\boldsymbol{\xi} = [\xi \ \zeta]^T$ and $\mathbf{u} = [u \ w]^T$.

5.3.3 Viscoelastic deformation

This subsection summarizes the theory of viscoelastic deformations. Consider a solid particle at a position given by the Lagrangian coordinate vectors \mathbf{x} in the undeformed medium and \mathbf{X} in the deformed medium. The displacement or deformation vector $\boldsymbol{\xi}$ with components ξ_i is then given by $\boldsymbol{\xi} = \mathbf{X} - \mathbf{x}$. The particle's velocity $u_i(\mathbf{x}, t)$ is the time derivative of its actual position: $u_i = \partial X_i / \partial t = \partial \xi_i / \partial t$. The equations of motion in the undeformed coordinates are (Chung, 2007):

$$\rho_s \frac{\partial u_i}{\partial t} = \frac{\partial \sigma_{ij}}{\partial x_j} + \rho_s f_i, \quad (5.3)$$

with stress tensor σ_{ij} and body force f_i . The present study is restricted to displacement fields that slowly vary in space (Lautrup, 2011): $|\partial \xi_i(\mathbf{x}, t) / \partial x_j| \ll 1$ for all i, j, \mathbf{x}, t . That allows us to ignore density changes and nonlinear deformations. The corresponding strain tensor is Cauchy's (infinitesimal) strain tensor ϵ_{ij} :

$$\epsilon_{ij} = \frac{1}{2} \left(\frac{\partial \xi_i}{\partial x_j} + \frac{\partial \xi_j}{\partial x_i} \right). \quad (5.4)$$

For linear time-translation-invariant homogeneous isotropic media, the constitutive stress-strain relation can be written in integral form as (Robertsson et al., 1994; Carcione, 2015):

$$\sigma_{ij} = \dot{\psi}_\Lambda * \epsilon_{kk} \delta_{ij} + 2\dot{\psi}_G * \epsilon_{ij}, \quad (5.5)$$

where the dot denotes a time derivative and the asterisk symbolizes convolution:

$$f(t) * g(t) \equiv \int_{-\infty}^{\infty} f(\tau) g(t - \tau) d\tau. \quad (5.6)$$

The constitutive equation contains two relaxation functions, namely $\psi_\Lambda(t)$ for dilatation and $\psi_G(t)$ for shear. The convolution expresses that the stress depends on the strain history (assuming causality).

When the boundary conditions and body forces of a viscoelastic problem are steady state harmonic functions of time, as was assumed in section 5.3.2, all field variables will have the same time dependence (Christensen, 1982). Consider a harmonic time dependence of the form $e^{i\omega_m t}$ (cf. equation 5.2), then the convolution with an arbitrary function $f(t)$ can be simplified: $f(t) * e^{i\omega_m t} = F(\omega_m) e^{i\omega_m t}$ with $F(\omega) = \mathcal{F}\{f(t)\} = \int_{-\infty}^{+\infty} f(t) e^{-i\omega t} dt$ the Fourier transform of $f(t)$. Using this property, the viscoelastic stress-strain relation for mode m becomes:

$$\sigma_{ij} = \Lambda(\omega_m) \epsilon_{kk} \delta_{ij} + 2G(\omega_m) \epsilon_{ij}, \quad (5.7)$$

where $\Lambda(\omega) = \mathcal{F}\{\dot{\psi}_\Lambda(t)\}$ and $G(\omega) = \mathcal{F}\{\dot{\psi}_G(t)\}$ are the complex dilatational and shear moduli (Tschöegl et al., 2002; Carcione, 2015). In absence of body forces,

the equations of motion 5.3 for mode m then become the following viscoelastic wave equations:

$$\rho_s \frac{\partial^2 \xi_i}{\partial t^2} = \left(\Pi(\omega_m) - G(\omega_m) \right) \frac{\partial}{\partial x_i} \left(\frac{\partial \xi_k}{\partial x_k} \right) + G(\omega_m) \frac{\partial^2 \xi_i}{\partial x_j^2}, \quad (5.8)$$

with compressional-wave modulus $\Pi = \Lambda + 2G$. These equations are the same as for linear elasticity, except for the use of complex, frequency dependent moduli: $G(\omega) = |G(\omega)|e^{i\phi_G(\omega)}$ and $\Pi(\omega) = |\Pi(\omega)|e^{i\phi_\Pi(\omega)}$. The shear modulus has a magnitude $|G|$, a loss angle ϕ_G and a loss tangent $\eta_G = \tan(\phi_G)$, and similarly for the compressional-wave modulus.

5.3.4 Coating model

A coating model is required to prescribe the mechanical coating properties, namely the frequency-dependent modulus magnitude and loss angle for both the shear and the compressional-wave modulus. Unless stated otherwise, the frequency dependence of the moduli is neglected, which is motivated by the observation that the maximum coating response occurs in a limited frequency range (cf. section 5.6.4, figures 5.15 and 5.16).

Accurate determination of the coating moduli requires simultaneous measurements of the coating response in shear and compression. In this way, researchers have measured the relation between the bulk modulus $K = \Pi - (4/3)G$ and the shear modulus G . Here we use the relations obtained by Pritz (2009) that were validated for three solid polymeric materials. Specifically, the loss properties of the bulk and the shear modulus can be related through:

$$\frac{\eta_K}{\eta_G} = \frac{\tan \phi_K}{\tan \phi_G} = 1 - (2\nu_{pr})^n, \quad n = 2,3, \quad (5.9)$$

where η represents the loss tangent, ϕ the loss angle, and ν_{pr} the (real part of the) Poisson's ratio. The above relation shows good agreement with experimental data for three different polymeric materials and $0.35 \lesssim \nu_{pr} \lesssim 0.5$. Equation 5.9 quantifies that the loss tangent of the bulk modulus is smaller than that of the shear modulus. The ratio between the magnitudes of the bulk and shear modulus was computed from:

$$\left| \frac{K}{G} \right| = \left| \frac{2 + 2\nu_p}{3(1 - 2\nu_p)} \right|, \quad \nu_p = \nu_{pr}(1 - i\eta_{\nu_p}), \quad (5.10)$$

with the (complex) Poisson's ratio ν_p , its real part ν_{pr} and its dissipation factor or loss tangent η_{ν_p} . The latter can be estimated from $\eta_{\nu_p}/\eta_G \approx 1 - 2\nu_{pr}$ when the medium is close to incompressible ($\nu_{pr} \approx 0.5$) (Pritz, 2009). The relation $\Pi = K + (4/3)G$ together with the definitions $G = \rho_s c_s^2$ and $\Pi = \rho_s c_p^2$ can finally be used to compute the ratio of the compressional-wave speed c_p and the

shear-wave speed c_s :

$$\frac{K}{G} = \left| \frac{K}{G} \frac{e^{i\phi_K}}{e^{i\phi_G}} \right|, \quad \frac{\Pi}{G} = \frac{K}{G} + \frac{4}{3}, \quad \frac{c_p}{c_s} = \sqrt{\frac{\Pi}{G}}. \quad (5.11)$$

Hence, the (complex) ratio c_p/c_s can be determined from the shear loss angle ϕ_G and the (real part of the) Poisson's ratio ν_{pr} . In this way, the shear and compression properties of the coating are related through a loss angle and a Poisson's ratio.

5.3.5 Summary of model and assumptions

This subsection summarizes the model and the underlying assumptions. The implication of the most important assumptions on the results is addressed in section 5.7. The deformation of a compliant coating in a turbulent flow is computed analytically using the one-way coupling method: turbulent flow stresses deform the compliant coating, but these coating deformations have negligible influence on the turbulent flow, like in the recent study by Zhang et al. (2017). The turbulent surface stresses are expressed as a sum of streamwise-travelling and spanwise-homogeneous waves (cf. equation 5.1). The amplitudes of the waves are obtained from point frequency spectra of turbulent stresses in flow over a rigid wall, as detailed in sections 5.5.2 and 5.6.2. The compliant coating is considered to be a linear time-translation-invariant homogeneous isotropic viscoelastic medium (cf. equations 5.4, 5.7, 5.8). It is attached at the bottom to a rigid wall, and it has infinite length in the streamwise direction. The frequency dependence of the viscoelastic moduli is neglected. The relations between the coating's shear and compression properties are obtained from a model by Pritz (2009) for solid polymeric materials.

5.4 Coating deformation for a single surface stress wave

5.4.1 Analytical solution and dimensionless parameters

This section considers the compliant wall deformation for a single travelling stress wave. Specifically, the stresses at the fluid-coating interface are:

$$\sigma_{13}|_{z=0} \equiv \sigma_{tc} = \sigma_{tc0} e^{-i(kx-\omega t)}, \quad \sigma_{33}|_{z=0} \equiv \sigma_{nc} = \sigma_{nc0} e^{-i(kx-\omega t)}. \quad (5.12)$$

This stress wave has wave number k , angular frequency ω , wavelength $\lambda = 2\pi/k$, period $T = 2\pi/\omega$ and wave speed $c = \omega/k = \lambda/T$. The wave amplitudes can be complex numbers to allow a phase difference between the tangential and the normal stress. Note that the subscript m has been dropped for the remainder of this section. The wall underneath the coating is rigid, so the displacements

should vanish at the coating-wall interface:

$$\xi|_{z=-\delta} = 0, \quad \zeta|_{z=-\delta} = 0. \quad (5.13)$$

The viscoelastic equations 5.7 and 5.8 were solved using the Helmholtz decomposition (see appendix C.1, cf. Lamb (1904); Chase (1991); Kulik (2012); Zhang et al. (2017)). The analytical solution was simplified by using k , ω , ρ_f and derived parameters for nondimensionalization:

$$\tilde{x}_i = kx_i, \quad \tilde{t} = \omega t, \quad \tilde{\xi}_i = k\xi_i, \quad \tilde{u}_i = \frac{u_i}{c}, \quad \tilde{\sigma}_{ij} = \frac{\sigma_{ij}}{\rho_f c^2}. \quad (5.14)$$

The following dimensionless numbers appear in the analytical solution:

$$\begin{aligned} \rho_r &= \frac{\rho_f}{\rho_s} = \frac{\text{fluid density}}{\text{solid density}}, \\ \omega_{rs} &= \frac{\omega\delta}{c_s} = \frac{\text{forcing frequency}}{\text{frequency of shear waves}}, \\ \omega_{rp} &= \frac{\omega\delta}{c_p} = \frac{\text{forcing frequency}}{\text{frequency of compressional waves}}, \\ \delta_{r\lambda} &= \frac{\delta}{\lambda} = \frac{\text{coating thickness}}{\text{wavelength of forcing}}, \end{aligned} \quad (5.15)$$

where ρ_r is the density ratio. There are two frequency-related dimensionless numbers: ω_{rs} is relative to a typical shear-wave frequency, whereas ω_{rp} is relative to a typical compressional-wave frequency. The last parameter compares the coating thickness with the wavelength, the latter being the length-scale that is introduced by the forcing. Some additional dimensionless numbers can be derived from the ones provided in equation 5.15:

$$\begin{aligned} \tilde{\delta} &= 2\pi\delta_{r\lambda} = \frac{|\omega_{rs}|}{|c_{rs}|}, \quad c_{rs} = \frac{c}{c_s} = \frac{1}{\tilde{c}_s} = \frac{\omega}{kc_s} = \frac{\omega_{rs}}{\tilde{\delta}}, \\ c_{rp} &= \frac{c}{c_p} = \frac{1}{\tilde{c}_p} = \frac{\omega}{kc_p} = \frac{\omega_{rp}}{\tilde{\delta}}. \end{aligned} \quad (5.16)$$

The analytical solution provided in appendix C.1 is fully determined by the following dimensionless numbers: $\tilde{\sigma}_{tc0}$, $\tilde{\sigma}_{nc0}$, ρ_r , ω_{rs} , ω_{rp} and $\delta_{r\lambda}$. Note that ω_{rs} and ω_{rp} can be calculated as follows:

$$\omega_{rs} = |\omega_{rs}|e^{i\phi_{\omega_{rs}}}, \quad \phi_{\omega_{rs}} = -\frac{\phi_G}{2}, \quad \frac{\omega_{rp}}{\omega_{rs}} = \frac{c_s}{c_p} = \sqrt{\frac{G}{\Pi}}. \quad (5.17)$$

Using these relations and the coating model from section 5.3.4, the possibly complex numbers ω_{rs} and ω_{rp} can be computed from three real dimensionless numbers, namely $|\omega_{rs}|$, ϕ_G and ν_{pr} . Hence, the analytical solution can also be obtained from these dimensionless numbers: $\tilde{\sigma}_{tc0}$, $\tilde{\sigma}_{nc0}$, ρ_r , $\delta_{r\lambda}$, $|\omega_{rs}|$, ϕ_G and ν_{pr} . The purpose of the next subsection is to elucidate how the surface deformation

depends on these dimensionless numbers, with a specific focus on the nontrivial dependence of the vertical surface displacement on $\delta_{r\lambda}$, $|\omega_{rs}|$, ϕ_G and ν_{pr} .

5.4.2 Dimensionless parameters dependence

Before showing some results, it should be remarked that special care is required for the numerical computation of the interface quantities. The analytical solutions are fractions that contain sines and cosines of possibly large complex arguments. Hence, the numerator and denominator can become exponentially large, which might result in numerically calculated fractions that are completely wrong. For that reason, the functions to compute the interface quantities were equipped with statements to check the accuracy of the calculations. Specifically, the solid stress at the interface was computed from the numerically calculated coefficients that appear in the analytical solution. The computations, most of which were performed with MATLAB using double precision, were considered sufficiently accurate when the difference between the thus obtained solid stress and the applied fluid stress was smaller than 10^{-6} . Otherwise, the function switched to variable precision arithmetic (vpa) in MATLAB or the computations were performed in MAPLE. The MAPLE function was equipped with a similar accuracy check; the number of digits was doubled till sufficient precision was obtained.

Figures 5.2 and 5.3 show contours of the normal surface displacement as function of $|\omega_{rs}|$ and $|c_{rs}|$, which are related through $\tilde{\delta} = 2\pi\delta_{r\lambda} = |\omega_{rs}|/|c_{rs}|$ (equation 5.16). The two subplots in figure 5.2 differ in the way how the displacement is normalized, namely with coating thickness (left) and wavenumber (right). Figure 5.3 is the same as figure 5.2, except that the horizontal and vertical axes are linear instead of logarithmic, and that the subfigures correspond with two loss angles instead of two normalizations. The stress amplitudes were fixed at $\tilde{\sigma}_{tc0} = 0.0041$ and $\tilde{\sigma}_{nc0} = 0.0238$, which were computed from $\tilde{\sigma} = \sigma^+ / (c^+)^2$ with σ^+ from the rms values of the tangential and normal stress (cf. equation 5.26) and $c^+ = 10$. Note, however, that the magnitude of these stresses is not very relevant at this stage, since the figures should primarily facilitate a qualitative understanding of the dynamics.

The contour lines in figure 5.2 show a clear change of direction around $\delta_{r\lambda} \approx 0.33$, which is an important value, also according to other studies (Kulik et al., 2008; Kulik, 2012; Zhang et al., 2017). Two interesting limits can be distinguished accordingly, namely (1) a long-wave limit and (2) a short-wave limit (Kulik, 2012; Vedeneev, 2016). The long-wave limit corresponds with $\delta_{r\lambda} \ll 1$, so the wavelength is much larger than the coating thickness. On the other hand, $\delta_{r\lambda} \gg 1$ indicates the short-wave limit, such that the wavelength is much smaller than the coating thickness. Both limits are described below in more detail.

The solution in the long-wave limit ($\delta_{r\lambda} \ll 1$) is derived in appendix C.1.2. The main outcome is presented here, namely the surface displacements for a single wave:

$$\frac{\xi_c}{\delta} = \frac{\tan(\omega_{rs}) \sigma_{tc}}{\omega_{rs} G}, \quad \frac{\zeta_c}{\delta} = \frac{\tan(\omega_{rp}) \sigma_{nc}}{\omega_{rp} \Pi}. \quad (5.18)$$

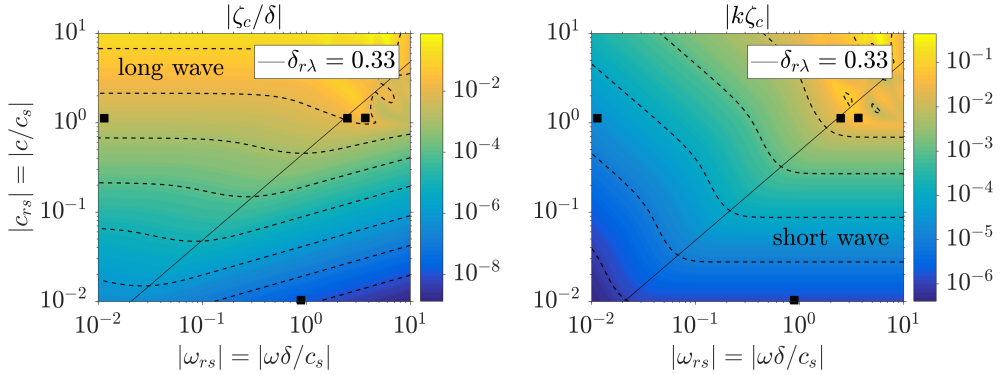


FIGURE 5.2: The vertical surface displacement as function of the dimensionless frequency $|\omega_{rs}|$ and the dimensionless convection velocity $|c_{rs}|$. The other parameters are $\tilde{\sigma}_{tc0} = 0.0041$, $\tilde{\sigma}_{nc0} = 0.0238$, $\rho_r = 1$, $\phi_G = 10^\circ$, $\nu_{pr} = 0.45$. Both subfigures are the same, except that the vertical displacement is normalized with the coating thickness (*left*) and with the wavenumber (*right*). The four square symbols indicate the dimensionless parameters for which figure 5.9 shows a displacement vector field.

The displacements scale with δ : the coating thickness is the characteristic length scale in the long-wave limit, somewhat similar to the shallow-water limit for water waves. In the low-frequency limit (both $|\omega_{rs}| \ll 1$ and $|\omega_{rp}| \ll 1$), the displacements become independent of the frequency ω :

$$\frac{\xi_c}{\delta} = \frac{\sigma_{tc}}{G} = \rho_r c_{rs}^2 \tilde{\sigma}_{tc}, \quad \frac{\zeta_c}{\delta} = \frac{\sigma_{nc}}{\Pi} = \rho_r c_{rp}^2 \tilde{\sigma}_{nc}. \quad (5.19)$$

The normalized displacement then only depends on c_{rs}^2 (since also $c_{rp}^2 \propto c_{rs}^2$), which corresponds with the horizontal contour lines in the top left corner of figure 5.2 (left).

Apparent from figure 5.3 (left) are lines for which the coating strongly responds to the external travelling-wave forcing. These lines, which we denote as resonances, correspond quite well with the dispersion curves that were obtained by Kulik et al. (2008) for a similar viscoelastic solid. In agreement with their work and with Benschop and Breugem (2017), the resonances in the long-wave limit only occur when $|\omega_{rs}| \gtrsim 1$. More specifically, for an elastic solid ($\phi_G = 0^\circ$) they occur when ω_{rs} and ω_{rp} are odd multiples of $\pi/2$ (cf. equation 5.18), as indicated with the symbols on the top axes of figure 5.3. The resonances indeed coincide with these symbols when $\delta_{r\lambda} \ll 1$, which is equivalent to $|c_{rs}| \gg |\omega_{rs}|$. The resonance at $\omega_{rp} = \pi/2$ becomes dominant in that limit, as the vertical displacement then solely depends on ω_{rp} (not clearly visible in figure 5.3 due to the limited range of the vertical axis). The strong resonances for an elastic solid are less pronounced or even absent for a viscoelastic solid (cf. figure 5.3 left vs. right), which agrees with the findings from previous studies (Kulik, 2012; Benschop and Breugem, 2017).

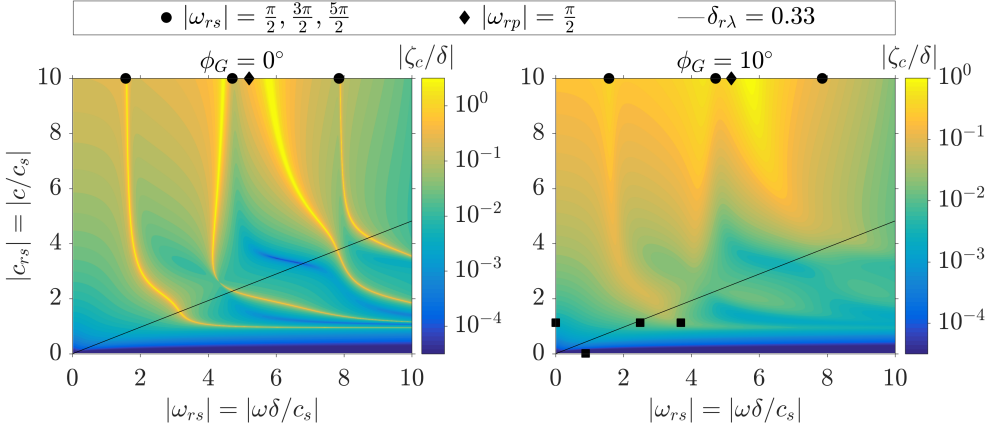


FIGURE 5.3: The vertical surface displacement as function of the dimensionless frequency $|\omega_{rs}|$ and the dimensionless convection velocity $|c_{rs}|$ for two loss angles, namely $\phi_G = 0^\circ$ (*left*) and $\phi_G = 10^\circ$ (*right*). The other parameters are $\tilde{\sigma}_{tc0} = 0.0041$, $\tilde{\sigma}_{nc0} = 0.0238$, $\rho_r = 1$, $\nu_{pr} = 0.45$. The *right* subfigure is the same as figure 5.2 (*left*), except that the axes are linear instead of logarithmic. Like in figure 5.2, the four square symbols in the right figure indicate the dimensionless parameters for which figure 5.9 shows a displacement vector field.

The solution in the short-wave limit ($\delta_{r\lambda} \gg 1$) is derived in appendix C.1.3. The main outcome is presented here, namely the surface displacements for a single wave:

$$\tilde{\xi}_c = \rho_r c_{rs}^2 \frac{\left(-2\sqrt{1-c_{rp}^2}\sqrt{1-c_{rs}^2} - (c_{rs}^2 - 2)\right) i\tilde{\sigma}_{nc} + c_{rs}^2\sqrt{1-c_{rs}^2}\tilde{\sigma}_{tc}}{d_{sw}}, \quad (5.20a)$$

$$\tilde{\zeta}_c = \rho_r c_{rs}^2 \frac{c_{rs}^2\sqrt{1-c_{rp}^2}\tilde{\sigma}_{nc} + \left(2\sqrt{1-c_{rp}^2}\sqrt{1-c_{rs}^2} + (c_{rs}^2 - 2)\right) i\tilde{\sigma}_{tc}}{d_{sw}}, \quad (5.20b)$$

$$d_{sw} = 4\sqrt{1-c_{rp}^2}\sqrt{1-c_{rs}^2} - (c_{rs}^2 - 2)^2. \quad (5.20c)$$

The displacements scale with $1/k \propto \lambda$, so the wavelength is the characteristic length scale in the short-wave limit, somewhat similar to the deep-water limit for water waves. The coating thickness δ does not appear in the expressions, which is typical for the short-wave limit. This is also observed in the lower right corner of the right subfigure in figure 5.2: the contour lines are horizontal, so the displacement is independent of $|\omega_{rs}| \propto \delta$. Note that $c_{rs} = \omega/kc_s$ can be interpreted as the short-wave analogue of $\omega_{rs} = \omega\delta/c_s$: one obtains c_{rs} from ω_{rs} when δ is replaced by $1/k$.

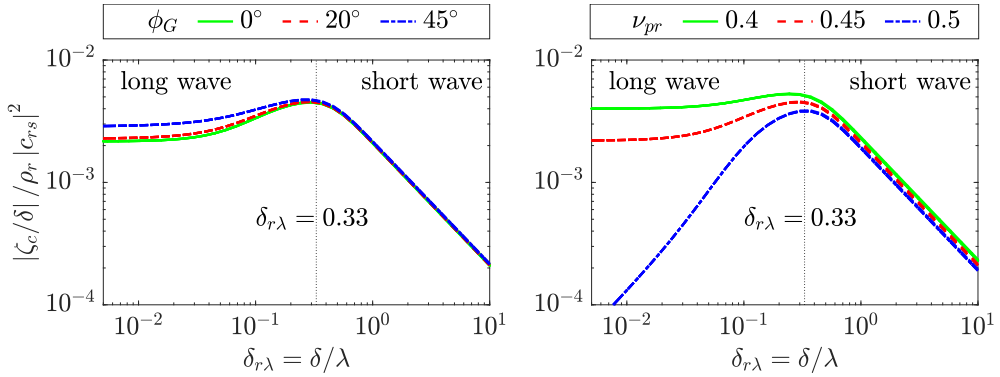


FIGURE 5.4: The vertical surface displacement as function of the dimensionless coating thickness $\delta_{r\lambda}$ for three loss angles ϕ_G (left) and three Poisson's ratios ν_{pr} (right). The other parameters are $\tilde{\sigma}_{tc0} = 0.0041$, $\tilde{\sigma}_{nc0} = 0.0238$, $\phi_G = 10^\circ$ (right), $\nu_{pr} = 0.45$ (left). The graphs are independent of ρ_r due to the normalization of the vertical displacement. The curves are shown for four values of $|c_{rs}|$ (0.01, 0.05, 0.1, 0.2), but the difference is not visible because of the normalization.

The above expressions simplify in the limit that $c_{rs} \rightarrow 0$ at fixed $c_s/c_p = c_{rp}/c_{rs}$:

$$\tilde{\xi}_c = \frac{1}{2} \rho_r c_{rs}^2 \frac{\tilde{\sigma}_{tc} + i \tilde{\sigma}_{nc} (c_s/c_p)^2}{1 - (c_s/c_p)^2}, \quad (5.21a)$$

$$\tilde{\zeta}_c = \frac{1}{2} \rho_r c_{rs}^2 \frac{-i \tilde{\sigma}_{tc} (c_s/c_p)^2 + \tilde{\sigma}_{nc}}{1 - (c_s/c_p)^2}. \quad (5.21b)$$

In this limit, the displacements (when normalized with the wavenumber) are proportional to c_{rs}^2 , in agreement with figure 5.2. In case the solid is close to incompressible ($c_s/c_p \rightarrow 0$), the displacements become $\tilde{\xi}_c = \sigma_{tc}/2G$ and $\tilde{\zeta}_c = \sigma_{nc}/2G$.

Resonances are also possible in the short-wave limit and they are especially strong for an elastic solid, cf. figure 5.3. The elastic resonances occur when the denominator of the expressions equals zero ($d_{sw} = 0$, cf. equation 5.20), which yields an expression that can be solved for c_{rs} for a given wave-speed ratio $c_p/c_s = c_{rs}/c_{rp}$. For the elastic solid with $\nu_{pr} = 0.45$ (as in figure 5.3), that ratio equals $c_p/c_s = \sqrt{\Pi/G} = \sqrt{2(1 - \nu_p)/(1 - 2\nu_p)} = 3.3$ and the equation $d_{sw} = 0$ is solved by $c_{rs} = c/c_s = 0.95$. Figure 5.3 (left) shows indeed a large coating response for $\delta_{r\lambda} \gg 1$ and $c_{rs} = 0.95$. The corresponding waves are denoted as Rayleigh waves (Rayleigh (1885), cf. the dispersion curves of Gad-el Hak et al. (1984)), which are surface waves that are well-known in the field of seismology.

The results for the long- and short-wave limits can be collapsed on a single curve when $|c_{rs}| \lesssim 0.2$, see figure 5.4. The surface displacements are proportional to $\rho_r c_{rs}^2$ in both limits, so similarity is observed when this factor is used for

normalization. The normalized surface displacements only depend on $\delta_{r\lambda}$, ϕ_G and ν_{pr} when the stresses $\tilde{\sigma}_{tc0}$ and $\tilde{\sigma}_{nc0}$ are fixed. The dependence on $\delta_{r\lambda}$ clearly reveals the long- and short-wave limits: the displacement is proportional to the coating thickness in the long-wave limit, whereas it is proportional to the wavelength in the short-wave limit. The peak response occurs at $\delta/\lambda \approx 0.33$, in agreement with other studies (Kulik et al., 2008; Kulik, 2012; Zhang et al., 2017).

Though the loss angle has a pronounced influence on the displacement when resonances are present (figure 5.3), it has a much smaller influence when resonances are absent (figure 5.4 left). The vertical displacement is slightly affected by ϕ_G in the long-wave limit, which results from the fact that $|\text{II}|$ changes with ϕ_G for the coating model that is used (see section 5.3.4).

The influence of the (real part of the) Poisson's ratio ν_{pr} is depicted in figure 5.4 (right). Note that ν_{pr} was varied over a small range (from 0.4 to 0.5), as some of the expressions used for the coating model are only valid when the material is close to incompressible (see section 5.3.4). The Poisson's ratio has a significant influence on the vertical displacement in the long-wave limit: when $\nu_{pr} \rightarrow 0.5$, the compressional-wave modulus $|\text{II}| \rightarrow \infty$, such that the vertical displacement approaches zero (cf. equation 5.19).

5.5 Coating deformation in turbulent channel flow

5.5.1 Viscous units

Since this study considers turbulent flow, viscous units are used for normalization:

$$\begin{aligned} \sigma^+ &= \frac{\sigma}{\rho_f u_\tau^2}, & k^+ &= \frac{k\nu}{u_\tau}, & c^+ &= \frac{c}{u_\tau}, \\ \omega^+ &= \frac{\omega\nu}{u_\tau^2} = k^+ c^+, & \xi^+ &= \frac{\xi u_\tau}{\nu}, & u^+ &= \frac{u}{u_\tau}. \end{aligned} \quad (5.22)$$

Note that the viscous units are based on the flow over a rigid wall; see also the definition of u_τ in section 5.3.1. It was shown in section 5.4.1 that the deformation by a single stress wave is fully specified with these dimensionless numbers: $\tilde{\sigma}_{tc0}$, $\tilde{\sigma}_{nc0}$, ρ_r , $\delta_{r\lambda}$, $|\omega_{rs}|$, ϕ_G and ν_{pr} . The following relations demonstrate the conversion between $\tilde{}$ and $^+$ normalization, as well as the computation of $\delta_{r\lambda}$ and $|\omega_{rs}|$ from viscous quantities:

$$\sigma^+ = (c^+)^2 \tilde{\sigma}, \quad \xi^+ = \frac{\tilde{\xi}}{k^+}, \quad u^+ = c^+ \tilde{u}, \quad \delta_{r\lambda} = \frac{\delta^+}{\lambda^+}, \quad |\omega_{rs}| = \frac{\omega^+ \delta^+}{|c_s^+|}. \quad (5.23)$$

When viscous units are used, the solution for a single stress wave is fully specified with 9 dimensionless numbers. Four dimensionless variables are required to specify the fluid-stress properties, namely σ_{tc0}^+ , σ_{nc0}^+ , c^+ and ω^+ , with the latter two related through $k^+ = \omega^+/c^+$. Note that these four variables are not independent, since the stresses σ_{tc0}^+ , σ_{nc0}^+ and the convection velocity c^+ depend on the frequency ω^+ , as explained in section 5.5.2. Five dimensionless variables are

required to specify five corresponding coating properties, namely ρ_r (density), δ^+ (thickness), $|c_s^+|$ (stiffness), ϕ_G (viscoelasticity) and ν_{pr} (compressibility). Later on, the coating softness $|c_s^+|^{-1}$ will sometimes be used instead of the coating stiffness $|c_s^+|$.

5.5.2 Turbulent surface stresses

Stress spectra and the assumption of spanwise homogeneity

This study employs the one-way coupling method, such that the turbulent flow stresses are not influenced by the coating deformation. Hence, it can be assumed that the coating is simply driven by the same stresses that the turbulent flow exerts on a rigid wall. Consider therefore a three-dimensional and time-dependent turbulent flow that is statistically homogeneous in the streamwise and spanwise directions, and statistically steady in time. Let $\sigma(x, y, t)$ denote a wall stress, where x represents the streamwise, y the spanwise and t the temporal coordinate. The fluctuations of σ can be quantified with a wavevector-frequency spectrum $\Phi_\sigma(k_x, k_y, \omega)$, with streamwise wavenumber k_x , spanwise wavenumber k_y and angular frequency ω (Hwang et al., 2009):

$$\Phi_\sigma(k_x, k_y, \omega) = E_\sigma(\omega)(c/\omega)^2 f_\sigma(\tilde{k}_x, \tilde{k}_y), \quad \tilde{k}_x = \frac{k_x c}{\omega}, \quad \tilde{k}_y = \frac{k_y c}{\omega}, \quad (5.24)$$

with one-sided point frequency spectrum $E_\sigma(\omega)$, convection velocity c , normalized dimensionless wavevector spectrum $f_\sigma(\tilde{k}_x, \tilde{k}_y)$ and dimensionless wavenumbers \tilde{k}_x and \tilde{k}_y . Integration of the spectrum yields the mean square stress, which is equivalent to the square of the root-mean-square (rms) stress:

$$\begin{aligned} \sigma_{\text{rms}}^2 &= \int_0^\infty \int_{-\infty}^\infty \int_{-\infty}^\infty \Phi_\sigma(k_x, k_y, \omega) dk_x dk_y d\omega \\ &= \underbrace{\int_{-\infty}^\infty \int_{-\infty}^\infty f_\sigma(\tilde{k}_x, \tilde{k}_y) d\tilde{k}_x d\tilde{k}_y}_{=1} \int_0^\infty E_\sigma(\omega) d\omega = \int_0^\infty E_\sigma(\omega) d\omega. \end{aligned} \quad (5.25)$$

Modelling of the turbulent surface stresses requires knowledge of the three-dimensional wavenumber-frequency spectra of the streamwise, spanwise and normal stress at the wall. Insufficient knowledge of these three-dimensional spectra for the streamwise and spanwise shear stress was a first important reason for the assumption of spanwise homogeneity. Section 5.5.2 shows that the spectra for turbulent channel flow were obtained from Hu et al. (2006), since that is - to our knowledge - one of the few references that also presents the shear stress spectra, although only as function of frequency without reference to the streamwise and/or spanwise wavenumber.

A second reason for the assumption of spanwise homogeneity is the observation that spanwise coherent modes ($k_y = 0$) are most energetic. Indeed, the wavevector spectrum $f_\sigma(\tilde{k}_x, \tilde{k}_y)$ for wall pressure typically peaks at $\tilde{k}_x = 1$ and

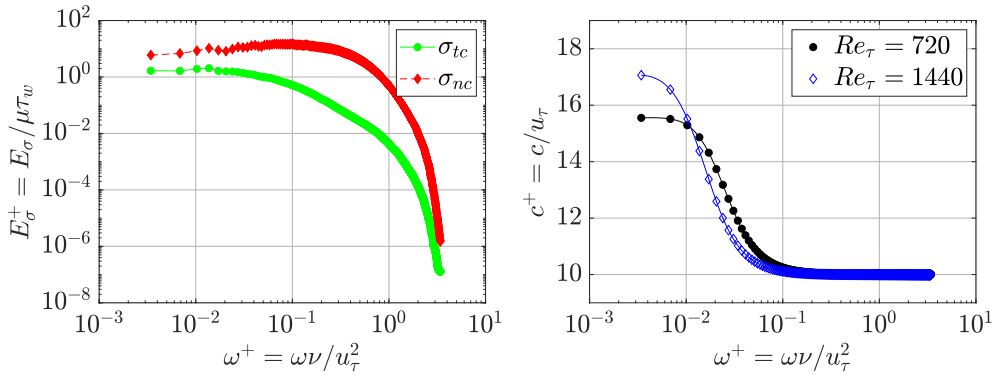


FIGURE 5.5: Point spectra of the turbulent surface stresses (*left*) and the convection velocity (*right*) as function of the angular frequency in viscous units. The spectra of the streamwise wall shear (σ_{tc}) and wall pressure (σ_{nc}) were obtained from a direct numerical simulation (DNS) by Hu et al. (2006) of a plane channel flow at $Re_\tau = 720$. The convection velocity for two different Reynolds numbers was calculated from a model that Del Álamo and Jiménez (2009) derived from DNS data.

$\tilde{k}_y = 0$ (Hwang et al., 2009), which corresponds with $k_x = \omega/c$ and $k_y = 0$. The same is true for turbulent boundary-layer flow over a compliant coating, as is confirmed in appendix C.2 with the wavevector spectrum of the vertical surface displacement that was obtained from the measurements described in section 5.6.1. A similar result was also reported for a direct numerical simulation (DNS) of turbulent channel flow over a compliant wall: the spanwise wavenumber spectra of wall pressure, wall displacement and wall velocity peak at the smallest spanwise wavenumber (Kim and Choi, 2014). In summary, the assumption of spanwise homogeneity was mainly motivated by insufficient knowledge of the three-dimensional shear-stress spectra and the predominant contribution of the spanwise homogeneous mode to the stress and displacement rms.

Stress amplitudes from stress spectra

While section 5.5.2 motivated the specific choice for one wavevector ($k_x = \omega/c$, $k_y = 0$), the frequency-dependent response still needs to be incorporated with use of frequency spectra. Figure 5.5 (left) therefore shows the point spectra of the streamwise wall shear stress and the wall pressure as function of the angular frequency at $Re_\tau = 720$. The data was obtained from direct numerical simulations by Hu et al. (2006) of turbulent flow in a plane channel with rigid walls. Their data was interpolated to an equispaced set of $N_m = 995$ frequencies ranging from $\omega^+ = 3.4 \cdot 10^{-3}$ to $\omega^+ = 3.4$ with $\Delta\omega^+ = 3.4 \cdot 10^{-3}$; each symbol in the figure corresponds with one mode. The root-mean-square (rms) values of the stresses can be obtained by integration of the frequency spectra (cf. equation 5.25), or analogously by summation of the discrete spectra (cf. equation C.23a):

$$\sigma_{tc,\text{rms}}^+ = \sqrt{\sum_{m=1}^{N_m} E_{\sigma_{tc},m}^+ \Delta\omega^+} = 0.41, \quad (5.26a)$$

$$\sigma_{nc,\text{rms}}^+ = \sqrt{\sum_{m=1}^{N_m} E_{\sigma_{nc},m}^+ \Delta\omega^+} = 2.38, \quad (5.26b)$$

where $E_{\sigma_{tc}}^+$ and $E_{\sigma_{nc}}^+$ are the point spectra for tangential and normal stress at the interface, respectively.

These spectra can be used to prescribe the amplitudes of the stress modes. Remember that each travelling wave mode has a complex amplitude $\sigma_{c,m}^+$ with two components:

$$\sigma_{tc,m}^+ = |\sigma_{tc,m}^+| e^{i\phi_{tc,m}}, \quad \sigma_{nc,m}^+ = |\sigma_{nc,m}^+| e^{i\phi_{nc,m}}. \quad (5.27)$$

Unless stated otherwise, the phases $\phi_{tc,m}$ and $\phi_{nc,m}$ are assumed to be zero, since their influence on the coating deformation is small (cf. section 5.5.4). The stress amplitudes can be obtained from the stress spectra as explained in appendix C.3 (cf. equation C.23a):

$$|\sigma_{tc,m}^+| = \sqrt{2E_{\sigma_{tc},m}^+ \Delta\omega^+}, \quad |\sigma_{nc,m}^+| = \sqrt{2E_{\sigma_{nc},m}^+ \Delta\omega^+}. \quad (5.28)$$

Convection velocity

The relation between wavenumber and angular frequency is given by $\omega_m = k_m c_m$, with c_m the mode-dependent convection velocity. The latter was estimated from a semi-empirical model proposed by Del Álamo and Jiménez (2009), which is based on a semi-empirical fit to DNS data at four different Reynolds numbers. The model requires four inputs, namely the Reynolds number (Re_τ), the spanwise wavelength of the mode (λ_y), the streamwise wavelength of the mode (λ_x) and the wall-normal location (z). The convection velocity at the wall ($z = 0$) was computed for two Reynolds numbers ($Re_\tau = 720$ and 1440) and a very large spanwise wavelength ($\lambda_y \rightarrow \infty$), since the present study does not include spanwise inhomogeneity. In this way, the convection velocity c_m was obtained as function of the (streamwise) wavenumber $k_m = 2\pi/\lambda_{x,m}$, and the dependence on ω_m then followed from $\omega_m = k_m c_m$.

Figure 5.5 (right) shows the convection velocity as function of the angular frequency in viscous units for two different Reynolds numbers. The modes with higher frequency (and lower wavelength) propagate at a speed of approximately 10 times the wall-friction velocity. This velocity agrees well with the highest frequencies and wavenumbers in the stress or velocity spectra at a comparable Reynolds number, namely $\omega^+ \approx 3$ (Hu et al., 2006) and $k^+ \approx 0.3$ (Abe et al., 2004), such that the estimated convection velocity $c^+ = \omega^+/k^+ \approx 10$. These high frequencies correspond with near-wall turbulence, as is apparent from the

scaling of the convection velocity in inner units. The modes with low frequency (and long wavelength) are associated with fluctuations in the outer layer. The corresponding convection velocity is larger than for the high frequencies, and it scales in outer units, which explains why c^+ increases with Re_τ at low ω^+ .

5.5.3 Coating deformation computation

The following overview summarizes how the surface displacements were computed; the same procedure also applies to the surface velocities:

$$\left\{ \begin{array}{l} \left[E_{\sigma_{tc},m}^+ \right] \\ \left[E_{\sigma_{nc},m}^+ \right] \end{array} \right\} \xrightarrow{\text{from spectra}} \left\{ \begin{array}{l} \left[\sigma_{tc,m}^+ \right] \\ \left[\sigma_{nc,m}^+ \right] \end{array} \right\} \xrightarrow{\text{from analytical solution}} \left\{ \begin{array}{l} \left[\xi_{c,m}^+ \right] \\ \left[\zeta_{c,m}^+ \right] \end{array} \right\} \xrightarrow{\text{for all modes}} \left\{ \begin{array}{l} \left[\xi_{c,\text{rms}}^+ \right] \\ \left[\zeta_{c,\text{rms}}^+ \right] \end{array} \right\}, \quad \left\{ \begin{array}{l} \left[E_{\xi_c}^+ \right] \\ \left[E_{\zeta_c}^+ \right] \end{array} \right\}. \quad (5.29)$$

For a single mode m with frequency ω_m^+ , the stress amplitudes were obtained from the stress spectra (section 5.5.2), the convection velocity from a semi-empirical model (section 5.5.2), and the surface displacements and velocities from the analytical solution (section 5.4.1). This procedure was followed for all N_m modes, after which the rms-values and the point spectra were computed using equation C.23a:

$$\xi_{c,\text{rms}}^+ = \sqrt{\sum_{m=1}^{N_m} \frac{1}{2} |\xi_{c,m}^+|^2}, \quad E_{\xi_c,m}^+ = \frac{\frac{1}{2} |\xi_{c,m}^+|^2}{\Delta\omega^+}, \quad (5.30)$$

and similarly for ζ_c , u_c and w_c .

Before considering the influence of the coating properties in detail, we derive a simplified equation for the rms-values of the surface displacements in the long-wave, low-frequency limit. Equation 5.19 reads in viscous units as:

$$\xi_c^+ = \frac{\delta^+}{G^+} \sigma_{tc}^+ = \frac{\rho_r \delta^+}{(c_s^+)^2} \sigma_{tc}^+, \quad \zeta_c^+ = \frac{\delta^+}{\Pi^+} \sigma_{nc}^+ = \frac{\rho_r \delta^+}{(c_p^+)^2} \sigma_{nc}^+. \quad (5.31)$$

Assuming that these relations hold for every mode m , the rms then follows from equation 5.30, e.g.

$$\left(\xi_{c,\text{rms}}^+ \right)^2 = \sum_{m=1}^{N_m} \frac{1}{2} |\xi_{c,m}^+|^2 = \left(\frac{\delta^+}{|G^+|} \right)^2 \sum_{m=1}^{N_m} \frac{1}{2} |\sigma_{tc,m}^+|^2 = \left(\frac{\delta^+}{|G^+|} \sigma_{tc,\text{rms}}^+ \right)^2. \quad (5.32)$$

Hence, the rms-values for ξ_c and ζ_c can be easily derived from the rms-values of σ_{tc} and σ_{nc} :

$$\xi_{c,\text{rms}}^+ = \frac{\sigma_{tc,\text{rms}}^+}{|G^+|} \delta^+ = \frac{\rho_r \delta^+}{|c_s^+|^2} \sigma_{tc,\text{rms}}^+, \quad \zeta_{c,\text{rms}}^+ = \frac{\sigma_{nc,\text{rms}}^+}{|\Pi^+|} \delta^+ = \frac{\rho_r \delta^+}{|c_p^+|^2} \sigma_{nc,\text{rms}}^+. \quad (5.33)$$

The rms-values in the short-wave limit can be derived in a similar way from equations 5.20 and 5.30, but the resulting expressions are not so concise and therefore not reported here.

5.5.4 Influence of coating properties

Coating density

All analytical expressions are linear in $\rho_r = \rho_f/\rho_s$, such that the coating deformation increases linearly with the density ratio as long as the one-way coupling approach is accurate. This agrees with the finding that the wall response to pressure perturbations is much smaller for a low ratio between fluid density and solid density (Luhar et al., 2016). For high density ratios, two-way coupling starts to play a role and the dependence on ρ_r becomes non-trivial (Benschop and Breugem, 2017).

Coating softness and thickness

The influence of coating softness and thickness is considered simultaneously, because they are related through the parameter $\omega_{r,s}$. Figure 5.6 shows contour plots for $\xi_{c,rms}^+$, $\zeta_{c,rms}^+$, $u_{c,rms}^+$ and $w_{c,rms}^+$ as function of coating thickness δ^+ and softness $|c_s^+|^{-1}$. Note that all the axes are logarithmic, so the dependence on a wide range of parameters is displayed. Typically, the coating deformation increases with increasing thickness and softness.

There are three regions in the contour plots for which the computed coating deformation might not be very accurate. The *first* region is designated as the ‘instability region’: the fluid-structure interaction can lead to instabilities (such as travelling-wave flutter or static-divergence waves) when $U_\infty/|c_s|$ exceeds a critical value, with U_∞ the free-stream velocity in turbulent boundary-layer flow. According to experiments summarized in Gad-el Hak (2002), that critical value might depend on the coating thickness: when the coating became thicker, the critical value decreased from approximately 12 to 4 for static-divergence waves and from 4 to 1 for travelling-wave flutter. A theoretical analysis by Duncan (1986) for $\rho_f/\rho_s = 1$ yielded a critical value of $U_\infty/|c_s|$ that decreased from approximately 3 for thin coatings and/or high damping to 1 for thick coatings and/or low damping. Based on these numbers, the instability region can be identified with $U_\infty/|c_s| \gtrsim 2$. Note that the number 2 is nothing more than an estimate for the stability boundary, since the precise value depends on coating thickness and damping in a way yet to be determined. Duncan et al. (1985) showed that the criterion for the onset of instability is actually given by $U_\infty/|c_s| = \sqrt{K\rho_s/\rho_f}$ for a certain constant K , which is equivalent to $\rho_f U_\infty^2/\rho_s |c_s|^2 = K$. This allows the interpretation of the instability criterion as a critical ratio of a characteristic fluid stress $\rho_f U_\infty^2$ and a characteristic coating modulus $\rho_s |c_s|^2 = |G|$. Hence, it might be more appropriate to include the density ratio in the criterion: the instability region then becomes $\sqrt{\rho_r} U_\infty/|c_s| \gtrsim 2$. Assuming that these results also apply to the bulk velocity U_b in channel flow, then instabilities

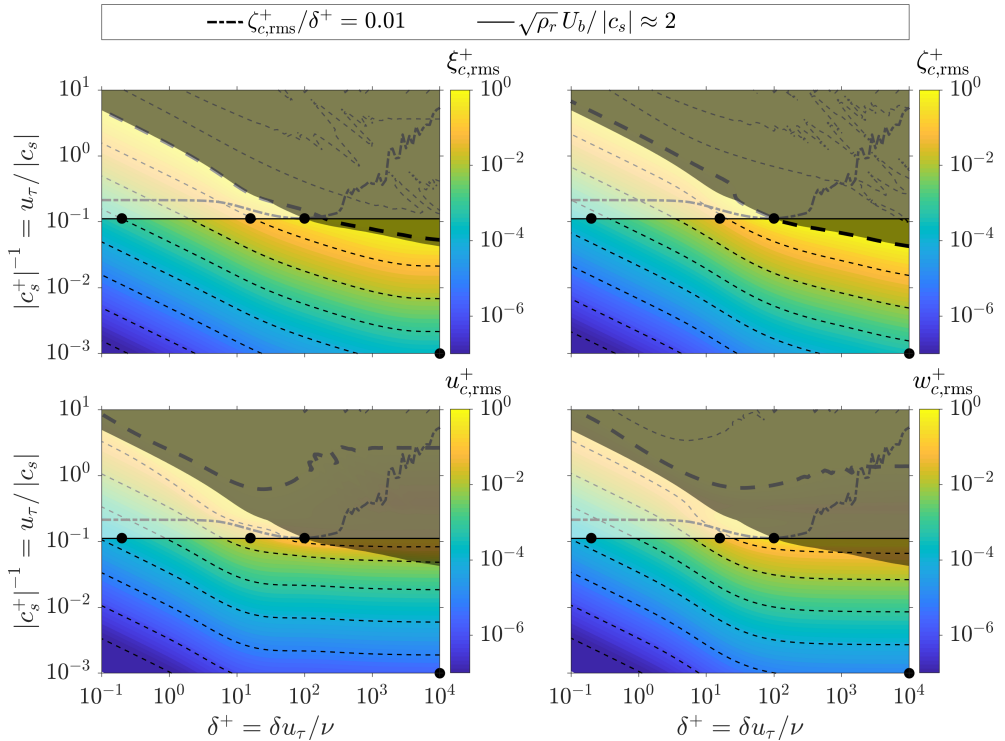


FIGURE 5.6: Contour plots of the root-mean-square displacement (*top, left and right*) and velocity (*bottom, left and right*) at the fluid-solid interface as function of coating thickness (δ^+) and coating softness ($|c_s^+|^{-1}$). The other parameters are $Re_\tau = 720$, $\rho_r = 1$, $\phi_G = 10^\circ$, $\nu_{pr} = 0.45$. The dashed lines are contour lines at integer powers of 10; the bold dashed line corresponds to 10^0 . The white transparent area indicates the ‘instability region’, while the black transparent area corresponds with the ‘interaction region’. The four dots indicate the parameter values for which subsequent figures show the point spectra (figure 5.8), a displacement vector field (5.9), the dependence on ϕ_G (5.10), the dependence on ν_{pr} (5.11) and the dependence on the phase angle of the stress waves (5.12).

are expected to arise when $\sqrt{\rho_r} U_b / |c_s| \approx 2$. For figure 5.6 this amounts to $u_\tau / |c_s| = |c_s^+|^{-1} \approx 0.11$, since $\rho_r = 1$ and $Re_\tau = 720$ corresponds with $u_\tau / U_b = 0.053$. The resulting instability region is marked with a white transparent area in figure 5.6.

The computed coating deformation is also not very reliable in a *second* region that is denoted as the ‘interaction region’: the significant coating deformation will influence the flow, which implies that the one-way coupling approach (as employed in this study) cannot be used reliably anymore. This region is differentiated by the requirement that at least one of the quantities $\{\xi_{c,rms}^+, \zeta_{c,rms}^+, u_{c,rms}^+, w_{c,rms}^+\} \gtrsim 1$, as indicated with a black transparent area in figure 5.6. Note that this interaction region corresponds quite well with the area

where resonances can be expected in the coating response. Figure 5.3 shows that resonances only occur when $|\omega_{rs}| = \omega^+ \delta^+ / |c_s^+| \gtrsim 1$ and $|c_{rs}| = (c/U_b) \cdot (U_b/|c_s|) \gtrsim 1$. The stress spectra of figure 5.5 indicate that the dominant frequencies are in the range $\omega^+ \lesssim 1$, while the maximum convection velocity is typically smaller than the bulk velocity ($c/U_b \lesssim 1$), such that the resonances will appear for sufficiently thick and soft coatings with $\delta^+ / |c_s^+| \gtrsim 1$ and $U_b / |c_s| \gtrsim 1$. That part of the contour plots indeed shows anomalous behaviour, which is for instance apparent from the changed spacing and the wiggling of the contour lines.

Finally, the model results cannot be trusted in a *third* region which is called the ‘nonlinear region’, since it is characterized by nonlinear material behaviour that is not well represented by the linear coating model used in this study. This region, which is quantified with the criterion $\zeta_{c,rms}^+ / \delta^+ = \zeta_{c,rms} / \delta \gtrsim 0.01$, is not sketched in figure 5.6 because it completely overlaps with the instability region and the interaction region.

The coating softness has a pronounced influence on the deformation outside these three unreliable regions: figure 5.6 shows that the displacements and velocities are approximately proportional to $1/|c_s^+|^2 \propto 1/|G|$, the inverse of the shear modulus. This is in line with the observation that the displacement for relatively stiff coatings scales with $\rho_r |c_{rs}|^2$ (cf. equations 5.19, 5.21 and figure 5.4). Using that the convection velocity is proportional to the bulk velocity ($c \propto U_b$), this dimensionless number can also be interpreted as the ratio of a fluid stress and a coating modulus:

$$\rho_r |c_{rs}|^2 = \frac{\rho_f}{\rho_s} \frac{c^2}{|c_s|^2} \propto \frac{\rho_f}{\rho_s} \frac{U_b^2}{|c_s|^2} = \frac{\rho_f U_b^2}{|G|}. \quad (5.34)$$

It thus follows that the surface displacements and velocities are linearly proportional to $\rho_f U_b^2 / |G|$, in agreement with Rosti and Brandt (2017).

The influence of the coating thickness reveals the long-wave and short-wave behaviour discussed in section 5.4.2. This is more clearly demonstrated in figure 5.7 (left), which shows the rms surface displacements as function of coating thickness δ^+ for a given coating softness $|c_s^+|^{-1}$, together with the results in the long-wave, low-frequency and short-wave limits. For very thin coatings, the displacements increase proportional to δ^+ (cf. equation 5.33), which is characteristic of the long-wave response. For very thick coatings, the displacements become independent of the coating thickness δ^+ , which identifies the short-wave limit. Section 5.6.3 derives criteria to check whether the coating response is in the long-wave limit, the short-wave limit, or in between.

The relative importance of the horizontal and vertical displacements and velocities can be clarified with figure 5.7 (right). The trends in that subfigure are typical for almost any value of $|c_s^+|^{-1}$. In particular, the horizontal and vertical displacements generally have a comparable magnitude. In the long-wave limit, the horizontal displacements can be larger than the vertical displacements, especially for materials that are close to incompressible. In the short-wave limit, the vertical displacement is larger ($\zeta_{c,rms}^+ = 0.20 > \xi_{c,rms}^+ = 0.097$), although

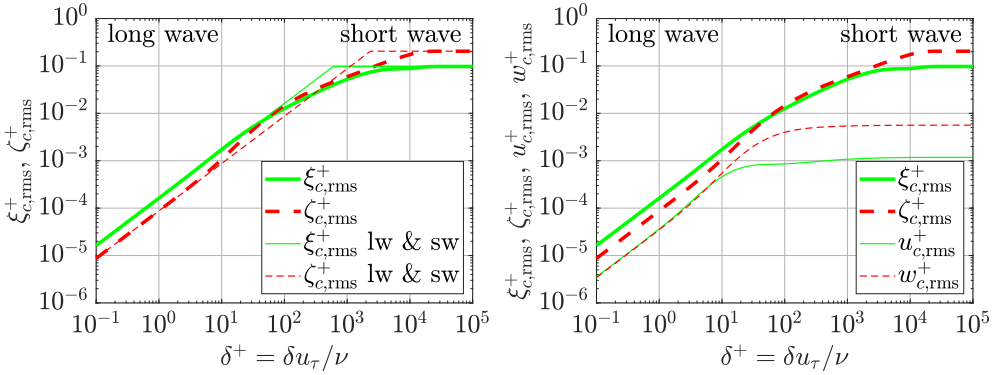


FIGURE 5.7: Root-mean-square surface displacements and velocities as function of coating thickness (δ^+) for $Re_\tau = 720$, $\rho_r = 1$, $|c_s^+|^{-1} = 0.02$, $\phi_G = 10^\circ$, $\nu_{pr} = 0.45$. *Left*: surface displacements, including the results in the long-wave, low-frequency (lw) and short-wave (sw) limits. *Right*: surface displacements and velocities.

the horizontal displacement still has a comparable magnitude. Similarly, the horizontal and vertical velocities are always comparable in magnitude, although the vertical component is clearly larger than the horizontal component in the short-wave limit ($u_{c,rms}^+ = 1.2 \cdot 10^{-3}$ versus $w_{c,rms}^+ = 5.6 \cdot 10^{-3}$).

In comparing the displacements and velocities (figure 5.7 (right)), two typical features can be noticed. First, the short-wave limit starts at a lower thickness for the velocities as compared to the displacements. Since the relations between the interface velocity and displacement for a certain mode m are given by $u_{c,m}^+ = i\omega_m^+ \xi_{c,m}^+$ and $w_{c,m}^+ = i\omega_m^+ \zeta_{c,m}^+$, the higher frequencies are more prominent for the velocity, while the high frequencies are also the first to enter the short-wave regime. As a second observation, the interface velocity is smaller than the interface displacement when both are normalized in viscous units, which is typical for most parameters, especially in the short-wave limit. In that limit, the largest response comes from the longest wave with the lowest frequency ($\omega^+ \ll 1$), such that the relations $u_{c,m}^+ = i\omega_m^+ \xi_{c,m}^+$ and $w_{c,m}^+ = i\omega_m^+ \zeta_{c,m}^+$ explain why $u_{c,rms}^+ \ll \xi_{c,rms}^+$ and $w_{c,rms}^+ \ll \zeta_{c,rms}^+$.

The type of coating response can be clarified with point spectra of the interface displacements and velocities, see figure 5.8. The displacement spectra (left, logarithmic axes) and velocity spectra (right, linear axes) are displayed for four different coatings, corresponding to the four dots in the contour plots of figure 5.6. For increasing coating thickness, the associated values of $\zeta_{c,rms}^+$ are $5.5 \cdot 10^{-4}$, $6.9 \cdot 10^{-2}$, 0.99 and $4.1 \cdot 10^{-4}$.

The first coating is very thin, which yields a characteristic long-wave response. The displacement spectra are the same as the stress spectra (figure 5.5), except for a mode-independent factor. The rms displacement is very well predicted by equation 5.33, which yields $\zeta_{c,rms}^+ = 5.5 \cdot 10^{-4}$ for $|c_p/c_s| = 3.3$. The velocity spectra are the displacement spectra multiplied with $(\omega^+)^2$, so the higher frequencies become more important.

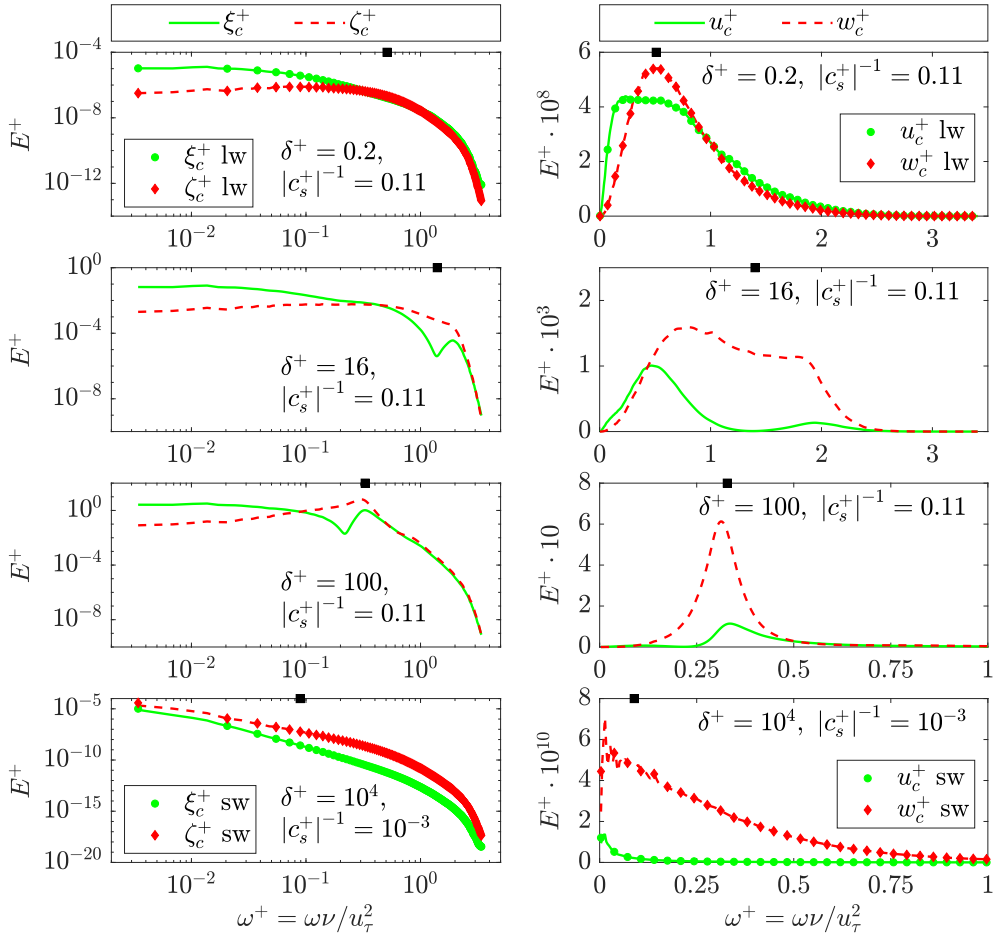


FIGURE 5.8: Point spectra of the surface displacements (*left*, logarithmic axes) and the surface velocities (*right*, linear axes) as function of the angular frequency in viscous units for four parameter sets (see title inside subfigures, corresponding to the four dots in figure 5.6). The other parameters are $Re_\tau = 720$, $\rho_r = 1$, $\phi_G = 10^\circ$, $\nu_{pr} = 0.45$. The square symbols on the top axes of the subfigures indicate the frequencies for which figure 5.9 shows a displacement vector field. The long-wave (lw) and short-wave (sw) results are included in the *top* and *bottom* figures, respectively.

The second coating has the same softness as the first one, but it is thicker by a factor 80. A resonance starts to appear at the higher frequencies, close to $\omega^+ = 2$, $|\omega_{rs}| = 3.5$, $|c_{rs}| = 1.1$ and $\delta_{r\lambda} = 0.51$. Note that Kim and Choi (2014) also report the appearance of a resonance in the frequency spectra of wall displacement and wall velocity. The resonance makes the long-wave expressions for the surface displacements inaccurate: equation 5.33 returns $\zeta_{c,rms}^+ = 4.4 \cdot 10^{-2}$, whereas the actual value is $\zeta_{c,rms}^+ = 6.9 \cdot 10^{-2}$. The third coating has again the same softness, but it is approximately 6 times thicker than the second coating. The resonance now appears at lower frequencies, around $\omega^+ = 0.3$, which corresponds with

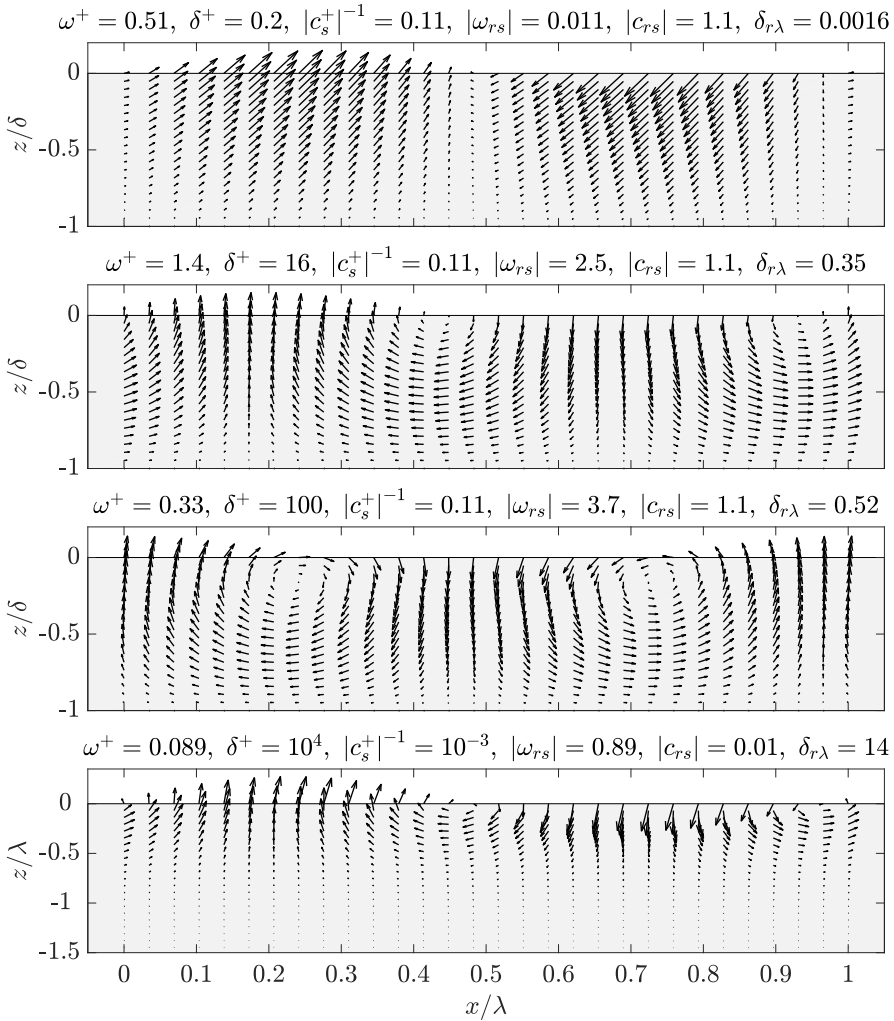


FIGURE 5.9: Displacement vector fields for four different sets of angular frequency (ω^+), coating thickness (δ^+) and coating softness ($|c_s^+|^{-1}$) as given in the titles. The other parameters are $Re_\tau = 720$, $\rho_r = 1$, $\phi_G = 10^\circ$, $\nu_{pr} = 0.45$. The coating thickness and softness correspond to the dots in the contour plots of figure 5.6. The frequencies are indicated with black squares in figure 5.8, whereas black squares in figures 5.2 and 5.3 provide the corresponding dimensionless parameters. The vertical axis is stretched (*top* figure) or compressed (*bottom* three figures) for clarity and compactness. The first three subfigures show the full coating thickness, whereas the last subfigure contains only the top part of the coating (namely 1.5λ , while the coating is 14λ thick).

$|\omega_{rs}| = 3.3$, $|c_{rs}| = 1.1$, $\delta_{r\lambda} = 0.48$. The long-wave prediction of $\zeta_{c,rms}^+ = 0.28$ is again inaccurate compared to $\zeta_{c,rms}^+ = 0.99$.

The fourth coating is very thick and very stiff, which yields a response that is characteristic for the short-wave limit. The displacements are proportional to the

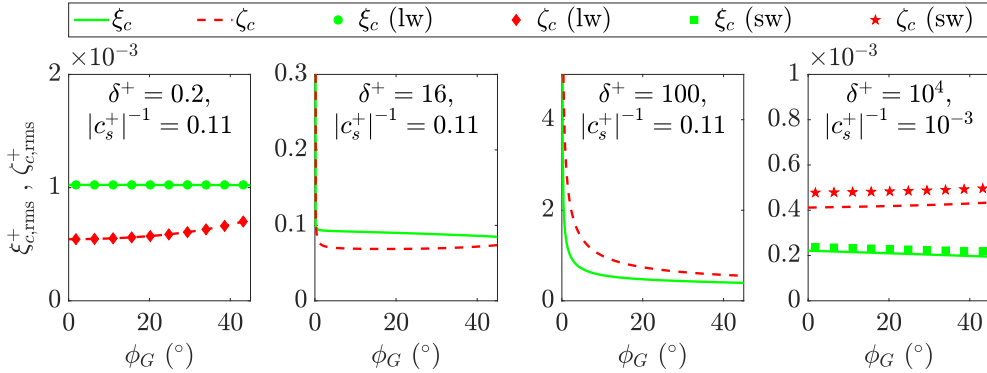


FIGURE 5.10: Horizontal and vertical surface displacement as function of the loss angle ϕ_G for four parameter sets (see title subfigures, corresponding to the four dots in figure 5.6). The other parameters are $Re_\tau = 720$, $\rho_r = 1$, $\nu_{pr} = 0.45$. The long-wave (lw) and short-wave (sw) results are included in the *left* and *right* figures, respectively.

wavelength, so the largest wavelengths (corresponding to the lowest frequencies) dominate the spectra. The spectra follow the short-wave predictions very well, except for a small difference at the first frequency, corresponding to $\delta_{r\lambda} = 0.35$, which is just on the border of the short-wave region (cf. figure 5.2).

Figure 5.9 shows displacement vector fields for the four coatings just considered. The vector fields belong to the parameters that are indicated with a square in figures 5.2, 5.3 (right) and 5.8. The selected frequencies belong to modes which have a large contribution to $w_{c,rms}^+$ (see figure 5.8). The first vector field corresponds with a low frequency and a long wavelength, as can be judged from the values of $|\omega_{rs}|$ and $\delta_{r\lambda}$ in the figure's title. The horizontal and vertical displacements are decoupled, although the ratio between both displacements stays the same due to the assumption of zero phase difference between the tangential and normal stresses.

The vector fields for the second and third coating belong to modes close to resonance, which is not only evident from figure 5.8, but also from figure 5.3 (right). The vector fields resemble vortices that are separated by half a wavelength. The parameters for the second coating are such that the horizontal surface displacement is close to zero, whereas the vertical displacement is significant.

The fourth vector field is characteristic for the short-wave response: the coating is much thicker than the wavelength, namely a factor 14 for this specific case. Note that only the top part of the coating is shown, i.e. 1.5λ of the 14λ in total. The deformation wave, which is only present near the surface, has a characteristic penetration depth on the order of one wavelength.

Viscoelasticity

Figure 5.10 displays how the surface displacement depends on the viscoelastic properties of the coating, the loss angle ϕ_G in particular. The four subfigures

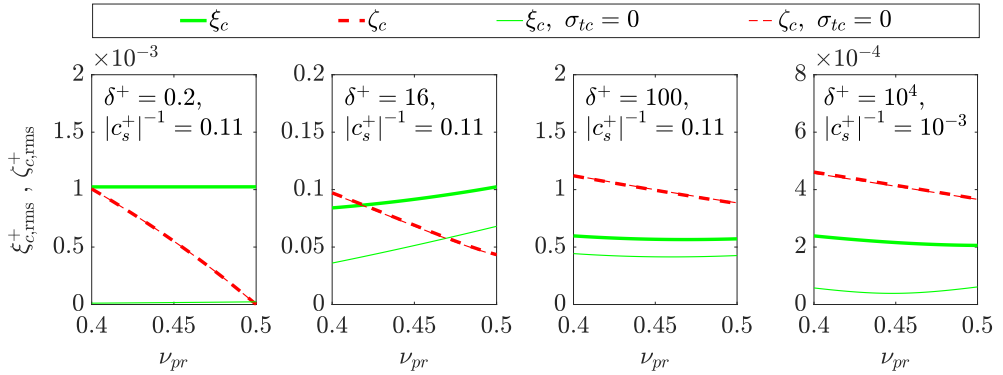


FIGURE 5.11: Horizontal and vertical surface displacement as function of the real part of the Poisson's ratio ν_{pr} for four parameter sets (see title subfigures, corresponding to the four dots in figure 5.6). The other parameters are $Re_\tau = 720$, $\rho_r = 1$, $\phi_G = 10^\circ$.

correspond with the four coatings that have been introduced above. The streamwise displacement of the first coating is not affected by ϕ_G , since $\xi_{c,rms}^+$ in the long-wave limit only depends on the modulus magnitude $|G|$, cf. equation 5.33. The vertical displacement is slightly affected by ϕ_G , as has been explained in the context of figure 5.4.

The deformation of the second and third coatings is quite sensitive to the loss angle when it is close to zero, which is due to the presence of resonances in the coating response (cf. figure 5.8). The displacements are very large for $\phi_G = 0^\circ$, which is attributed to the very strong resonances for an elastic coating (cf. figure 5.3 (left); Kulik (2012); Benschop and Breugem (2017)). The resonances are less pronounced for a viscoelastic solid (cf. figure 5.3), such that the surface displacements do not vary much for $\phi_G \gtrsim 10^\circ$.

The fourth coating is close to the short-wave limit, and the influence of the loss angle is small, in agreement with figure 5.4. The subfigure shows that the short-wave predictions are slightly different from the actual values for the reason that the first frequency (which dominates the response) is just on the border of the short-wave region, as has been remarked in the context of figure 5.8. Overall, the surface displacements are relatively insensitive to changes in the loss angle as long as resonances in the coating response are absent.

Compressibility

Figure 5.11 displays how the surface displacement depends on the compressibility of the coating, the real part of the Poisson's ratio ν_{pr} in particular. The four subfigures correspond again with the four coatings that have been introduced above. The figures also show the deformations that result in the absence of shear stress, as will be discussed in the next subsection. The streamwise displacement of the first coating is not affected by the Poisson's ratio, which is a consequence

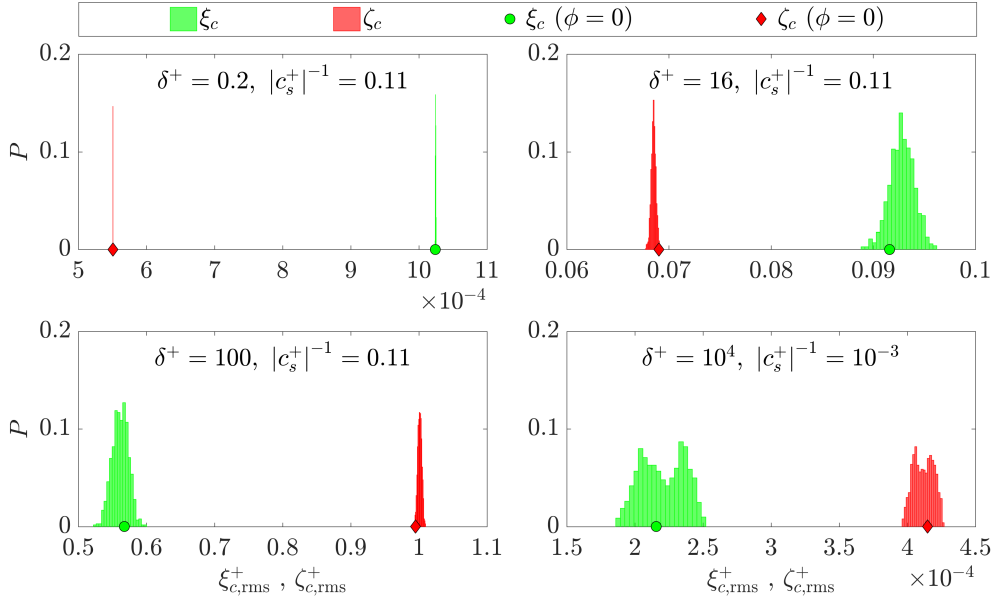


FIGURE 5.12: Influence of the phase angle of the stress waves on the root-mean-square value of the surface displacements. The displacements were calculated for 1000 sets of random angles for all the 995 shear and pressure waves. The results are shown as histograms with 20 bins for four parameter sets (see title subfigures, corresponding to the four dots in figure 5.6). P represents the probability to find a displacement within a certain bin; the sum of all the bar heights equals 1. The markers on the bottom axes correspond with stresses for which all phases are zero ($\phi_{tc,m} = 0 = \phi_{nc,m}$ for all m), as is assumed throughout the paper. The other parameters are $Re_\tau = 720$, $\rho_r = 1$, $\phi_G = 10^\circ$, $\nu_{pr} = 0.45$.

of the fact that $\xi_{c,rms}^+$ in the long-wave limit only depends on the shear modulus G , independent of ν_{pr} (cf. equation 5.33). In contrast, the Poisson's ratio has a significant influence on the vertical displacement: when $\nu_{pr} \rightarrow 0.5$, the compressional-wave modulus $|\Pi| \rightarrow \infty$, such that the vertical displacement approaches zero (cf. equation 5.33, figure 5.4). The influence of the Poisson's ratio is small for the other coatings: there is a slight change of $\xi_{c,rms}^+$, and $\zeta_{c,rms}^+$ typically decreases with increasing ν_{pr} , while it does not approach zero.

Influence of shear stress

To determine whether the shear stress has an important contribution to the surface deformation, figure 5.11 also shows the displacements that result in the absence of shear stress ($\sigma_{tc} = 0$). The influence of shear on the vertical displacement is marginal for all cases: the difference between the curves with and without shear stress is barely visible. The vertical displacement is thus predominantly determined by the normal stress, in agreement with similar observations by other researchers (Kulik, 2012; Zhang et al., 2017).

The influence of the shear stress on the horizontal displacement is, however, more pronounced: $\xi_{c,\text{rms}}^+$ decreases in absence of shear for all cases. The reduction is most substantial in the long-wave limit, i.e. for very thin and stiff coatings: the horizontal deformation is then solely driven by the shear stress (cf. equation 5.33), so $\xi_{c,\text{rms}}^+ = 0$ when shear is absent. For the other three cases shown in figure 5.11, the removal of shear results in a decrease of the horizontal displacement by a factor of approximately 1.7, 1.4 and 4.8.

Phase angle of stress waves

The stresses of the individual waves not only have an amplitude, but also a phase (cf. section 5.5.2). It has been noted in the context of equation 5.27 that the influence of these phases on the deformation is small, which is quantified here for the four coatings that have been considered above. The surface displacements were calculated for 1000 sets of random angles for all the 995 shear and pressure modes, and the results are shown in figure 5.12 as histograms of $\xi_{c,\text{rms}}^+$ and $\zeta_{c,\text{rms}}^+$ for the four parameter sets. There is practically no difference for the first coating, as the rms of the displacements only depends on the rms of the surface stresses (equation 5.33). There is some influence of the phase for the other coatings, especially for the very thick one, but the spreading is not huge since the order of magnitude of the surface displacements remains unchanged.

5.6 Coating deformation in turbulent boundary-layer flow

This section applies the presented model to turbulent boundary-layer flow in order to allow a comparison with recent experiments. The first subsection outlines the experiments, followed by a description of the analytical model in the second subsection, some additional remarks regarding the long-wave and short-wave coating response in the third subsection, and a comparison with the experiments in the last subsection.

5.6.1 Experiments²

The deformation of a compliant coating on a rigid wall underneath a turbulent boundary-layer flow was studied experimentally. Preliminary results were presented by Delfos et al. (2017) and Greidanus et al. (2017), whose work was continued to allow a comparison with the model proposed in this paper. Three coatings were produced in-house, applied to a rigid plate and tested in a water tunnel. Three quantities were measured, namely the flow velocity with planar particle image velocimetry (PIV, Adrian and Westerweel (2011)), the drag force on the plate with a force balance, and the vertical coating displacement with

²The experiments described in this section were performed by Greidanus et al. (2017) and Delfos et al. (2017).

TABLE 5.1: Properties of the turbulent boundary-layer flow in the experiments performed by Greidanus et al. (2017) and Delfos et al. (2017).

ρ_f (kg m^{-3})	ν ($\text{m}^2 \text{s}^{-1}$)	U_∞ (m s^{-1})	δ_{bl} (m)	u_τ (m s^{-1})	Re_δ	Re_τ	R_T
		0.87	0.059	0.035	$5.1 \cdot 10^4$	$2.1 \cdot 10^3$	83
998	$1.0 \cdot 10^{-6}$	to 5.39	to 0.045	to 0.19	to $2.4 \cdot 10^5$	to $8.5 \cdot 10^3$	to $3.0 \cdot 10^2$

high-speed background-oriented schlieren (BOS, Raffel (2015)). Below, we provide a short description of the water tunnel, the flow, the drag force, the three coatings, and the deformation measurements.

The water tunnel has an optically fully accessible test section that has a length of 2 m and an inlet with a cross-sectional area of $300 \times 300 \text{ mm}^2$. The top wall of the test section can be replaced to mount the test plates with a surface area of $1998 \times 297 \text{ mm}^2$. The PIV and BOS measurements were performed at 1.7 m downstream of the test section's entrance.

The flow properties are listed in table 5.1, e.g. the free-stream velocity U_∞ was varied from about 0.9 to 5.4 m/s. The velocity profiles, as measured by PIV, approximately satisfy $u/U_\infty = (z/\delta_{bl})^{1/8}$, with streamwise velocity u , the vertical distance to the surface z , and the boundary-layer thickness δ_{bl} (note the difference with the coating thickness δ). The momentum thickness θ was computed by integration of the velocity profiles, and the boundary-layer thickness then followed from the relation $\delta_{bl} = (45/4)\theta$ for velocity profiles with a power 1/8. The thus obtained boundary-layer thickness follows quite well the power law $\delta_{bl} = 0.057U_\infty^{-1/7}$, which was henceforth used to compute the boundary-layer thickness for a given free-stream velocity. From now on, the superscript $^\circ$ is used to denote quantities that are normalized with outer units (U_∞ and δ_{bl}):

$$\omega^\circ = \frac{\omega \delta_{bl}}{U_\infty}, \quad k^\circ = k \delta_{bl}, \quad c^\circ = \frac{c}{U_\infty}. \quad (5.35)$$

Drag measurements were performed both on smooth rigid plates and on coated plates. The force balance measured the total drag on the whole test plate, from which the plate-averaged shear stress $\langle \tau_w \rangle$ was obtained. The local shear stress τ_w (at the location of the PIV and BOS measurements) was estimated from $\tau_w = (6/7) \langle \tau_w \rangle$ (Greidanus et al., 2017), and the local wall friction velocity then followed from $u_\tau = \sqrt{\tau_w / \rho_f}$. A fit to the thus obtained shear velocity yields the power law $u_\tau = 0.041U_\infty^{0.91}$ for the smooth rigid wall. Like in the analytical model, viscous scaling is based on the shear velocity of the smooth-wall flow. Next, three different Reynolds numbers can be defined:

$$Re_\tau = \frac{\delta_{bl} u_\tau}{\nu}, \quad Re_\delta = \frac{\delta_{bl} U_\infty}{\nu}, \quad R_T = \frac{\delta_{bl} / U_\infty}{\nu / u_\tau^2} = \frac{Re_\tau^2}{Re_\delta}, \quad (5.36)$$

where R_T represents the ratio of the outer-layer-to-inner-layer timescale that

TABLE 5.2: Properties of the coatings employed in the experiments by Greidanus et al. (2017) and Delfos et al. (2017), together with the dimensionless numbers that the analytical model requires to predict the coating deformation.

Coating	ρ_s (kg m^{-3})	G_1 (kPa)	G_2 (kPa)	δ (mm)	$ c_s $ (m s^{-1})	ρ_r	δ^+	$ c_s^+ ^{-1}$	ϕ_G ($^\circ$)	ν_{pr}
1	862	1.38	0.50	5	1.31	1.16	$1.8 \cdot 10^2$ to $9.5 \cdot 10^2$	$2.7 \cdot 10^{-2}$ to $1.4 \cdot 10^{-1}$	20.0	0.499
2	864	6.11	0.38	5	2.66	1.16	$1.8 \cdot 10^2$ to $9.5 \cdot 10^2$	$1.3 \cdot 10^{-2}$ to $7.1 \cdot 10^{-2}$	3.52	0.499
3	866	14.59	0.80	5	4.11	1.15	$1.8 \cdot 10^2$ to $9.2 \cdot 10^2$	$8.5 \cdot 10^{-3}$ to $4.5 \cdot 10^{-2}$	3.14	0.499

appears later in the analytical model. Note that table 5.1 provides the range of the numerical values for the free-stream velocity, boundary-layer thickness, shear velocity and three Reynolds numbers.

The properties of the three coatings are given in table 5.2: all coatings have the same thickness of 5 mm and approximately the same mass density. In contrast, the moduli of the coatings are significantly different, with coating 1 being the softest and coating 3 the stiffest. The frequency-dependent shear modulus ($G = G_1 + iG_2$) of the three coatings was measured using a commercial rheometer (ARES-G2, TA Instruments) with a parallel plate geometry of 25 mm in diameter. Specifically, the storage modulus G_1 and the loss modulus G_2 were measured in a frequency range of $\omega = 0.1$ rad/s to $\omega = 100$ rad/s at 20 °C and 0.5% strain. The measurements were limited to 100 rad/s, which is the maximum frequency that the rheometer could reach. In theory, modulus values at higher frequencies can be obtained with use of the time-temperature superposition (TTS) principle. In practice, however, measurements below room temperature resulted in vapour condensation on the measurement facility and the samples, such that the obtained values were considered unreliable. The table lists the values at 100 rad/s, as that turned out to be the frequency closest to the most dominant frequency in the coating response. There is one exception: the loss properties at 100 rad/s for coating 1 are $G_2 = 0.20$ kPa and $\phi_G = 8.1^\circ$, while the table provides somewhat larger values, as is motivated in the context of the displacement spectra in section 5.6.4. While the shear modulus of the three coatings is on the order of kPa, the bulk modulus is on the order of GPa, such that the coatings are practically incompressible: $\nu_{pr} \approx 0.5$.

Small height variations of the optically transparent coating were measured with the background-oriented schlieren (BOS) method of Moisy et al. (2009), which they call a synthetic schlieren method. A high-speed camera was used for time-resolved measurements of the optical distortion of a random dot pattern,

placed behind the coating, due to refraction of light at the deforming coating interface. The displacement field of the dots was determined from digital image correlation (DIC, Adrian and Westerweel (2011)) between the deformed and the undeformed dot pattern. The dot displacements were related to the interface slope, and the vertical interface displacement was subsequently obtained from spatial integration. This method was applied at approximately 180×180 points within the field of view of size $100 \times 100 \text{ mm}^2$. The measurement signals contain 2000 time samples with a measurement frequency f , which was fixed at $f = 1200$ Hz for coating 1. It was increased in linear proportion to the free-stream velocity for coatings 2 and 3, namely from $f = 200$ Hz at $U_\infty = 0.87$ m/s to $f = 1240$ Hz at $U_\infty = 5.39$ m/s.

The long-wave coating deformation could not be reliably measured. Specifically, long waves result in displacement fields that are almost spatially uniform, whereas plate vibrations also result in such uniform fields. As independent measurements of the plate position were not performed, the distinction between long-wave coating deformations and plate vibrations could not be made. Therefore, coating deformation waves with a wavelength larger than the length of the field of view (i.e. $\lambda > \lambda_{\max} = 100$ mm) could not be quantified reliably.

Since long waves could not be accurately measured, the same is true for low frequencies. Specifically, the minimum frequency that can be measured relates to the maximum wavelength according to $\omega_{\min} = 2\pi c/\lambda_{\max}$ or $\omega_{\min}^o = 2\pi c^o/\lambda_{\max}^o$. Given that $\lambda_{\max}^o = \lambda_{\max}/\delta_{bl}$ increases from 1.7 to 2.2, and assuming that $c^o = c/U_\infty \approx 0.75$ (Delfos et al., 2017), it follows that ω_{\min}^o varies between 2.8 and 2.1. The low-frequency response ($\omega \lesssim \omega_{\min}$) is most likely attributed to non-advected features that could result from resonances or reflected waves associated with the finite length of the compliant wall (Zhang et al., 2017). Indeed, the response below ω_{\min}^o partially results from pronounced tunnel vibrations at $f = 5$ Hz (independent of flow velocity), which corresponds with a dimensionless frequency ω^o that decreases from 2.1 to 0.26 when the flow velocity increases.

The focus of the present study is on advected phenomena, like in the study by Zhang et al. (2017). For that reason, the measured surface displacement was filtered to exclude frequencies below ω_{\min}^o . First, the displacement point spectra were computed using the Fast Fourier Transform (FFT): the time signal was written as $\zeta(t) = \sum_m \zeta_m \exp(i\omega_m t)$, the amplitudes ζ_m were obtained from the FFT, and the point spectra followed from equation C.23a. Next, frequencies below ω_{\min}^o were removed from the spectra. To smooth the quite spiky spectra, a filtered time signal was reconstructed from an inverse FFT, this time signal was cut in 40 pieces of 50 time samples each, and a spectrum was computed for each piece using the FFT. Finally, the spectra were averaged over all pieces and all points within the field of view. For all coatings and flow velocities, the rms of the filtered data varied between 83% and 98% of the rms for the unfiltered data.

5.6.2 Analytical model

The analytical model requires the turbulent stress spectra, the convection velocity and the frequency dependent coating properties as input, as described below in more detail. Several models for the turbulent pressure spectra exist, as reviewed by Hwang et al. (2009). According to their review, the model by Goody (2004) provides the best overall prediction of the spectra. It is given by:

$$E_{\sigma_{nc}^+}^o = \frac{E_{\sigma_{nc}}(\omega)U_\infty}{\tau_w^2 \delta_{bl}} = \frac{C_2(\omega\delta_{bl}/U_\infty)^2}{[(\omega\delta_{bl}/U_\infty)^{0.75} + C_1]^{3.7} + [C_3(\omega\delta_{bl}/U_\infty)]^7}, \quad (5.37)$$

with model parameters $C_1 = 0.5$, $C_2 = 3.0$ and $C_3 = 1.1R_T^{-0.57}$. The spectrum is defined as $E_{\sigma_{nc}^+}^o = E_{\sigma_{nc}^+} U_\infty / \delta_{bl}$, which is the spectrum $E_{\sigma_{nc}^+}$ normalized in outer units, where $E_{\sigma_{nc}^+} = E_{\sigma_{nc}} / \tau_w^2$ represents the spectrum of σ_{nc}^+ . Note that $E_{\sigma_{nc}^+}^o$ depends on ω in the ratio $\omega\delta_{bl}/U_\infty = \omega^o$, which is the frequency normalized with a characteristic frequency of the outer layer. The ratio of C_1 to C_3 determines the size of the overlap range, which depends on the ratio R_T of the outer-layer-to-inner-layer timescale (cf. equation 5.36).

Figure 5.13 (left) displays the Goody spectrum at four different Reynolds numbers that are typical for the experiments. The spectra collapse for low frequencies because outer scaling is used, while inner scaling will collapse the spectra at high frequencies. The extent of the overlap range increases with increasing Reynolds number. Hwang et al. (2009) provide more information about the use of different scales to collapse the spectra in different frequency regions. The Goody spectrum at $Re_\tau = 720$ is very similar to the channel-flow spectrum of Hu et al. (2006) (figure 5.5), except that the latter does not include the very low frequencies for which the Goody spectrum exhibits a decay when $\omega \rightarrow 0$.

An important characteristic of the spectrum is its integral, which provides a measure of the root-mean-square (rms) of the fluctuations. Goody (2002) obtained a relation (their equation 8) that should describe the variation of the mean square pressure with R_T for the Goody spectrum. His relation, however, does not yield the numerical values that were reported in table 3 from his paper, which explains why we propose a slightly different relation. The Goody spectrum was integrated numerically for a range of R_T between 10 and 10^3 , using equation C.23b for logarithmically distributed frequencies in the range $\omega^o = 10^{-4}$ to $\omega^o = 10^4$. The resulting rms-values were fitted to the following curve:

$$(\sigma_{nc,rms}^+)^2 = 0.0309 + 0.745(\ln(R_T))^2, \quad (5.38)$$

which is the same relation as in Goody (2002), except for different coefficients. Given that R_T in the experiments varied between 83 and 300 (table 5.1), the corresponding pressure rms $\sigma_{nc,rms}^+$ ranges from 3.8 to 4.9.

Next to the pressure spectrum, the analytical model also requires a shear stress spectrum. To the authors' knowledge, an equivalent of the Goody spectrum for shear stress fluctuations does not exist. However, the contribution of the shear

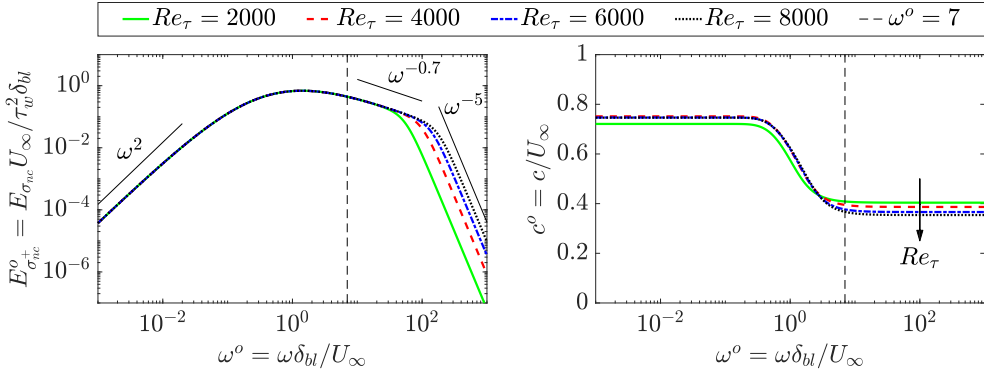


FIGURE 5.13: Pressure spectrum (*left*) and convection velocity (*right*) as function of frequency for four Reynolds numbers, using outer scaling. The pressure spectrum was obtained from the analytical relation provided by Goody (2004) for turbulent boundary-layer flow (equation 5.37). The convection velocity was calculated from a model that Del Álamo and Jiménez (2009) derived from DNS data of turbulent channel flow.

stress to the vertical displacement is presumably marginal (cf. section 5.5.4). To check that assumption, two computations were performed for all three coatings, namely one without shear stress ($E_{\sigma_{tc}} = 0$) and another with $E_{\sigma_{tc}} = 0.28E_{\sigma_{nc}}$. The factor 0.28 was chosen because that is the maximum of the ratio $E_{\sigma_{tc}}/E_{\sigma_{nc}}$ for the channel flow spectra shown in figure 5.5. The results (shown later) indicate that the contribution of shear to the vertical surface displacement is indeed marginal.

Another important ingredient of the analytical model is the convection velocity, which was estimated from the semi-empirical model proposed by Del Álamo and Jiménez (2009) (cf. section 5.5.2). That model prescribes how the convection velocity in a turbulent *channel* flow depends on the wavenumber and the Reynolds number. The model parameters were derived mostly from DNSs at $Re_\tau \approx 550$ and $Re_\tau \approx 950$. To the authors' knowledge, a comparable model for turbulent *boundary-layer* flow does not exist, which is why we assumed that the model by Del Álamo and Jiménez (2009) can also be used to estimate the convection velocity for turbulent boundary-layer flow in the range of $Re_\tau = 2100$ to 8500. Figure 5.13 (right) displays c/U_∞ for four different Reynolds numbers. The convection velocity scales with U_∞ at the lowest frequencies (except for $Re_\tau = 2000$), with U_∞ the characteristic velocity for the outer layer. In contrast, the highest frequencies scale in viscous units, with a characteristic velocity of $c^+ = 10$ (cf. figure 5.5), such that c/U_∞ decreases from 0.40 to 0.35 when the Reynolds number increases.

The model also requires the frequency-dependent coating properties, namely the shear and compressional-wave modulus. The previous section already explained that the complex shear modulus could only be measured for ω between 0.1 and 100 rad/s, which corresponds with $\omega^o = 6.7 \cdot 10^{-3}$ to 6.7 at $Re_\tau = 2.1 \cdot 10^3$

and $\omega^o = 8.4 \cdot 10^{-4}$ to 0.84 at $Re_\tau = 8.5 \cdot 10^3$. From figure 5.13 (left) we estimate that the frequencies in the range $\omega^o = 10^{-1}$ to 10^2 are most relevant, but the shear moduli data do not span this range. As it is unknown how the storage and loss moduli should be extrapolated to higher frequencies, the model calculations were performed with frequency-independent mechanical properties. Table 5.2 lists the dimensionless coating properties that the analytical model requires, namely ρ_r , δ^+ , $|c_s^+|^{-1}$, ϕ_G and ν_{pr} .

Finally, the numerical computations were performed in a way comparable to what has been described above. For each Reynolds number, the corresponding spectra $E_{\sigma_{tc}}(\omega^o)$ and $E_{\sigma_{nc}}(\omega^o)$, convection velocity $c(\omega^o)$, coating thickness δ^+ and coating softness $|c_s^+|^{-1}$ were calculated. A set of 1000 frequencies was distributed logarithmically over the range $\omega^o = 10^{-3}$ to 10^3 , and the response for each individual frequency was calculated in MAPLE. This procedure was followed for all Reynolds numbers for which experimental data were available, namely 18 Reynolds numbers for coating 1, 11 for coating 2 and 10 for coating 3.

5.6.3 Long-wave vs. short-wave coating response

This subsection derives criteria to check whether the expected coating response is in the long-wave limit, the short-wave limit, or in between, since this will facilitate the interpretation of the results that are presented in the next subsection. Based on figure 5.7, three regions can be distinguished in the coating response, dependent on the coating thickness:

$$\begin{aligned} \delta &\lesssim \delta_{lw}, & \text{long-wave coating response;} \\ \delta_{lw} &\lesssim \delta \lesssim \delta_{sw}, & \text{combined long- and short-wave coating response;} \\ \delta &\gtrsim \delta_{sw}, & \text{short-wave coating response.} \end{aligned} \quad (5.39)$$

The long-wave response is characterized by an rms displacement that linearly increases with the coating thickness, while the short-wave response yields a displacement that is independent of the coating thickness.

Two length-scales have been introduced to separate the three different coating responses: δ_{lw} is the maximum coating thickness for a long-wave response, and δ_{sw} is the minimum coating thickness for a short-wave response. Figures 5.2 and 5.4 are helpful to distinguish the long- and short-wave response for a *single* travelling stress wave: $\delta_{r,\lambda} = 0.33$ (equivalent to $k\delta = 2\pi\delta_{r,\lambda} \approx 2$) is taken as an approximate value to separate the long- and short-wave regions. However, the coating deformation in a turbulent flow is the result of the coating response to a *whole spectrum* of stress waves. The longest stress waves might induce a long-wave response, whereas the shortest waves could excite a short-wave response. In what follows, the coating response is denoted long-wave (short-wave) when all the relevant stress waves in the spectrum generate a long-wave (short-wave) response. The wording ‘relevant waves’ is used to denote those waves that have a significant contribution to the square of the stress rms, i.e. the integral of the spectrum.

The coating response is denoted ‘long-wave’ when all the relevant stress waves in the spectrum generate a long-wave response. In other words, we require that $k\delta \lesssim 2$ for all wave modes, which is guaranteed when the shortest wave (or highest wavenumber and frequency) satisfies this requirement. For the highest frequencies, the pressure spectrum scales in inner units and it decays quickly with $(\omega^+)^{-5}$ (Goody, 2004). An estimate for the highest relevant frequency is $\omega_{\max}^+ \approx 2$ (cf. the spectrum in figure 5.5). The corresponding convection velocity is $c^+ = 10$, such that $k_{\max}^+ \approx 2/10$. The relation $k\delta = k^+\delta^+ \lesssim 2$ applied to k_{\max}^+ yields the following long-wave criterion:

$$\frac{\delta u_\tau}{\nu} = \delta^+ \lesssim 10 \quad \text{or} \quad \delta \lesssim \delta_{lw} = 10 \frac{\nu}{u_\tau}, \quad \text{long-wave coating response.} \quad (5.40)$$

The coating response is denoted ‘short-wave’ when all the relevant stress waves in the spectrum generate a short-wave response. In other words, we require that $k\delta \gtrsim 2$ for all wave modes, which is guaranteed when the longest wave (or lowest wavenumber and frequency) satisfies this requirement. For the lowest frequencies, the pressure spectrum scales in outer units and it rises as $(\omega^o)^2$ (Goody, 2004). An estimate for the lowest relevant frequency is $\omega_{\min}^o \approx 10^{-1}$ (cf. the spectrum in figure 5.13). The corresponding convection velocity is $c^o = 0.75$, such that $k_{\min}^o \approx 2/15$. The relation $k\delta = k^o\delta^o \gtrsim 2$ applied to k_{\min}^o yields the following short-wave criterion:

$$\frac{\delta}{\delta_{bl}} = \delta^o \gtrsim 15 \quad \text{or} \quad \delta \gtrsim \delta_{sw} = 15\delta_{bl}, \quad \text{short-wave coating response.} \quad (5.41)$$

These criteria can also be applied to channel flow. Figures 5.6 and 5.7 show that $\delta^+ \lesssim 10$ is a good estimate for the long-wave response as characterized by displacements that linearly increase with δ^+ . In case the half-channel height h is used instead of the boundary-layer thickness δ_{bl} , the short-wave criterion reads $\delta/h = \delta^+/h^+ \gtrsim 15$. Since $h^+ = hu_\tau/\nu = Re_\tau = 720$, the short-wave requirement becomes $\delta^+ \gtrsim 15Re_\tau = 10800$. Figures 5.6 and 5.7 show indeed that the displacements become independent of the coating thickness when $\delta^+ \gtrsim 10^4$.

Next, the above criteria are applied to the experiments reported in section 5.6.1. The coating thickness in inner units (δ^+) ranges from 180 to 950, while it varies in outer units between $\delta^o = 0.085$ and 0.11, such that the coating deformation in the experiments is neither a long-wave nor a short-wave response. A long-wave response at the highest flow velocity requires a coating that is about 100 times thinner, namely $\delta = \delta_{lw} = 0.053$ mm. In contrast, a short-wave response at the highest flow velocity is obtained when the coating is approximately 140 times thicker, namely $\delta = \delta_{sw} = 0.68$ m. This example illustrates that a long-wave response requires very thin coatings, whereas a short-wave response demands very thick coatings. The ratio of δ_{sw} and δ_{lw} increases with the Reynolds number:

$$\frac{\delta_{sw}}{\delta_{lw}} = 1.5Re_\tau, \quad (5.42)$$

with $\delta_{sw}/\delta_{lw} = 1.3 \cdot 10^4$ for the highest velocity in the experiments.

When $\delta_{lw} \lesssim \delta \lesssim \delta_{sw}$, the coating response is a combination of long-wave and short-wave behaviour: the lowest frequencies (or longest waves) in the spectrum induce a long-wave response, whereas the highest frequencies (or shortest waves) excite a short-wave response. For the experiments reported above, we want to distinguish the long- and short-wave parts of the spectrum with a criterion based on ω^o . Long- and short-wave behaviour is again separated by $k\delta = k^o\delta^o = 2$ or $\omega^o = k^o c^o = 2c^o/\delta^o$. As all three coatings have the same thickness, this relation yields a value for ω^o that only depends on the Reynolds number. Specifically, ω^o decreases from 9.5 at $Re_\tau = 2.1 \cdot 10^3$ to 6.6 at $Re_\tau = 8.5 \cdot 10^3$, and it follows quite well the power law $\omega^o = 70.6 Re_\tau^{-0.261}$. From now on, the value of $\omega^o = 7$ is taken as an approximate value to separate long- and short-wave scaling in the spectra, as indicated by a vertical line in figure 5.13 and other figures that follow.

5.6.4 Comparison experiments and analytical model

Figure 5.14 shows the experimentally measured root-mean-square (rms) of the vertical interface displacement ζ_c (normalized using viscous units) as function of the Reynolds number for the three coatings. The displacement increases with increasing Re_τ (or flow speed), in line with the experimental finding that tangential wall-displacement fluctuations increase with increasing Reynolds number (Srinivas and Kumaran, 2017). The surface displacement also increases with decreasing $|G|$ (or coating stiffness), in agreement with other studies (Kim and Choi, 2014; Rosti and Brandt, 2017). Coating 1, which is the softest coating, displays a sudden increase of the displacement around $U_\infty = 4.5$ m/s or $Re_\tau = 7500$, with a corresponding drag increase beyond that of a smooth plate (Greidanus et al., 2017). At $U_\infty = 4.5$ m/s, the rms of the vertical displacement is 2.4 viscous units, which agrees with the presumption that the two-way coupling becomes important when the rms displacement is on the order of a viscous wall unit. The speed of $U_\infty = 4.5$ m/s corresponds with $\sqrt{\rho_r} U_\infty / |c_s| = 3.7$, which is close to the values at which other researchers have found the onset of instabilities, namely $\sqrt{\rho_r} U_\infty / |c_s| \approx 1$ to 3 (Duncan, 1986) and $\sqrt{\rho_r} U_\infty / |c_s| \approx 1$ to 12 (Gad-el Hak, 2002).

Figure 5.14 also shows the rms displacement as obtained from the analytical model. Note that the figure plots $\zeta_{c,rms}^+$ for the experiments, but $0.35\zeta_{c,rms}^+$ for the model. The factor 0.35 was chosen to have a close match with the experimental data, which indicates that the present model seems not able to accurately predict the numerical value of the surface displacement. This should not be surprising, however, for several reasons. First, the model is restricted to spanwise-homogeneous and streamwise-travelling deformations. Second, the pressure spectra were not measured, so we cannot check whether the Goody spectrum is an accurate representation of the actual pressure fluctuations at the wall. Third, the convection velocity was estimated from a semi-empirical model based on channel flow data at relatively low Reynolds numbers; there is no guarantee that this model is also accurate for boundary-layer flow at higher

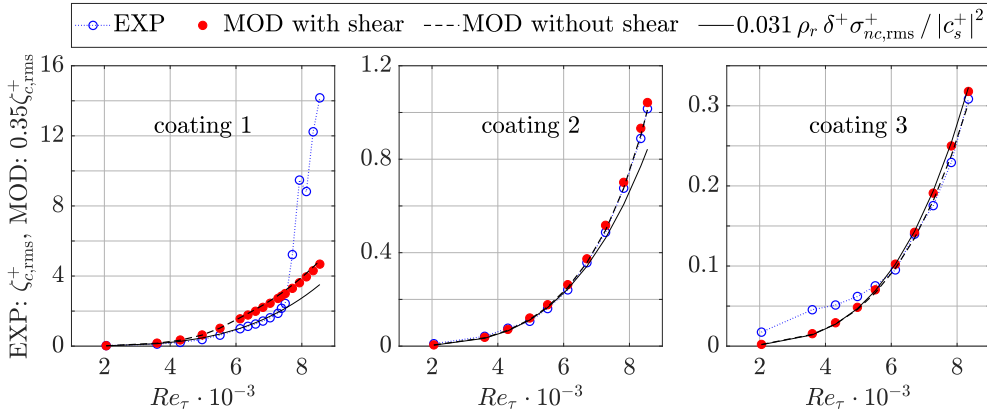


FIGURE 5.14: The measured and modelled vertical surface displacement as a function of the Reynolds number for three different coatings mentioned in table 5.2. As explained in the text, the figures display $\zeta_{c,rms}^+$ for the experiments and $0.35\zeta_{c,rms}^+$ for the model. Two model results are shown, one with shear ($E_{\sigma_{tc}} = 0.28E_{\sigma_{nc}}$) and another without shear ($E_{\sigma_{tc}} = 0$). The continuous line represents a simple analytical relation, with $\sigma_{nc,rms}^+$ estimated from equation 5.38. The experimental data were obtained from measurements performed by Greidanus et al. (2017) and Delfos et al. (2017).

Reynolds numbers. Finally, the frequency dependence of the shear modulus was neglected, as the available data was not sufficient to span the whole range of relevant flow frequencies. In summary, a perfect match between the analytical and experimental data cannot be expected because of the modelling assumptions and limited knowledge of the experimental conditions.

Figure 5.14 shows the analytical results both for cases with shear and without shear. Adding shear has only a marginal influence on the vertical displacement, in agreement with the results presented in section 5.5.4. The vertical displacement thus appears to be mainly driven by pressure fluctuations, which is why the analytical results in subsequent figures correspond with absence of shear, simply denoted as MOD. The model predicts quite well the increase of the displacement with flow speed and coating softness, especially for coatings 2 and 3. The prediction for coating 1 deviates from the experiments, but a closer agreement would be obtained when $0.23\zeta_{c,rms}^+$ for the model is compared with $\zeta_{c,rms}^+$ from the experiments, which shows that the factor 0.35 introduced above is not universal. There is also a slight deviation for coating 3 at the lower Reynolds numbers, which is most likely caused by insufficient accuracy to precisely measure the correspondingly small displacements.

The theoretical framework of the previous sections can be used to propose a scaling for the vertical surface displacement. In section 5.6.3 it was shown that the coating response to the complete spectrum of stress waves is neither long-wave nor short-wave, such that there is no preference for scaling with either the coating thickness δ or the wavelength λ . The coating thickness was used to scale the vertical surface displacement (as in figure 5.4), since that is a fixed

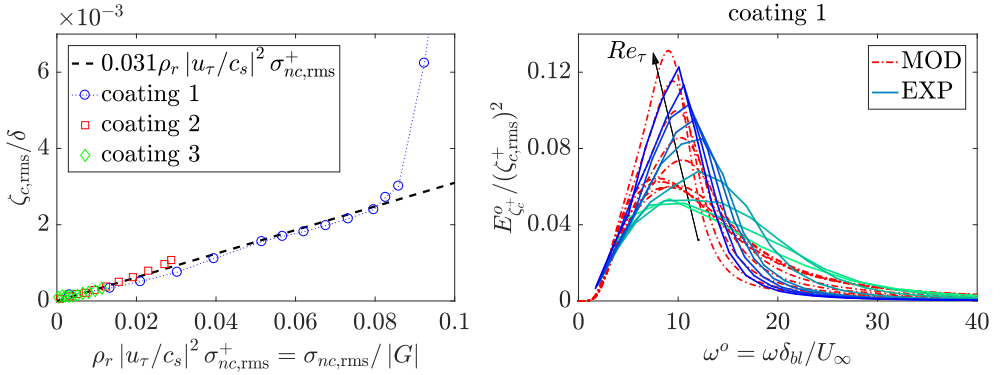


FIGURE 5.15: *Left*: the measured vertical surface displacement for all three coatings as function of the normalized stress, with $\sigma_{nc,rms}^+$ estimated from equation 5.38. *Right*: the measured and modelled point spectra of the vertical surface displacement as function of the angular frequency in outer units for coating 1. The figure shows 9 spectra in the one-way coupling regime, namely for Re_τ from $3.6 \cdot 10^3$ to $7.0 \cdot 10^3$. The spectra at the lowest Re_τ are not shown because of the difficulty to accurately measure very small displacements. The experimental data for both subfigures were obtained from measurements performed by Greidanus et al. (2017) and Delfos et al. (2017).

quantity, whereas the wavelength varies with the spectrum. In section 5.4.2 it was shown that the displacement in the long-wave and short-wave limits is proportional to $\rho_r c_{rs}^2 \tilde{\sigma} = \sigma/G$, while it was demonstrated in section 5.5.4 that the vertical displacement is primarily determined by the normal stress. Hence, the scaling $\zeta_{c,rms}/\delta = 0.031 \sigma_{nc,rms}/|G|$ is proposed, where the factor 0.031 is a fit parameter that captures the influence of all the unknown factors that have been mentioned above. This theoretical relation can be rewritten in viscous units as $\zeta_{c,rms}^+ = 0.031 \rho_r \delta^+ \sigma_{nc,rms}^+ / |c_s^+|^2$. Note that $\sigma_{nc,rms}^+$ is not available from the experiments, but it was estimated from equation 5.38.

Figure 5.14 demonstrates that this simple analytical relation predicts the experimental data quite well. Furthermore, figure 5.15 (left) confirms that it can be used to collapse the experimental data for the one-way coupling regime onto a single line. That figure also corroborates the assumption that the coatings behave as linear solids, since $\zeta_{c,rms}/\delta < 0.01$ for most measurements. Nonlinear solid behaviour might become relevant for coating 1 at the highest Reynolds numbers: the displacement reaches $\zeta_{c,rms}^+ = 14$ at $Re_\tau = 8.5 \cdot 10^3$, which corresponds with $\zeta_{c,rms}/\delta = 0.015$.

Figure 5.15 (right) shows the point spectra of the vertical surface displacement for coating 1, both for the experiments and the analytical model. The spectrum is defined as $E_{\zeta_c^+}^o = E_{\zeta_c^+} U_\infty / \delta_{bl}$, which is the spectrum $E_{\zeta_c^+}$ normalized in outer units, where $E_{\zeta_c^+} = E_{\zeta_c} u_\tau^2 / \nu^2$ represents the spectrum of ζ_c^+ . Each spectrum is normalized with $(\zeta_{c,rms}^+)^2$, which is the integral of the spectrum. The figure displays the normalized spectra for 9 different Reynolds numbers, ranging from $Re_\tau = 3.6 \cdot 10^3$ to $7.0 \cdot 10^3$. The spectra at the lowest Reynolds number are not

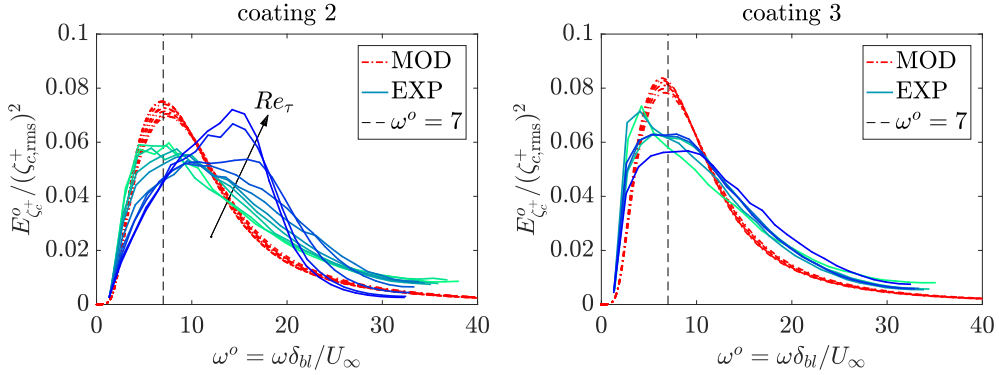


FIGURE 5.16: The measured and modelled point spectra of the vertical surface displacement as function of the angular frequency in outer units for coating 2 (*left*) and coating 3 (*right*). The left figure shows 10 spectra for Re_τ from $3.6 \cdot 10^3$ to $8.5 \cdot 10^3$. The right figure displays 6 spectra for Re_τ from $5.5 \cdot 10^3$ to $8.3 \cdot 10^3$. The spectra at the lowest Re_τ are not shown because of the difficulty to accurately measure very small displacements. The experimental data were obtained from measurements performed by Greidanus et al. (2017) and Delfos et al. (2017).

shown because of the difficulty to accurately measure very small displacements. Furthermore, the spectra for $Re_\tau \gtrsim 7 \cdot 10^3$ are also excluded, since the significant drag increase in this Reynolds-number range indicates the invalidity of the one-way coupling assumption.

A clear peak in the experimental spectra is observed: when the Reynolds number increases, the peak becomes narrower and higher, while it shifts from $\omega^o \approx 9.1$ to higher frequencies ($\omega^o \approx 12.4$) and then returns to $\omega^o \approx 10$. Note that these trends are quite well reproduced by the analytical model. Table 5.3 lists the parameters for which the spectra exhibit a peak. The values of $|\omega_{rs}| \approx 3$ and $|c_{rs}| \approx 1$ indicate that the narrowing peak corresponds to a resonance (cf. figure 5.3), which is significantly influenced by the loss properties of the material (cf. section 5.5.4). However, the viscoelastic properties of coating 1 are unknown for the relevant frequency range: $\omega^o = 10$ corresponds to a radial frequency between 330 rad/s ($Re_\tau = 3.6 \cdot 10^3$) and 1190 rad/s ($Re_\tau = 8.5 \cdot 10^3$), while the shear modulus could only be measured up to $\omega = 100$ rad/s. The shear loss modulus G_2 showed an increase near $\omega = 100$ rad/s, namely from 36 Pa at 10 rad/s to 197 Pa at 100 rad/s, with a corresponding increase of ϕ_G from 1.4° to 8.1° . Hence, one might expect that $\phi_G > 8.1^\circ$ for the frequency with the maximum coating response. To check the influence of the loss angle, the spectra according to the model were computed for $\phi_G = 8^\circ, 10^\circ, 15^\circ, 20^\circ, 25^\circ, 30^\circ, 40^\circ$. The magnitude of the peak response decreased with increasing loss angle (as expected from figure 5.3), but the shape of the spectra was more or less unchanged. A fairly good agreement between the modelled and measured spectra was obtained for $\phi_G = 20^\circ$, which is the value that was assumed for all frequencies.

Figure 5.16 shows the normalized displacement spectra of the experiments

TABLE 5.3: Parameters corresponding to the maxima in the point spectra of the vertical surface displacement. A parameter range is indicated, as the peak values vary with the Reynolds number. The Reynolds number range is the same as for the spectra shown in figures 5.15 (*right*) and 5.16. The experimental data were obtained from measurements performed by Greidanus et al. (2017) and Delfos et al. (2017).

Coating	$Re_\tau/10^3$	ω^o	c^o	$ \omega_{rs} $	$ c_{rs} $	$\delta_{r\lambda}$
1 MOD	3.6 - 7.0	7.9 - 10.4	0.37 - 0.40	0.99 - 3.1	0.53 - 1.2	0.30 - 0.47
2 MOD	3.6 - 8.5	6.9 - 7.6	0.36 - 0.40	0.45 - 1.7	0.26 - 0.73	0.28 - 0.37
3 MOD	5.5 - 8.3	6.3 - 6.6	0.37 - 0.38	0.50 - 0.89	0.28 - 0.47	0.28 - 0.30
1 EXP	3.6 - 7.0	9.1 - 12.4	0.75 - 0.80	1.1 - 3.4	1.0 - 2.5	0.18 - 0.27
2 EXP	3.6 - 8.5	4.4 - 15.8	0.70 - 0.80	0.35 - 3.2	0.46 - 1.6	0.09 - 0.35
3 EXP	5.5 - 8.3	4.1 - 9.1	0.72 - 0.79	0.32 - 1.3	0.54 - 1.0	0.09 - 0.20

and the model for coating 2 and 3 at various Reynolds numbers. The spectra collapse well for the model and reasonably well for the experiments. The model reproduces two important spectral properties, namely a decay for $\omega^o \gtrsim 15$ and a peak response around $\omega^o = 7$. The experimental spectra for coating 2 also peak around $\omega^o = 7$ for the lower Reynolds numbers, but the peak shifts to approximately $\omega^o = 15$ for the three highest Reynolds numbers. This might be an indication of fluid-structure interaction, as the vertical surface displacement is close to $\zeta_{c,rms}^+ = 1$. The experimental spectra for coating 3 also exhibit a peak for $\omega^o \approx 7$ at the highest Reynolds numbers. The unfiltered spectra do not show a clear peak for the lower Reynolds numbers, so the peak around $\omega^o = 4$ in the filtered spectra results from the removal of the low frequencies by the filtering procedure explained in section 5.6.1. Note that Zhang et al. (2017) have also found a large response for $\omega h/U_0 \lesssim 4$ (channel half-height h , channel centreline velocity U_0), which they attribute to non-advected features with nearly zero phase speed.

Figure 5.17 shows the point spectra for coatings 1 and 3 on a logarithmic scale, which is useful to investigate the scaling of the spectra. Long-wave scaling applies for $\omega^o \lesssim 7$ (cf. section 5.6.3), and the relevant length scale is the coating thickness δ , independent of the frequency. As a result, the stress and displacement spectra should exhibit the same scaling with frequency. Indeed, the modelled stress and displacement spectra both scale with ω^2 for $\omega^o \lesssim 10^{-2}$ (cf. figures 5.13 and 5.17). The scaling is less clear for $10^{-2} \lesssim \omega^o \lesssim 7$, which is caused by the transition in the stress spectra from ω^2 to $\omega^{-0.7}$ scaling (figure 5.13), and the transition in the coating response from long-wave to short-wave behaviour (figure 5.4). Long-wave scaling of the experimental spectra could not be confirmed because of the difficulty to measure low frequencies (section 5.6.1).

Short-wave scaling appears when $\omega^o \gtrsim 7$, and the relevant length scale is the wavelength $\lambda \propto \omega^{-1}$. The scaling of the displacement spectra for mode m can

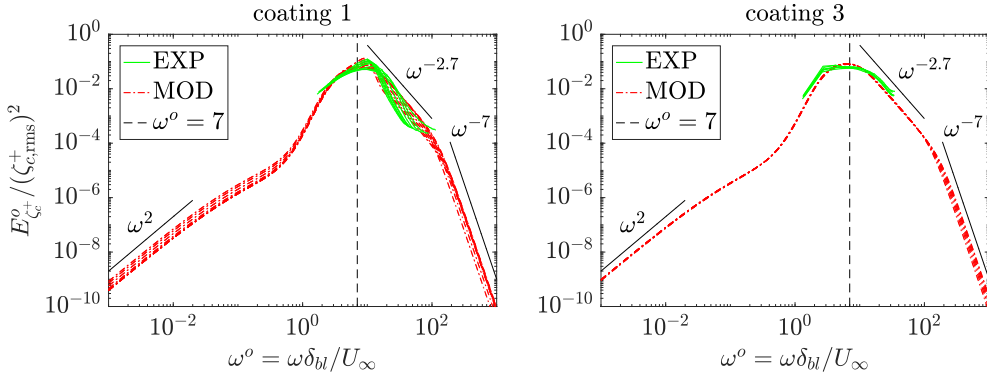


FIGURE 5.17: Scaling of the modelled point spectra of the vertical surface displacement for coating 1 (*left*) and coating 3 (*right*). The spectra are shown for the same range of Reynolds numbers as in figures 5.15 and 5.16. The experimental data were obtained from measurements performed by Greidanus et al. (2017) and Delfos et al. (2017).

be derived as follows:

$$E_{\zeta_{c,m}} \propto |\zeta_{c,m}|^2 \propto \left| \frac{\sigma_{nc,m}}{\omega} \right|^2 \propto \omega^{-2} E_{\sigma_{nc,m}}. \quad (5.43)$$

Hence, the stress spectra scalings of $\omega^{-0.7}$ and ω^{-5} (figure 5.13) become $\omega^{-2.7}$ and ω^{-7} for the displacement spectra of materials with frequency-independent mechanical properties, as is indeed confirmed by figure 5.17 for the modelled spectra. The experimental spectra for coating 1 show a more rapid decay than $\omega^{-2.7}$, which might result from the expected increase of the coating stiffness with increasing frequency. The spectral decay for coating 3 seems closer to $\omega^{-2.7}$, while the measurement frequency is too low to resolve the spectrum for $\omega^o \gtrsim 10^2$. The spectra for coating 3 are very similar in shape to the displacement spectrum of Zhang et al. (2017) (their figure 10), except that they kept the low frequencies that we filtered out. In addition, the frequency dependence of their spectrum was estimated to be approximately $\omega^{-2.4}$ for $4 \lesssim \omega h / U_0 \lesssim 20$, which is close to the $\omega^{-2.7}$ scaling shown in figure 5.17.

Table 5.3 lists the dimensionless parameters for which the modelled and measured spectra exhibit a peak response. The model typically predicts a maximum for ω^o around 7 and $\delta_r \lambda$ close to 0.33, in agreement with other researchers that also found a peak response for $\delta / \lambda \approx 0.33$ (Kulik et al., 2008; Kulik, 2012; Zhang et al., 2017). The modelled and measured convection velocities differ by a factor of 2, namely $c^o \approx 0.35 - 0.40$ (model) vs. $c^o \approx 0.70 - 0.80$ (experiments). A model for low-Reynolds-number turbulent channel flow was used to estimate the convection velocity in a turbulent boundary-layer flow at higher Reynolds numbers, which presumably explains this difference.

To check the influence of the convection velocity on the displacements, another approach was attempted, namely a frequency-independent convection velocity

(like Zhang et al. (2017)). Specifically, the displacement spectra were computed for $c^o = 0.75$ and compared with the spectra from figure 5.17. There was no influence on the lower frequencies ($\omega^o \lesssim 0.4$, for which the convection velocity was already $0.75 U_\infty$), but the response at the higher frequencies was significantly larger. For example, the maximum response for coating 3 occurred between $\omega^o = 13$ ($Re_\tau = 5.5 \cdot 10^3$) and 38 ($Re_\tau = 8.3 \cdot 10^3$), clearly contrasting with the experimental spectra. Also, a frequency-independent convection velocity does not capture the differences in scaling for the inner and the outer layer. Hence, the model of Del Álamo and Jiménez (2009) was still used for the model results presented here, as it is (to our knowledge) the best model that is currently available.

5.7 Conclusions and perspectives

We computed the deformation of a compliant coating in a turbulent flow for a wide range of parameters, using the one-way coupling approach. The surface stresses were expressed as a sum of streamwise-travelling waves that are homogeneous in the spanwise direction. The amplitude of each wave was determined from stress spectra obtained from DNSs of turbulent channel flow (Hu et al., 2006), or from an analytical expression for the pressure spectra in turbulent boundary-layer flow (Goody, 2004). The convection velocity of each wave was determined from a semi-empirical model derived from DNS data (Del Álamo and Jiménez, 2009). The linear, isotropic and viscoelastic coating with frequency-independent properties was assumed to be of infinite length, and attached at the bottom to a rigid wall. The coating deformation by a single travelling stress wave was computed analytically, and the total deformation followed from a summation over all the waves.

The present study systematically investigated how the coating deformation is influenced by five coating properties, namely density, stiffness, thickness, viscoelasticity and compressibility, as is summarized below:

- The surface displacements increase linearly with the ratio ρ_r of fluid and solid density, in agreement with the finding that the wall response is much smaller for a low density ratio (Luhar et al., 2016). For high density ratios, two-way coupling starts to play a role and the dependence on ρ_r becomes non-trivial (Benschop and Breugem, 2017).
- The influence of the coating stiffness can be characterized with the parameter $\rho_f U_b^2 / |G|$, which is proportional to the inverse of the shear modulus. For relatively stiff coatings, the surface displacements and velocities are linearly proportional to this ratio, in line with the finding that softer coatings yield an increase of the surface deformation (Kim and Choi, 2014; Rosti and Brandt, 2017). Care is required with the model predictions for soft coatings ($\rho_f U_b^2 / |G| \gtrsim 1$), since they could be inaccurate for three reasons: the large

coating deformations might yield fluid-structure interaction (two-way coupling), nonlinear solid behaviour and fluid-solid instabilities (Duncan, 1986; Gad-el Hak, 2002).

- Two limits can be distinguished regarding the influence of the coating thickness δ on the surface displacements. For very thin coatings ($\delta \lesssim \delta_{lw} = 10\nu/u_\tau$), the coating response is long-wave and the surface displacements linearly increase with the coating thickness. For very thick coatings ($\delta \gtrsim \delta_{sw}$ with $\delta_{sw} = 15\delta_{bl}$ for boundary-layer flow and $\delta_{sw} = 15h$ for channel flow), however, the coating response is short-wave and the surface displacements become independent of the coating thickness.
- The viscoelastic properties of the coating are quantified with a loss angle ϕ_G . The surface displacements increase considerably for $\phi_G \rightarrow 0$ when the other coating properties are such that the turbulent stresses excite resonances within the coating. The loss angle has only a minor effect when resonances are absent, in agreement with Kulik (2012) and Benschop and Breugem (2017).
- The real part of the Poisson's ratio ν_{pr} specifies the compressibility of the coating. The vertical surface displacement typically decreases when ν_{pr} approaches 0.5.

There are some other important findings regarding the influence of the shear stress, the horizontal surface displacement and the surface velocities. First, while the shear stress has a marginal influence on the *vertical* surface displacement, it significantly affects the *horizontal* surface displacement. Second, the horizontal surface displacement is similar in magnitude as the vertical surface displacement, as was also found by Rosti and Brandt (2017) for turbulent channel flow over a viscous hyper-elastic wall. Hence, the assumption that the coating surface only moves vertically - which has often been presumed in numerical simulations - seems not to have a strong foundation. Third, the interface velocity is typically smaller than the interface displacement when both quantities are normalized in viscous units. This is in line with the direct numerical simulations performed by Kim and Choi (2014) and Xia et al. (2017) for a compliant wall whose deformation had negligible influence on the mean flow drag (i.e. one-way coupling): both studies report a typical vertical displacement of $\zeta_{c,rms}^+ \approx 0.5$ with a much lower vertical velocity of $w_{c,rms}^+ \approx 0.05$. A few numerical studies neglected the surface displacement and only implemented the surface velocity as a boundary condition for the fluid flow, but this is not preferred since the dimensionless displacement is typically larger than the dimensionless velocity. Instead of comparing the effect of a compliant wall on the flow with blowing and suction (as suggested by Kulik (2012)), it seems that the compliant wall is more analogous to travelling waves of wall deformation.

The analytical model was compared with experiments by Delfos et al. (2017) and Greidanus et al. (2017). The model was useful in three ways: first, it predicted the order of magnitude of the surface displacements, although the

exact values were difficult to estimate because of limitations of the model (e.g. two-dimensionality) and the limited knowledge of the experimental conditions (e.g. the stress spectra, the frequency-dependent coating properties). Second, the model qualitatively reproduced the trend of the coating response, such as the increase of the coating displacement with the Reynolds number and with the coating softness. Third, the model provided a theoretical framework for the interpretation of the experimental results. For example, it was instrumental to propose a relation that collapses the measured displacements and to understand the scaling of the displacement spectra.

The two main assumptions of the presented model, namely spanwise homogeneity and one-way coupling, need some further discussion. The turbulent flow and the resulting coating deformation were assumed to be spanwise homogeneous. As a result, the presence of spanwise alternating regions of low and high momentum (streamwise streaks) is not captured by the model. Still, the model results are in qualitative agreement with the experimental data (cf. section 5.6.4), which suggests that the model captures the elementary physics. This might be explained with the observation that the spanwise coherent pressure motions and wall deformations are most energetic, see section 5.5.2 and appendix C.2. Though the model discards the spanwise structure of the overlying turbulent flow, it still accounts for the streamwise and wall-normal flow structure through the frequency-dependent stresses and convection velocity. Nonetheless, the extension to three-dimensional coating deformations is a logical next step towards a more accurate model. Although models for the wavenumber-frequency spectrum of wall pressure are available (e.g. Graham (1997); Hwang et al. (2009)), such models have still to be developed for streamwise and spanwise wall shear stress. In addition, the model of Del Álamo and Jiménez (2009) for the convection velocity should be extended to channel and boundary-layer flows at higher Reynolds numbers (e.g. Re_τ on the order of 5000).

A second important assumption of the current study is the one-way coupling: turbulent flow stresses deform the compliant coating, but these coating deformations have negligible influence on the turbulent flow. As a result, the presented model yields only limited insight into the influence of the coating deformations on the fluid mechanics. For instance, the model cannot be used to investigate the possible use of compliant coatings for turbulent drag reduction. Still, the results presented in this paper can be useful in different ways. First, they provide insight when the two-way coupling starts and how that is influenced by coating parameters like softness and thickness. The present study also provides some guidelines for modelling in the two-way coupling regime (cf. a previous paragraph in this section). For instance, the interface velocity is typically smaller than the interface displacement when both quantities are normalized with viscous units, which implies that a compliant wall cannot simply be modelled as time-dependent blowing/suction. Finally, models like the one presented here could be used to validate two-way coupling models: two-way coupling can typically be implemented with numerical models, but their reliability depends heavily on sufficient validation (Gad-el Hak, 2002).

The present work opens up a few interesting directions for future research. First, there are three regions in figure 5.6 that have quite some overlap, namely the regions where (a) the literature suggests that the fluid-structure interaction yields instabilities, (b) resonances occur in the coating response, and (c) the surface displacements are on the order of a viscous unit or larger. Future studies might investigate whether this overlap is a coincidence or not. Second, it seems still unclear how the coating thickness influences the onset of instabilities. Figure 5.6 reveals that a soft, thin coating ($\delta^+ = 10^2$, $|c_s^+|^{-1} = 0.11$) and a stiff, thick coating ($\delta^+ = 10^4$, $|c_s^+|^{-1} = 0.040$) can yield the same surface displacement ($\zeta_{c,rms}^+ = 1$), but the soft coating will exhibit resonant behaviour while the stiff coating displays a short-wave response. One could thus investigate whether the instabilities for very thick coatings are different as compared to thinner coatings. Finally, there remains a need for direct numerical simulations of turbulent flow over single-layer homogeneous viscoelastic coatings, as pointed out by Kulik et al. (2008). While the present work was restricted to one-way coupling, future studies should consider the two-way coupling regime in order to understand how the coating deformation influences the turbulent flow.

Acknowledgements

The research leading to these results has received funding from the European Union Seventh Framework Programme in the SEAFRONT project under grant agreement nr. 614034. The experimental part of this research was cofunded by InnosportNL.

Chapter 6

Numerical simulations of a deforming compliant layer

6.1 Introduction

Compliance of a solid object can be used advantageously in many situations. For instance, flapping flyers or swimmers rely on the flexibility of their wings or body to passively increase their efficiency (Ramananarivo et al., 2011; Kang et al., 2011; Paraz et al., 2016). Compliant coatings have been studied for laminar-to-turbulence transition delay, turbulent skin-friction drag reduction, noise control, vibration damping and aeroelastic flutter reduction (Gad-el Hak, 2002; Rao, 2003; Shorter, 2004; Zhou et al., 2016; Cunha-Filho et al., 2016). Elastomeric materials are used as vibration isolators, vibration dampers and antivibration mountings, and their loss tangent can be as high as 1.0 (Capps, 1983).

Compliant materials are not only able to suppress vibrations, but there are also some indications from experiments that they can suppress turbulence and reduce turbulent drag. Lee et al. (1993) studied the turbulent water flow over a single-layer viscoelastic compliant surface. They reported reductions of skin friction, streamwise turbulence intensity and Reynolds shear stress. An intermittent laminarization-like phenomenon was observed. Choi et al. (1997) investigated two compliant coatings in a turbulent water flow. They reported a maximum drag reduction of 7% for one coating, together with reduced streamwise velocity fluctuations.

Many analytical, experimental and numerical studies have appeared to better understand the interaction between a turbulent flow and a compliant wall, as reviewed in the introduction of chapter 5. In most numerical studies, the compliant walls were modelled as spring-damper-supported plates or membranes with vertical surface motion only, although a homogeneous viscoelastic layer is more appropriate to model the coatings that are typically used in experiments (Kulik

et al., 2008). Fischer and Ash (1974) wrote: “A finite-thickness elastic layer is far more desirable from a structural point of view (as compared with a flexible membrane), but it is much more complicated to analyze.” Another unrealistic modelling assumption is the absence of shear and horizontal displacements. For (nearly) incompressible material, the horizontal and vertical displacements can have a similar magnitude (Kulik et al., 2005), see also chapter 5 of this thesis. To better understand the drag-reducing capabilities of a more realistic compliant coating, an important next step is the direct numerical simulation (DNS) of a fully turbulent flow coupled to a single homogeneous layer of viscoelastic material attached to a rigid substrate.

The objective of the present chapter is to provide some literature, theory and simple examples to guide future numerical work regarding the interaction between a turbulent flow and a compliant layer. Our work is not yet in that stage that a fully-coupled DNS can be presented. Instead, some first steps in that direction are reported. Since we presume a fluid background, little attention is paid to the numerical simulation of fluid flows. Instead, we demonstrate possible techniques for the numerical computation of a deforming viscoelastic solid, and for the stable integration of coupled problems.

This chapter is organized as follows. Section 6.2 describes some of the literature regarding numerical simulations of fluid-structure interaction problems. Section 6.3 provides the theory and section 6.4 the numerical methods that are relevant to the numerical examples that follow in three subsequent sections. Section 6.5 considers a spanwise-homogeneous impulse forcing on a viscoelastic coating with the purpose of demonstrating the shear and compressional waves, thereby providing a qualitative understanding of the underlying dynamics. Section 6.6 investigates the deformation of a compliant wall due to spanwise-homogeneous streamwise-travelling stress waves; the description is more quantitative, since the numerically calculated coating deformation is compared with the analytical solution. The main focus is on the third example of the two-way coupling between an oscillatory flow and a compliant wall (section 6.7). The chapter closes with the conclusions and recommendations in section 6.8.

6.2 Literature

Many methods exist to solve the elastic wave equations. One can distinguish frequency-domain or time-domain methods. Alternatively, most methods can be classified as either boundary or domain methods. The boundary element method is likely the most well-known boundary method. However, this method is rarely employed for elastic wave problems in the time-domain (Liu et al., 2011). Domain methods are more generally used for elastic wave propagation. Examples include spectral, pseudo-spectral, finite-difference, finite-element and finite-volume techniques, many of which are reviewed by Carcione et al. (2002) and Virieux et al. (2011). The choice for any of these approaches is difficult and depends on the applications (Virieux et al., 2011).

Finite-difference time-domain (FDTD) methods, although very old, still remain very popular because of their efficiency and easy implementation when a uniform regular grid is used (Kampanis et al., 2008). Higher-order methods and compact schemes are frequently used. Derivatives on stretched meshes can be computed with either a transformed plane method (TPM) or physical space differencing (PSD) (Gaitonde et al., 1999).

In case the solid is incompressible, its volume remains constant. This isochoric constraint can be enforced in two ways, namely as near incompressibility using penalty methods or full incompressibility using Lagrange multiplier methods (Govindjee and Mihalic, 1998). Full incompressibility results in the appearance of an isotropic stress that can be identified as a static internal pressure in the solid (Ohayon and Chadwick, 1988; Skovoroda et al., 1994; Baek and Srinivasa, 2004). The stress tensor becomes a function of displacement and pressure, where the former satisfies the additional isochoric constraint also known as the incompressibility condition (Vavourakis and Polyzos, 2008).

To numerically solve a coupled problem, two approaches are generally distinguished: a monolithic and a partitioned approach (Degroote, 2010; Hou et al., 2012). The fluid and structure equations are solved simultaneously in a monolithic, and separately in a partitioned method. In turn, two partitioned approaches can be discerned, namely explicit, loose or weak coupling, and implicit or strong coupling (Degroote, 2010). In explicit coupling, the separate equations are solved for a fixed number of times (typically only once), such that stress and velocity equality at the interface is not guaranteed. In implicit coupling, however, the equations are solved iteratively in each time step till the equilibrium of interface stress and velocity is obtained.

It is not the purpose of this chapter to review all possible coupling methods, since there are many. We refer the reader to other resources, e.g. Matthies et al. (2006); Küttler and Wall (2008); Degroote (2010); Hou et al. (2012). The most popular coupling methods for partitioned approaches are fixed-point methods and interface Newton Krylov methods; the most basic and yet highly efficient approach is the fixed-point method with dynamic relaxation (Küttler and Wall, 2008). The dynamic relaxation factor can be obtained with the method usually denoted as Aitken relaxation or Aitken acceleration, which is highly valued because of its simplicity and efficiency (Borazjani et al., 2008; Küttler and Wall, 2008).

Two classes of time integration algorithms can be identified: Adams-Bashford or multi-step methods, and Runge-Kutta or multi-stage methods (Bailly and Bogey, 2006), see also the review by Butcher (2000). Alternatively, one can distinguish explicit and implicit time integration methods. Implicit time integration is beneficial for two reasons, namely to avoid time step restrictions and to assure dynamic equilibrium at each time step with use of iterations (Sluys, 1992). Second-order implicit time integration methods are often employed, but efficiency can be gained when higher-order implicit methods are used (van Zuijlen, 2006). A different time integration of the fluid and the solid phase can have unwanted effects (Degroote, 2010).

One of the challenges in numerical computations of fluid-structure interaction problems is the movement of the fluid/solid interface. Two methods can be distinguished to deal with such moving interfaces, namely an interface-tracking (moving-mesh) technique or an interface-capturing (nonmoving-mesh) technique (Takizawa and Tezduyar, 2016). Mesh movement is typically a costly operation, but it yields a more accurate representation of the interface as compared to nonmoving-mesh techniques. Complicated techniques are required when the topology of the simulation domain changes, e.g. due to contact between moving solid surfaces (Takizawa and Tezduyar, 2016).

A common moving-mesh approach is to use the arbitrary Lagrangian-Eulerian (ALE) formulation, in which the fluid grid does deform (as in a Lagrangian approach), but at an arbitrary grid velocity, such that the fluid quantities still flow through the mesh (as in an Eulerian approach) (De Boer, 2008; Degroote, 2010). Two comparable fixed grid techniques are the immersed boundary or embedded interface methods and the fictitious domain methods (Yang and Balaras, 2006; Zhao et al., 2008; Degroote, 2010).

In case the fluid or solid domain is not too complicated, a boundary conforming grid can be obtained with use of a coordinate transformation. The physical domain is then mapped onto a Cartesian computational domain. This technique has been used in combination with Chebyshev and Fourier spectral methods for elastic wave propagation (Tessmer and Kosloff, 1994), as well as for finite-difference viscoelastic wave modelling (Hestholm, 1999). The mapping approach has also been used for flow simulations over stationary wavy walls (De Angelis et al., 1997; Cherukat et al., 1998), traveling wavy walls (Shen et al., 2003; Nakanishi et al., 2012; Tomiyama and Fukagata, 2013), a deforming compliant wall (Xu et al., 2003; Kim and Choi, 2014) or a deforming air/water interface (Fulgosi et al., 2003; Zonta et al., 2015). In the latter case, the deformed physical domain was transformed to a Cartesian domain at each time step, and the governing equations were solved using a pseudospectral technique with Fourier series in the homogeneous directions and Chebyshev polynomials in the interface-normal direction.

Several grid transformations are possible. Hodges and Street (1999) used a boundary-orthogonal curvilinear moving grid to simulate steep waves. They do not recommend their method for small-amplitude waves, since it is a significant complication that is unnecessary when waves are not steep. A vertical linear stretch of the computational grid is an alternative that was used in most studies reported above, both for wave propagation and flow problems. Shen et al. (2003) found the algebraic mapping to be efficient in their simulations when $ka \lesssim 0.5$ (equivalent to $a/\lambda \lesssim 0.08$), with wave amplitude a , wavenumber k and wavelength λ . Hence, their technique is restricted to waves that are not steep.

The grid mapping introduces several nonlinear terms in the Laplacian operator (Shen et al., 2003). Those terms usually have a small contribution, unless the grid is severely skewed (De Angelis et al., 1997). They can be moved to the right-hand side of the equation, such that the left-hand side matrix keeps its nice properties. The resulting matrix system can be solved either in a single step

(De Angelis et al., 1997) or using a few iterations (Shen et al., 2003).

6.3 Theory

6.3.1 Structural viscoelasticity

Equations of motion

Consider a solid particle at a position given by the Lagrangian coordinate vectors \mathbf{x} in the undeformed medium and \mathbf{X} in the deformed medium. The displacement or deformation vector $\boldsymbol{\xi}$ with components ξ_i is then given by $\boldsymbol{\xi} = \mathbf{X} - \mathbf{x}$. The particle's velocity $u_i(\mathbf{x}, t)$ is the time derivative of its actual position: $u_i = \partial X_i / \partial t = \partial \xi_i / \partial t$. The equations of motion in the undeformed coordinates are (Chung, 2007):

$$\rho_s \frac{\partial u_i}{\partial t} = \frac{\partial \sigma_{ij}}{\partial x_j} + \rho_s f_i, \quad (6.1)$$

with stress tensor σ_{ij} and body force f_i . The mass density $\rho_s = \rho_s(\mathbf{x}, t)$ changes due to the deformations (Chung, 2007):

$$\rho_s = \frac{\rho_{s0}}{J}, \quad J = \det \left(\frac{\partial X_i}{\partial x_j} \right), \quad \frac{\partial X_i}{\partial x_j} = \delta_{ij} + \frac{\partial \xi_i}{\partial x_j}, \quad (6.2)$$

with ρ_{s0} the density of the undeformed medium, J the Jacobian, $\partial X_i / \partial x_j$ the deformation gradient tensor, and δ_{ij} the Kronecker delta function. The present study is restricted to displacement fields that slowly vary in space (Lautrup, 2011):

$$\left| \frac{\partial \xi_i(\mathbf{x}, t)}{\partial x_j} \right| \ll 1 \quad \text{for all } i, j, \mathbf{x}, t. \quad (6.3)$$

That allows us to ignore nonlinear deformations and density changes, such that ρ_s becomes a constant.

Constitutive equation

To close the structural equations, one needs a constitutive model that relates the stress tensor σ_{ij} to the strain tensor γ_{ij} , which is defined as:

$$\gamma_{ij} = \frac{1}{2} \left(\frac{\partial \xi_i}{\partial x_j} + \frac{\partial \xi_j}{\partial x_i} + \frac{\partial \xi_k}{\partial x_i} \frac{\partial \xi_k}{\partial x_j} \right). \quad (6.4)$$

As small deformations are considered, the nonlinear terms can be neglected, which yields Cauchy's (infinitesimal) strain tensor ϵ_{ij} :

$$\epsilon_{ij} = \frac{1}{2} \left(\frac{\partial \xi_i}{\partial x_j} + \frac{\partial \xi_j}{\partial x_i} \right). \quad (6.5)$$

For linear time-translation-invariant homogeneous isotropic media, the constitutive stress-strain relation can be written in integral form as (Robertsson et al., 1994; Carcione, 2015):

$$\sigma_{ij} = \dot{\psi}_\Lambda * \epsilon_{kk} \delta_{ij} + 2\dot{\psi}_G * \epsilon_{ij}, \quad (6.6)$$

where the dot denotes a time derivative and the asterisk symbolizes convolution:

$$f(t) * g(t) \equiv \int_{-\infty}^{\infty} f(\tau)g(t - \tau) d\tau. \quad (6.7)$$

The constitutive equation contains two relaxation functions, namely $\psi_\Lambda(t)$ for dilatation and $\psi_G(t)$ for shear. A relaxation function describes how stress decays as a function of time in response to a unit step in strain. In other words, the relaxation functions are step responses, while their time derivatives are impulse responses. The unit step is mathematically denoted by the Heaviside step function $H_s(t)$:

$$H_s(t) = \begin{cases} 0, & \text{if } t < 0. \\ 1, & \text{if } t > 0. \end{cases} \quad (6.8)$$

Assuming causality ($\psi_\Lambda(t) = 0$ and $\psi_G(t) = 0$ for $t < 0$), equation 6.6 expresses that the stress depends on the strain history.

For purely elastic media, the stress responds immediately to changes in strain. When the strain is a step function, so is the stress: the relaxation functions are simply $\psi_\Lambda = \Lambda H_s(t)$ and $\psi_G = G H_s(t)$, where the dilatational modulus Λ and the shear modulus G are the elastic Lamé constants. Since the time derivative of the unit step function is the Dirac delta function ($\dot{H}_s(t) = \delta(t)$) and using the convolution property $f(t) * \delta(t) = f(t)$, the above stress-strain relation reduces to:

$$\sigma_{ij} = \Lambda \epsilon_{kk} \delta_{ij} + 2G \epsilon_{ij}, \quad (6.9)$$

which is well-known from linear elasticity.

Viscoelastic wave equations

Equations 6.1, 6.5 and 6.6 can be combined into a single vector equation:

$$\rho_s \frac{\partial^2 \boldsymbol{\xi}}{\partial t^2} = \dot{\psi}_\Lambda * \nabla (\nabla \cdot \boldsymbol{\xi}) + \dot{\psi}_G * \left(\nabla^2 \boldsymbol{\xi} + \nabla (\nabla \cdot \boldsymbol{\xi}) \right) + \rho_s \mathbf{f}, \quad (6.10)$$

which is the viscoelastic wave equation for linear isotropic media. One generally distinguishes two wave types, namely compressional waves (also called primary or P-waves) and shear waves (also called secondary or S-waves). P-waves are described by an equation for the dilatation $\theta \equiv \nabla \cdot \boldsymbol{\xi} = \epsilon_{kk}$, while S-waves are identified by an equation for $\boldsymbol{\Gamma} \equiv \nabla \times \boldsymbol{\xi}$. When the divergence and curl operators are applied to the vector equation, the following evolution equations for the P-

and S-waves are obtained:

$$\text{P-waves: } \rho_s \frac{\partial^2 \theta}{\partial t^2} = \dot{\psi}_\Pi * \nabla^2 \theta + \rho_s \nabla \cdot \mathbf{f}, \quad (6.11a)$$

$$\text{S-waves: } \rho_s \frac{\partial^2 \mathbf{\Gamma}}{\partial t^2} = \dot{\psi}_G * \nabla^2 \mathbf{\Gamma} + \rho_s \nabla \times \mathbf{f}. \quad (6.11b)$$

Compressional waves are described by the relaxation function $\psi_\Pi \equiv \psi_\Lambda + 2\psi_G$, and shear waves by the relaxation function ψ_G (Yang et al., 2015). In linear elasticity, $\Pi = \Lambda + 2G$ is called the compressional-wave modulus, P-wave modulus or longitudinal bulk modulus (Tschoegl et al., 2002).

Complex moduli

The viscoelastic response of a linear time-translation-invariant homogeneous isotropic medium is fully characterized by two relaxation functions, but one might also provide the related complex moduli. First, the Fourier transform pair is defined for an arbitrary function $\psi(t)$ as:

$$\mathcal{F}\{\psi(t)\} = \Psi(\omega) = \int_{-\infty}^{+\infty} \psi(t) e^{-i\omega t} dt, \quad (6.12a)$$

$$\mathcal{F}^{-1}\{\Psi(\omega)\} = \psi(t) = \frac{1}{2\pi} \int_{-\infty}^{+\infty} \Psi(\omega) e^{i\omega t} d\omega. \quad (6.12b)$$

Let the symbol M for now denote one of the (visco)elastic moduli (e.g. Λ , G , Π) with the corresponding relaxation function $\psi_M(t)$. The complex modulus $M(\omega)$ is defined as the $i\omega$ -multiplied Fourier transform of the relaxation function (Tschoegl et al., 2002; Carcione, 2015):

$$M(\omega) \equiv \mathcal{F}\{\dot{\psi}_M\} = i\omega \mathcal{F}\{\psi_M\}. \quad (6.13)$$

The complex modulus can be written as a complex number with either amplitude and phase, or real and imaginary part:

$$M(\omega) = |M| e^{i\phi_M} = M_1 + iM_2, \quad (6.14a)$$

$$\eta_M(\omega) = \frac{M_2}{M_1} = \tan(\phi_M), \quad (6.14b)$$

with the frequency-dependent modulus magnitude $|M|$, loss angle ϕ_M , storage modulus M_1 , loss modulus M_2 and dissipation factor η_M . The storage modulus is a measure for stored strain energy, while the loss modulus is a measure for the rate of energy dissipation (Carcione, 2015). The loss angle ϕ_M represents the phase shift between stress and strain. The dissipation factor is also called ‘loss factor’ (Carfagni et al., 1998) or ‘loss tangent’ since it is the tangent of the loss angle (Pipkin, 1986).

6.3.2 Mechanical model

The mechanical properties of a medium are specified by its relaxation functions or the corresponding complex moduli. An overview of several models for these quantities can be found in the literature (Moczo and Kristek, 2005; Jansen, 2007; Carcione, 2015). Here, we immediately introduce the relaxation function and the complex modulus for the generalized mechanical model:

$$\psi_M(t) = \left[M_R + \sum_{l=1}^{N_l} M_l e^{-t/\tau_l} \right] H_s(t), \quad (6.15a)$$

$$M(\omega) = M_R + \sum_{l=1}^{N_l} \frac{i\omega\tau_l M_l}{1 + i\omega\tau_l}. \quad (6.15b)$$

The series expression in equation 6.15a is often referred to as a Prony series, where the equilibrium modulus M_R , relaxation strengths M_l and relaxation times τ_l are all positive real constants (Park and Schapery, 1999). The set $\{M_l, \tau_l; l = 1, \dots, N_l\}$ forms the discrete relaxation distribution or relaxation spectrum (Tschoegl, 1997), with N_l the number of relaxation mechanisms. Apart from the term M_R , the relaxation function is expressed as a series of exponentially decaying stresses, each with its own relaxation time and strength. The different timescales indicate that there are both fast and slow mechanisms or processes by which a solid medium responds to a strain unit step. To fit a Prony series to experimental data, one typically uses one or two timescales per decade in time or frequency (Blanch et al., 1995; Park and Schapery, 1999; Park, 2001).

To understand the behaviour of a mechanical model, one can consider the short-term and long-term responses (Moczo and Kristek, 2005). The equilibrium response is given by the relaxed modulus M_R , while the unrelaxed modulus M_U describes the instantaneous response:

$$M_R = \lim_{t \rightarrow \infty} \psi_M(t) = \lim_{\omega \rightarrow 0} M(\omega), \quad (6.16a)$$

$$M_U = \lim_{t \rightarrow 0} \psi_M(t) = \lim_{\omega \rightarrow \infty} M(\omega). \quad (6.16b)$$

The difference between both moduli is defined as the modulus defect $M_\delta \equiv M_U - M_R$. For the present model, the unrelaxed modulus is $M_U = M_R + \sum_l M_l$, and the modulus defect is $M_\delta = \sum_l M_l$.

The generalized model for a viscoelastic material comprises two important phenomena, namely attenuation and dispersion of waves. The attenuation results from the exponential decay of the relaxation function and the related imaginary part of the complex modulus. Dispersion refers to the characteristic that the propagation velocity of a wave depends on its wavelength and/or frequency, which is caused by the frequency dependence of the modulus. A solid typically becomes stiffer at higher frequencies.

Later on in this chapter we will restrict ourselves to a single relaxation mechanism, such that the complex modulus, the storage modulus and the loss modulus

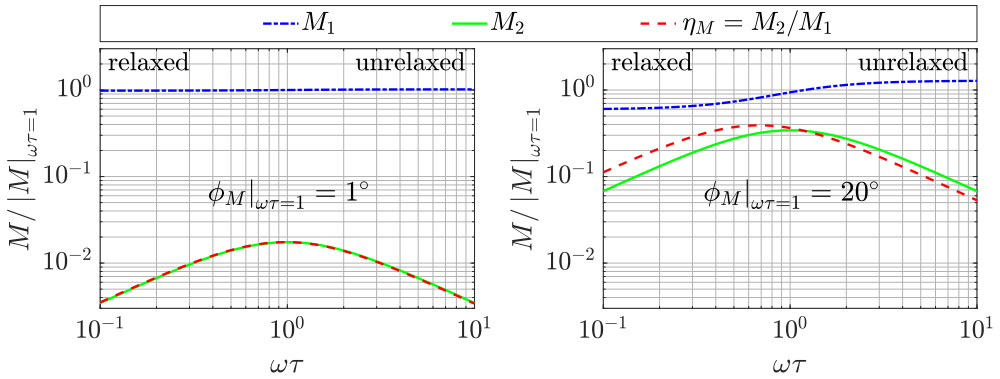


FIGURE 6.1: The storage modulus M_1 , loss modulus M_2 and loss tangent η_M as function of frequency according to the generalized mechanical model with one relaxation mechanism. The two subfigures correspond with an almost elastic solid (*left*) and a viscoelastic solid (*right*).

become:

$$M(\omega) = \frac{M_R + i\omega\tau M_U}{1 + i\omega\tau}, \quad (6.17a)$$

$$M_1(\omega) = \frac{M_R + (\omega\tau)^2 M_U}{1 + (\omega\tau)^2}, \quad (6.17b)$$

$$M_2(\omega) = \frac{(M_U - M_R)\omega\tau}{1 + (\omega\tau)^2}. \quad (6.17c)$$

We prefer to describe the mechanical properties of a medium with use of the modulus magnitude and loss angle at a specific frequency (as in chapter 5), from which the relaxed and unrelaxed moduli can be computed as follows. We take $\omega\tau = 1$ as a characteristic frequency, since the loss modulus M_2 peaks there. For $\omega\tau = 1$, the following relations can be derived:

$$\tan \phi_M = \frac{M_U - M_R}{M_U + M_R}, \quad M_R^2 + M_U^2 = 2|M|^2. \quad (6.18)$$

By inverting these equations, one obtains:

$$\frac{M_R}{M_U} = \frac{1 - \tan \phi_M}{1 + \tan \phi_M}, \quad M_R^2 = \frac{2|M|^2 (M_R/M_U)^2}{1 + (M_R/M_U)^2}, \quad M_U^2 = \frac{2|M|^2}{1 + (M_R/M_U)^2}, \quad (6.19)$$

where we require that $0 \leq \phi_M \leq 45^\circ$ with $M_U \geq 0$ and $M_R \geq 0$. These equations show how M_R and M_U can be computed from $|M|$ and ϕ_M at the characteristic frequency $\omega\tau = 1$.

Figure 6.1 shows the storage modulus, loss modulus and loss tangent as function of frequency for two loss angles and a single relaxation mechanism. When the loss angle is very small, the storage modulus is almost constant and the loss

modulus is very small. For larger loss angles, the storage modulus increases with increasing frequency: the solid becomes stiffer at higher frequencies, such that the unrelaxed modulus is larger than the relaxed modulus. The previously mentioned phenomena of dispersion and attenuation are apparent from the frequency dependence of the moduli and the nonzero loss modulus, respectively.

6.3.3 Memory stresses

Several alternative formulations of the elastic wave equations are in use for numerical implementation. Examples include the displacement, displacement-stress, displacement-velocity-stress and velocity-stress formulations (Moczo et al., 2007), depending on which variables are considered as the unknowns. The velocity-stress formulation is used particularly often; it is given by (cf. equations 6.1, 6.5, 6.6):

$$\frac{\partial u_i}{\partial t} = \frac{1}{\rho_s} \frac{\partial \sigma_{ij}}{\partial x_j} + f_i, \quad (6.20a)$$

$$\frac{\partial \sigma_{ij}}{\partial t} = \psi_\Lambda * \dot{\epsilon}_{kk} \delta_{ij} + 2\psi_G * \dot{\epsilon}_{ij}, \quad (6.20b)$$

$$\dot{\epsilon}_{ij} = \frac{1}{2} \left(\frac{\partial u_i}{\partial x_j} + \frac{\partial u_j}{\partial x_i} \right). \quad (6.20c)$$

The sub- or superscripts s to indicate the solid phase are left out, except for the density. The above equations use the convolution to incorporate viscoelasticity. A direct numerical implementation of the convolution operator is however not efficient, since that would require the storage of the full strain history. The convolution can be eliminated at the cost of additional partial differential equations for the so-called memory variables, which yields in general a more memory-efficient numerical implementation.

Below, we derive the viscoelastic equations that use the memory variables. The approach is similar to that of Yang et al. (2015), although the notation is more compact. The generalized model (cf. equation 6.15) is used for all relaxation functions with the assumption that the compressional and shear deformations share the same set of relaxation time-scales τ_l , $l = 1, 2, \dots, N_l$. The viscoelastic equations require the time derivative of the relaxation functions; for the general model (equation 6.15) it is given by:

$$\begin{aligned} \dot{\psi}_M(t) &= \left[M_R + \sum_l M_l e^{-t/\tau_l} \right] \delta(t) + \sum_l \left(-\frac{1}{\tau_l} \right) M_l e^{-t/\tau_l} H_s(t) \\ &= \underbrace{M_U \delta(t)}_{\text{elastic}} + \underbrace{\sum_l \left(-\frac{1}{\tau_l} \right) M_l e^{-t/\tau_l} H_s(t)}_{\text{viscous}}. \end{aligned} \quad (6.21)$$

Using this result for $\dot{\psi}_\Lambda$ and $\dot{\psi}_G$, the evolution equation for the stress σ_{ij} becomes:

$$\begin{aligned} \frac{\partial \sigma_{ij}}{\partial t} = & \left[\Lambda_U \delta(t) + \sum_l \left(-\frac{1}{\tau_l} \right) \Lambda_l e^{-t/\tau_l} H_s(t) \right] * \dot{\epsilon}_{kk} \delta_{ij} + \\ & \left[2G_U \delta(t) + \sum_l \left(-\frac{1}{\tau_l} \right) 2G_l e^{-t/\tau_l} H_s(t) \right] * \dot{\epsilon}_{ij}. \end{aligned} \quad (6.22)$$

Because of the convolution property $\delta(t) * f(t) = f(t)$, the last relation can be rewritten as:

$$\frac{\partial \sigma_{ij}}{\partial t} = \frac{\partial}{\partial t} \left\{ \underbrace{\Lambda_U \epsilon_{kk} \delta_{ij} + 2G_U \epsilon_{ij}}_{\text{elastic stress}} + \underbrace{\sum_l r_{ijl}}_{\text{memory stress}} \right\}, \quad (6.23)$$

$$r_{ijl} = \Lambda_l \left(-\frac{1}{\tau_l} \right) e^{-t/\tau_l} H_s(t) * \epsilon_{kk} \delta_{ij} + 2G_l \left(-\frac{1}{\tau_l} \right) e^{-t/\tau_l} H_s(t) * \epsilon_{ij}, \quad (6.24)$$

where r_{ijl} are the memory variables, anelastic variables or memory stresses for the l th relaxation mechanism. The stress is now decomposed into an elastic and a memory stress. The latter depends on the strain history, as is apparent from the convolution that appears in its definition. Next, an evolution equation for the memory stresses is derived. To that purpose, the time derivative of r_{ijl} is computed, employing the convolution property $\partial(f * g)/\partial t = \dot{f} * g = f * \dot{g}$. Here, the derivative is applied to the first argument of the convolution. Reusing the definition of r_{ijl} , one can derive the following equation for \dot{r}_{ijl} :

$$\frac{\partial \dot{r}_{ijl}}{\partial t} = -\frac{1}{\tau_l} \left\{ \dot{r}_{ijl} + \Lambda_l \dot{\epsilon}_{kk} \delta_{ij} + 2G_l \dot{\epsilon}_{ij} \right\}. \quad (6.25)$$

A closed set of viscoelastic equations is thus obtained:

$$\frac{\partial u_i}{\partial t} = \frac{1}{\rho_s} \frac{\partial \sigma_{ij}}{\partial x_j} + f_i, \quad (6.26a)$$

$$\frac{\partial \sigma_{ij}}{\partial t} = \Lambda_U \dot{\epsilon}_{kk} \delta_{ij} + 2G_U \dot{\epsilon}_{ij} + \sum_l \dot{r}_{ijl}, \quad (6.26b)$$

$$\frac{\partial \dot{r}_{ijl}}{\partial t} = -\frac{1}{\tau_l} \left\{ \dot{r}_{ijl} + \Lambda_l \dot{\epsilon}_{kk} \delta_{ij} + 2G_l \dot{\epsilon}_{ij} \right\}, \quad (6.26c)$$

$$\dot{\epsilon}_{ij} = \frac{1}{2} \left(\frac{\partial u_i}{\partial x_j} + \frac{\partial u_j}{\partial x_i} \right), \quad (6.26d)$$

which can be solved for the velocities and stresses when the initial and boundary conditions are provided. Note that all variables in the above equations are real numbers.

It might be insightful to demonstrate the behaviour of these equations in the limits of small and large relaxation time scales. When the relaxation is very

quick ($\tau_l \rightarrow 0$), a quasi-static equilibrium is obtained ($\dot{r}_{ijl} = -\Lambda_l \dot{\epsilon}_{kk} \delta_{ij} - 2G_l \dot{\epsilon}_{ij}$, cf. equation 6.26c) and the solid exhibits elastic behaviour with the relaxed moduli ($\dot{\sigma}_{ij} = \Lambda_R \dot{\epsilon}_{kk} \delta_{ij} + 2G_R \dot{\epsilon}_{ij}$, cf. equation 6.26b). When the relaxation is very slow ($\tau_l \rightarrow \infty$), there is practically no memory stress ($r_{ijl} \rightarrow 0$, cf. equation 6.24) and the solid shows elastic behaviour with the unrelaxed moduli ($\dot{\sigma}_{ij} = \Lambda_U \dot{\epsilon}_{kk} \delta_{ij} + 2G_U \dot{\epsilon}_{ij}$, cf. equation 6.26b).

6.3.4 Boundary conditions using characteristic treatment

As a direct application of the boundary conditions can lead to numerical instability, the boundary conditions need to be implemented using the characteristic treatment (Kosloff et al., 1990). Below, we derive the adjusted equations at the boundaries, following the method of Carcione (1994). The remainder of this chapter is restricted to two spatial dimensions (x and z) and one relaxation mechanism ($N_l = 1$), such that $\Lambda_l = \Lambda_\delta$, $G_l = G_\delta$ and the subscript l can be dropped. The following relations are used for simplicity:

$$\begin{aligned} \Pi_U &= \Lambda_U + 2G_U, & \Pi_\delta &= \Lambda_\delta + 2G_\delta, \\ c_{pu} &= \sqrt{\frac{\Pi_U}{\rho_s}}, & c_{su} &= \sqrt{\frac{G_U}{\rho_s}}, \\ \Lambda_\tau &= \frac{\Lambda_\delta}{\tau}, & G_\tau &= \frac{G_\delta}{\tau}, & \Pi_\tau &= \frac{\Pi_\delta}{\tau}. \end{aligned} \quad (6.27)$$

The viscoelastic equations with memory stresses reduce to 8 partial differential equations:

$$\begin{aligned} \frac{\partial u_1}{\partial t} &= \frac{1}{\rho_s} \frac{\partial \sigma_{11}}{\partial x} + \frac{1}{\rho_s} \frac{\partial \sigma_{13}}{\partial z} + f_1, \\ \frac{\partial u_3}{\partial t} &= \frac{1}{\rho_s} \frac{\partial \sigma_{13}}{\partial x} + \frac{1}{\rho_s} \frac{\partial \sigma_{33}}{\partial z} + f_3, \\ \frac{\partial \sigma_{11}}{\partial t} &= \Pi_U \frac{\partial u_1}{\partial x} + \Lambda_U \frac{\partial u_3}{\partial z} + \dot{r}_{11}, \\ \frac{\partial \sigma_{33}}{\partial t} &= \Lambda_U \frac{\partial u_1}{\partial x} + \Pi_U \frac{\partial u_3}{\partial z} + \dot{r}_{33}, \\ \frac{\partial \sigma_{13}}{\partial t} &= G_U \frac{\partial u_3}{\partial x} + G_U \frac{\partial u_1}{\partial z} + \dot{r}_{13}, \\ \frac{\partial \dot{r}_{11}}{\partial t} &= -\Pi_\tau \frac{\partial u_1}{\partial x} - \Lambda_\tau \frac{\partial u_3}{\partial z} - \frac{1}{\tau} \dot{r}_{11}, \\ \frac{\partial \dot{r}_{33}}{\partial t} &= -\Lambda_\tau \frac{\partial u_1}{\partial x} - \Pi_\tau \frac{\partial u_3}{\partial z} - \frac{1}{\tau} \dot{r}_{33}, \\ \frac{\partial \dot{r}_{13}}{\partial t} &= -G_\tau \frac{\partial u_3}{\partial x} - G_\tau \frac{\partial u_1}{\partial z} - \frac{1}{\tau} \dot{r}_{13}. \end{aligned} \quad (6.28)$$

They can be expressed in the following matrix-vector form (Carcione, 1994):

$$\begin{aligned} \frac{\partial \mathbf{v}}{\partial t} &= \mathbf{A} \frac{\partial \mathbf{v}}{\partial x} + \mathbf{B} \frac{\partial \mathbf{v}}{\partial z} + \mathbf{C} \mathbf{v} + \mathbf{d}, \\ \mathbf{v} &= [u_1 \ u_3 \ \sigma_{11} \ \sigma_{33} \ \sigma_{13} \ \dot{r}_{11} \ \dot{r}_{33} \ \dot{r}_{13}]^T, \end{aligned} \quad (6.29)$$

where T indicates a transpose. The vector \mathbf{v} has 8 entries, so the matrices \mathbf{A} , \mathbf{B} and \mathbf{C} have size 8×8 . It is assumed that the boundary is normal to the z -direction. Hence, the implementation of the boundary conditions requires the adjustment of the $\partial/\partial z$ terms. All remaining terms are denoted with the superscript R as in this vector equation:

$$\frac{\partial \mathbf{v}}{\partial t} = \mathbf{B} \frac{\partial \mathbf{v}}{\partial z} + \left(\frac{\partial \mathbf{v}}{\partial t} \right)^R. \quad (6.30)$$

Next, the matrix \mathbf{B} is written in diagonal form as $\mathbf{B} = \mathbf{S} \mathbf{\Lambda} \mathbf{S}^{-1}$, such that the vector equation becomes:

$$\frac{\partial \mathbf{v}}{\partial t} = \mathbf{S} \mathbf{H} + \left(\frac{\partial \mathbf{v}}{\partial t} \right)^R, \quad \mathbf{H} = \mathbf{\Lambda} \mathbf{S}^{-1} \frac{\partial \mathbf{v}}{\partial z}. \quad (6.31)$$

The diagonal matrix $\mathbf{\Lambda}$ is formed with the eigenvalues of \mathbf{B} , which are denoted as λ_i with $i = 1, 2, \dots, 8$. The components of the vector \mathbf{H} with the corresponding eigenvalues are:

$$\begin{aligned} H_1 &= -\frac{1}{2} \Pi_\tau \frac{\partial u_3}{\partial z} - \frac{1}{2} \frac{\Pi_\tau}{\rho_s c_{pu}} \frac{\partial \sigma_{33}}{\partial z}, & \lambda_1 &= c_{pu}, \\ H_2 &= -\frac{1}{2} \Pi_\tau \frac{\partial u_3}{\partial z} + \frac{1}{2} \frac{\Pi_\tau}{\rho_s c_{pu}} \frac{\partial \sigma_{33}}{\partial z}, & \lambda_2 &= -c_{pu}, \\ H_3 &= -\frac{1}{2} G_\tau \frac{\partial u_1}{\partial z} - \frac{1}{2} \frac{G_\tau}{\rho_s c_{su}} \frac{\partial \sigma_{13}}{\partial z}, & \lambda_3 &= c_{su}, \\ H_4 &= -\frac{1}{2} G_\tau \frac{\partial u_1}{\partial z} + \frac{1}{2} \frac{G_\tau}{\rho_s c_{su}} \frac{\partial \sigma_{13}}{\partial z}, & \lambda_4 &= -c_{su}, \\ H_5 &= H_6 = H_7 = H_8 = 0, & \lambda_5 &= \lambda_6 = \lambda_7 = \lambda_8 = 0. \end{aligned} \quad (6.32)$$

The equations for \mathbf{v} can be expressed in terms of H_i :

$$\begin{aligned} \dot{u}_1 &= -\frac{c_{su}}{G_\tau} (H_3 - H_4) + \dot{u}_1^R, \\ \dot{u}_3 &= -\frac{c_{pu}}{\Pi_\tau} (H_1 - H_2) + \dot{u}_3^R, \\ \dot{\sigma}_{11} &= -\frac{\Lambda_U}{\Pi_\tau} (H_1 + H_2) + \dot{\sigma}_{11}^R, \\ \dot{\sigma}_{33} &= -\frac{\Pi_U}{\Pi_\tau} (H_1 + H_2) + \dot{\sigma}_{33}^R, \end{aligned} \quad (6.33)$$

$$\begin{aligned}
\dot{\sigma}_{13} &= -\frac{G_U}{G_\tau}(H_3 + H_4) + \dot{\sigma}_{13}^R, \\
\ddot{r}_{11} &= \frac{\Lambda_\tau}{\Pi_\tau}(H_1 + H_2) + \ddot{r}_{11}^R, \\
\ddot{r}_{33} &= (H_1 + H_2) + \ddot{r}_{33}^R, \\
\ddot{r}_{13} &= (H_3 + H_4) + \ddot{r}_{13}^R.
\end{aligned}$$

The diagonalization of \mathbf{B} allows the identification of characteristic decoupled wave modes in the z -direction. Specifically, the multiplication of equation 6.31 with \mathbf{S}^{-1} yields:

$$\frac{\partial \mathbf{w}}{\partial t} = \mathbf{H} + \mathbf{S}^{-1} \left(\frac{\partial \mathbf{v}}{\partial t} \right)^R, \quad \mathbf{w} = \mathbf{S}^{-1} \mathbf{v}, \quad \mathbf{H} = \mathbf{\Lambda} \frac{\partial \mathbf{w}}{\partial z}. \quad (6.34)$$

The equations decouple, since $\mathbf{\Lambda}$ is a diagonal matrix. Neglecting the remaining terms for the moment, then w_i satisfies (no repeated summation here):

$$\frac{\partial w_i}{\partial t} = \lambda_i \frac{\partial w_i}{\partial z} \quad \Rightarrow \quad w_i = f(z + \lambda_i t), \quad (6.35)$$

for an arbitrary function f . In a similar way (again no repeated summation):

$$H_i = \lambda_i \frac{\partial w_i}{\partial z} = \lambda_i f'(z + \lambda_i t), \quad (6.36)$$

where f' denotes the derivative of the function f with respect to its argument. The dependence on z and t reveals the characteristics $z + \lambda_i t = \text{constant}$. Modes with $\lambda_i < 0$ travel in the positive z -direction. Similarly, $\lambda_i > 0$ corresponds with waves that travel in the negative z -direction. Finally, modes with $\lambda_i = 0$ are not travelling at all. Based on the eigenvalues given above, four travelling waves can be identified:

$$\begin{aligned}
\lambda_1 &= c_{pu}, & \text{P-wave travelling in the negative } z\text{-direction,} \\
\lambda_2 &= -c_{pu}, & \text{P-wave travelling in the positive } z\text{-direction,} \\
\lambda_3 &= c_{su}, & \text{S-wave travelling in the negative } z\text{-direction,} \\
\lambda_4 &= -c_{su}, & \text{S-wave travelling in the positive } z\text{-direction.}
\end{aligned} \quad (6.37)$$

The concept of characteristics for the implementation of the boundary conditions is well described by Carcione (1994). Outgoing waves are determined from the physics inside the domain of interest, so they should not be modified by the boundary conditions. In contrast, incoming waves do not originate from the interior of the domain, so they should be prescribed by the boundary conditions. Below, we first illustrate this approach for one boundary condition, after which we provide all the equations that can be obtained in a similar way.

Consider that the acceleration \dot{u}_1 is prescribed at the bottom boundary: $\dot{u}_1 = \dot{u}_1^{\text{pres}}$. Equation 6.33 shows that two characteristics are related to \dot{u}_1 , namely H_3 and H_4 , both corresponding to shear waves. The wave with $\lambda_4 = -c_{su}$ travels

in the positive z -direction, so that is an incoming wave at the bottom boundary. Hence, the boundary condition should prescribe H_4 . Solving the \dot{u}_1 -equation for H_4 and requiring that $\dot{u}_1 = \dot{u}_1^{\text{pres}}$ yields:

$$H_4 = \frac{G_\tau}{c_{su}} \left(\dot{u}_1^{\text{pres}} - \dot{u}_1^{\text{R}} \right) + H_3. \quad (6.38)$$

The incoming S-wave given by H_4 appears in the equations for $\dot{\sigma}_{13}$ and \ddot{r}_{13} , so these equations should be adjusted. As H_4 appears in the combination $H_3 + H_4$, it is convenient to compute this sum first:

$$\begin{aligned} H_3 + H_4 &= 2H_3 + \frac{G_\tau}{c_{su}} \left(\dot{u}_1^{\text{pres}} - \dot{u}_1^{\text{R}} \right) \\ &= -G_\tau \frac{\partial u_1}{\partial z} - \frac{G_\tau}{\rho_s c_{su}} \frac{\partial \sigma_{13}}{\partial z} + \frac{G_\tau}{c_{su}} \left(\dot{u}_1^{\text{pres}} - \dot{u}_1^{\text{R}} \right) \\ &= -G_\tau \frac{\partial u_1}{\partial z} + \frac{G_\tau}{c_{su}} \left(\dot{u}_1^{\text{pres}} - \frac{1}{\rho_s} \frac{\partial \sigma_{13}}{\partial z} - \dot{u}_1^{\text{R}} \right). \end{aligned} \quad (6.39)$$

When this is substituted in the equation for $\dot{\sigma}_{13}$, one obtains:

$$\begin{aligned} \dot{\sigma}_{13} &= -\frac{G_U}{G_\tau} \left(H_3 + H_4 \right) + \dot{\sigma}_{13}^{\text{R}} \\ &= \left\{ G_U \frac{\partial u_1}{\partial z} + \dot{\sigma}_{13}^{\text{R}} \right\} - \frac{G_U}{c_{su}} \left(\dot{u}_1^{\text{pres}} - \left\{ \frac{1}{\rho_s} \frac{\partial \sigma_{13}}{\partial z} + \dot{u}_1^{\text{R}} \right\} \right). \end{aligned} \quad (6.40)$$

Within curly braces one recognizes the original equations for $\dot{\sigma}_{13}$ and \dot{u}_1 (cf. equations 6.28 and 6.30). We use the term ‘original’ and the superscript ^{org} to refer to the equations in the absence of boundaries, such as given in equation 6.28. The equation for $\dot{\sigma}_{13}$ can then be written in a more compact way:

$$\dot{\sigma}_{13} = \dot{\sigma}_{13}^{\text{org}} - \frac{G_U}{c_{su}} \left(\dot{u}_1^{\text{pres}} - \dot{u}_1^{\text{org}} \right). \quad (6.41)$$

Using a similar approach, the equation for \ddot{r}_{13} becomes:

$$\ddot{r}_{13} = \ddot{r}_{13}^{\text{org}} + \frac{G_\tau}{c_{su}} \left(\dot{u}_1^{\text{pres}} - \dot{u}_1^{\text{org}} \right). \quad (6.42)$$

In a later stage, we will consider a solid layer with prescribed velocities at the bottom and prescribed stresses at the top. More precisely, the combination of the velocity-stress formulation of the viscoelastic equations with the characteristic treatment actually requires the time derivatives of velocity and/or stress as boundary conditions. Below we provide the adjusted equations at the bottom and top boundaries, with the subscript b for bottom and t for top:

$$\text{prescribe } \dot{u}_1 \text{ at bottom: } \begin{cases} \dot{u}_1|_b &= \dot{u}_1|_b^{\text{pres}}, \\ \dot{\sigma}_{13}|_b &= \dot{\sigma}_{13}|_b^{\text{org}} - \frac{G_U}{c_{su}} \left(\dot{u}_1|_b^{\text{pres}} - \dot{u}_1|_b^{\text{org}} \right), \\ \ddot{r}_{13}|_b &= \ddot{r}_{13}|_b^{\text{org}} + \frac{G_\tau}{c_{su}} \left(\dot{u}_1|_b^{\text{pres}} - \dot{u}_1|_b^{\text{org}} \right). \end{cases} \quad (6.43)$$

$$\text{prescribe } \dot{u}_3 \text{ at bottom: } \begin{cases} \dot{u}_3|_b &= \dot{u}_3|_b^{\text{pres}}, \\ \dot{\sigma}_{11}|_b &= \dot{\sigma}_{11}|_b^{\text{org}} - \frac{\Lambda_U}{c_{pu}} \left(\dot{u}_3|_b^{\text{pres}} - \dot{u}_3|_b^{\text{org}} \right), \\ \dot{\sigma}_{33}|_b &= \dot{\sigma}_{33}|_b^{\text{org}} - \frac{\Pi_U}{c_{pu}} \left(\dot{u}_3|_b^{\text{pres}} - \dot{u}_3|_b^{\text{org}} \right), \\ \ddot{r}_{11}|_b &= \ddot{r}_{11}|_b^{\text{org}} + \frac{\Lambda_\tau}{c_{pu}} \left(\dot{u}_3|_b^{\text{pres}} - \dot{u}_3|_b^{\text{org}} \right), \\ \ddot{r}_{33}|_b &= \ddot{r}_{33}|_b^{\text{org}} + \frac{\Pi_\tau}{c_{pu}} \left(\dot{u}_3|_b^{\text{pres}} - \dot{u}_3|_b^{\text{org}} \right). \end{cases} \quad (6.44)$$

$$\text{prescribe } \dot{\sigma}_{13} \text{ at top: } \begin{cases} \dot{\sigma}_{13}|_t &= \dot{\sigma}_{13}|_t^{\text{pres}}, \\ \dot{u}_1|_t &= \dot{u}_1|_t^{\text{org}} + \frac{c_{su}}{G_U} \left(\dot{\sigma}_{13}|_t^{\text{pres}} - \dot{\sigma}_{13}|_t^{\text{org}} \right), \\ \ddot{r}_{13}|_t &= \ddot{r}_{13}|_t^{\text{org}} - \frac{G_\tau}{G_U} \left(\dot{\sigma}_{13}|_t^{\text{pres}} - \dot{\sigma}_{13}|_t^{\text{org}} \right). \end{cases} \quad (6.45)$$

$$\text{prescribe } \dot{\sigma}_{33} \text{ at top: } \begin{cases} \dot{\sigma}_{33}|_t &= \dot{\sigma}_{33}|_t^{\text{pres}}, \\ \dot{u}_3|_t &= \dot{u}_3|_t^{\text{org}} + \frac{c_{pu}}{\Pi_U} \left(\dot{\sigma}_{33}|_t^{\text{pres}} - \dot{\sigma}_{33}|_t^{\text{org}} \right), \\ \dot{\sigma}_{11}|_t &= \dot{\sigma}_{11}|_t^{\text{org}} + \frac{\Lambda_U}{\Pi_U} \left(\dot{\sigma}_{33}|_t^{\text{pres}} - \dot{\sigma}_{33}|_t^{\text{org}} \right), \\ \ddot{r}_{11}|_t &= \ddot{r}_{11}|_t^{\text{org}} - \frac{\Lambda_\tau}{\Pi_U} \left(\dot{\sigma}_{33}|_t^{\text{pres}} - \dot{\sigma}_{33}|_t^{\text{org}} \right), \\ \ddot{r}_{33}|_t &= \ddot{r}_{33}|_t^{\text{org}} - \frac{\Pi_\tau}{\Pi_U} \left(\dot{\sigma}_{33}|_t^{\text{pres}} - \dot{\sigma}_{33}|_t^{\text{org}} \right). \end{cases} \quad (6.46)$$

The derivation of these equations is very similar to what has been described above for \dot{u}_1 at the bottom boundary. In summary, these are the boundary equations that should be solved together with equations 6.28 for the interior.

6.4 Numerical methods

This section describes the numerical methods that will be used in subsequent sections. The (pseudo)spectral Fourier and Chebyshev methods were chosen for their accuracy and easy implementation on rectangular grids (Fornberg and Sloan, 1994; Fornberg, 1998; Boyd, 2001). The discretized equations were implemented in MATLAB, which was greatly facilitated by the manual of Trefethen (2000) called *Spectral Methods in Matlab*.

This section is structured as follows. The first subsection considers the time integration, which is common to both the fluid and the solid phase. Subsection 6.4.2 outlines the spatial discretization of the fluid with use of the Chebyshev method. The discretization of the solid is explained in subsection 6.4.3, which also introduces the Fourier method. The coupling between the fluid and the solid phase is outlined in subsection 6.4.4.

6.4.1 Time integration

After spatial discretization of the fluid or the solid phase, the resulting partial differential equation can be expressed in matrix-vector form:

$$\frac{\partial \mathbf{v}}{\partial t} = \mathbf{M}\mathbf{v} + \mathbf{d}, \quad (6.47)$$

with \mathbf{v} the vector of unknowns, \mathbf{M} a matrix and \mathbf{d} a source vector. This equation is a convenient starting point to explain the time integration (or temporal discretization). Let the integer n denote an individual time step and Δt the time step size, then the temporal grid is given by $t^{(n)} = n\Delta t$, $n = 0, 1, \dots, N_t - 1$, with $t^{(0)} = 0$ and N_t the number of time steps in the simulation.

To facilitate the coupling between the fluid and the solid phase, a combination of implicit and explicit integration was performed:

$$\frac{\mathbf{v}^{(n+1)} - \mathbf{v}^{(n)}}{\Delta t} = \alpha_{\text{imp}}\mathbf{M}\mathbf{v}^{(n+1)} + \alpha_{\text{exp}}\mathbf{M}\mathbf{v}^{(n)} + \mathbf{d}^{(n+1/2)}. \quad (6.48)$$

A consistent discretization requires $\alpha_{\text{imp}} + \alpha_{\text{exp}} = 1$. For most simulations, a Crank-Nicolson time integration was employed ($\alpha_{\text{imp}} = \alpha_{\text{exp}} = 0.5$). A similar time integration, alternatively denoted as the trapezoidal method, was used for other wave propagation problems (Wineberg et al., 1991). For a few cases, numerical stability required an implicit Euler time integration ($\alpha_{\text{imp}} = 1$, $\alpha_{\text{exp}} = 0$). The above equation can be rewritten as:

$$\begin{aligned} \mathbf{M}^{\text{left}}\mathbf{v}^{(n+1)} &= \mathbf{r}, & \mathbf{r} &= \mathbf{M}^{\text{right}}\mathbf{v}^{(n)} + \mathbf{d}^{(n+1/2)}\Delta t, \\ \mathbf{M}^{\text{left}} &= (\mathbf{I} - \alpha_{\text{imp}}\mathbf{M}\Delta t), & \mathbf{M}^{\text{right}} &= (\mathbf{I} + \alpha_{\text{exp}}\mathbf{M}\Delta t), \end{aligned} \quad (6.49)$$

where \mathbf{r} is the right-hand-side vector and \mathbf{I} is the identity matrix. The superscript $(n+1/2)$ denotes that the source term is evaluated at time $t = t^{(n+1/2)} = t^{(n)} + (1/2)\Delta t$. The following algorithm was used to progressively solve the equations:

1. Compute \mathbf{M}^{left} and $\mathbf{M}^{\text{right}}$.
2. Compute LU decomposition of \mathbf{M}^{left} .
3. Initialize the vector $\mathbf{v}^{(n)}$, e.g. with the analytical solution.
4. Time stepping; for n from 0 to $N_t - 2$ do:
 - (a) Compute \mathbf{r} , including boundary conditions and source terms.
 - (b) Solve $\mathbf{M}^{\text{left}}\mathbf{v}^{(n+1)} = \mathbf{r}$ for $\mathbf{v}^{(n+1)}$, using the LU decomposition of \mathbf{M}^{left} .

When there is no coupling between a fluid and a solid phase, an explicit time integration can be used instead. For instance, the Runge-Kutta method proposed by Sommeijer et al. (1994) was used for the impulse forcing on a compliant coating. Specifically, that method can be used to solve equation 6.47 by repeating

these substeps 4 times (Wesseling, 2001):

$$\frac{\partial \mathbf{v}^{(s-1)}}{\partial t} = \mathbf{M}\mathbf{v}^{(s-1)} + \mathbf{d}^{(s-1)}, \quad \mathbf{v}^{(s)} = \mathbf{v}^{(n)} + \alpha_s \Delta t \frac{\partial \mathbf{v}^{(s-1)}}{\partial t}, \quad (6.50)$$

with integer s to indicate the substeps ($s = 1, 2, 3, 4$), and α_s an element of the vector $[\frac{1}{4}, \frac{1}{3}, \frac{1}{2}, 1]$. This method was called the SHK method by Wesseling (2001). The vector $\mathbf{v}^{(s)}$ can be interpreted as an estimate of \mathbf{v} at time $t^{(n)} + \alpha_s \Delta t$, such that $\mathbf{v}^{(0)} = \mathbf{v}^{(n)}$ and $\mathbf{v}^{(4)} = \mathbf{v}^{(n+1)}$. This interpretation was used to implement the prescribed time-dependent boundary conditions in the matrix \mathbf{M} and the vector \mathbf{d} .

6.4.2 Fluid

The fluid equations only need to be solved for the case of oscillatory flow coupled to a compliant viscoelastic layer. Given the streamwise and spanwise homogeneity of the flow, we can restrict ourselves to the streamwise velocity $u(z, t)$. The corresponding unsteady Stokes equation is (cf. equation 4.22):

$$\frac{\partial u}{\partial t} = \nu \frac{\partial^2 u}{\partial z^2} + f_0 \cos(\omega t), \quad 0 \leq z \leq h, \quad (6.51)$$

where the sub- or superscripts f to indicate the fluid phase are left out. The harmonic forcing $f_0 e^{i\omega t}$ was replaced by its real part, since the simulations were performed with real numbers.

A Chebyshev method was used for spatial discretization in the z -direction. This spectral method uses polynomial interpolation in unevenly spaced points, which is suitable for bounded, non-periodic domains (Trefethen, 2000). Its analogue for periodic domains is the spectral Fourier method, which is based on interpolation using trigonometric functions on an equispaced grid. The Chebyshev points are given by:

$$z_{\text{cheb},k} = \cos\left(\frac{k\pi}{N_z - 1}\right), \quad k = 0, 1, \dots, N_z - 1, \quad (6.52)$$

where N_z denotes the number of grid points in the z -direction. The Chebyshev points range from $+1$ to -1 , and they cluster at the boundaries. The dense concentration near the boundaries has some disadvantages. For example, the stability of explicit time integration typically depends on the minimum grid spacing. Coordinate transformations can be used for grid adaptation (Carcione, 1996). We used the following symmetric mapping (Kosloff and Tal-Ezer, 1993; Carcione, 1996):

$$z = z_{\min} + (z_{\max} - z_{\min}) \left[\frac{q(z_{\text{cheb}}) - q(1)}{q(-1) - q(1)} \right], \quad q(z_{\text{cheb}}) = \frac{\arcsin(\gamma z_{\text{cheb}})}{\arcsin(\gamma)}, \quad (6.53)$$

which maps the interval $1 \geq z_{\text{cheb}} \geq -1$ onto $z_{\min} \leq z \leq z_{\max}$, and stretches the mesh at the boundaries. The amount of stretching is quantified with the

parameter γ : the Chebyshev grid corresponds with $\gamma \rightarrow 0$, while an equispaced grid is obtained for $\gamma \rightarrow 1$. We have used $\gamma = 0.8$ as stretching parameter, since that allowed us to relax the time-step criterion without compromising the accuracy too much.

Trefethen (2000) provides a MATLAB function that computes the Chebyshev grid z_{cheb} and the differentiation matrix \mathbf{D}_{cheb} of size $N_z \times N_z$. The latter simplifies the computation of derivatives on a Chebyshev grid. For example, let \mathbf{f} be a vector with components f_k , $k = 0, 1, \dots, N_z - 1$. Its derivative simply follows from a matrix-vector multiplication:

$$\frac{\partial \mathbf{f}}{\partial z_{\text{cheb}}} = \mathbf{D}_{\text{cheb}} \mathbf{f}. \quad (6.54)$$

In the present work, the transformed grid of equation 6.53 was used instead of z_{cheb} . The differentiation matrix was modified accordingly. Specifically, the derivative of f can be written as (Carcione, 1996):

$$\begin{aligned} \frac{\partial f}{\partial z} &= \frac{dq}{dz} \frac{dz_{\text{cheb}}}{dq} \frac{\partial f}{\partial z_{\text{cheb}}}, \\ \frac{dq}{dz} &= \frac{q(-1) - q(1)}{z_{\text{max}} - z_{\text{min}}}, \\ \frac{dz_{\text{cheb}}}{dq} &= \frac{\arcsin(\gamma)}{\gamma} \sqrt{1 - (\gamma z_{\text{cheb}})^2}. \end{aligned} \quad (6.55)$$

The derivative reads in vector form as:

$$\begin{aligned} \frac{\partial \mathbf{f}}{\partial z} &= \mathbf{P} \mathbf{D}_{\text{cheb}} \mathbf{f} \equiv \mathbf{D} \mathbf{f}, \\ P_{ik} &= \delta_{ik} \left. \frac{dq}{dz} \frac{dz_{\text{cheb}}}{dq} \right|_{z_{\text{cheb}}=z_{\text{cheb},k}}, \end{aligned} \quad (6.56)$$

with diagonal matrix \mathbf{P} and Kronecker delta function δ_{ik} . The diagonal entries depend on k , as dz_{cheb}/dq depends on $z_{\text{cheb},k}$.

Using the differentiation matrix \mathbf{D} for the vertical derivative, equation 6.51 can be rewritten in vector form as:

$$\frac{\partial \mathbf{u}}{\partial t} = \mathbf{M} \mathbf{u} + \mathbf{d}, \quad \mathbf{M} = \nu \mathbf{D}^2, \quad \mathbf{d} = f_0 \cos(\omega t) \mathbf{1}, \quad (6.57)$$

where $\mathbf{1}$ denotes a vector with all entries equal to one. The velocity vector \mathbf{u} has length N_z^f and components u_k , where the index k labels the vertical coordinate. Each element of the source vector \mathbf{d} equals $f_0 \cos(\omega t)$, independent of the vertical coordinate. Note the similarity of the last equation with equation 6.47. The Crank-Nicolson time integration requires the source term at time $t = t^{(n+1/2)} = t^{(n)} + (1/2)\Delta t$, such that $\mathbf{d}^{(n+1/2)} = f_0 \cos(\omega(t^{(n)} + \Delta t/2)) \mathbf{1}$.

Equation 6.51 requires two boundary conditions, one at $z = 0$ (the interface, denoted with subscript c) and another at $z = h$ (the top, denoted with subscript

t). We have used the same boundary conditions as in chapter 4, namely a time-dependent velocity at the interface and a symmetry condition at the top. These conditions were implemented by adjusting \mathbf{M}^{left} and \mathbf{r} at the boundaries. The velocity is prescribed at the interface: $u|_c^{(n+1)} = u|_c^{\text{pres}}$, which was implemented with $M_{pj}^{\text{left}} = \delta_{pj}$ ($\forall j$) and $r_p = u|_c^{\text{pres}}$, where the index p corresponds with the interface. The velocity derivative is specified at the top: $\left. \frac{\partial u}{\partial z} \right|_t^{(n+1)} = \left. \frac{\partial u}{\partial z} \right|_t^{\text{pres}}$, which was incorporated with $M_{qj}^{\text{left}} = D_{qj}$ ($\forall j$) and $r_q = \left. \frac{\partial u}{\partial z} \right|_t^{\text{pres}}$, where q represents the index of the top boundary.

6.4.3 Solid

Since viscoelastic solids were considered, the velocity-stress formulation with memory variables was used as a starting point. The relevant equations for two spatial dimensions and one relaxation mechanism have been listed before (cf. equations 6.28 and 6.29).

For the example of an oscillatory flow coupled to a viscoelastic coating, only the vertical coordinate z is relevant, so the derivative with respect to x can be neglected for now (cf. equation 6.29):

$$\frac{\partial \mathbf{v}}{\partial t} = \mathbf{B} \frac{\partial \mathbf{v}}{\partial z} + \mathbf{C} \mathbf{v} + \mathbf{d}. \quad (6.58)$$

A Chebyshev method was used for the vertical direction, very similar to what was used for the fluid in the previous subsection. The resulting grid has N_z^s grid points between $z_{\min} \leq z \leq z_{\max}$ with $z_{\min} = -\delta$ and $z_{\max} = 0$. Next, the above equation is vectorized on a grid with N_z^s grid cells:

$$\frac{\partial \mathbf{v}_\Delta}{\partial t} = \mathbf{B}_{\partial/\partial z, \Delta} \mathbf{v}_\Delta + \mathbf{C}_\Delta \mathbf{v}_\Delta + \mathbf{d}_\Delta. \quad (6.59)$$

The subscripts Δ denote the spatial discretization. The vector \mathbf{v}_Δ is the same as \mathbf{v} in equation 6.29 with every variable replaced by the corresponding vector of N_z^s elements; hence, \mathbf{v}_Δ is a column vector with $8N_z^s$ elements. The vector \mathbf{d}_Δ is obtained in a similar way from \mathbf{d} . The matrix $\mathbf{B}_{\partial/\partial z, \Delta}$ is used to denote the operation $\mathbf{B}\partial/\partial z$ after discretization. It is obtained from the matrix \mathbf{B} of size 8×8 by replacing each element by its value times the differentiation matrix \mathbf{D} of size $N_z^s \times N_z^s$, which yields a matrix of size $8N_z^s \times 8N_z^s$. In a comparable way, the matrix \mathbf{C}_Δ is obtained by replacing each element of \mathbf{C} by its value times the identity matrix of size $N_z^s \times N_z^s$. Omitting the subscripts Δ for convenience, the last equation can be rewritten in a more compact form:

$$\frac{\partial \mathbf{v}}{\partial t} = \mathbf{M}^{\text{org}} \mathbf{v} + \mathbf{d}^{\text{org}}, \quad \mathbf{M}^{\text{org}} = \mathbf{B}_{\partial/\partial z} + \mathbf{C}, \quad (6.60)$$

where $^{\text{org}}$ denotes the equations in absence of boundaries. Although there are no body forces in the present study ($\mathbf{d}^{\text{org}} = \mathbf{0}$), we keep \mathbf{d}^{org} for completeness.

When the boundary conditions are included, the matrix \mathbf{M}^{org} and the vector \mathbf{d}^{org} change (details are provided below), such that the vector equation becomes:

$$\frac{\partial \mathbf{v}}{\partial t} = \mathbf{M}\mathbf{v} + \mathbf{d}. \quad (6.61)$$

In case the solution also depends on the horizontal coordinate, the dependence on x cannot be neglected. Starting from equation 6.29 and using the same vertical discretization as above, the equations become:

$$\frac{\partial \mathbf{v}^{(i)}}{\partial t} = \mathbf{A} \frac{\partial \mathbf{v}^{(i)}}{\partial x} + \mathbf{B}_{\partial/\partial z} \mathbf{v}^{(i)} + \mathbf{C}\mathbf{v}^{(i)} + \mathbf{d}^{(i)}. \quad (6.62)$$

The vector $\mathbf{v}^{(i)}$ has again a length of $8N_z^s$, and the superscript $^{(i)}$ denotes the dependence on x .

Periodic boundary conditions were assumed in the horizontal x -direction. That allowed the use of a Fourier method and a uniform grid with N_x grid cells and spacing Δx . The numerical solution is thus fully specified by $\mathbf{v}^{(i)}$, $i = 1, 2, \dots, N_x$. Next, the last equation is transformed in the x -direction, using the Fast Fourier Transform (FFT) as implemented in MATLAB. Using a caron \checkmark to denote transformed variables, then $\check{f} \equiv \mathcal{F}_x \{f\}$, where $f = f(x)$ is an arbitrary function in physical space, $\check{f} = \check{f}(k_x)$ denotes the same function in wavenumber space, and $\mathcal{F}_x \{\}$ symbolizes the transform. The transformation of a derivative with respect to x yields a simplified relation:

$$\mathcal{F}_x \left\{ \frac{\partial \mathbf{v}^{(i)}}{\partial x} \right\} = ik_x^{(i)} \check{\mathbf{v}}^{(i)}, \quad \text{no repeated summation}, \quad (6.63)$$

where $k_x^{(i)}$ are elements of the wavenumber vector \mathbf{k}_x . One should be careful with the definition of this vector, as pointed out by Trefethen (2000). The ordering of the wavenumbers in MATLAB's FFT functions requires the following wavenumber vector for differentiation:

$$\mathbf{k}_x = \frac{2\pi}{L_x} \left[0, 1, \dots, \frac{N_x}{2}, -\frac{N_x}{2} + 1, -\frac{N_x}{2} + 2, \dots, -1 \right]^T, \quad (6.64)$$

where N_x is even and $L_x = N_x \Delta x$ represents the domain size in the x -direction. For odd derivatives (such as $\partial/\partial x$), symmetry requires that the element with value $(2\pi/L_x)N_x/2$ is set to zero (Trefethen, 2000). When a transform is applied to equation 6.62, one obtains:

$$\frac{\partial \check{\mathbf{v}}^{(i)}}{\partial t} = ik_x^{(i)} \mathbf{A} \check{\mathbf{v}}^{(i)} + \mathbf{B}_{\partial/\partial z} \check{\mathbf{v}}^{(i)} + \mathbf{C} \check{\mathbf{v}}^{(i)} + \check{\mathbf{d}}^{(i)}, \quad (6.65)$$

again without summation over repeated indices. This equation reads in compact form:

$$\begin{aligned} \frac{\partial \check{\mathbf{v}}^{(i)}}{\partial t} &= \mathbf{M}^{\text{org},(i)} \check{\mathbf{v}}^{(i)} + \check{\mathbf{d}}^{\text{org},(i)}, \quad \text{no repeated summation,} \\ \mathbf{M}^{\text{org},(i)} &= ik_x^{(i)} \mathbf{A} + \mathbf{B}_{\partial/\partial z} + \mathbf{C}. \end{aligned} \quad (6.66)$$

When the boundary conditions are included (details are provided below), the vector equation becomes:

$$\frac{\partial \check{\mathbf{v}}^{(i)}}{\partial t} = \mathbf{M}^{(i)} \check{\mathbf{v}}^{(i)} + \check{\mathbf{d}}^{(i)}, \quad \text{no repeated summation.} \quad (6.67)$$

The time integration methods are the same as in section 6.4.1, with the only exceptions that all vectors have to be transformed (e.g. $\check{\mathbf{v}}$ instead of \mathbf{v}), and that the whole procedure has to be repeated for every $i \in \{1, \dots, N_x\}$.

Next, we describe how the boundary conditions were implemented numerically. In absence of boundaries, the vector equations are given by 6.60 or 6.66. Given the similarity between these two equations, we only explain how equation 6.60 turns into equation 6.61 when the boundary conditions are applied. Away from the boundaries, the matrix and vector are unchanged: $\mathbf{M} = \mathbf{M}^{\text{org}}$ and $\mathbf{d} = \mathbf{d}^{\text{org}}$. At the boundaries, however, the matrix and source vector do change to incorporate the adjusted equations 6.43, 6.44, 6.45, 6.46. To illustrate that, consider the bottom boundary with a prescribed horizontal acceleration (cf. equation 6.43):

$$\dot{\sigma}_{13}|_b = \dot{\sigma}_{13}|_b^{\text{org}} - \frac{GU}{c_{su}} \left(\dot{u}_1|_b^{\text{pres}} - \dot{u}_1|_b^{\text{org}} \right), \quad (6.68a)$$

$$\dot{u}_1|_b = \dot{u}_1|_b^{\text{pres}}. \quad (6.68b)$$

For conciseness, only the adjusted equations for $\dot{\sigma}_{13}$ and \dot{u}_1 are considered. Suppose that the prescribed acceleration corresponds with position p in the vector of unknowns: $\dot{u}_1|_b = \dot{v}_p$. Similarly, let q denote the index that corresponds with the shear-stress time derivative on the bottom boundary: $\dot{\sigma}_{13}|_b = \dot{v}_q$. By definition:

$$\dot{u}_1|_b = \dot{v}_p = M_{pj} v_j + d_p, \quad \dot{\sigma}_{13}|_b = \dot{v}_q = M_{qj} v_j + d_q, \quad (6.69)$$

and similarly when the superscript org is included. Hence, equation 6.68a for the stress derivative becomes:

$$M_{qj} v_j + d_q = M_{qj}^{\text{org}} v_j + d_q^{\text{org}} - \frac{GU}{c_{su}} \left(\dot{u}_1|_b^{\text{pres}} - \left(M_{pj}^{\text{org}} v_j + d_p^{\text{org}} \right) \right), \quad (6.70)$$

which requires the following adjustments to \mathbf{M} and \mathbf{d} :

$$\forall j : M_{qj} = M_{qj}^{\text{org}} + \frac{GU}{c_{su}} M_{pj}^{\text{org}}, \quad d_q = d_q^{\text{org}} - \frac{GU}{c_{su}} \left(\dot{u}_1|_b^{\text{pres}} - d_p^{\text{org}} \right). \quad (6.71)$$

Similarly, equation 6.68b for the velocity derivative becomes $\dot{u}_1|_b = \dot{v}_p = M_{pj} v_j + d_p = \dot{u}_1|_b^{\text{pres}}$, such that $M_{pj} = 0$ ($\forall j$) and $d_p = \dot{u}_1|_b^{\text{pres}}$. For the Crank-Nicolson

time integration, the time derivatives of the velocity and the stress at the boundaries need to be prescribed at time level $n + 1/2$.

To close the viscoelastic equations 6.28, the relaxed and unrelaxed moduli need to be provided. Like in chapter 5, the solid properties were specified with a shear modulus $|G| = \rho_s |c_s|^2$, a shear loss angle ϕ_G and a Poisson's ratio ν_{pr} , all at $\omega\tau = 1$. The magnitude and the phase of the bulk modulus K were computed with use of the model described in section 5.3.4, while the relaxed and unrelaxed bulk and shear moduli followed from equation 6.19. Finally, standard conversion formulas were employed to compute other moduli, e.g. the dilatational modulus $\Lambda = K - (2/3)G$ and the compressional-wave modulus $\Pi = K + (4/3)G$.

6.4.4 Coupling

This subsection describes the coupling procedure for an oscillatory flow over a compliant viscoelastic layer. The situation is the same as in chapter 4, with the only exception that the present chapter considers the streamwise wall deformation that solely results from the shear stress. The analytical solution is unchanged, except that the normal stress is absent, which corresponds with $\chi_{pg} = 0$.

To numerically simulate this problem, the flow and structural solver need to be coupled, using either the monolithic or the partitioned approach. The monolithic method is especially suitable for the present problem, since the same spatial discretization method is used for both the fluid and the solid phase. The partitioned approach was chosen, however, because it is presumably the preferred approach for future large-scale simulations.

The coupling method that was used is similar to the Dirichlet-Neumann partitioning described by Küttler and Wall (2008). The fluid is the Dirichlet partition (with a prescribed interface velocity), while the solid represents the Neumann partition (with a prescribed interface stress). We performed the coupling based on the interface velocity, while a coupling based on the interface stress would have been possible as well. As the fluid-solid interface does not deform in the vertical direction, there was no need for mesh deformations. The combined fluid and solid dynamics was computed numerically with the Crank-Nicolson time integration, using the following procedure:

1. Initialize fluid and solid solvers.
2. Time stepping; for n from 0 to $N_t - 2$ do:
 - (a) Initialize iteration: $conv = 0$, $i = 0$.
 - (b) Iteration; for i from 1 to $N_{i,max}$, while $conv = 0$, do:
 - i. Flow solver:
 - A. Solve for $\mathbf{u}^{(n+1)}$, using the boundary conditions:

$$u|_c^{(n+1)} = u_{c,(i-1)}^{(n+1)}, \quad \left. \frac{\partial \mathbf{u}}{\partial z} \right|_t^{(n+1)} = 0.$$
 - B. Compute the interface stress $\sigma_{13,c}^{(n+1)}$ from $\mathbf{u}^{(n+1)}$.

- C. Calculate the time derivative of the interface stress:
 $\dot{\sigma}_{13}|_c^{(n+1/2)} = (\sigma_{13,c}^{(n+1)} - \sigma_{13,c}^{(n)}) / \Delta t.$
- ii. Solid solver:
- A. Solve for $\mathbf{v}^{(n+1)}$, using the boundary conditions:
 $\dot{u}_1|_b^{(n+1/2)} = 0$, $\dot{u}_3|_b^{(n+1/2)} = 0$, $\dot{\sigma}_{13}|_c^{(n+1/2)}$ from fluid solver,
 $\dot{\sigma}_{33}|_c^{(n+1/2)} = 0.$
- B. Obtain the surface velocity $\hat{u}_{c,(i)}^{(n+1)}$ from $\mathbf{v}^{(n+1)}$.
- iii. Check convergence and adjust boundary conditions:
- A. Compute residual $r^{(i)} = \hat{u}_{c,(i)}^{(n+1)} - u_{c,(i-1)}^{(n+1)}$.
- B. If $|r^{(i)}| < \epsilon_{\text{conv}}$, the surface velocity has converged, so $\text{conv} = 1$.
 Else, update the surface velocity using dynamic relaxation:
 $u_{c,(i)}^{(n+1)} = \alpha_{\text{relax}}^{(i)} \hat{u}_{c,(i)}^{(n+1)} + (1 - \alpha_{\text{relax}}^{(i)}) u_{c,(i-1)}^{(n+1)}.$

The coupling basically consists of three steps. First, the fluid velocity is computed using an estimate for the interface velocity. The interface stresses follow from the obtained fluid velocity. Second, these stresses are applied to the solid and the resulting solid deformation is calculated. Third, the thus obtained surface velocity is compared with the initial estimate. In case their difference is small enough, the coupling has converged; otherwise, the interface velocity is updated and the three steps start again.

The update of the interface velocity is performed with a dynamic relaxation factor $\alpha_{\text{relax}}^{(i)}$, which was computed as follows:

$$\alpha_{\text{relax}}^{(i)} = \begin{cases} 0.5 & \text{if } i = 1 \text{ or } r^{(i)} - r^{(i-1)} = 0. \\ -\alpha_{\text{relax}}^{(i-1)} \frac{r^{(i-1)}}{r^{(i)} - r^{(i-1)}} & \text{else,} \end{cases} \quad (6.72)$$

where the integer i numbers the iterations. The second relation was obtained from Küttler and Wall (2008), based on the method given by Irons and Tuck (1969). It is usually denoted as Aitken relaxation or Aitken acceleration (cf. section 6.2). The iteration stops when the maximum number of iterations $N_{i,\text{max}}$ is reached or when the solution is converged (which is marked by $\text{conv} = 1$). Convergence is ascertained when the absolute value of the residual is smaller than ϵ_{conv} , with $\epsilon_{\text{conv}} = 10^{-10}$ for most cases.

6.5 Spanwise-homogeneous impulse forcing on compliant coating

This section considers an impulse forcing on a viscoelastic compliant coating with the purpose of demonstrating the compressional waves and shear waves. The initially undeformed coating of thickness δ is forced by a spanwise-homogeneous pressure pulse in absence of shear:

$$\sigma_{tc}(x, t) = 0, \quad (6.73a)$$

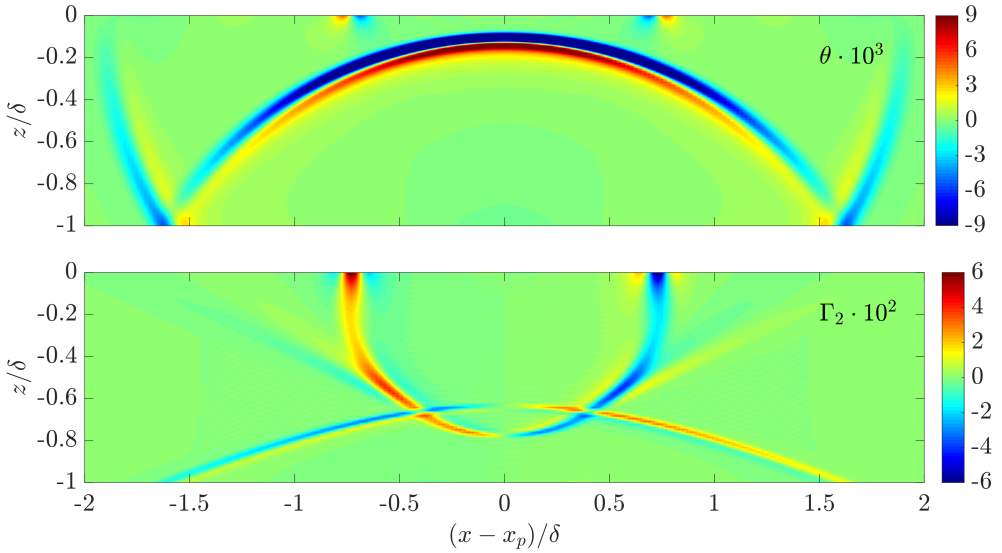


FIGURE 6.2: Compressional waves (*top*) and shear waves (*bottom*) after a spanwise-homogeneous impulse forcing on the surface of a compliant coating. The compressional waves are visualized by means of the divergence of the displacement field (θ), and the shear waves with the spanwise component of the curl (Γ_2). The forcing, coating and numerical parameters are provided in the text.

$$\sigma_{nc}(x, t) = -|\sigma_{nc0}| \exp\left(-\frac{(x - x_p)^2}{2\sigma_x^2}\right) \exp\left(-\frac{(t - t_p)^2}{2\sigma_t^2}\right), \quad (6.73b)$$

with subscript t for tangential stress, n for normal stress and c for coating surface. The pressure forcing is localized in space and time with use of a Gaussian. The maximum forcing amplitude is reached at (x_p, t_p) . The properties of the forcing are: $|\sigma_{nc0}|/\rho_s|c_s|^2 = 1$, $\sigma_x/\delta = 0.04$ and $\sigma_t|c_s|/\delta = 0.006$, which yields a narrow and short pulse. The coating is compressible and slightly viscoelastic with $\tau|c_s|/\delta = 1$, $\phi_G = 1^\circ$ and $\nu_{pr} = 0.4$. The unrelaxed wave speeds are $c_{su}/|c_s| = 1.009$ and $c_{pu}/|c_s| = 2.46$.

The coating deformation was computed numerically with the SHK time integration method and a time step $\Delta t|c_s|/\delta = 2 \cdot 10^{-4}$. The horizontal grid was uniformly spaced in the interval $-L_x/2 \leq x - x_p < L_x/2$ with $L_x/\delta = 5$ and $N_x = 250$ grid cells. A Chebyshev grid with $N_z = 100$ grid cells was used in the vertical direction for $-\delta \leq z \leq 0$. The spatial and temporal grid were relatively fine to capture the narrow and short impulse pressure. The simulation started at $t_{\min} - t_p = -10\sigma_t$ with a coating at rest. The compressional waves were visualized by means of the divergence of the displacement field (θ), and the shear waves with the spanwise component of the curl (Γ_2), cf. equation 6.11. For the present case:

$$\theta = \frac{\partial \xi}{\partial x} + \frac{\partial \zeta}{\partial z}, \quad \Gamma_2 = \frac{\partial \xi}{\partial z} - \frac{\partial \zeta}{\partial x}, \quad (6.74)$$

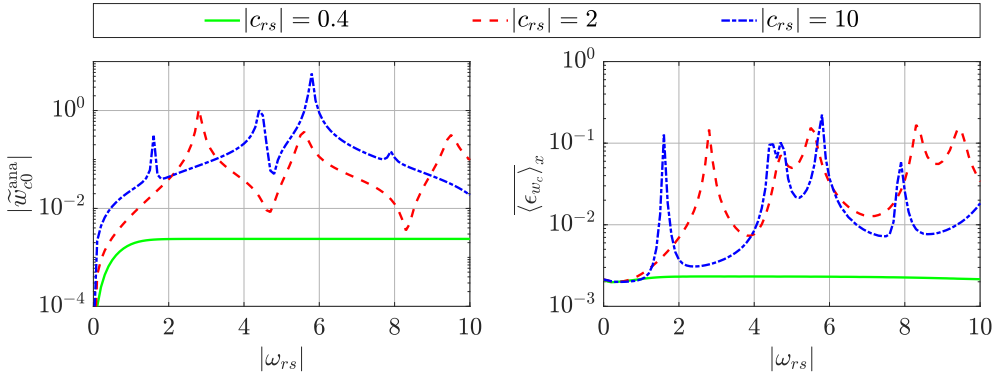


FIGURE 6.3: The accuracy of the numerically-computed vertical interface velocity of a compliant wall forced by a spanwise-homogeneous streamwise-travelling stress wave. The velocity amplitude according to the analytical solution (*left*) and the averaged numerical error (*right*) are shown as function of $|\omega_{rs}|$ for three different values of $|c_{rs}|$. The other dimensionless problem parameters are $\tilde{\sigma}_{tc0} = 0.0041$, $\tilde{\sigma}_{nc0} = 0.0238$, $\rho_r = 1$, $\phi_G = 1^\circ$, $\nu_{pr} = 0.45$. The numerical parameters are $N_x = 10$, $N_z = 20$, $T/\Delta t = 40$.

with ξ the horizontal and ζ the vertical displacement. These displacements were obtained from the velocity by integration (cf. equation 6.50):

$$\boldsymbol{\xi}^{(s)} = \boldsymbol{\xi}^{(n)} + \alpha_s \Delta t \mathbf{u}^{(s-1)}, \quad (6.75)$$

with displacement vector $\boldsymbol{\xi} = [\xi \ \zeta]^T$ and velocity vector $\mathbf{u} = [u_1 \ u_3]^T$.

Figure 6.2 displays contours of θ and Γ_2 for a snapshot at time $(t - t_p)c_{pu}/\delta = 1.9$ or $(t - t_p)c_{su}/\delta = 0.77$. The compressional wave has reflected at the bottom and almost returned to the coating surface. The shear wave originating from the impulse forcing did not yet reach the coating bottom. This is generally true for materials that are not very compressible: compressional waves travel faster than shear waves. A shear wave not only originates from the impulse forcing, but also from the compressional wave where it hits the rigid bottom wall. This confirms that wave type conversion is possible when a wave reflects, in agreement with other studies (Virieux, 1986).

6.6 Deformation of a compliant wall by a travelling stress wave

The deformation of a compliant wall due to a spanwise-homogeneous streamwise-travelling stress wave was computed numerically. Details of the stress wave, the relevant dimensionless numbers, the coating model and the analytical results have been provided in sections 5.3 and 5.4. The simulation employed a Crank-Nicolson time integration with $T/\Delta t$ time steps per wave period T , and a Chebyshev grid with N_z grid cells in the wall-normal direction. The deformation was computed

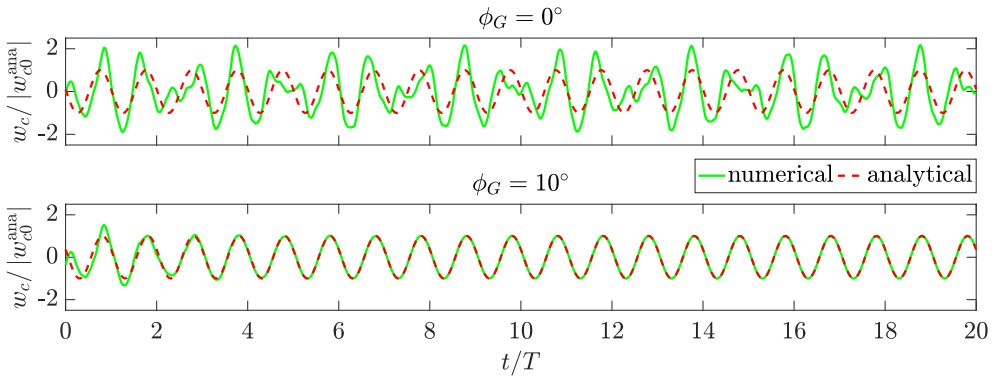


FIGURE 6.4: The dependence of the numerical solution on a wrong initial condition for an elastic solid (*top*) and a viscoelastic solid (*bottom*). The initial condition is the analytical solution at $t = 0$ multiplied with -1 . The figures show the time evolution of the vertical interface velocity at a single streamwise location for a compliant wall forced by a spanwise-homogeneous streamwise-travelling stress wave. The velocity is normalized with its amplitude according to the analytical solution. The dimensionless problem parameters are $\tilde{\sigma}_{tc0} = 0.0041$, $\tilde{\sigma}_{nc0} = 0.0238$, $\rho_r = 1$, $|\omega_{rs}| = 1.5$, $|c_{rs}| = 2$, ϕ_G (see figure title), $\nu_{pr} = 0.45$. The numerical parameters are $N_x = 10$, $N_z = 20$, $T/\Delta t = 40$.

for one wavelength in the x -direction, which allowed the use of periodic boundary conditions and a Fourier method with N_x grid cells in the horizontal direction.

The accuracy of the numerical simulations was determined from the numerical error, which is defined for an arbitrary function f as:

$$\epsilon_f = \left| \frac{f^{\text{num}} - f^{\text{ana}}}{f^c} \right|, \quad f^c = \max |f^{\text{ana}}|, \quad (6.76)$$

with numerical solution f^{num} , analytical solution f^{ana} and characteristic function value f^c . In words, ϵ_f represents the absolute value of the normalized difference between the numerical and the analytical solution. The same notation as in equation 3.3 is used to denote averages, e.g. $\langle \epsilon_f \rangle_x$ for a streamwise average and $\bar{\epsilon}_f$ for a time average. For the present section, the interval of the time average is $50 \leq t/T \leq 100$, which was chosen such that the time signal had reached a steady-state oscillation.

Figure 6.3 shows the analytical solution and the numerical error of the vertical interface velocity, both as function of $|\omega_{rs}|$ for three different values of $|c_{rs}|$. The analytical solution confirms the presence of resonances when $|\omega_{rs}| \gtrsim 1$ and $|c_{rs}| \gtrsim 1$, in agreement with figure 5.3. The numerical error exhibits remarkably similar trends as compared to the analytical solution. For instance, the numerical error is significantly larger when an extremum appears in the analytical solution.

Figure 6.4 demonstrates the influence of the initial condition on the deformation of an elastic and a viscoelastic solid. The numerical simulation started with the wrong initial condition, namely the analytical solution at $t = 0$ multiplied

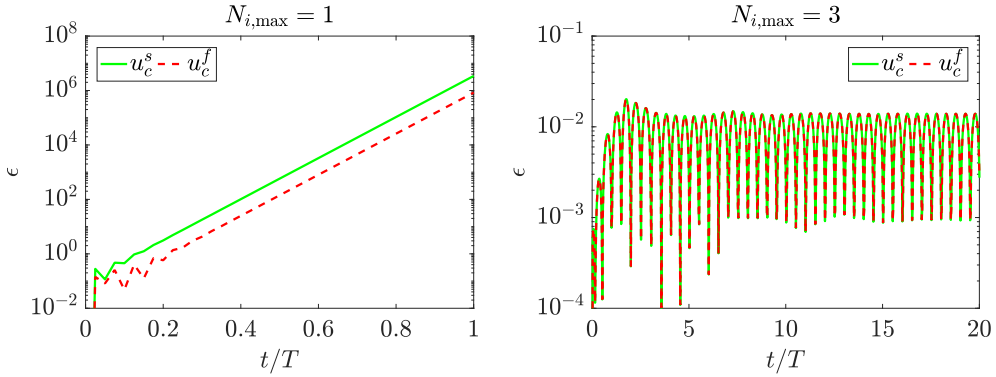


FIGURE 6.5: The importance of iterations for a stable numerical simulation of oscillatory flow coupled to a compliant wall. The figures show the time evolution of the numerical error for a single iteration (*left*) and three iterations (*right*). The five dimensionless problem parameters are $\rho_r = 1$, $h_r = 1$, $\omega_{rf} = 10^2$, $|\omega_{rs}| = 1.75\pi$, $\phi_G = 0^\circ$. The numerical parameters are $N_z^f = 20$, $N_z^s = 20$, $T/\Delta t = 40$.

with -1 . The subfigures show how the vertical interface velocity evolves in time after the wrong initialization. The numerical solution returns relatively quickly to the analytical solution for the viscoelastic solid, while the elastic solid is more sensitive to the initial condition. This might be counter-intuitive at first sight, since it is actually a property of viscoelastic systems that the stress is determined by the strain history. However, an elastic solid can be interpreted as a viscoelastic solid with infinite relaxation time ($\tau \rightarrow \infty$, $\psi_M(t) = M_U H_s(t)$, $r_{ij} = 0$, cf. equations 6.15 and 6.24 with $N_l = 1$). Hence, an elastic solid does not have a mechanism to discard information from the past in a finite time as opposed to a viscoelastic solid.

6.7 Oscillatory flow coupled to a compliant wall

In contrast to the previous sections, here we investigate numerically an example of the two-way coupling between a fluid and a solid phase: oscillatory laminar flow coupled to a viscoelastic layer on a rigid base. Details of the coupling procedure have been provided in section 6.4.4. The accuracy of the numerical simulations was determined with use of the numerical error (cf. equation 6.76) of the fluid interface velocity u_c^f , the solid interface velocity u_c^s , the fluid interface shear stress σ_{tc}^f and/or the solid interface shear stress σ_{tc}^s . The interval $50 \leq t/T \leq 100$ was used to compute the time-averaged numerical error, with $T = 2\pi/\omega$ the oscillation period.

Figure 6.5 illustrates the importance of iterations for a stable numerical simulation of oscillatory flow coupled to a compliant wall. When only a single iteration is used, convergence is not attained (note the difference between the numerical error of the fluid and solid interface velocity), and the numerical solution becomes unstable. The linear error increase in the semi-log plot of figure 6.5 (left)

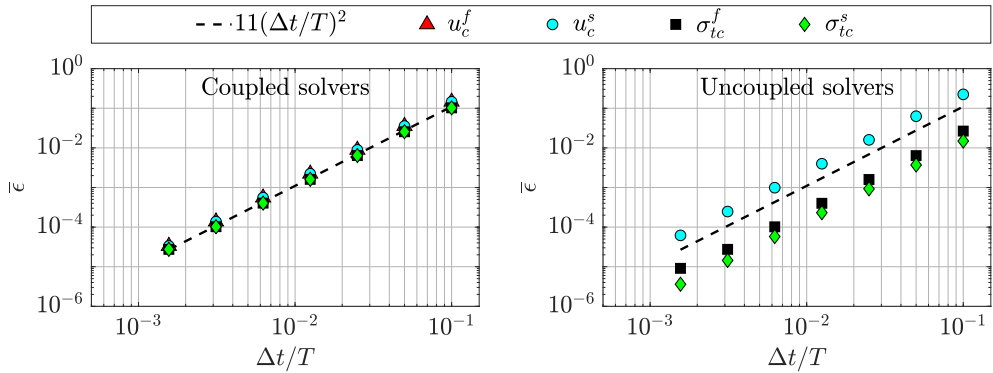


FIGURE 6.6: The time-averaged numerical error as function of the normalized time step. The dimensionless problem parameters are $\rho_r = 1$, $h_r = 1$, $\omega_{rf} = 10^2$, $|\omega_{rs}| = 1.75\pi$, $\phi_G = 0^\circ$. The numerical parameters are $N_z^f = 20$, $N_z^s = 20$, $T/\Delta t = 10, 20, 40, 80, 160, 320, 640$. *Left*: coupled fluid and solid solvers, using the iterative procedure outlined in section 6.4.4. *Right*: uncoupled solvers, using the analytical solution to prescribe the boundary conditions at the interface.

indicates an exponential error growth. In contrast, the right subfigure shows that three iterations are sufficient for a stable integration. Convergence is apparent from the fact that the error signal for the interface velocity is the same for the fluid and the solid solver. The error starts at zero, because the numerical solution is the same as the analytical solution at the start of the simulation ($t = 0$). It takes a few periods for the numerical solution to adjust to the discretized equations. Thereafter, the error becomes a steady periodic signal, which reflects the periodicity of the forcing.

The temporal convergence of the error is visualized in figure 6.6. The subfigures show the error in the interface velocity and shear stress for both the flow and the structure solver. The left figure displays the error when both solvers were coupled, using the iterative procedure outlined in section 6.4.4. The right figure presents the error when the solvers were uncoupled: the fluid and solid solutions were computed independently, using the analytical solution to prescribe the boundary conditions at the interface (i.e. the velocity for the fluid solver, and the time derivative of the stress for the solid solver). Both subfigures show that $\bar{\epsilon} \propto (\Delta t)^2$, which confirms the second-order convergence that is expected for the Crank-Nicolson time integration.

The iterative procedure yields a fully converged solution, which is apparent from the equality of the interface velocity and stress (left subfigure). However, the interface quantities in the fluid and the solid phase are unequal when the solvers are uncoupled (right subfigure). The surface velocity in the fluid phase is prescribed, so it has zero error, which is not visible because of the logarithmic scale of the vertical axis. The error in the solid surface stress is not zero, because the *time derivative* of the interface stress has been prescribed from the analytical

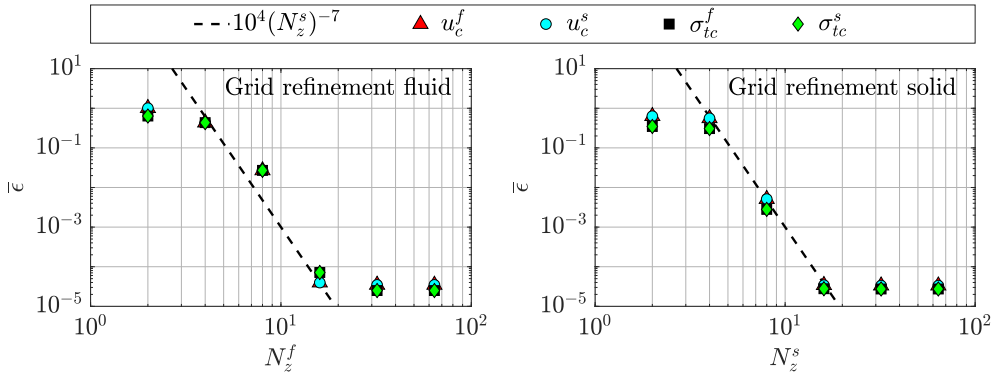


FIGURE 6.7: The time-averaged numerical error as function of the number of fluid grid cells (*left*) and solid grid cells (*right*). The dimensionless problem parameters are $\rho_r = 1$, $h_r = 1$, $\omega_{r,f} = 10^2$, $|\omega_{r,s}| = 1.75\pi$, $\phi_G = 0^\circ$. The numerical parameters are $N_z^s = 20$ (*left*), $N_z^f = 20$ (*right*), $T/\Delta t = 640$. The number of fluid cells (*left*) or solid cells (*right*) is 2, 4, 8, 16, 32, 64.

solution; the stress itself follows from a time integration step with the corresponding finite accuracy. The error in the solid surface velocity is even slightly larger than for the coupled solvers.

The spatial convergence of the error is visualized in figure 6.7, both for the fluid grid (*left*) and the solid grid (*right*). The dependence of the error on the number of grid cells in the fluid or the solid is very similar. The rapid error decrease is typical for the Chebyshev and other spectral methods. The error quickly saturates, reaching $\bar{\epsilon} \approx 3 \cdot 10^{-5}$, which is the same value as in figure 6.6 for $T/\Delta t = 640$. The error is thus limited from below by the temporal resolution.

Figure 6.8 presents the analytical solution and the time-averaged numerical error of the horizontal interface velocity as a function of two dimensionless problem parameters, namely $\omega_{r,f}$ and $|\omega_{r,s}|$. The figure confirms the convergence of the numerical solution, also for viscoelastic solids (with $\phi_G \neq 0^\circ$). Still, the error magnitude varies significantly with the problem parameters. It is quite large for $\omega_{r,f} = 10^4$, since the high fluid-velocity gradient near the interface (cf. figures 4.2, 4.3) is not well-resolved when only 20 grid cells in the fluid are used. The error is much smaller for $\omega_{r,f} = 10^2$ and $\omega_{r,f} = 10^{-2}$, typically less than 10^{-2} . It exhibits oscillatory behaviour, with a strong dependence on $|\omega_{r,s}|$. The error peaks correspond quite well with the extrema in the analytical solution (cf. left and right subfigure), in agreement with the results from section 6.6.

There are some challenges for the present simulation algorithm. Figure 6.9 shows the time evolution of the numerical error for a very stiff solid. The interface-velocity error exhibits three fluctuations, one with a large period of approximately $5T$, another with an intermediate period of $T/2$ and a third one with a period of $2\Delta t$. The oscillation with period $T/2$ corresponds with the periodicity of the forcing (cf. figure 6.5). The slow and fast oscillations are numerical instabilities. Since the interface velocity is small ($|u_{c0}^{\text{ana}}/u_{ft}| = 10^{-7}$),

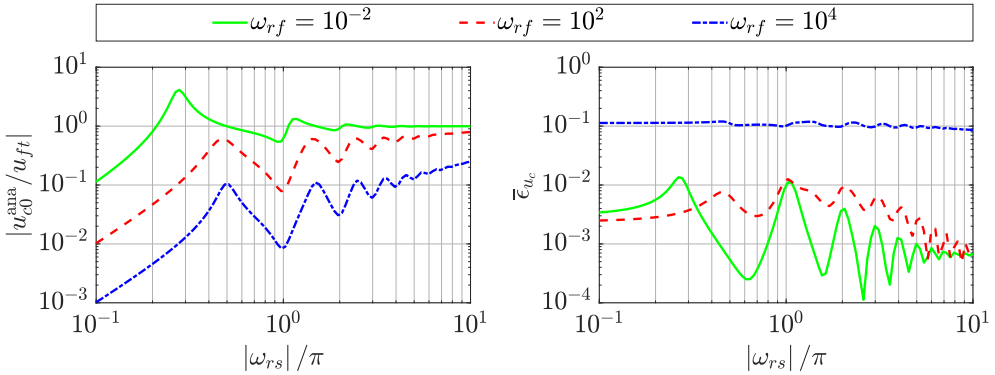


FIGURE 6.8: The accuracy of the numerically-computed horizontal interface velocity of a compliant wall coupled to an oscillatory flow. The velocity amplitude according to the analytical solution (*left*) and the time-averaged numerical error (*right*) are shown as function of $|\omega_{rs}|$ for three different values of ω_{rf} . The other dimensionless problem parameters are $\rho_r = 1$, $h_r = 1$, $\phi_G = 10^\circ$. The numerical parameters are $N_z^f = 20$, $N_z^s = 20$, $T/\Delta t = 40$.

these instabilities do not significantly influence the accuracy of the fluid velocity, which is apparent from the stable and accurate simulation of the interface shear stress. The numerical instabilities result from the time integration scheme, as is confirmed by figure 6.9 (right), which displays the error time signals for the implicit Euler integration. The two numerical instabilities disappear at the cost of a lower accuracy.

Another challenge is the stable and accurate numerical simulation of a resonance (cf. section 4.7). Figure 6.8 has already shown that the error is typically larger when resonances in the coupling appear. Still, the viscoelastic resonances from figure 6.8 (left) are not the strongest; *elastic* resonances (for $\phi_G = 0^\circ$) are stronger. Figure 6.10 exhibits the time evolution of the numerical interface-velocity error for such a resonance at two values of the time step. Time series for the interface shear stress are not presented, since they are very similar in magnitude and trend. Three periods of oscillation are again visible in the error time signal. The lowest period of $T/2$ corresponds with the periodicity of the forcing. The two other oscillations have a period that depends on Δt : the two periods are $8T$ and $82T$ for $T/\Delta t = 20$, while they are $5T$ and $210T$ for $T/\Delta t = 80$. As these periods change with Δt , the corresponding oscillations most likely have a numerical origin. Like in figure 6.9, they disappear when implicit Euler time integration is used. However, the resulting error is very large, for example around 0.95 for the interface velocity; compared to the analytical solution, the numerically computed interface velocity has a much smaller amplitude and a different phase. Further research is required for a stable and more accurate numerical simulation of the coupling resonances. The instabilities and inaccuracies possibly disappear when a higher-order time integration scheme is used. In addition, the numerical instabilities might signify the presence of physical instabilities, which have not been

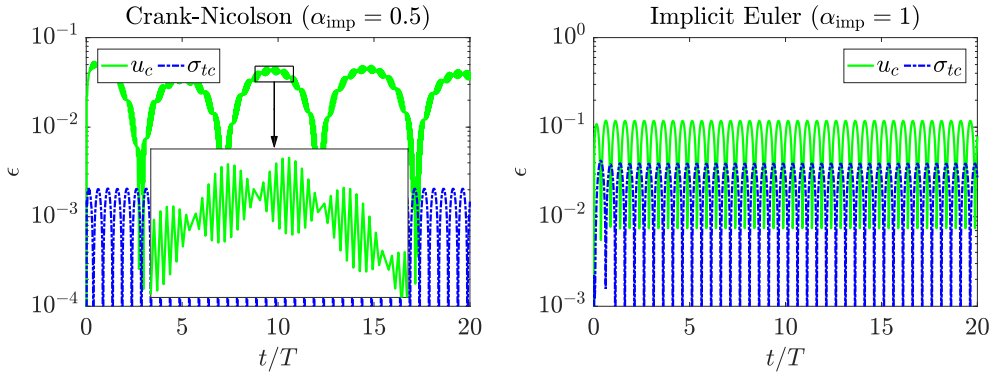


FIGURE 6.9: The time evolution of the numerical error for a very stiff solid with Crank-Nicolson (*left*) and implicit Euler (*right*) time integration. The dimensionless problem parameters are $\rho_r = 1$, $h_r = 1$, $\omega_{rf} = 10^2$, $|\omega_{rs}| = 10^{-3}$, $\phi_G = 0^\circ$. The numerical parameters are $N_z^f = 20$, $N_z^s = 20$, $T/\Delta t = 40$, $\epsilon_{\text{conv}} = 10^{-15}$. Note that ϵ_{conv} was reduced, because the interface velocity for this case is already very small, namely $|u_{c0}^{\text{ana}}/u_{ft}| = 10^{-7}$. The inset in the left figure corresponds with $8.8 \leq t/T \leq 10.8$.

considered in chapter 4.

6.8 Conclusions and recommendations

The purpose of this chapter was to provide some literature, theory and simple examples to guide future numerical work regarding the interaction between a turbulent flow and a compliant layer. We demonstrated possible techniques for the numerical computation of a deforming viscoelastic solid, and for the stable integration of coupled problems.

The viscoelastic stress-strain relation contains a convolution with two stress relaxation functions that describe how the stress decays in time after application of a strain unit step. A general model for these functions consists of a series of exponentially decaying stresses, each term with its own relaxation time and corresponding memory stress. Additional partial differential equations for these memory stresses can be derived, such that a direct but inefficient numerical implementation of the convolution operator can be avoided. To enforce the boundary conditions, adjusted equations at the boundaries can be obtained with use of a characteristic treatment.

The viscoelastic equations were solved for three types of surface stresses, namely a spanwise-homogeneous impulse forcing, a spanwise-homogeneous streamwise-travelling stress wave, and the shear stress from an oscillatory flow. The simulations typically employed a Crank-Nicolson time integration, a Fourier method for the horizontal direction and a Chebyshev grid for the vertical direction. The point forcing on a compliant wall revealed the presence of compressional and shear waves, with the possible conversion between these wave types upon reflection at the boundaries. The example of a travelling stress

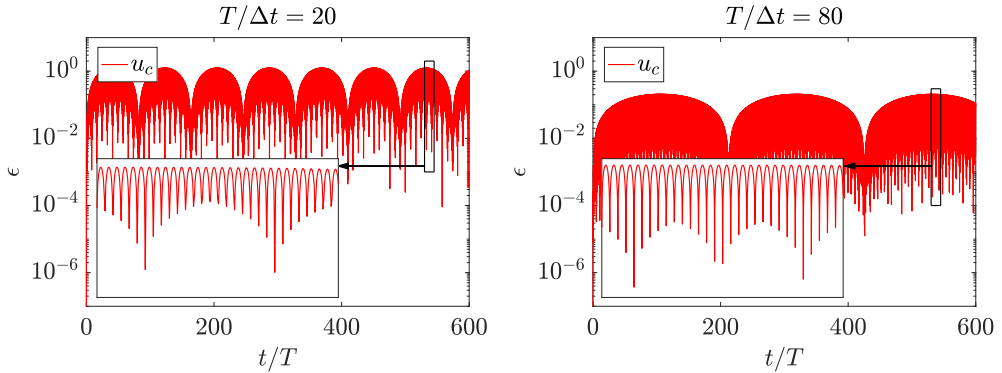


FIGURE 6.10: The time evolution of the numerical error for a resonance. The dimensionless problem parameters are $\rho_r = 1$, $h_r = 1$, $\omega_{rf} = 10^{-4}$, $|\omega_{rs}| = 1.095\pi$, $\phi_G = 0^\circ$, such that $|u_{c0}^{\text{ana}}/u_{ft}| = 18$. The numerical parameters are $N_z^f = 20$, $N_z^s = 20$, $T/\Delta t = 20$ (left) and $T/\Delta t = 80$ (right). The insets correspond with $530 \leq t/T \leq 545$.

wave was used to demonstrate that viscoelastic media with the corresponding stress relaxation are able to discard information from the past, in contrast to purely elastic media.

The largest part of this chapter was devoted to the numerical simulation of oscillatory flow coupled to a viscoelastic solid. A stable coupling was obtained in three iterations with use of the Aitken relaxation method. The simulation accuracy was quantified with the absolute value of the normalized difference between the numerical and the analytical solution. The second-order convergence of the Crank-Nicolson time integration was confirmed. The time-averaged error not only depends on the numerical parameters, but also on the dimensionless numbers that appear in the analytical solution. The error peaks correspond quite well with the extrema in the analytical solution. Numerical instabilities were demonstrated for two cases, namely a very stiff solid and a resonance. The instabilities were apparent from periodic error oscillations that are not clearly connected to the forcing periodicity. Further research is required to clarify whether the instabilities only have a numerical or also a physical origin.

As mentioned in section 6.1, the ultimate goal is to perform a direct numerical simulation of turbulent flow coupled to a single homogeneous layer of viscoelastic material on a rigid base. The corresponding numerical code should satisfy, in our opinion, the following requirements:

- High-performance parallel computing is typically used for direct numerical simulations of turbulent flows. Domain methods are preferred, since boundary methods are presumably less appropriate for parallelization.
- Since the flow and structure solvers are often developed independently, the partitioned method for the fluid/solid coupling seems more suitable.
- Implicit or strong coupling is presumably required to prevent that numerical instabilities arise (cf. figure 6.5).

- The wall deformation cannot be neglected, since the surface displacements are typically larger than the surface velocities when inner scaling is applied (cf. section 5.7).
- The analysis can be limited to coatings that are not extremely soft, such that the deformations are small. Hence, the numerical code should not necessarily be able to incorporate steep surface waves or changes of flow topology (e.g. when part of the fluid phase becomes encapsulated by the solid phase).
- The simulation domain changes in time, so it is convenient to use a time-domain instead of a frequency-domain method.
- Implicit time integration is required for a stable and accurate simulation of coupling problems.
- The same time integration scheme should be used for both the fluid and the solid phase, since unwanted effects otherwise appear.

Based on this list, there is no single answer as to which numerical method is most suitable (cf. literature in section 6.2). For the fluid phase, the deforming domain can be incorporated with a mapping approach (Fulgosi et al., 2003; Xu et al., 2003; Kim and Choi, 2014; Zonta et al., 2015) or a fixed computational grid (Yang and Balaras, 2006; Zhao et al., 2008). For the solid domain, one can use a finite element method with a Lagrangian mesh (Zhao et al., 2008), or a grid transformation in combination with finite-difference (Hestholm, 1999) or spectral methods (Tessmer and Kosloff, 1994). Parallel implementations are possible (Bohlen, 2002), also for the finite element method (Tezduyar et al., 1993). Aitken relaxation seems a suitable method to couple the fluid and the solid phase. The strength of the physical interaction presumably determines whether weak coupling is sufficient or strong coupling is necessary.

Chapter 7

Conclusions and perspectives

While specific conclusions and recommendations have already been provided in the separate chapters, here we focus on the bigger picture by concentrating on the two objectives mentioned in the introduction (cf. section 1.4). The conclusions and perspectives regarding textured surfaces are presented in the first section, while the second section considers compliant surfaces.

7.1 Textured surfaces¹

Using riblets for turbulent drag reduction is a relatively old concept. Still, riblets have not yet found widespread application, possibly because of the following reasons. First, there are several manufacturing challenges, such as the large-scale application of microscale manufacturing techniques to possibly curved and nonsmooth surfaces. Second, the maximum drag reduction (e.g. 6% in chapter 2) seen for riblet coatings under controlled laboratory conditions might not be achieved in practice. The optimum performance is only obtained when:

- the riblets are everywhere aligned with the mean flow.
- the riblet size increases along the surface due to boundary layer growth.
- the texture is not damaged by wear or obscured by fouling.
- the vehicle (e.g. vessel, aircraft) moves at its designed speed, whether it is loaded or unloaded.

In addition, riblets can possibly not be applied everywhere, and they primarily reduce the frictional drag as opposed to pressure and wave drag. Nevertheless,

¹Part of this section was adapted from the conclusions and future work of H. O. G. Benschop, A. J. Guerin, A. Brinkmann, M. L. Dale, A. A. Finnie, W.-P. Breugem, A. S. Clare, D. Stübing, C. Price, and K. J. Reynolds. Drag-reducing riblets with fouling-release properties: development and testing. *Biofouling*, pages 1–13, 2018.

even a small reduction in drag will potentially provide significant economic and environmental benefits.

An important step towards the use of riblets in the marine environment has been the development and preliminary testing of the Modified Intersleek[®] Riblets: a drag-reducing riblet texture with fouling-control properties. Fraunhofer IFAM has contributed with an embossing-curing technology for large-scale riblet manufacturing (Stenzel et al., 2011; Kordy, 2015), while AkzoNobel has provided the fouling-release functionality of their Intersleek[®] 1100SR coating system. With use of a Taylor-Couette setup, we measured an optimum drag reduction of 6%, like for the riblet texture without fouling-release properties (Dual-cure Riblets). Hence, the riblet-textured coating can be augmented with fouling-release properties without compromising its drag-reducing performance.

Future work should focus on the potential benefit of Modified Intersleek[®] Riblets to moving vessels. There is no obvious advantage to the use of riblets under stationary conditions, as these can increase settlement and growth of biofilms. In addition, riblets are designed to reduce the drag in turbulent flow, which requires motion of the riblet surface through a fluid. In turn, the accumulation of fouling might also be different when the vessel is sailing at the specific speed for which the riblets are drag-reducing.

It is especially important to investigate whether the texture would stay clean and intact during normal use on an appropriate vessel. If the texture is rapidly lost through fouling or wear, then the drag-reducing properties will be lost as well and the application of riblets would not be beneficial. Demonstration of the long-term stability and fouling-release performance of the riblet-textured Modified Intersleek[®] under in-service conditions is the next logical step towards the implementation of the technology for shipping applications. In the end, this may contribute to meet the requirements of the International Maritime Organization (IMO) on emissions reduction of ships.

While efforts to apply conventional riblets are ongoing, the search for textures with an improved drag-reducing performance can still continue. To our knowledge, there is no proof that the maximum drag reduction is obtained with conventional riblet geometries. The drag-reduction capabilities of future textured coatings can be investigated with use of simulations or experiments. The immersed boundary method (IBM) seems a promising candidate for numerical simulations. The IBM of chapter 3 was especially designed for the herringbone riblet texture; it is not suitable for other textures. To allow a relatively quick check, the development of a more flexible IBM is recommended, e.g. using the techniques described by Tseng and Ferziger (2003) and Yang and Balaras (2006). Regarding experiments, the developments in rapid prototyping could be exploited to manufacture unconventional textures (Bhushan and Caspers, 2017). For instance, a synthetic shark skin with thousands of denticles was fabricated using 3D printing and was subsequently used for hydrodynamic testing (Wen et al., 2014). One of the challenges is to manufacture textures with sharp edges, e.g. the riblet tips.

7.2 Compliant surfaces

Like for riblets, the use of compliant surfaces for hydrodynamic drag reduction is also a relatively old concept. In contrast to riblets, however, compliant coatings are not yet in a stage that their full-scale application for turbulent drag reduction can be deliberated, mainly because their drag-reducing potential is far from convincing. Detailed, carefully conducted and independently verified experimental studies are very scarce. In addition, a complete picture of the interaction between a turbulent flow and a compliant coating is still missing.

Chapters 4 and 5 aimed at increased understanding of the interaction between a time-dependent flow and the resulting coating deformation. Chapter 4 considered a relatively simple problem, namely the two-way coupling between an oscillatory laminar flow and a compliant coating. That example helps to understand the influence of the coating parameters on its deformation. Except very near resonances, the one-way coupling approach yields a quite accurate estimate of the deformation. Chapter 5 investigated the coating deformation in a turbulent flow, using the one-way coupling method and the assumption of spanwise homogeneity. The deformation was computed analytically as the response to a spectrum of surface stress waves. The influence of five coating properties on the surface displacement was investigated. The modelled surface displacements were compared with recent measurements on the deformation of three different coatings in a turbulent boundary-layer flow. The model captured the increase of the coating displacement with the Reynolds number and the coating softness.

Future work could include efforts to improve the agreement between the analytical and experimental study. Gad-el Hak (2002) remarked that the most significant results had been obtained when a strong cooperation existed between theory and experiment. The analytical work could be extended to include three-dimensional deformations, since the experiments show that spanwise inhomogeneous deformations are also present (though the spanwise homogeneous mode contains the most energy). On the other hand, in future experiments one could try to measure the frequency-dependent stress spectra, convection velocity and coating modulus for the relevant frequency range, since the analytical model reveals the significance of these properties for the coating deformation.

While chapter 5 provides a reasonably complete picture of the wall deformation in the one-way coupling limit, future work should be extended to include the two-way interaction. Since the fluid stresses are unchanged by the solid deformation for the one-way coupling, the extension to two-way coupling is the only way to investigate the influence of the deformation on the turbulent drag. Analytical studies are presumably not feasible due to the complexity of the turbulent flow and the non-regular deforming domains. Instead, a combination of experimental and numerical approaches is recommended.

Direct numerical simulations (DNSs) seem most promising to numerically investigate the drag change due to the coating deformation. The importance of a DNS coupled to a compliant wall has already been recognized by Gad-el Hak (2002). At that time, however, numerical schemes to couple the solvers

were extremely expensive. With the increase of the computational power, such simulations appear to be within reach nowadays. Section 6.8 has already provided some requirements and hints for possible numerical techniques. To start with, one could consider the one-way coupling to provide a link between the analytical and experimental results of chapter 5. Future work, however, should focus on the two-way coupling between the fluid and the solid, and the associated influence on the turbulent drag.

Although research in the near future should focus on the behaviour of isotropic coatings of infinite length, it remains interesting to also consider anisotropic coatings or compliant panels of finite length (Gad-el Hak, 2002; Kim and Choi, 2014; Rosti and Brandt, 2017). If the vertical deformation could be restricted with use of an anisotropic coating, then form drag would be almost absent, while the streamwise and spanwise coating displacement could still affect the frictional drag. A compliant wall of finite length might also be interpreted as an anisotropic coating. A finite length could possibly be used to obtain a desired phase relation between the fluctuating velocity and pressure at the wall (Xu et al., 2003) or to select a limited range of wavelengths and frequencies. In case the coating response at high frequencies could be emphasized, then one could obtain significant surface velocities (on the order of the wall-friction velocity) with small surface displacements (less than a wall unit). The significant surface velocities would allow an interaction with the turbulent flow, whereas the small displacements would be beneficial to reduce the form drag.

Appendix A

Direct Numerical Simulations¹

A.1 Time advancement at fixed bulk velocity

For simplicity, equation 3.1 is rewritten as:

$$\frac{\partial u_i}{\partial t} = -\frac{\partial p}{\partial x_i} + r_i + \gamma_f f^{\text{driving}} \delta_{i1}, \quad (\text{A.1})$$

where r_i contains the advection, diffusion and IBM terms. Let the integer n denote the time steps. The used Runge–Kutta scheme (RK3) employs three sub-steps, which are numbered by the integer s . RK3 introduces intermediate velocities $u_i^{(s)}$, where $u_i^{(0)} = u_i^n$ and $u_i^{(3)} = u_i^{n+1}$. Similarly, intermediate pressures $p^{(s)}$ and driving forces $f^{\text{driving}(s)}$ are introduced. Because of the Crank–Nicolson scheme for pressure, $p^{(s)} = p^{(s-1)} + \tilde{p}^{(s)}$ with correction pressure $\tilde{p}^{(s)}$. The time advancement is illustrated here for an arbitrary sub-step s :

$$\begin{aligned} u_i^{(s)} + \alpha_{(s)} \Delta t \frac{\partial \tilde{p}^{(s)}}{\partial x_i} &= u_i^{(s-1)} - \alpha_{(s)} \Delta t \frac{\partial p^{(s-1)}}{\partial x_i} + \Delta t \left(\gamma_{(s)} r_i^{(s-1)} + \zeta_{(s-1)} r_i^{(s-2)} \right) + \\ &\quad \alpha_{(s)} \Delta t \gamma_f f^{\text{driving}(s)} \delta_{i1} \\ &\equiv u_i^{*(s)} + \alpha_{(s)} \Delta t \gamma_f f^{\text{driving}(s)} \delta_{i1} \\ &\equiv u_i^{**(s)}, \end{aligned} \quad (\text{A.2})$$

where $u_i^{*(s)}$ is the first and $u_i^{**(s)}$ the second prediction velocity. Note that the asterisk here is not used to denote dimensional quantities. The parameters $\alpha_{(s)}$, $\gamma_{(s)}$ and $\zeta_{(s-1)}$ are RK3 parameters (see e.g. Wesseling (2001)). To obtain the driving force, the equation for the streamwise velocity is volume-averaged, which

¹This appendix is part of the publication by H. O. G. Benschop and W.-P. Breugem. Drag reduction by herringbone riblet texture in direct numerical simulations of turbulent channel flow. *Journal of Turbulence*, 18(8):717–759, 2017.

yields:

$$\langle u^{(s)} \rangle_V + \alpha_{(s)} \Delta t \left\langle \frac{\partial \tilde{p}^{(s)}}{\partial x} \right\rangle_V = \langle u^{*(s)} \rangle_V + \alpha_{(s)} \Delta t \langle \gamma_f \rangle_V f^{\text{driving}(s)}. \quad (\text{A.3})$$

The first term represents the intermediate bulk velocity in sub-step s , which is set equal to one to obtain the constant bulk flow. The second term disappears because of periodic boundary conditions. The first prediction velocity is known, so the third term can be computed. The resulting equation can be solved for $f^{\text{driving}(s)}$, which yields:

$$f^{\text{driving}(s)} = \frac{1 - \langle u^{*(s)} \rangle_V}{\alpha_{(s)} \Delta t \langle \gamma_f \rangle_V}. \quad (\text{A.4})$$

Next, $u_i^{** (s)}$ is computed. With use of the continuity equation, the divergence of equation A.2 yields a Poisson equation for the correction pressure:

$$\frac{\partial^2 \tilde{p}^{(s)}}{\partial x_j^2} = \frac{1}{\alpha_{(s)} \Delta t} \frac{\partial u_j^{** (s)}}{\partial x_j}. \quad (\text{A.5})$$

When this is solved, the updated velocity and pressure are computed:

$$u_i^{(s)} = u_i^{** (s)} - \alpha_{(s)} \Delta t \frac{\partial \tilde{p}^{(s)}}{\partial x_i}, \quad p^{(s)} = p^{(s-1)} + \tilde{p}^{(s)}. \quad (\text{A.6})$$

This procedure guarantees that the bulk velocity equals one in each RK3 sub-step, which results in three values of the driving force. The total forcing (i.e. one per time step) is calculated as follows:

$$f^{\text{driving}} = \sum_{s=1}^3 \alpha_{(s)} f^{\text{driving}(s)}. \quad (\text{A.7})$$

A.2 Immersed boundary method for blade riblet textures

The IBM adjusts diffusive and advective fluxes around blades with help of indicator functions, as is described below for parallel riblets without and in yaw. The third subsection explains how the f_i^{IBM} term in equation 3.1 is computed. The final subsection describes how well the IBM approximates the no-slip and no-penetration conditions at the texture surface.

A.2.1 Parallel riblets without yaw

Figure A.1 shows the numerical grid used for parallel riblets without yaw. As a staggered grid is used, the velocity vectors are located at the faces of the grid

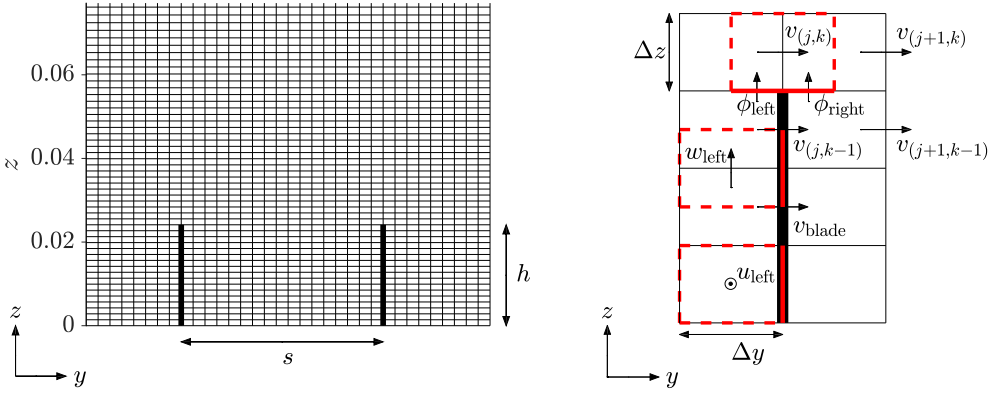


FIGURE A.1: Numerical grid and IBM used for parallel riblets without yaw. *Left*: Part of the numerical grid used for $s^+ = 17$ simulations at $Re_b = 5500$, showing two unit cells in the spanwise direction. Both for blade spacing and blade height, 17 grid cells were used. *Right*: Small part of the numerical grid (8 grid cells) around the blade tip. The text explains the IBM with use of this subfigure. The three dashed boxes represent staggered grid cells that belong to the velocity components shown in their centres. Each of these cells has one face indicated with a thick and solid line. At that cell face, the IBM adjusts the advective and diffusive fluxes.

cells. A few of these vectors are shown in the right figure. The blade coincides with a few grid points of the spanwise velocity v . The right figure helps to explain the IBM. The dashed boxes in that figure indicate three staggered grid cells that belong to the velocity components u_{left} , $v_{(j,k)}$ and w_{left} . The IBM implements an adjustment of the advective and diffusive fluxes at the cell faces marked with a thick solid line, as is explained below.

The streamwise velocity u was only adjusted in grid cells next to the blades (both on the left and right side). For the grid cell of u_{left} , the two spanwise fluxes through its thick solid face were changed: the advective flux $uv = 0$ and the diffusive flux $\partial u / \partial y = -2u_{\text{left}} / \Delta y$.

The spanwise velocity v was changed for two reasons, namely to enforce no-penetration at the blades and to adjust the fluxes above the blade tip. To enforce no-penetration, the prediction velocity was set to zero at the grid points that coincide with a blade. Let v_{blade} represent a spanwise velocity component that coincides with a blade (see figure A.1) and let $*$ represent the first prediction velocity (as in equation A.2), then $v_{\text{blade}}^* = 0$. The actual velocity v_{blade} follows from the correction step (equation A.6) and is very close to zero, although not exactly zero (details follow in section A.2.4).

The second change to v comprises the adjustment of advective and diffusive fluxes in the grid cell just above the blade tip (shown as a dashed box in figure A.1). The vertical fluxes of v at the bottom face of that cell were adjusted. The diffusive flux $\partial v / \partial z$ was split into two contributions, namely from the left and right side of the blade (indicated by ϕ_{left} and ϕ_{right} in the figure). It accounts

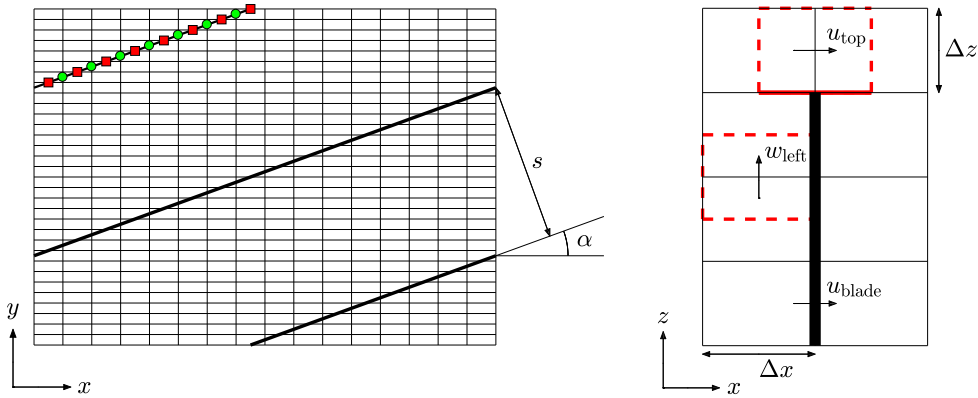


FIGURE A.2: Numerical grid and IBM used for parallel riblets in yaw. *Left*: Top view of the texture with $\alpha = 20^\circ$, showing one unit cell in the streamwise and two in the spanwise direction. The numerical grid consists of $N_{cg} = 16$ grid cells per groove. The markers on one blade indicate that the blades intersect the grid cells at the locations of the staggered velocity vectors u (circle) and v (square). *Right*: Small part of the numerical grid (8 grid cells) around the blade tip. The text explains the IBM with use of this subfigure, see also figure A.1.

for the fact that the thin blade does not inhibit vertical transport. Specifically, $\partial v / \partial z = 0.5\phi_{\text{left}} + 0.5\phi_{\text{right}}$. The flux ϕ_{right} was computed by linear interpolation of the four velocity components labelled with indices in the figure: $\phi_{\text{right}} = (v_t - v_b) / \Delta z$ with $v_t = 0.75v_{(j,k)} + 0.25v_{(j+1,k)}$ and $v_b = 0.75v_{(j,k-1)} + 0.25v_{(j+1,k-1)}$. The flux ϕ_{left} was computed in a similar way. As advection near the blade tips is likely less important than diffusion, the advective flux was not split but simply set to zero (i.e. $vw = 0$ at the thick solid face).

The wall-normal velocity w was only adjusted in grid cells next to the blades, similarly to what was done for u . For the grid cell of w_{left} , two spanwise fluxes at the thick solid face were changed: the advective flux $vw = 0$ and the diffusive flux $\partial w / \partial y = -2w_{\text{left}} / \Delta y$. These adjustments were also applied for the w -cell next to the blade tip, so this diffusive flux was not split into two contributions (although the blade covers only half of the cell face). To justify this choice, the simulation with $s^+ = 24$ at $Re_b = 5500$ was repeated. The diffusive flux near the blade tip was separated into two contributions, namely from above and below the blade tip. No significant difference in drag was found.

A.2.2 Parallel riblets in yaw

To simulate the turbulent flow over blades in yaw, the riblet texture was rotated with respect to the grid, see figure A.2 (left). That required a different Immersed Boundary Method (IBM), as the surfaces were not anymore aligned with the Cartesian directions. As the left figure shows, the grid was generated in such a way that the obstacle surface still coincides with part of the staggered velocity

vectors. The main disadvantage of this approach is that the streamwise and spanwise grid spacings cannot be chosen independently: they depend on α . However, the major advantage is a relatively simple IBM. Due to the specific alignment of grid and texture, the number of grid cells per groove N_{cg} is equal for the streamwise and spanwise directions. The grid shown in figure A.2 has $N_{cg} = 16$.

The IBM is explained with the use of figure A.2 (right). Staggered grid cells for u_{top} and w_{left} are shown as dashed boxes. The IBM implements an adjustment of the advective and diffusive fluxes at the cell faces marked with a thick solid line, as is explained below.

The streamwise and spanwise velocities were adjusted in a similar way, so only the change to u is described here. The changes to u were almost identical to that for v in the previous subsection. To enforce no-penetration, the streamwise prediction velocity was set to zero (i.e. $u_{\text{blade}}^* = 0$) at the grid points that coincide with a blade. At the bottom cell face of the grid cell for u_{top} , both the advective and diffusive fluxes were modified. The advective flux was set to zero: $uw = 0$. The diffusive flux was not split into two contributions: $\partial u / \partial z = 2u_{\text{top}} / \Delta z$.

For the wall-normal velocity, two indicator functions were used, namely one for streamwise and another one for spanwise transport of wall-normal momentum. As the treatment of streamwise and spanwise transport of w is analogous, only the former is described here. The wall-normal prediction velocity was not changed directly, as w never coincides with blades. Therefore, only the fluxes in w -cells next to the blades were modified. Specifically, the fluxes at the right cell face of the grid cell for w_{left} were adjusted as follows: $uw = 0$ and $\partial w / \partial x = -2w_{\text{left}} / \Delta x$.

A.2.3 Computation of f_i^{IBM}

Although the IBM forcing f_i^{IBM} appears as a separate term in equation 3.1 and following equations, it is not implemented as an explicit relation. The two previous subsections have shown instead that the numerical code for smooth walls was adjusted to obtain the zero velocity at the blades. However, the IBM term was needed as a separate term for the postprocessing. Its computation is illustrated with reference to appendix A.1. The first prediction velocity $u_i^{*(s)}$ that appears there contains all adjustments that are needed to obtain the zero velocity at the blades. Next, all these adjustments are left out to compute the prediction velocity $u_i^{*(s) \text{ no IBM}}$ in absence of the IBM forcing. The intermediate IBM forcing $f_i^{\text{IBM}(s)}$ then follows from $u_i^{*(s)} = u_i^{*(s) \text{ no IBM}} + \alpha_{(s)} \Delta t f_i^{\text{IBM}(s)}$. Finally, the total IBM forcing f_i^{IBM} is obtained from summing $\alpha_{(s)} f_i^{\text{IBM}(s)}$, similar to equation A.7.

A.2.4 Boundary conditions at the texture surface

The no-slip and no-penetration conditions at the texture surface need to be sufficiently satisfied for the IBM to be accurate. Let a penetration velocity denote the absolute value of a texture-collocated velocity component. As u_{blade} and v_{blade} denote two velocity components that coincide with the texture, then

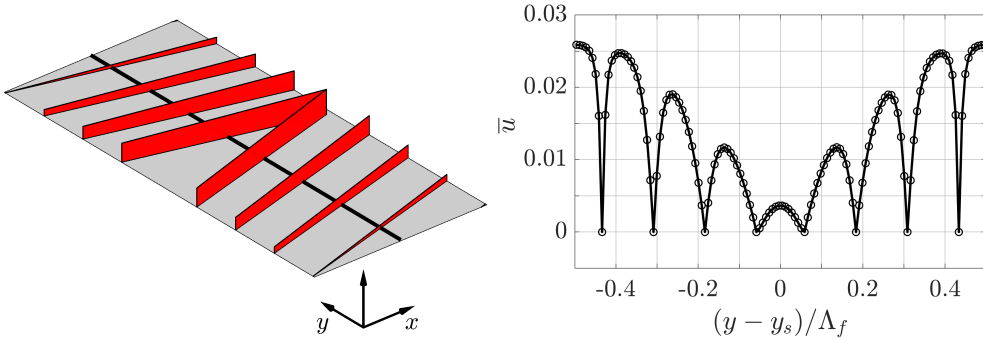


FIGURE A.3: Spanwise profile of streamwise velocity. *Left*: Bird’s-eye view of one unit cell of a herringbone texture with $N_{\text{groove}} = 4$, $\alpha = 165^\circ$. The thick line parallel to the y -axis cuts through the centre of the first grid cell above the bottom wall. *Right*: Time-averaged streamwise velocity as function of spanwise distance along the thick line in the left subfigure.

the corresponding penetration velocities are $u_{\text{pen}} = |u_{\text{blade}}|$ and $v_{\text{pen}} = |v_{\text{blade}}|$. Note that w_{pen} does not exist, as w does not coincide with the textures studied in the present work. To check whether the no-penetration condition was sufficiently satisfied, each tenth simulation time-step three penetration-related velocities were computed, namely $\langle u_{\text{pen}} \rangle$, $\langle v_{\text{pen}} \rangle$ and $\max(u_{\text{pen}}, v_{\text{pen}})$, where $\langle \dots \rangle$ denotes an average. The resulting time series were time averaged, yielding $\overline{\langle u_{\text{pen}} \rangle}$, $\overline{\langle v_{\text{pen}} \rangle}$ and $\overline{\max(u_{\text{pen}}, v_{\text{pen}})}$. The magnitude of these penetration velocities (normalised with the bulk velocity) is similar for all the simulations, namely a mean on the order of 10^{-6} to 10^{-5} and a maximum on the order of 10^{-4} to 10^{-3} . This shows that the penetration velocities are very small, so the no-slip and no-penetration conditions are sufficiently satisfied.

Figure A.3 presents a streamwise velocity profile as function of the spanwise distance for a herringbone riblet texture with 4 grooves per feather half (so $N_{\text{groove}} = 4$). The left subfigure shows the texture together with a line parallel to the y -axis. The right subfigure shows the time-averaged streamwise velocity profile that was extracted along that line. Clearly, the velocity is zero at the eight riblet locations. This illustrates that the boundary conditions at the riblet surfaces are satisfied.

A.3 Simulation parameters

An overview of all simulations with the corresponding parameters can be found in table A.1.

TABLE A.1: Parameters of all Direct Numerical Simulations presented in this paper. The simulations are grouped based on the type of texture. The short name indicates which parameters have been varied for a certain texture. The addition (sp. res.) refers to a case with double spanwise resolution; (res.) indicates a double streamwise and spanwise resolution. The parallel riblet variant with $N_{\text{groove}} = 0.5$ refers to the conventional parallel-riblet texture. The averaging time T is normalised with δ/u_τ derived from smooth-wall flow at the same bulk Reynolds number.

Short name	s^+	α ($^\circ$)	h/s	N_{groove}	L_x	L_y	N_x	N_y	N_z	Δx^+	Δy^+	Δz_w^+	Δz_c^+	N_{cg}	Re_b	Tu_τ/δ	$d^{\text{tot}} \cdot 10^3$	DC (%)	
Smooth wall																			
Re5500	-	-	-	-	5.8	2.9	512	512	320	4.0	2.0	0.50	1.7	-	5500	136	8.10 ± 0.02	0.0 ± 0.4	
Re11000	-	-	-	-	4.9	2.5	800	800	512	4.0	2.0	0.50	2.0	-	11000	66	6.81 ± 0.02	0.0 ± 0.5	
Re22000	-	-	-	-	5.4	2.7	1600	1600	1024	3.9	2.0	0.49	1.8	-	22000	14	5.70 ± 0.02	0.0 ± 0.6	
Parallel riblets																			
splus10	9.9	0	0.5	-	4.1	2.7	360	960	320	4.0	1.0	0.50	1.8	10	5500	95	7.54 ± 0.04	-6.9 ± 0.5	
splus17	16.9	0	0.5	-	4.1	2.9	360	1020	320	4.0	1.0	0.50	1.8	17	5500	120	7.49 ± 0.05	-7.6 ± 0.7	
splus24	23.9	0	0.5	-	4.1	2.7	360	960	320	4.0	1.0	0.50	1.9	24	5500	113	8.34 ± 0.04	3.0 ± 0.6	
splus24 (sp. res.)	23.9	0	0.5	-	4.1	2.7	360	1920	320	4.0	0.5	0.50	1.9	48	5500	69	8.38 ± 0.04	3.4 ± 0.6	
splus17 Re11000	16.8	0	0.5	-	4.3	2.9	704	1904	512	4.0	1.0	0.50	2.1	17	11000	39	6.17 ± 0.03	-9.3 ± 0.5	
splus24 Re11000	23.8	0	0.5	-	4.2	2.7	680	1728	512	4.0	1.0	0.50	2.2	24	11000	50	6.78 ± 0.04	-0.5 ± 0.7	
splus24 Re22000	24.0	0	0.5	-	4.1	2.6	1200	3072	1024	4.0	1.0	0.50	1.9	24	22000	13	5.61 ± 0.04	-1.6 ± 0.8	
Parallel riblets in yaw																			
alpha10	16.9	10	0.5	-	4.4	2.5	384	1200	320	4.1	0.7	0.50	1.8	24	5500	124	7.77 ± 0.05	-4.0 ± 0.7	
alpha15	16.9	15	0.5	-	4.5	2.5	384	800	320	4.1	1.1	0.50	1.8	16	5500	124	8.02 ± 0.03	-0.9 ± 0.4	
alpha15 (res.)	16.9	15	0.5	-	4.5	2.5	768	1600	320	2.0	0.5	0.50	1.8	32	5500	133	8.01 ± 0.04	-1.2 ± 0.5	
alpha20	16.9	20	0.5	-	4.5	2.6	512	800	320	3.1	1.1	0.50	1.8	16	5500	124	8.40 ± 0.04	3.7 ± 0.6	

Short name	s^+	α ($^\circ$)	h/s	N_{groove}	L_x	L_y	N_x	N_y	N_z	Δx^+	Δy^+	Δz_w^+	Δz_c^+	N_{cg}	Re_b	Tu_τ/δ	$d^{\text{tot}} \cdot 10^3$	DC (%)	
Herringbone riblets: $\alpha = 15^\circ$																			
ngroove1	17.0	15	0.5	1	4.7	3.2	400	1024	320	4.1	1.1	0.50	1.8	16	5500	77	12.46 ± 0.06	53.8 ± 0.8	
ngroove4	17.0	15	0.5	4	4.7	3.2	400	1024	320	4.1	1.1	0.50	1.8	16	5500	82	14.0 ± 0.1	73.4 ± 1.4	
ngroove4 (res.)	17.0	15	0.5	4	4.7	3.2	800	2048	320	2.1	0.5	0.50	1.8	32	5500	46	14.24 ± 0.09	75.7 ± 1.3	
ngroove16	17.0	15	0.5	16	4.7	3.2	400	1024	320	4.1	1.1	0.50	1.8	16	5500	72	10.86 ± 0.05	34.1 ± 0.7	
ngroove128	17.0	15	0.5	128	4.7	12.9	400	4096	320	4.1	1.1	0.50	1.8	16	5500	77	8.29 ± 0.02	2.3 ± 0.4	
Herringbone riblets: $\alpha = 165^\circ$																			
ngroove1	17.0	165	0.5	1	4.7	3.2	400	1024	320	4.1	1.1	0.50	1.8	16	5500	77	13.1 ± 0.1	61.2 ± 1.5	
ngroove4	17.0	165	0.5	4	4.7	3.2	400	1024	320	4.1	1.1	0.50	1.8	16	5500	75	11.98 ± 0.07	47.9 ± 1.0	
ngroove16	17.0	165	0.5	16	4.7	3.2	400	1024	320	4.1	1.1	0.50	1.8	16	5500	77	8.71 ± 0.04	7.5 ± 0.5	
ngroove32	17.0	165	0.5	32	4.7	3.2	400	1024	320	4.1	1.1	0.50	1.8	16	5500	73	8.27 ± 0.04	2.1 ± 0.5	
ngroove128	17.0	165	0.5	128	4.7	12.9	400	4096	320	4.1	1.1	0.50	1.8	16	5500	77	7.94 ± 0.02	-2.0 ± 0.4	
Herringbone riblets: $\alpha = 165^\circ$, shifted variant																			
ngroove1	17.0	165	0.5	1	4.7	3.2	400	1024	320	4.1	1.1	0.50	1.8	16	5500	76	13.0 ± 0.1	60.3 ± 1.3	
ngroove4	17.0	165	0.5	4	4.7	3.2	400	1024	320	4.1	1.1	0.50	1.8	16	5500	76	11.9 ± 0.1	47.2 ± 1.4	
ngroove16	17.0	165	0.5	16	4.7	3.2	400	1024	320	4.1	1.1	0.50	1.8	16	5500	77	8.79 ± 0.03	8.5 ± 0.5	
ngroove32	17.0	165	0.5	32	4.7	3.2	400	1024	320	4.1	1.1	0.50	1.8	16	5500	65	8.27 ± 0.05	2.1 ± 0.7	
Herringbone riblets: $\alpha = 0^\circ$, parallel variant																			
ngroove0.5	17.0	0	0.5	0.5	4.6	3.1	400	1024	320	4.0	1.1	0.50	1.8	16	5500	81	7.49 ± 0.03	-7.6 ± 0.5	
ngroove1	17.0	0	0.5	1	4.6	3.1	400	1024	320	4.0	1.1	0.50	1.8	16	5500	71	8.06 ± 0.03	-0.5 ± 0.5	
ngroove4	17.0	0	0.5	4	4.6	3.1	400	1024	320	4.0	1.1	0.50	1.8	16	5500	75	7.77 ± 0.04	-4.1 ± 0.6	
ngroove16	17.0	0	0.5	16	4.6	3.1	400	1024	320	4.0	1.1	0.50	1.8	16	5500	78	7.64 ± 0.08	-5.7 ± 1.0	

Appendix B

Coating deformation by oscillatory flow¹

B.1 Deformation of a compressible solid due to surface stresses

Starting from equation 4.16, the viscoelastic wave equation for ζ reduces to a simple homogeneous wave equation (cf. equation 4.10):

$$\frac{\partial^2 \zeta}{\partial t^2} - \frac{\Pi}{\rho_s} \frac{\partial^2 \zeta}{\partial z^2} = 0, \quad (\text{B.1})$$

with compressional-wave speed $c_p = \sqrt{\Pi/\rho_s}$. Using the boundary conditions for ζ and σ_{nc} (cf. equation 4.15), this equation can be solved to obtain:

$$\begin{aligned} \zeta_0(x, z) &= \zeta_1(x) \sin\left(\omega_{rp} \frac{z + \delta}{\delta}\right), \\ \zeta_1(x) &= \frac{f_0}{\omega^2} \frac{\rho_r \omega_{rp}}{\cos(\omega_{rp})} \frac{x}{\delta}. \end{aligned} \quad (\text{B.2})$$

The equation for ξ becomes an inhomogeneous wave equation with wave speed $c_s = \sqrt{G/\rho_s}$ (cf. equation 4.10):

$$\frac{\partial^2 \xi}{\partial t^2} - \frac{G}{\rho_s} \frac{\partial^2 \xi}{\partial z^2} = \frac{\Lambda + G}{\rho_s} \frac{\partial^2 \zeta}{\partial x \partial z}. \quad (\text{B.3})$$

¹ This appendix is (nearly) identical to the appendix of H. O. G. Benschop and W.-P. Breugem. Oscillatory pressure-driven laminar flow coupled to a compliant viscoelastic layer on a rigid base. 2018c, to be submitted.

Given the solution for ζ , the inhomogeneous term is independent of x , such that an x -independent solution for ξ can indeed be obtained. The resulting inhomogeneous second-order linear differential equation can be solved with the method of undetermined coefficients, using the boundary conditions for ξ and σ_{tc} (cf. equation 4.15):

$$\begin{aligned}\xi_0(z) &= \xi_1 \sin\left(\omega_{rs} \frac{z + \delta}{\delta}\right) + \xi_2 \left\{ \cos\left(\omega_{rs} \frac{z + \delta}{\delta}\right) - \cos\left(\omega_{rp} \frac{z + \delta}{\delta}\right) \right\}, \\ \xi_1 &= \frac{f_0}{\omega^2} \left\{ \frac{\rho_r \tan(\omega_{rs})}{\cos(\omega_{rp})} - \frac{2 \rho_r \omega_{rp} \tan(\omega_{rp})}{\omega_{rs} \cos(\omega_{rs})} + \frac{\rho_r h_r \omega_{rs} \sigma_{tc0}}{\cos(\omega_{rs}) \tau_{wt}} \right\}, \\ \xi_2 &= \frac{f_0}{\omega^2} \frac{\rho_r}{\cos(\omega_{rp})}.\end{aligned}\tag{B.4}$$

B.2 Interaction parameters in limiting cases

The expressions for χ_{pg} in the limits of small and large $|\omega_{rs}|$ are:

$$|\omega_{rs}| \rightarrow 0 \quad \chi_{pg} = \frac{1}{2} \rho_r \omega_{rs}^2, \tag{B.5a}$$

$$|\omega_{rs}| \rightarrow \infty \quad \chi_{pg} = -\rho_r. \tag{B.5b}$$

To obtain similar expressions for χ_s , we use the mathematical limits $\tan(\omega_{rs}) = \omega_{rs}$ for $|\omega_{rs}| \rightarrow 0$, $\tan(\omega_{rs}) = -i$ for $|\omega_{rs}| \rightarrow \infty$ and $0 < \phi_G \leq 45^\circ$, $\tanh(\sqrt{i\omega_{rf}})/\sqrt{i\omega_{rf}} = 1$ for $\omega_{rf} \rightarrow 0$, and $\tanh(\sqrt{i\omega_{rf}}) = 1$ for $\omega_{rf} \rightarrow \infty$, which yields:

$$|\omega_{rs}| \rightarrow 0 \quad \omega_{rf} \rightarrow 0 \quad \chi_s = \rho_r h_r \omega_{rs}^2 = \rho_r \frac{\omega^2 h \delta}{c_s^2}, \tag{B.6a}$$

$$|\omega_{rs}| \rightarrow 0 \quad \omega_{rf} \rightarrow \infty \quad \chi_s = \frac{\rho_r h_r \omega_{rs}^2}{\sqrt{i\omega_{rf}}} = \rho_r \sqrt{\frac{\omega^3 \delta^2 \nu}{ic_s^4}}, \tag{B.6b}$$

$$|\omega_{rs}| \rightarrow \infty \quad \omega_{rf} \rightarrow 0 \quad \chi_s = -i \rho_r \frac{\omega h}{c_s}, \tag{B.6c}$$

$$|\omega_{rs}| \rightarrow \infty \quad \omega_{rf} \rightarrow \infty \quad \chi_s = -\rho_r \sqrt{\frac{i\omega \nu}{c_s^2}}. \tag{B.6d}$$

The shear interaction parameter depends on the density ratio ρ_r and a dimensionless frequency that changes with the limiting conditions. For instance, when both channel height and coating thickness become very large, the relevant dimensionless frequency is $\omega \nu / c_s^2$.

Appendix C

Coating deformation by turbulent flow¹

C.1 Coating deformation by single travelling stress wave

C.1.1 General

Using the dimensionless numbers that have been introduced in section 5.4, the solid stress (5.7) and the viscoelastic wave equations (5.8) become:

$$\tilde{\sigma}_{ij} = \frac{\tilde{c}_p^2 - 2\tilde{c}_s^2}{\rho_r} \frac{\partial \tilde{\xi}_k}{\partial \tilde{x}_k} \delta_{ij} + \frac{\tilde{c}_s^2}{\rho_r} \left(\frac{\partial \tilde{\xi}_i}{\partial \tilde{x}_j} + \frac{\partial \tilde{\xi}_j}{\partial \tilde{x}_i} \right), \quad (\text{C.1a})$$

$$\frac{\partial^2 \tilde{\xi}_i}{\partial \tilde{t}^2} = (\tilde{c}_p^2 - \tilde{c}_s^2) \frac{\partial}{\partial \tilde{x}_i} \left(\frac{\partial \tilde{\xi}_k}{\partial \tilde{x}_k} \right) + \tilde{c}_s^2 \frac{\partial^2 \tilde{\xi}_i}{\partial \tilde{x}_j^2}. \quad (\text{C.1b})$$

The wave equations are solved using the Helmholtz decomposition, following several other authors (Lamb, 1904; Chase, 1991; Kulik, 2012; Zhang et al., 2017). Specifically, the displacement vector is expressed in terms of a scalar potential $\tilde{\phi}$ for compressional waves and a vector potential (nonzero y -component) $\tilde{\psi}$ for shear waves:

$$\tilde{\xi} = \frac{\partial \tilde{\phi}}{\partial \tilde{x}} + \frac{\partial \tilde{\psi}}{\partial \tilde{z}}, \quad \tilde{\zeta} = \frac{\partial \tilde{\phi}}{\partial \tilde{z}} - \frac{\partial \tilde{\psi}}{\partial \tilde{x}}. \quad (\text{C.2})$$

¹ This appendix is (nearly) identical to the appendix of H. O. G. Benschop, A. J. Greidanus, R. Delfos, J. Westerweel, and W.-P. Breugem. Deformation of a linear viscoelastic compliant coating in a turbulent flow. *Journal of Fluid Mechanics*, 2018b, accepted.

The viscoelastic wave equations are solved when both potentials satisfy a wave equation:

$$\frac{\partial^2 \tilde{\phi}}{\partial \tilde{t}^2} = \tilde{c}_p^2 \left\{ \frac{\partial^2 \tilde{\phi}}{\partial \tilde{x}^2} + \frac{\partial^2 \tilde{\phi}}{\partial \tilde{z}^2} \right\}, \quad \frac{\partial^2 \tilde{\psi}}{\partial \tilde{t}^2} = \tilde{c}_s^2 \left\{ \frac{\partial^2 \tilde{\psi}}{\partial \tilde{x}^2} + \frac{\partial^2 \tilde{\psi}}{\partial \tilde{z}^2} \right\}. \quad (\text{C.3})$$

Given the assumption that the solid behaves linearly, all quantities share the same dependence on time t and streamwise coordinate x :

$$\tilde{\phi}(\tilde{x}, \tilde{z}, \tilde{t}) = \tilde{\phi}_0(\tilde{z})e^{-i(\tilde{x}-\tilde{t})}, \quad \tilde{\psi}(\tilde{x}, \tilde{z}, \tilde{t}) = \tilde{\psi}_0(\tilde{z})e^{-i(\tilde{x}-\tilde{t})}, \quad (\text{C.4})$$

and similarly for the displacements, velocities and stresses. The stresses can be conveniently expressed in terms of $\tilde{\phi}$ and $\tilde{\psi}$:

$$\tilde{\sigma}_{13} = -\frac{2i\tilde{c}_s^2}{\rho_r} \frac{\partial \tilde{\phi}}{\partial \tilde{z}} + \frac{2\tilde{c}_s^2 - 1}{\rho_r} \tilde{\psi}, \quad \tilde{\sigma}_{33} = \frac{2\tilde{c}_s^2 - 1}{\rho_r} \tilde{\phi} + \frac{2i\tilde{c}_s^2}{\rho_r} \frac{\partial \tilde{\psi}}{\partial \tilde{z}}. \quad (\text{C.5})$$

The wave equations simplify to two ordinary differential equations:

$$\frac{d^2 \tilde{\phi}_0}{d(\tilde{z}/\tilde{\delta})^2} + \alpha_p^2 \tilde{\phi}_0 = 0, \quad \alpha_p = \tilde{\delta} \sqrt{\frac{1}{\tilde{c}_p^2} - 1} = \sqrt{\omega_{rp}^2 - \tilde{\delta}^2}, \quad (\text{C.6a})$$

$$\frac{d^2 \tilde{\psi}_0}{d(\tilde{z}/\tilde{\delta})^2} + \alpha_s^2 \tilde{\psi}_0 = 0, \quad \alpha_s = \tilde{\delta} \sqrt{\frac{1}{\tilde{c}_s^2} - 1} = \sqrt{\omega_{rs}^2 - \tilde{\delta}^2}, \quad (\text{C.6b})$$

with the following general solutions:

$$\tilde{\phi}_0 = \tilde{\phi}_1 \cos\left(\alpha_p \frac{\tilde{z} + \tilde{\delta}}{\tilde{\delta}}\right) + \tilde{\phi}_2 \sin\left(\alpha_p \frac{\tilde{z} + \tilde{\delta}}{\tilde{\delta}}\right), \quad (\text{C.7a})$$

$$\tilde{\psi}_0 = \tilde{\psi}_1 \cos\left(\alpha_s \frac{\tilde{z} + \tilde{\delta}}{\tilde{\delta}}\right) + \tilde{\psi}_2 \sin\left(\alpha_s \frac{\tilde{z} + \tilde{\delta}}{\tilde{\delta}}\right). \quad (\text{C.7b})$$

The dependence on \tilde{z} is written as $(\tilde{z} + \tilde{\delta})/\tilde{\delta} = (z + \delta)/\delta$ with $0 \leq (\tilde{z} + \tilde{\delta})/\tilde{\delta} \leq 1$ in the solid. The four coefficients that appear can be computed from four boundary conditions, cf. equations 5.12 and 5.13:

$$\begin{aligned} \tilde{\xi} \Big|_{\tilde{z}=-\tilde{\delta}} &= 0, & \tilde{\sigma}_{13} \Big|_{\tilde{z}=0} &= \tilde{\sigma}_{te0} e^{-i(\tilde{x}-\tilde{t})}, \\ \tilde{\zeta} \Big|_{\tilde{z}=-\tilde{\delta}} &= 0, & \tilde{\sigma}_{33} \Big|_{\tilde{z}=0} &= \tilde{\sigma}_{nc0} e^{-i(\tilde{x}-\tilde{t})}. \end{aligned} \quad (\text{C.8})$$

Given these relations, the four coefficients $\tilde{\phi}_1, \tilde{\phi}_2, \tilde{\psi}_1, \tilde{\psi}_2$ can be expressed in terms of $\tilde{\sigma}_{te0}$ and $\tilde{\sigma}_{nc0}$:

$$\begin{aligned}
\tilde{\phi}_1 &= \frac{-i\tilde{\psi}_2 \alpha_s}{\tilde{\delta}}, & \tilde{\psi}_1 &= \frac{i\tilde{\phi}_2 \alpha_p}{\tilde{\delta}}, & \tilde{\phi}_2 &= \rho_r \tilde{\delta}^2 \frac{n_{\tilde{\phi}_2}}{d_{\tilde{\phi}, \tilde{\psi}}}, & \tilde{\psi}_2 &= \rho_r \tilde{\delta}^2 \frac{n_{\tilde{\psi}_2}}{d_{\tilde{\phi}, \tilde{\psi}}}, \\
n_{\tilde{\phi}_2} &= \left(- \left(\tilde{c}_s^2 - \frac{1}{2} \right) \tilde{\delta}^2 \sin(\alpha_s) - \sin(\alpha_p) \alpha_p \alpha_s \tilde{c}_s^2 \right) \tilde{\sigma}_{nc0} \\
&\quad + \left(-i \left(\tilde{c}_s^2 - \frac{1}{2} \right) \tilde{\delta} \alpha_s \cos(\alpha_p) + i \cos(\alpha_s) \alpha_s \tilde{c}_s^2 \tilde{\delta} \right) \tilde{\sigma}_{tc0}, \\
n_{\tilde{\psi}_2} &= \left(i \left(\tilde{c}_s^2 - \frac{1}{2} \right) \tilde{\delta} \alpha_p \cos(\alpha_s) - i \cos(\alpha_p) \tilde{\delta} \tilde{c}_s^2 \alpha_p \right) \tilde{\sigma}_{nc0} \\
&\quad + \left(- \left(\tilde{c}_s^2 - \frac{1}{2} \right) \tilde{\delta}^2 \sin(\alpha_p) - \tilde{c}_s^2 \sin(\alpha_s) \alpha_p \alpha_s \right) \tilde{\sigma}_{tc0}, \\
d_{\tilde{\phi}, \tilde{\psi}} &= 2 \left(\left(\tilde{c}_s^2 - \frac{1}{2} \right)^2 \tilde{\delta}^4 + \alpha_p^2 \alpha_s^2 \tilde{c}_s^4 \right) \sin(\alpha_s) \sin(\alpha_p) \\
&\quad - 4 \alpha_s \tilde{\delta}^2 \alpha_p \left(\cos(\alpha_s) \left(\tilde{c}_s^4 - \frac{1}{2} \tilde{c}_s^2 + \frac{1}{8} \right) \cos(\alpha_p) - \tilde{c}_s^4 + \frac{1}{2} \tilde{c}_s^2 \right).
\end{aligned} \tag{C.9}$$

The displacements then follow from equation C.2 and the velocities are $\tilde{u}_i = \partial \tilde{\xi}_i / \partial \tilde{t} = i \tilde{\xi}_i$. The interface displacements and velocities are obtained by evaluating $\tilde{\xi}_i$ and \tilde{u}_i at $\tilde{z} = 0$.

C.1.2 Long-wave limit

The long-wave limit corresponds with $\delta_{r\lambda} \ll 1$. Starting from equations 5.7 and 5.8, all derivatives with respect to x can be neglected, such that the equations for ξ and ζ decouple:

$$\rho_s \frac{\partial^2 \xi}{\partial t^2} = G \frac{\partial^2 \xi}{\partial z^2}, \quad \sigma_{13} = G \frac{\partial \xi}{\partial z}, \quad \xi|_{z=-\delta} = 0, \quad \sigma_{13}|_{z=0} = \sigma_{tc}, \tag{C.10a}$$

$$\rho_s \frac{\partial^2 \zeta}{\partial t^2} = \Pi \frac{\partial^2 \zeta}{\partial z^2}, \quad \sigma_{33} = \Pi \frac{\partial \zeta}{\partial z}, \quad \zeta|_{z=-\delta} = 0, \quad \sigma_{33}|_{z=0} = \sigma_{nc}, \tag{C.10b}$$

and the following solutions are obtained:

$$\frac{\xi(z, t)}{\delta} = \frac{\sin(\omega_{rs}(1+z/\delta))}{\omega_{rs} \cos(\omega_{rs})} \frac{\sigma_{tc}(t)}{G}, \quad \frac{\zeta(z, t)}{\delta} = \frac{\sin(\omega_{rp}(1+z/\delta))}{\omega_{rp} \cos(\omega_{rp})} \frac{\sigma_{nc}(t)}{\Pi}. \tag{C.11}$$

C.1.3 Short-wave limit

The short-wave limit corresponds with $\delta_{r\lambda} \gg 1$. The first part of the derivation is the same as in appendix C.1.1 till equation C.5. The wave equations simplify to two ordinary differential equations, which are this time written as:

$$\frac{d^2 \tilde{\phi}_0}{d\tilde{z}^2} - \beta_p^2 \tilde{\phi}_0 = 0, \quad \beta_p = \sqrt{1 - c_{rp}^2}, \tag{C.12a}$$

$$\frac{d^2 \tilde{\psi}_0}{d\tilde{z}^2} - \beta_s^2 \tilde{\psi}_0 = 0, \quad \beta_s = \sqrt{1 - c_{rs}^2}, \quad (\text{C.12b})$$

with the following general solutions:

$$\tilde{\phi}_0 = \tilde{\phi}_3 e^{\beta_p \tilde{z}} + \tilde{\phi}_4 e^{-\beta_p \tilde{z}}, \quad (\text{C.13a})$$

$$\tilde{\psi}_0 = \tilde{\psi}_3 e^{\beta_s \tilde{z}} + \tilde{\psi}_4 e^{-\beta_s \tilde{z}}. \quad (\text{C.13b})$$

The short-wave solution should also apply when $\delta_{r\lambda} \propto \tilde{\delta} \rightarrow \infty$. To prevent that the solution grows exponentially when $\tilde{z} \rightarrow -\tilde{\delta} \rightarrow -\infty$, we require that $\tilde{\phi}_4 = 0 = \tilde{\psi}_4$. The two other constants, $\tilde{\phi}_3$ and $\tilde{\psi}_3$, then follow from the prescribed stresses at the coating surface (as in equation C.8), yielding:

$$\tilde{\phi}_3 = \rho_r c_{rs}^2 \frac{(c_{rs}^2 - 2) \tilde{\sigma}_{nc0} + 2i\sqrt{1 - c_{rs}^2} \tilde{\sigma}_{tc0}}{d_{sw}}, \quad (\text{C.14a})$$

$$\tilde{\psi}_3 = \rho_r c_{rs}^2 \frac{-2i\sqrt{1 - c_{rp}^2} \tilde{\sigma}_{nc0} + (c_{rs}^2 - 2) \tilde{\sigma}_{tc0}}{d_{sw}}, \quad (\text{C.14b})$$

$$d_{sw} = 4\sqrt{1 - c_{rp}^2} \sqrt{1 - c_{rs}^2} - (c_{rs}^2 - 2)^2. \quad (\text{C.14c})$$

The resulting surface displacements are given in equation 5.20.

C.2 Wavevector spectrum of measured surface displacement

This appendix considers the assumption of the spanwise homogeneity of the turbulent flow and the resulting surface displacements with use of the experiments described in section 5.6.1. Figure C.1 shows both an instantaneous two-dimensional vertical displacement field, as well as a space-time plot of the time-dependent vertical displacement for one spanwise coordinate at the centre of the coating. Although the instantaneous field is clearly nonhomogeneous in the spanwise direction, all structures travel predominantly in the streamwise direction with a relatively uniform speed. This suggests that a significant part of the wave energy is concentrated in a single streamwise-travelling mode. To check this hypothesis, the wavevector-frequency spectrum of the measured vertical surface displacement was computed. Specifically, the displacement can be written as the following sum of travelling waves:

$$\zeta(x, y, t) = \sum_{k_x} \sum_{k_y} \sum_{\omega} \Phi_{\zeta}(k_x, k_y, \omega) e^{-i(k_x x + k_y y - \omega t)}. \quad (\text{C.15})$$

The three-dimensional wavevector-frequency spectrum $\Phi_{\zeta}(k_x, k_y, \omega)$ was computed with use of MATLAB's Fast Fourier Transform (FFT) routine. The distribution of energy over the different wavevectors can conveniently be determined with use of the normalized dimensionless wavevector spectrum f_{ζ} . The relation

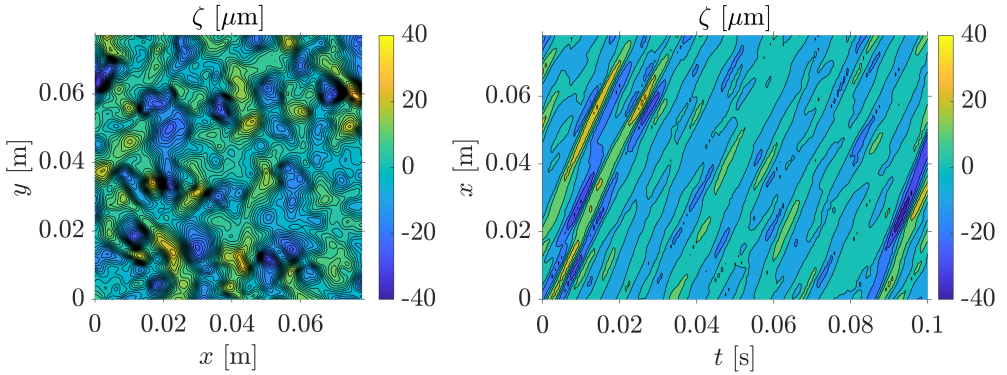


FIGURE C.1: Contour plots of the experimentally measured vertical surface displacement for coating 1 at $U_\infty = 3.5$ m/s, $Re_\tau = 6.1 \cdot 10^3$. The measurements were performed by Greidanus et al. (2017) and Delfos et al. (2017), see section 5.6 for details. *Left*: example of an instantaneous displacement field as function of the streamwise- and spanwise coordinates. *Right*: example of the time-dependent displacement as function of the streamwise and the temporal coordinate for one spanwise coordinate at the centre of the coating.

between Φ_ζ and f_ζ is given by (cf. equation 5.24):

$$\Phi_\zeta(k_x, k_y, \omega) = E_\zeta(\omega)(c/\omega)^2 f_\zeta(\tilde{k}_x, \tilde{k}_y), \quad \tilde{k}_x = \frac{k_x c}{\omega}, \quad \tilde{k}_y = \frac{k_y c}{\omega}. \quad (\text{C.16})$$

The dimensionless wavevector spectrum was computed using the following steps. The spatially-uniform point frequency spectrum $E_\zeta(\omega)$ was obtained by integration of $\Phi_\zeta(k_x, k_y, \omega)$ over k_x and k_y , cf. Hwang et al. (2009). The convection velocity was determined with use of a space-time correlation of the vertical displacement for one spanwise coordinate at the centre of the coating, see also Delfos et al. (2017). The thus obtained convection velocity was presumed to be constant for all wavevectors and frequencies. For every set of (k_x, k_y, ω) , equation C.16 was used to compute the dimensionless wavevector spectrum $f_\zeta(\tilde{k}_x, \tilde{k}_y)$. Finally, all sets of $(\tilde{k}_x, \tilde{k}_y)$ were uniformly distributed over the wavevector space with use of binning (63 bins between -2 and +2 for both \tilde{k}_x and \tilde{k}_y). The resulting dimensionless wavevector spectrum is shown in figure C.2, together with Corcos's model spectrum for wall pressure:

$$f_p(\tilde{k}_x, \tilde{k}_y) = \frac{\alpha_1 \alpha_2}{\pi^2 (\alpha_1^2 + (1 - \tilde{k}_x)^2) (\alpha_2^2 + \tilde{k}_y^2)}. \quad (\text{C.17})$$

The constants α_1 and α_2 are the longitudinal and lateral decay rates of the correlation, which typically range from 0.10 to 0.12 and 0.7 to 1.2, respectively (Hwang et al., 2009). The wavevector mode with $\tilde{k}_x = 1$ and $\tilde{k}_y = 0$ is most energetic for both the measured displacement spectrum and the modelled pressure spectrum. This observation is the second reason why spanwise homogeneity was assumed

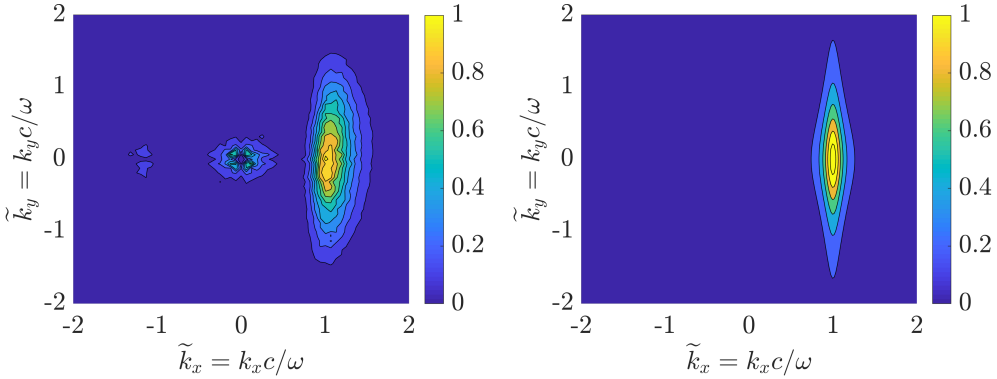


FIGURE C.2: Two-dimensional, dimensionless, normalized wavevector spectra of the vertical surface displacement and the wall pressure. *Left*: spectrum of the measured vertical surface displacement for coating 1 at $U_\infty = 3.5$ m/s, $Re_\tau = 6.1 \cdot 10^3$. The measurements were performed by Greidanus et al. (2017) and Delfos et al. (2017), see section 5.6 for details. *Right*: spectrum of the wall pressure as modelled by the Corcos spectrum with $\alpha_1 = 0.11$ and $\alpha_2 = 0.7$ (cf. equation C.17).

in the present study.

C.3 Travelling waves and point spectra

This appendix explains how the concept of travelling waves can be used to compute root-mean-square (rms) values and point spectra. Consider a function $f_{\text{comp}}(x, t)$ as a summation of travelling waves:

$$f_{\text{comp}}(x, t) = \sum_{m=1}^{N_m} f_m e^{-i(k_m x - \omega_m t)}, \quad f_m = |f_m| e^{i\phi_m}. \quad (\text{C.18})$$

The subscript ‘comp’ denotes that the function is complex. Spectra and rms-values require multiplications, so it is important to use the real signal $f(x, t) = \text{Re}\{f_{\text{comp}}(x, t)\}$:

$$f(x, t) = \sum_{m=1}^{N_m} |f_m| \cos(k_m x - \omega_m t - \phi_m). \quad (\text{C.19})$$

The rms is defined as $f_{\text{rms}}^2 = \langle \overline{f^2} \rangle_x$ with a temporal and a spatial average given by:

$$\overline{\psi} = \frac{1}{T} \int_{-T/2}^{T/2} \psi dt, \quad \langle \psi \rangle_x = \frac{1}{L_x} \int_{-L_x/2}^{L_x/2} \psi dx. \quad (\text{C.20})$$

In the limit that the integration intervals approach infinity ($T \rightarrow \infty$, $L_x \rightarrow \infty$), one can derive the following relation to compute f_{rms} from $|f_m|$:

$$f_{\text{rms}}^2 = \langle \overline{f^2} \rangle_x = \sum_{m=1}^{N_m} \frac{1}{2} |f_m|^2. \quad (\text{C.21})$$

Next, we derive a relation between the mode amplitudes and the point spectrum. For continuous frequencies, the one-sided point spectrum $E_f(\omega)$ is defined such that integration over all positive frequencies results in the square of the rms (as in equation 5.25):

$$f_{\text{rms}}^2 = \int_0^\infty E_f(\omega) d\omega = \int_{-\infty}^\infty \omega E_f(\omega) d \ln(\omega). \quad (\text{C.22})$$

The integration variable is the frequency itself in the first integral and the logarithm of the frequency in the second integral. The discrete analogies are:

$$\text{linear scale} \quad f_{\text{rms}}^2 = \sum_{m=1}^{N_m} \frac{1}{2} |f_m|^2 = \sum_{m=1}^{N_m} E_{f,m} \Delta\omega, \quad (\text{C.23a})$$

$$\text{logarithmic scale} \quad f_{\text{rms}}^2 = \sum_{m=1}^{N_m} \frac{1}{2} |f_m|^2 = \sum_{m=1}^{N_m} \omega_m E_{f,m} \Delta \ln(\omega). \quad (\text{C.23b})$$

From these relations it is clear how the discrete point spectrum $E_{f,m}$ can be computed from $|f_m|$ for linearly and logarithmically distributed frequencies.

Bibliography

- H. A. Abdulbari, R. M. Yunus, N. H. Abdurahman, and A. Charles. Going against the flow—A review of non-additive means of drag reduction. *Journal of Industrial and Engineering Chemistry*, 19(1):27–36, 2013.
- H. Abe, H. Kawamura, and H. Choi. Very large-scale structures and their effects on the wall shear-stress fluctuations in a turbulent channel flow up to $Re_\tau = 640$. *Journal of fluids engineering*, 126(5):835–843, 2004.
- K. Abe, A. Matsumoto, H. Munakata, and I. Tani. Drag reduction by sand grain roughness. In A. Gyr, editor, *Structure of Turbulence and Drag Reduction*, pages 341–348. Springer Berlin Heidelberg, 1990.
- R. J. Adrian and J. Westerweel. *Particle Image Velocimetry*. Cambridge Aerospace Series. Cambridge University Press, 2011.
- W. Anderson, J. M. Barros, K. T. Christensen, and A. Awasthi. Numerical and experimental study of mechanisms responsible for turbulent secondary flows in boundary layer flows over spanwise heterogeneous roughness. *Journal of Fluid Mechanics*, 768:316–347, 2015.
- S. Baek and A. Srinivasa. Diffusion of a fluid through an elastic solid undergoing large deformation. *International Journal of non-linear Mechanics*, 39(2):201–218, 2004.
- C. Bailly and C. Bogey. An overview of numerical methods for acoustic wave propagation. In *European Conference on Computational Fluid Dynamics, EC-COMAS CFD*, P. Wesseling, E. Onate, J. Périaux (Eds). Citeseer, 2006.
- J. M. Barros and K. T. Christensen. Observations of turbulent secondary flows in a rough-wall boundary layer. *Journal of Fluid Mechanics*, 748:R1,1–13, 2014.
- P. W. Bearman and J. K. Harvey. Golf ball aerodynamics. *The Aeronautical Quarterly*, 27(2):112–122, 1976.

- D. W. Bechert, M. Bruse, W. Hage, J. G. T. Van der Hoeven, and G. Hoppe. Experiments on drag-reducing surfaces and their optimization with an adjustable geometry. *Journal of Fluid Mechanics*, 338(5):59–87, 1997.
- T. B. Benjamin. The threefold classification of unstable disturbances in flexible surfaces bounding inviscid flows. *Journal of Fluid Mechanics*, 16(3):436–450, 1963.
- H. O. G. Benschop. Deliverable 1.15: Report on hydrodynamic performance of provided specimens of WP1.1, August 2017. URL http://seafrost-project.eu/images/Deliverable_SEAFROST_1.15.pdf.
- H. O. G. Benschop and W.-P. Breugem. Drag reduction by herringbone riblet texture in direct numerical simulations of turbulent channel flow. *Journal of Turbulence*, 18(8):717–759, 2017.
- H. O. G. Benschop and W.-P. Breugem. Oscillatory laminar shear flow over a compliant viscoelastic layer on a rigid base. *ArXiv e-prints*, May 2017.
- H. O. G. Benschop and W.-P. Breugem. Oscillatory pressure-driven laminar flow coupled to a compliant viscoelastic layer on a rigid base. 2018c, to be submitted.
- H. O. G. Benschop, A. J. Guerin, A. Brinkmann, M. L. Dale, A. A. Finnie, W.-P. Breugem, A. S. Clare, D. Stübing, C. Price, and K. J. Reynolds. Drag-reducing riblets with fouling-release properties: development and testing. *Biofouling*, pages 1–13, 2018.
- H. O. G. Benschop, A. J. Greidanus, R. Delfos, J. Westerweel, and W.-P. Breugem. Deformation of a linear viscoelastic compliant coating in a turbulent flow. *Journal of Fluid Mechanics*, 2018b, accepted.
- D. Bergel. The dynamic elastic properties of the arterial wall. *The Journal of Physiology*, 156(3):458, 1961.
- M. Bernardini, S. Pirozzoli, and P. Orlandi. Velocity statistics in turbulent channel flow up to $Re_\tau = 4000$. *Journal of Fluid Mechanics*, 742:171–191, 2014.
- K. M. Berntsson, P. R. Jonsson, M. Lejhall, and P. Gatenholm. Analysis of behavioural rejection of micro-textured surfaces and implications for recruitment by the barnacle *Balanus improvisus*. *Journal of Experimental Marine Biology and Ecology*, 251(1):59–83, 2000.
- S. Bezuijen. Hydrodynamic drag reduction in turbulent boundary layer flow using riblets. Master’s thesis, Delft University of Technology, The Netherlands, 2017.
- B. Bhushan and M. Caspers. An overview of additive manufacturing (3D printing) for microfabrication. *Microsystem Technologies*, 23(4):1117–1124, 2017.

- J. O. Blanch, J. O. Robertsson, and W. W. Symes. Modeling of a constant Q: Methodology and algorithm for an efficient and optimally inexpensive viscoelastic technique. *Geophysics*, 60(1):176–184, 1995.
- T. Bohlen. Parallel 3-D viscoelastic finite difference seismic modelling. *Computers & Geosciences*, 28(8):887–899, 2002.
- I. Borazjani, L. Ge, and F. Sotiropoulos. Curvilinear immersed boundary method for simulating fluid structure interaction with complex 3D rigid bodies. *Journal of Computational physics*, 227(16):7587–7620, 2008.
- J. P. Boyd. *Chebyshev and Fourier Spectral Methods: Second Revised Edition*. Dover Books on Mathematics. Dover Publications, 2001.
- W. P. Breugem and B. J. Boersma. Direct numerical simulations of turbulent flow over a permeable wall using a direct and a continuum approach. *Physics of Fluids (1994-present)*, 17(2):025103, 2005.
- D. M. Bushnell and C. B. McGinley. Turbulence control in wall flows. *Annual Review of Fluid Mechanics*, 21(1):1–20, 1989.
- D. M. Bushnell and K. J. Moore. Drag reduction in nature. *Annual Review of Fluid Mechanics*, 23(1):65–79, 1991.
- D. M. Bushnell, J. N. Hefner, and R. L. Ash. Effect of compliant wall motion on turbulent boundary layers. *Physics of Fluids (1958-1988)*, 20(10):S31–S48, 1977.
- J. C. Butcher. Numerical methods for ordinary differential equations in the 20th century. In *Numerical analysis: Historical developments in the 20th century*, pages 449–477. Elsevier, 2000.
- J. A. Callow and M. E. Callow. Trends in the development of environmentally friendly fouling-resistant marine coatings. *Nature communications*, 2:244, 2011.
- S. Čanić, B. Muha, and M. Bukač. Fluid–structure interaction in hemodynamics: Modeling, analysis, and numerical simulation. In *Fluid-Structure Interaction and Biomedical Applications*, pages 79–195. Springer, 2014.
- R. N. Capps. Dynamic Young’s moduli of some commercially available polyurethanes. *The Journal of the Acoustical Society of America*, 73(6):2000–2005, 1983.
- J. Carcione. Boundary conditions for wave propagation problems. *Finite elements in analysis and design*, 16(3-4):317–327, 1994.
- J. Carcione. A 2D Chebyshev differential operator for the elastic wave equation. *Computer Methods in Applied Mechanics and Engineering*, 130(1-2):33–45, 1996.
- J. M. Carcione. *Wave Fields in Real Media (Third Edition)*. Elsevier, 2015.

- J. M. Carcione, G. C. Herman, and A. Ten Kroode. Seismic modeling. *Geophysics*, 67(4):1304–1325, 2002.
- M. Carfagni, E. Lenzi, and M. Pierini. The loss factor as a measure of mechanical damping. In *Proceedings of the 16th International Modal Analysis Conference*, volume 3243, page 580, 1998.
- P. Carpenter and A. Garrad. The hydrodynamic stability of flow over Kramer-type compliant surfaces. Part 2. Flow-induced surface instabilities. *Journal of Fluid Mechanics*, 170:199–232, 1986.
- S. L. Ceccio. Friction drag reduction of external flows with bubble and gas injection. *Annual Review of Fluid Mechanics*, 42:183–203, 2010.
- D. M. Chase. Generation of fluctuating normal stress in a viscoelastic layer by surface shear stress and pressure as in turbulent boundary-layer flow. *The Journal of the Acoustical Society of America*, 89(6):2589–2596, 1991.
- H. Chen, F. Rao, X. Shang, D. Zhang, and I. Hagiwara. Biomimetic drag reduction study on herringbone riblets of bird feather. *Journal of Bionic Engineering*, 10(3):341–349, 2013.
- H. Chen, F. Rao, X. Shang, D. Zhang, and I. Hagiwara. Flow over bio-inspired 3D herringbone wall riblets. *Experiments in Fluids*, 55(3):1–7, 2014a.
- H. Chen, D. Che, X. Zhang, and D. Zhang. UV grafting process for synthetic drag reduction of biomimetic riblet surfaces. *Journal of Applied Polymer Science*, 132(33):1–8, 2015.
- H. W. Chen, F. G. Rao, D. Y. Zhang, and X. P. Shang. Drag Reduction Study about Bird Feather Herringbone Riblets. *Applied Mechanics and Materials*, 461:201–205, 2014b.
- N.-S. Cheng. Formula for the viscosity of a glycerol-water mixture. *Industrial & engineering chemistry research*, 47(9):3285–3288, 2008.
- P. Cherukat, Y. Na, T. J. Hanratty, and J. B. McLaughlin. Direct numerical simulation of a fully developed turbulent flow over a wavy wall. *Theoretical and computational fluid dynamics*, 11(2):109–134, 1998.
- H. Choi, P. Moin, and J. Kim. Direct numerical simulation of turbulent flow over riblets. *Journal of Fluid Mechanics*, 255:503–539, 1993.
- H. Choi, P. Moin, and J. Kim. Active turbulence control for drag reduction in wall-bounded flows. *Journal of Fluid Mechanics*, 262:75–110, 1994.
- J. Choi, W.-P. Jeon, and H. Choi. Mechanism of drag reduction by dimples on a sphere. *Physics of Fluids (1994-present)*, 18(4):041702, 2006.

- K.-S. Choi, X. Yang, B. R. Clayton, E. J. Glover, M. Atlar, B. N. Semenov, and V. M. Kulik. Turbulent drag reduction using compliant surfaces. *Proceedings of the Royal Society of London. Series A: Mathematical, Physical and Engineering Sciences*, 453(1965):2229–2240, 1997.
- R. M. Christensen. *Theory of Viscoelasticity (Second Edition)*. Academic Press, 1982.
- D. Chung. Review: Materials for vibration damping. *Journal of Materials Science*, 36(24):5733–5737, 2001.
- D. Chung, L. Chan, M. MacDonald, N. Hutchins, and A. Ooi. A fast direct numerical simulation method for characterising hydraulic roughness. *Journal of Fluid Mechanics*, 773:418–431, 2015.
- T. J. Chung. *General Continuum Mechanics*. Cambridge University Press, 2007.
- R. H. Cox. Wave propagation through a Newtonian fluid contained within a thick-walled, viscoelastic tube. *Biophysical Journal*, 8(6):691–709, 1968.
- R. H. Cox. Wave propagation through a Newtonian fluid contained within a thick-walled viscoelastic tube: The influence of wall compressibility. *Journal of biomechanics*, 3(3):317–335, 1970.
- A. Cunha-Filho, A. de Lima, M. Donadon, and L. Leão. Flutter suppression of plates using passive constrained viscoelastic layers. *Mechanical Systems and Signal Processing*, 2016.
- G. Daschiel, T. Baier, J. Saal, and B. Frohnäpfel. On the flow resistance of wide surface structures. *PAMM*, 12(1):569–570, 2012.
- V. De Angelis, P. Lombardi, and S. Banerjee. Direct numerical simulation of turbulent flow over a wavy wall. *Physics of Fluids (1994-present)*, 9(8):2429–2442, 1997.
- A. De Boer. *Computational fluid-structure interaction: spatial coupling, coupling shell and mesh deformation*. PhD thesis, Delft University of Technology, 2008.
- B. Dean and B. Bhushan. Shark-skin surfaces for fluid-drag reduction in turbulent flow: a review. *Philosophical Transactions of the Royal Society A: Mathematical, Physical and Engineering Sciences*, 368(1929):4775–4806, 2010.
- J. Degroote. *Development of algorithms for the partitioned simulation of strongly coupled fluid-structure interaction problems*. PhD thesis, Ghent University, 2010.
- J. C. Del Álamo and J. Jiménez. Estimation of turbulent convection velocities and corrections to Taylor’s approximation. *Journal of Fluid Mechanics*, 640: 5–26, 2009.

- R. Delfos, A. J. Greidanus, F. Charruault, and J. Westerweel. Wave characteristics of a compliant coating under a turbulent flow. In *AMT'17 Conference Proceedings*, Glasgow, 2017. URL www.amt17.org.uk/Proceedings/tabid/6147/Default.aspx.
- Department for Transport UK. Shipping Fleet Statistics 2016. In *Maritime and shipping statistics*. Department for Transport, UK, 2017.
- G. Díez, M. Soto, and J. Blanco. Biological characterization of the skin of shortfin mako shark *Isurus oxyrinchus* and preliminary study of the hydrodynamic behaviour through computational fluid dynamics. *Journal of Fish Biology*, 87(1):123–137, 2015.
- Y. Du, V. Symeonidis, and G. Karniadakis. Drag reduction in wall-bounded turbulence via a transverse travelling wave. *Journal of Fluid Mechanics*, 457: 1–34, 2002.
- Y. Dubief and F. Delcayre. On coherent-vortex identification in turbulence. *Journal of Turbulence*, 1(11):1–22, 2000.
- J. H. Duncan. The response of an incompressible, viscoelastic coating to pressure fluctuations in a turbulent boundary layer. *Journal of Fluid Mechanics*, 171: 339–363, 1986.
- J. H. Duncan, A. M. Waxman, and M. P. Tulin. The dynamics of waves at the interface between a viscoelastic coating and a fluid flow. *Journal of Fluid Mechanics*, 158:177–197, 1985.
- T. Endo and R. Himeno. Direct numerical simulation of turbulent flow over a compliant surface. *Journal of Turbulence*, 3:N7, 2002.
- B. Fabre, J. Gilbert, A. Hirschberg, and X. Pelorson. Aeroacoustics of musical instruments. *Annual Review of Fluid Mechanics*, 44:1–25, 2012.
- E. Fadlun, R. Verzicco, P. Orlandi, and J. Mohd-Yusof. Combined immersed-boundary finite-difference methods for three-dimensional complex flow simulations. *Journal of Computational Physics*, 161(1):35–60, 2000.
- X. Fang, Z. Yang, B.-C. Wang, M. F. Tachie, and D. J. Bergstrom. Highly-disturbed turbulent flow in a square channel with v-shaped ribs on one wall. *International Journal of Heat and Fluid Flow*, 56:182–197, 2015.
- J. H. Ferziger and M. Perić. *Computational Methods for Fluid Dynamics*. Springer Berlin Heidelberg, 2002.
- A. A. Finnie and D. N. Williams. Paint and coatings technology for the control of marine fouling. In S. Dürr and J. C. Thomason, editors, *Biofouling*. Wiley-Blackwell, Oxford (UK), 2010.

- M. C. Fischer and R. L. Ash. A general review of concepts for reducing skin friction, including recommendations for future studies. Technical report, NASA Langley Research Center, 1974.
- B. Fornberg. *A Practical Guide to Pseudospectral Methods*. Cambridge Monographs on Applied and Computational Mathematics. Cambridge University Press, 1998.
- B. Fornberg and D. M. Sloan. A review of pseudospectral methods for solving partial differential equations. *Acta numerica*, 3:203–267, 1994.
- J. H. M. Fransson, A. Talamelli, L. Brandt, and C. Cossu. Delaying transition to turbulence by a passive mechanism. *Physical Review Letters*, 96(6):064501, 2006.
- B. Frohnafel, Y. Hasegawa, and M. Quadrio. Money versus time: evaluation of flow control in terms of energy consumption and convenience. *Journal of Fluid Mechanics*, 700:406–418, 2012.
- K. Fukagata, K. Iwamoto, and N. Kasagi. Contribution of Reynolds stress distribution to the skin friction in wall-bounded flows. *Physics of Fluids (1994-present)*, 14(11):L73–L76, 2002.
- K. Fukagata, S. Kern, P. Chatelain, P. Koumoutsakos, and N. Kasagi. Evolutionary optimization of an anisotropic compliant surface for turbulent friction drag reduction. *Journal of Turbulence*, 9(35):1–17, 2008.
- M. Fulgosi, D. Lakehal, S. Banerjee, and V. De Angelis. Direct numerical simulation of turbulence in a sheared air–water flow with a deformable interface. *Journal of fluid mechanics*, 482:319–345, 2003.
- M. Gad-el Hak. Compliant coatings for drag reduction. *Progress in Aerospace Sciences*, 38(1):77–99, 2002.
- M. Gad-el Hak, R. F. Blackwelder, and J. J. Riley. On the interaction of compliant coatings with boundary-layer flows. *Journal of Fluid Mechanics*, 140:257–280, 1984.
- D. V. Gaitonde, J. S. Shang, and J. L. Young. Practical aspects of higher-order numerical schemes for wave propagation phenomena. *International Journal for Numerical Methods in Engineering*, 45(12):1849–1869, 1999.
- X. Gao and B. Sunden. Heat transfer and pressure drop measurements in rib-roughened rectangular ducts. *Experimental Thermal and Fluid Science*, 24(1): 25–34, 2001.
- R. García-Mayoral and J. Jiménez. Drag reduction by riblets. *Philosophical Transactions of the Royal Society A: Mathematical, Physical and Engineering Sciences*, 369(1940):1412–1427, 2011a.

- R. García-Mayoral and J. Jiménez. Hydrodynamic stability and breakdown of the viscous regime over riblets. *Journal of Fluid Mechanics*, 678:317–347, 2011b.
- R. García-Mayoral and J. Jiménez. Scaling of turbulent structures in riblet channels up to $Re_\tau \approx 550$. *Physics of Fluids (1994-present)*, 24(10):105101, 2012.
- D. Gatti and M. Quadrio. Performance losses of drag-reducing spanwise forcing at moderate values of the Reynolds number. *Physics of Fluids (1994-present)*, 25(12):125109, 2013.
- T. Gervais, J. El-Ali, A. Günther, and K. F. Jensen. Flow-induced deformation of shallow microfluidic channels. *Lab on a Chip*, 6(4):500–507, 2006.
- S. Ghosh, T. K. Mandal, G. Das, and P. K. Das. Review of oil water core annular flow. *Renewable and Sustainable Energy Reviews*, 13(8):1957–1965, 2009.
- I. Glasgow, S. Lieber, and N. Aubry. Parameters influencing pulsed flow mixing in microchannels. *Analytical Chemistry*, 76(16):4825–4832, 2004.
- A. Glezer and M. Amitay. Synthetic jets. *Annual review of fluid mechanics*, 34(1):503–529, 2002.
- D. Goldstein and T.-C. Tuan. Secondary flow induced by riblets. *Journal of Fluid Mechanics*, 363:115–151, 1998.
- D. Goldstein, R. Handler, and L. Sirovich. Direct numerical simulation of turbulent flow over a modeled riblet covered surface. *Journal of Fluid Mechanics*, 302:333–376, 1995.
- M. Goody. An empirical spectral model of surface-pressure fluctuations that includes Reynolds number effects. *AIAA Paper*, 2565(8), 2002.
- M. Goody. Empirical spectral model of surface pressure fluctuations. *AIAA journal*, 42(9):1788–1794, 2004.
- S. Govindjee and P. A. Mihalic. Computational methods for inverse deformations in quasi-incompressible finite elasticity. *International Journal for Numerical Methods in Engineering*, 43(5):821–838, 1998.
- W. R. Graham. A comparison of models for the wavenumber–frequency spectrum of turbulent boundary layer pressures. *Journal of sound and vibration*, 206(4):541–565, 1997.
- A. Greidanus, R. Delfos, S. Tokgoz, and J. Westerweel. Turbulent Taylor–Couette flow over riblets: drag reduction and the effect of bulk fluid rotation. *Experiments in Fluids*, 56(5):107, 2015.
- A. J. Greidanus, R. Delfos, and J. Westerweel. Fluid-Structure Interaction of compliant coatings under turbulent flow conditions: Force and PIV analysis. In *AMT’17 Conference Proceedings*, Glasgow, 2017. URL www.amt17.org.uk/Proceedings/tabid/6147/Default.aspx.

- R. Grüneberger, F. Kramer, W. Hage, R. Meyer, F. Thiele, and E. Wassen. Experimental investigation of oscillating riblets for turbulent drag reduction. In A. Dillmann, G. Heller, H.-P. Kreplin, W. Nitsche, and I. Peltzer, editors, *New Results in Numerical and Experimental Fluid Mechanics VIII*, volume 121 of *Notes on Numerical Fluid Mechanics and Multidisciplinary Design*, pages 193–200. Springer Berlin Heidelberg, 2013.
- J. B. Grotberg and O. E. Jensen. Biofluid mechanics in flexible tubes. *Annual Review of Fluid Mechanics*, 36:121–147, 2004.
- R. Grüneberger, F. Kramer, E. Wassen, W. Hage, R. Meyer, and F. Thiele. Influence of wave-like riblets on turbulent friction drag. In C. Tropea and H. Bleckmann, editors, *Nature-Inspired Fluid Mechanics*, pages 311–329. Springer Berlin Heidelberg, 2012.
- M. Y. Gundogdu and M. O. Carpinlioglu. Present state of art on pulsatile flow theory. part 1. laminar and transitional flow regimes. *JSME International Journal Series B Fluids and Thermal Engineering*, 42(3):384–397, 1999.
- W. Hage, D. W. Bechert, and M. Bruse. Yaw angle effects on optimized riblets. In P. Thiede, editor, *Aerodynamic Drag Reduction Technologies*, pages 278–285. Springer Berlin Heidelberg, 2001.
- J. Hale, D. McDonald, and J. Womersley. Velocity profiles of oscillating arterial flow, with some calculations of viscous drag and the reynolds number. *The Journal of Physiology*, 128(3):629, 1955.
- M. Hamadiche and M. Gad-el Hak. Spatiotemporal stability of flow through collapsible, viscoelastic tubes. *AIAA Journal*, 42(4):772–786, 2004.
- B. S. Hardy, K. Uechi, J. Zhen, and H. P. Kavehpour. The deformation of flexible PDMS microchannels under a pressure driven flow. *Lab on a Chip*, 9(7):935–938, 2009.
- M. Heil and A. L. Hazel. Fluid-structure interaction in internal physiological flows. *Annual Review of Fluid Mechanics*, 43:141–162, 2011.
- S. Hestholm. Three-dimensional finite difference viscoelastic wave modelling including surface topography. *Geophysical Journal International*, 139(3):852–878, 1999.
- B. R. Hodges and R. L. Street. On simulation of turbulent nonlinear free-surface flows. *Journal of Computational Physics*, 151(2):425–457, 1999.
- S. Hodis and M. Zamir. Mechanical events within the arterial wall under the forces of pulsatile flow: a review. *Journal of the Mechanical behavior of biomedical materials*, 4(8):1595–1602, 2011.
- G. Hou, J. Wang, and A. Layton. Numerical methods for fluid-structure interaction — a review. *Communications in Computational Physics*, 12(2):337–377, 2012.

- S. Hoyas and J. Jiménez. Reynolds number effects on the Reynolds-stress budgets in turbulent channels. *Physics of Fluids (1994-present)*, 20(10):101511, 2008.
- Z. Hu, C. L. Morfey, and N. D. Sandham. Wall pressure and shear stress spectra from direct simulations of channel flow. *AIAA Journal*, 44(7):1541–1549, 2006.
- Y. Hwang, W. K. Bonness, and S. A. Hambric. Comparison of semi-empirical models for turbulent boundary layer wall pressure spectra. *Journal of Sound and Vibration*, 319(1):199–217, 2009.
- B. M. Irons and R. C. Tuck. A version of the Aitken accelerator for computer iteration. *International Journal for Numerical Methods in Engineering*, 1(3):275–277, 1969.
- O. O. Ivanov, V. V. Vedeneev, V. M. Kulik, and A. V. Boiko. The influence of compliant coatings on skin friction in the turbulent boundary layer. *Journal of Physics: Conference Series*, 894(1):012036, 2017.
- B. D. Iverson and S. V. Garimella. Recent advances in microscale pumping technologies: a review and evaluation. *Microfluidics and Nanofluidics*, 5(2):145–174, 2008.
- K. Iwamoto, Y. Suzuki, and N. Kasagi. Reynolds number effect on wall turbulence: toward effective feedback control. *International Journal of Heat and Fluid Flow*, 23(5):678–689, 2002.
- K. Iwamoto, K. Fukagata, N. Kasagi, and Y. Suzuki. Friction drag reduction achievable by near-wall turbulence manipulation at high Reynolds numbers. *Physics of Fluids (1994-present)*, 17(1):011702, 2005.
- K. M. B. Jansen. Thermomechanical modelling and characterisation of polymers, March 2007.
- J. Jiménez. Turbulent flows over rough walls. *Annual Review of Fluid Mechanics*, 36:173–196, 2004.
- T. Jung, H. Choi, and J. Kim. Effects of the air layer of an idealized superhydrophobic surface on the slip length and skin-friction drag. *Journal of Fluid Mechanics*, 790, 2016.
- R. Kamakoti and W. Shyy. Fluid–structure interaction for aeroelastic applications. *Progress in Aerospace Sciences*, 40(8):535–558, 2004.
- Y. Kametani and K. Fukagata. Direct numerical simulation of spatially developing turbulent boundary layers with uniform blowing or suction. *Journal of Fluid Mechanics*, 681:154–172, 2011.
- Y. Kametani and K. Fukagata. Direct numerical simulation of spatially developing turbulent boundary layer for skin friction drag reduction by wall surface-heating or cooling. *Journal of Turbulence*, 13(34):1–20, 2012.

- N. A. Kampanis, V. Dougalis, and J. A. Ekaterinaris. *Effective computational methods for wave propagation*. CRC Press, 2008.
- C.-K. Kang, H. Aono, C. E. S. Cesnik, and W. Shyy. Effects of flexibility on the aerodynamic performance of flapping wings. *Journal of fluid mechanics*, 689:32–74, 2011.
- G. E. Karniadakis and K.-S. Choi. Mechanisms on transverse motions in turbulent wall flows. *Annual Review of Fluid Mechanics*, 35(1):45–62, 2003.
- E. Kim and H. Choi. Space–time characteristics of a compliant wall in a turbulent channel flow. *Journal of Fluid Mechanics*, 756:30–53, 2014.
- J. Kim. Physics and control of wall turbulence for drag reduction. *Philosophical Transactions of the Royal Society A: Mathematical, Physical and Engineering Sciences*, 369(1940):1396–1411, 2011.
- K. Koeltzsch, A. Dinkelacker, and R. Grundmann. Flow over convergent and divergent wall riblets. *Experiments in Fluids*, 33(2):346–350, 2002.
- A. S. Kommeren. *Structured antifouling coatings for the marine environment*. PhD thesis, Eindhoven University of Technology, 2017.
- H. Kordy. Process abilities of the riblet-coating process with dual-cure lacquers. *CIRP Journal of Manufacturing Science and Technology*, 11:1–9, 2015.
- D. Kosloff and H. Tal-Ezer. A modified Chebyshev pseudospectral method with an $O(N^{-1})$ time step restriction. *Journal of Computational Physics*, 104(2):457–469, 1993.
- D. Kosloff, D. Kessler, A. Q. Filho, E. Tessmer, A. Behle, and R. Strahilevitz. Solution of the equations of dynamic elasticity by a Chebychev spectral method. *Geophysics*, 55(6):734–748, 1990.
- A. M. Kracht. Design of bulbous bows. *SNAME Transactions*, 86:197–217, 1978.
- M. O. Kramer. Boundary layer stabilization by distributed damping. *Naval Engineers Journal*, 74(2):341–348, 1962.
- V. M. Kulik. Action of a turbulent flow on a hard compliant coating. *International Journal of Heat and Fluid Flow*, 33(1):232–241, 2012.
- V. M. Kulik, S. V. Rodyakin, I. Lee, and H. Chun. Deformation of a viscoelastic coating under the action of convective pressure fluctuations. *Experiments in fluids*, 38(5):648–655, 2005.
- V. M. Kulik, I. Lee, and H. Chun. Wave properties of coating for skin friction reduction. *Physics of Fluids (1994-present)*, 20(7):075109, 2008.
- V. Kumaran. Stability of the viscous flow of a fluid through a flexible tube. *Journal of Fluid Mechanics*, 294:259–281, 1995.

- U. Küttler and W. A. Wall. Fixed-point fluid–structure interaction solvers with dynamic relaxation. *Computational Mechanics*, 43(1):61–72, 2008.
- H. Lamb. On the propagation of tremors over the surface of an elastic solid. *Philosophical Transactions of the Royal Society of London. Series A, Containing papers of a mathematical or physical character*, 203:1–42, 1904.
- B. Lautrup. *Physics of Continuous Matter, Second Edition: Exotic and Everyday Phenomena in the Macroscopic World*. Taylor & Francis, 2011.
- D. Lee and H. Choi. Magnetohydrodynamic turbulent flow in a channel at low magnetic Reynolds number. *Journal of Fluid Mechanics*, 439:367–394, 2001.
- M. Lee and R. D. Moser. Direct numerical simulation of turbulent channel flow up to $Re_\tau \approx 5200$. *Journal of Fluid Mechanics*, 774:395–415, 2015.
- T. Lee, M. Fisher, and W. Schwarz. Investigation of the stable interaction of a passive compliant surface with a turbulent boundary layer. *Journal of Fluid Mechanics*, 257:373–401, 1993.
- M. Lejars, A. Margaillan, and C. Bressy. Fouling release coatings: a nontoxic alternative to biocidal antifouling coatings. *Chemical reviews*, 112(8):4347–4390, 2012.
- W. Li, W. Jessen, D. Roggenkamp, M. Klaas, W. Silex, M. Schiek, and W. Schröder. Turbulent drag reduction by spanwise traveling ribbed surface waves. *European Journal of Mechanics-B/Fluids*, 53:101–112, 2015.
- G. M. Lilley. A study of the silent flight of the owl. *AIAA paper*, 2340(1998):1–6, 1998.
- J. C. Lin. Review of research on low-profile vortex generators to control boundary-layer separation. *Progress in Aerospace Sciences*, 38(4):389–420, 2002.
- Y. Liu, S. Mukherjee, N. Nishimura, M. Schanz, W. Ye, A. Sutradhar, E. Pan, N. Dumont, A. Frangi, and A. Saez. Recent advances and emerging applications of the boundary element method. *Applied Mechanics Reviews*, 64(3):030802, 2011.
- J. C. Lötters, W. Olthuis, P. H. Veltink, and P. Bergveld. The mechanical properties of the rubber elastic polymer polydimethylsiloxane for sensor applications. *Journal of micromechanics and microengineering*, 7(3):145, 1997.
- A. Lozano-Durán and J. Jiménez. Effect of the computational domain on direct simulations of turbulent channels up to $Re_\tau = 4200$. *Physics of Fluids (1994-present)*, 26(1):011702, 2014.
- M. Luhar, A. S. Sharma, and B. McKeon. A framework for studying the effect of compliant surfaces on wall turbulence. *Journal of Fluid Mechanics*, 768:415–441, 2015.

- M. Luhar, A. Sharma, and B. McKeon. On the design of optimal compliant walls for turbulence control. *Journal of Turbulence*, 17(8):787–806, 2016.
- H. Luo and T. R. Bewley. Accurate simulation of near-wall turbulence over a compliant tensegrity fabric. In *Proc. SPIE*, volume 5757, pages 184–197, 2005.
- T. Lutz and S. Wagner. Drag reduction and shape optimization of airship bodies. *Journal of Aircraft*, 35(3):345–351, 1998.
- H.-L. Ma and C.-H. Kuo. Theoretical analysis of an oscillatory plane Poiseuille flow—A link to the design of vortex flow meter. *Physics of Fluids*, 29(5):053602, 2017.
- H. Mamori and K. Fukagata. Drag reduction effect by a wave-like wall-normal body force in a turbulent channel flow. *Physics of Fluids (1994-present)*, 26(11):115104, 2014.
- H. G. Matthies, R. Niekamp, and J. Steindorf. Algorithms for strong coupling procedures. *Computer methods in applied mechanics and engineering*, 195(17-18):2028–2049, 2006.
- P. Moczo and J. Kristek. On the rheological models used for time-domain methods of seismic wave propagation. *Geophysical Research Letters*, 32(1), 2005.
- P. Moczo, J. O. Robertsson, and L. Eisner. The finite-difference time-domain method for modeling of seismic wave propagation. *Advances in Geophysics*, 48:421–516, 2007.
- A. Mohammadi and J. M. Floryan. Groove optimization for drag reduction. *Physics of Fluids (1994-present)*, 25(11):113601, 2013.
- F. Moisy, M. Rabaud, and K. Salsac. A synthetic Schlieren method for the measurement of the topography of a liquid interface. *Experiments in Fluids*, 46(6):1021, 2009.
- C. J. Morris and F. K. Forster. Oscillatory flow in microchannels. *Experiments in Fluids*, 36(6):928–937, Jun 2004.
- R. D. Moser, J. Kim, and N. N. Mansour. Direct numerical simulation of turbulent channel flow up to $Re_\tau = 590$. *Phys. Fluids*, 11(4):943–945, 1999.
- Y. Murai. Frictional drag reduction by bubble injection. *Experiments in fluids*, 55(7):1773, 2014.
- T. Nadesan, H. Mitsudharmadi, T. Lee, and S. Winoto. Quasi-streamwise counter-rotating vortices generated by convergent riblets in flat plate boundary layer. *Journal of Visualization*, 17(4):319–325, 2014.
- T. Nakamura and S. Kaneko. *Flow Induced Vibrations: Classifications and Lessons from Practical Experiences*. Elsevier, 2008.

- R. Nakanishi, H. Mamori, and K. Fukagata. Relaminarization of turbulent channel flow using traveling wave-like wall deformation. *International Journal of Heat and Fluid Flow*, 35:152–159, 2012.
- V. D. Narasimhamurthy and H. I. Andersson. Numerical simulation of the turbulent wake behind a normal flat plate. *International Journal of Heat and Fluid Flow*, 30(6):1037–1043, 2009.
- D. J. Newman and G. E. Karniadakis. A direct numerical simulation study of flow past a freely vibrating cable. *Journal of Fluid Mechanics*, 344:95–136, 1997.
- B. Nugroho, N. Hutchins, and J. P. Monty. Large-scale spanwise periodicity in a turbulent boundary layer induced by highly ordered and directional surface roughness. *International Journal of Heat and Fluid Flow*, 41:90–102, 2013.
- J. Ohayon and R. Chadwick. Effects of collagen microstructure on the mechanics of the left ventricle. *Biophysical journal*, 54(6):1077, 1988.
- P. Orlandi and S. Leonardi. DNS of turbulent channel flows with two-and three-dimensional roughness. *Journal of Turbulence*, 7(73):1–22, 2006.
- P. Orlandi, S. Leonardi, and R. Antonia. Turbulent channel flow with either transverse or longitudinal roughness elements on one wall. *Journal of Fluid Mechanics*, 561:279–305, 2006.
- B. E. Owolabi, D. J. C. Dennis, and R. J. Poole. Turbulent drag reduction by polymer additives in parallel-shear flows. *Journal of Fluid Mechanics*, 827, 2017.
- A. Pandey, S. Karpitschka, C. H. Venner, and J. H. Snoeijer. Lubrication of soft viscoelastic solids. *Journal of Fluid Mechanics*, 799:433–447, 2016.
- Y. Pang, H. Kim, Z. Liu, and H. A. Stone. A soft microchannel decreases polydispersity of droplet generation. *Lab on a Chip*, 14(20):4029–4034, 2014.
- F. Paraz, L. Schouveiler, and C. Eloy. Thrust generation by a heaving flexible foil: Resonance, nonlinearities, and optimality. *Physics of Fluids*, 28(1):011903, 2016.
- S. Park. Analytical modeling of viscoelastic dampers for structural and vibration control. *International Journal of Solids and Structures*, 38(44–45):8065 – 8092, 2001. ISSN 0020-7683.
- S. W. Park and R. A. Schapery. Methods of interconversion between linear viscoelastic material functions. part i—a numerical method based on prony series. *International Journal of Solids and Structures*, 36(11):1653–1675, 1999.
- Y. Peet and P. Sagaut. Theoretical prediction of turbulent skin friction on geometrically complex surfaces. *Physics of Fluids (1994-present)*, 21(10):105105, 2009.

- B. Pier and P. J. Schmid. Linear and nonlinear dynamics of pulsatile channel flow. *Journal of Fluid Mechanics*, 815:435–480, 2017.
- A. C. Pipkin. *Lectures on viscoelasticity theory*, volume 7 of *Applied Mathematical Sciences*. Springer-Verlag, 1986.
- F. Pluvinage, A. Kourta, and A. Bottaro. Instabilities in the boundary layer over a permeable, compliant wall. *Physics of Fluids*, 26(8):084103, 2014.
- S. B. Pope. *Turbulent flows*. Cambridge University Press, Cambridge, 2000.
- M. Pourquie, W. Breugem, and B. J. Boersma. Some issues related to the use of immersed boundary methods to represent square obstacles. *International Journal for Multiscale Computational Engineering*, 7(6):509–522, 2009.
- T. Pritz. Relation of bulk to shear loss factor of solid viscoelastic materials. *Journal of Sound and Vibration*, 324(3):514–519, 2009.
- M. Quadrio. Drag reduction in turbulent boundary layers by in-plane wall motion. *Philosophical Transactions of the Royal Society A: Mathematical, Physical and Engineering Sciences*, 369(1940):1428–1442, 2011.
- M. Quadrio and W. Xie. Turbulent drag reduction by traveling waves of spanwise forcing. In *Proceedings of the 15th European Turbulence Conference*, Delft, The Netherlands, August 25–28, 2015.
- M. Quadrio, J. Floryan, and P. Luchini. Effect of streamwise-periodic wall transpiration on turbulent friction drag. *Journal of Fluid Mechanics*, 576:425–444, 2007.
- M. Raffel. Background-oriented schlieren (BOS) techniques. *Experiments in Fluids*, 56(3):60, 2015.
- M. K. Raj, S. DasGupta, and S. Chakraborty. Hydrodynamics in deformable microchannels. *Microfluidics and Nanofluidics*, 21(4):70, Mar 2017.
- S. Ramananarivo, R. Godoy-Diana, and B. Thiria. Rather than resonance, flapping wing flyers may play on aerodynamics to improve performance. *Proceedings of the National Academy of Sciences*, 108(15):5964–5969, 2011.
- M. D. Rao. Recent applications of viscoelastic damping for noise control in automobiles and commercial airplanes. *Journal of Sound and Vibration*, 262(3):457–474, 2003.
- L. Rayleigh. On waves propagated along the plane surface of an elastic solid. *Proceedings of the London Mathematical Society*, 1(1):4–11, 1885.
- S. Rebouillat and D. Liksonov. Fluid–structure interaction in partially filled liquid containers: A comparative review of numerical approaches. *Computers & Fluids*, 39(5):739–746, 2010.

- R. Reynolds, P. Hayden, I. Castro, and A. Robins. Spanwise variations in nominally two-dimensional rough-wall boundary layers. *Experiments in Fluids*, 42(2):311–320, 2007.
- J. J. Riley, M. Gad-el Hak, and R. W. Metcalfe. Compliant coatings. *Annual Review of Fluid Mechanics*, 20(1):393–420, 1988.
- K. Ring. Recruitment of *Balanus improvisus* on micro-textures with different geometries and evaluation of methods for analyzing cyprid behaviour. Master's thesis, Göteborg University, Sweden, 2000.
- J. O. Robertsson, J. O. Blanch, and W. W. Symes. Viscoelastic finite-difference modeling. *Geophysics*, 59(9):1444–1456, 1994.
- C. Roh, J. Lee, and C. Kang. Physical Properties of PDMS (Polydimethylsiloxane) Microfluidic Devices on Fluid Behaviors: Various Diameters and Shapes of Periodically-Embedded Microstructures. *Materials*, 9(10):836, 2016.
- M. E. Rosti and L. Brandt. Numerical simulation of turbulent channel flow over a viscous hyper-elastic wall. *Journal of Fluid Mechanics*, 830:708–735, 2017.
- J. P. Rothstein. Slip on superhydrophobic surfaces. *Annual Review of Fluid Mechanics*, 42:89–109, 2010.
- W. Sagong, C. Kim, S. Choi, W.-P. Jeon, and H. Choi. Does the sailfish skin reduce the skin friction like the shark skin? *Physics of Fluids (1994-present)*, 20(10):101510, 2008.
- A. K. Saha. Far-wake characteristics of two-dimensional flow past a normal flat plate. *Physics of Fluids (1994-present)*, 19(12):128110, 2007.
- O. San and A. E. Staples. Dynamics of pulsatile flows through elastic microtubes. *International Journal of Applied Mechanics*, 04(01):1250006, 2012.
- M. Sasamori, H. Mamori, K. Iwamoto, and A. Murata. Experimental study on drag-reduction effect due to sinusoidal riblets in turbulent channel flow. *Experiments in Fluids*, 55(10):1–14, 2014.
- W. Schoppa and F. Hussain. A large-scale control strategy for drag reduction in turbulent boundary layers. *Physics of Fluids (1994-present)*, 10(5):1049–1051, 1998.
- M. P. Schultz. Effects of coating roughness and biofouling on ship resistance and powering. *Biofouling*, 23(5):331–341, 2007.
- S. Shahinfar, S. S. Sattarzadeh, J. H. M. Fransson, and A. Talamelli. Revival of classical vortex generators now for transition delay. *Physical Review Letters*, 109(7):074501, 2012.
- V. Shankar and V. Kumaran. Stability of non-parabolic flow in a flexible tube. *Journal of Fluid Mechanics*, 395:211–236, 1999.

- V. Shatrov and G. Gerbeth. Magnetohydrodynamic drag reduction and its efficiency. *Physics of Fluids (1994-present)*, 19(3):035109, 2007.
- L. Shen, X. Zhang, D. K. Yue, and M. S. Triantafyllou. Turbulent flow over a flexible wall undergoing a streamwise travelling wave motion. *Journal of Fluid Mechanics*, 484:197–221, 2003.
- J.-M. Shi, M. Breuer, and F. Durst. A combined analytical–numerical method for treating corner singularities in viscous flow predictions. *International Journal for Numerical Methods in Fluids*, 45(6):659–688, 2004.
- P. Shorter. Wave propagation and damping in linear viscoelastic laminates. *The Journal of the Acoustical Society of America*, 115(5):1917–1925, 2004.
- A. R. Skovoroda, S. Y. Emelianov, M. A. Lubinski, A. P. Sarvazyan, and M. O’Donnell. Theoretical analysis and verification of ultrasound displacement and strain imaging. *Ultrasonics, Ferroelectrics, and Frequency Control, IEEE Transactions on*, 41(3):302–313, 1994.
- L. J. Sluys. *Wave propagation, localisation and dispersion in softening solids*. TU Delft, Delft University of Technology, 1992.
- B. P. Sommeijer, P. J. Van der Houwen, and J. Kok. Time integration of three-dimensional numerical transport models. *Applied numerical mathematics*, 16(1-2):201–225, 1994.
- K. Son, J. Choi, W.-P. Jeon, and H. Choi. Mechanism of drag reduction by a surface trip wire on a sphere. *Journal of Fluid Mechanics*, 672:411–427, 2011.
- F. Sotiropoulos, T. B. Le, and A. Gilmanov. Fluid mechanics of heart valves and their replacements. *Annual Review of Fluid Mechanics*, 48:259–283, 2016.
- P. R. Spalart and J. D. McLean. Drag reduction: enticing turbulence, and then an industry. *Philosophical Transactions of the Royal Society of London A: Mathematical, Physical and Engineering Sciences*, 369(1940):1556–1569, 2011.
- S. Srinivas and V. Kumaran. Transitions to different kinds of turbulence in a channel with soft walls. *Journal of Fluid Mechanics*, 822:267–306, 2017.
- V. Stenzel, Y. Wilke, and W. Hage. Drag-reducing paints for the reduction of fuel consumption in aviation and shipping. *Progress in Organic Coatings*, 70(4):224–229, 2011.
- V. Stenzel, C. Schreiner, A. Brinkmann, and D. Stübing. Biomimetic approaches for ship drag reduction – feasible and efficient? In V. Bertram, editor, *Proceedings of the 10th Symposium on High-Performance Marine Vehicles*, pages 131–140, Cortona, Oct 17-19 2016.
- A. D. Stroock, S. K. Dertinger, A. Ajdari, I. Mezić, H. A. Stone, and G. M. Whitesides. Chaotic mixer for microchannels. *Science*, 295(5555):647–651, 2002.

- R. B. Stull. *An introduction to boundary layer meteorology*, volume 13. Springer Science & Business Media, 2012.
- M. N. Sudin, M. A. Abdullah, S. A. Shamsuddin, F. R. Ramli, and M. Mohd. Review of Research on Vehicles Aerodynamic Drag Reduction Methods. *International Journal of Mechanical & Mechatronics Engineering*, 14(2), 2014.
- K. Takizawa and T. E. Tezduyar. New directions in space–time computational methods. In *Advances in Computational Fluid-Structure Interaction and Flow Simulation*, pages 159–178. Springer, 2016.
- E. Tessmer and D. Kosloff. 3-D elastic modeling with surface topography by a Chebychev spectral method. *Geophysics*, 59(3):464–473, 1994.
- T. Tezduyar, S. Aliabadi, M. Behr, A. Johnson, and S. Mittal. Parallel finite-element computation of 3D flows. *Computer*, 26(10):27–36, 1993.
- R. Thaokar and V. Kumaran. Stability of oscillatory flows past compliant surfaces. *The European Physical Journal B-Condensed Matter and Complex Systems*, 41(1):135–145, 2004.
- Third IMO GHG Study 2014. International Maritime Organization (IMO) London, UK, April 2015. Smith, T. W. P.; Jalkanen, J. P.; Anderson, B. A.; Corbett, J. J.; Faber, J.; Hanayama, S.; O’Keeffe, E.; Parker, S.; Johansson, L.; Aldous, L.; Raucchi, C.; Traut, M.; Ettinger, S.; Nelissen, D.; Lee, D. S.; Ng, S.; Agrawal, A.; Winebrake, J. J.; Hoen, M.; Chesworth, S.; Pandey, A.
- C. Thomas, A. P. Bassom, P. Blennerhassett, and C. Davies. The linear stability of oscillatory Poiseuille flow in channels and pipes. In *Proceedings of the Royal Society of London A: Mathematical, Physical and Engineering Sciences*, volume 467, pages 2643–2662. The Royal Society, 2011.
- C. Thomas, A. P. Bassom, and P. J. Blennerhassett. The linear stability of oscillating pipe flow. *Physics of Fluids*, 24(1):014106, 2012.
- N. Tomiyama and K. Fukagata. Direct numerical simulation of drag reduction in a turbulent channel flow using spanwise traveling wave-like wall deformation. *Physics of Fluids (1994-present)*, 25(10):105115, 2013.
- A. M. Torres Rojas, I. Pagonabarraga, and E. Corvera Poiré. Resonances of newtonian fluids in elastomeric microtubes. *Physics of Fluids*, 29(12):122003, 2017.
- L. N. Trefethen. *Spectral methods in MATLAB*. SIAM, 2000.
- N. Tschoegl. Time dependence in material properties: An overview. *Mechanics of Time-Dependent Materials*, 1(1):3–31, 1997.
- N. W. Tschoegl, W. G. Knauss, and I. Emri. Poisson’s ratio in linear viscoelasticity—a critical review. *Mechanics of Time-Dependent Materials*, 6(1):3–51, 2002.

- Y.-H. Tseng and J. H. Ferziger. A ghost-cell immersed boundary method for flow in complex geometry. *Journal of computational physics*, 192(2):593–623, 2003.
- K. Tsigklifis and A. D. Lucey. Asymptotic stability and transient growth in pulsatile Poiseuille flow through a compliant channel. *Journal of Fluid Mechanics*, 820:370–399, 2017.
- I. U. Vakarelski, D. Y. C. Chan, and S. T. Thoroddsen. Leidenfrost vapour layer moderation of the drag crisis and trajectories of superhydrophobic and hydrophilic spheres falling in water. *Soft Matter*, 10:5662–5668, 2014.
- D. Valdez-Jasso, M. A. Haider, H. Banks, D. B. Santana, Y. Z. Germán, R. L. Armentano, and M. S. Olufsen. Analysis of viscoelastic wall properties in ovine arteries. *IEEE Transactions on Biomedical Engineering*, 56(2):210–219, 2009.
- E. van Bokhorst, R. de Kat, G. E. Elsinga, and D. Lentink. Feather roughness reduces flow separation during low Reynolds number glides of swifts. *Journal of Experimental Biology*, 218(20):3179–3191, 2015.
- R. C. van der Burgt, P. D. Anderson, J. M. den Toonder, and F. N. van de Vosse. A microscale pulsatile flow device for dynamic cross-slot rheometry. *Sensors and Actuators A: Physical*, 220:221 – 229, 2014.
- A. H. van Zuijlen. *Fluid-structure interaction simulations: efficient higher order time integration of partitioned systems*. PhD thesis, Delft University of Technology, 2006.
- C. Vanderwel and B. Ganapathisubramani. Effects of spanwise spacing on large-scale secondary flows in rough-wall turbulent boundary layers. *Journal of Fluid Mechanics*, 774:R2,1–12, 2015.
- V. Vavourakis and D. Polyzos. A MLPG (LBIE) numerical method for solving 2D incompressible and nearly incompressible elastostatic problems. *International Journal for Numerical Methods in Biomedical Engineering*, 24(4): 281–296, 2008.
- S. Vedel, L. H. Olesen, and H. Bruus. Pulsatile microfluidics as an analytical tool for determining the dynamic characteristics of microfluidic systems. *Journal of Micromechanics and Microengineering*, 20(3):035026, 2010.
- V. Vedenev. Propagation of waves in a layer of a viscoelastic material underlying a layer of a moving fluid. *Journal of Applied Mathematics and Mechanics*, 80(3):225–243, 2016.
- D. A. Vermaas, W. S. J. Uijttewaai, and A. J. F. Hoitink. Lateral transfer of streamwise momentum caused by a roughness transition across a shallow channel. *Water Resources Research*, 47(2):1–12, 2011.
- C. Viotti, M. Quadrio, and P. Luchini. Streamwise oscillation of spanwise velocity at the wall of a channel for turbulent drag reduction. *Physics of Fluids (1994-present)*, 21(11):115109, 2009.

- J. Virieux. P-SV wave propagation in heterogeneous media: Velocity-stress finite-difference method. *Geophysics*, 51(4):889–901, 1986.
- J. Virieux, H. Calandra, and R.-É. Plessix. A review of the spectral, pseudo-spectral, finite-difference and finite-element modelling techniques for geophysical imaging. *Geophysical Prospecting*, 59(5):794–813, 2011.
- I. S. Vodop'yanov, N. V. Nikitin, and S. I. Chernyshenko. Turbulent drag reduction by spanwise oscillations of a ribbed surface. *Fluid Dynamics*, 48(4):461–470, 2013.
- A. Vreman and J. Kuerten. Comparison of direct numerical simulation databases of turbulent channel flow at $Re_\tau = 180$. *Physics of Fluids (1994-present)*, 26(1):015102, 2014a.
- A. Vreman and J. Kuerten. Statistics of spatial derivatives of velocity and pressure in turbulent channel flow. *Physics of Fluids (1994-present)*, 26(8):085103, 2014b.
- R. Wahidi, W. Chakroun, and S. Al-Fahed. The behavior of the skin-friction coefficient of a turbulent boundary layer flow over a flat plate with differently configured transverse square grooves. *Experimental Thermal and Fluid Science*, 30(2):141–152, 2005.
- Z.-Q. Wang and N.-S. Cheng. Time-mean structure of secondary flows in open channel with longitudinal bedforms. *Advances in Water Resources*, 29(11):1634–1649, 2006.
- E. Wassen, F. Kramer, F. Thiele, R. Grüneberger, W. Hage, and R. Meyer. Turbulent drag reduction by oscillating riblets. In *Proceedings of the 4th AIAA Flow Control Conference*, volume 2, pages 740–754, Seattle, USA, June 23–26, 2008.
- L. Wen, J. C. Weaver, and G. V. Lauder. Biomimetic shark skin: design, fabrication and hydrodynamic function. *Journal of Experimental Biology*, 217(10):1656–1666, 2014.
- P. Wesseling. *Principles of Computational Fluid Dynamics*. Springer Series in Computational Mathematics. Springer Berlin Heidelberg, 2001.
- C. M. White and M. G. Mungal. Mechanics and prediction of turbulent drag reduction with polymer additives. *Annual Review of Fluid Mechanics*, 40:235–256, 2008.
- F. M. White. *Fluid Mechanics*. McGraw-Hill series in mechanical engineering. McGraw-Hill Higher Education, 2003. ISBN 9780072831801.
- S. P. Wilkinson, J. B. Anders, B. S. Lazos, and D. M. Bushnell. Turbulent drag reduction research at NASA Langley: progress and plans. *International Journal of Heat and Fluid Flow*, 9(3):266–277, 1988.

- S. B. Wineberg, J. F. McGrath, E. F. Gabl, L. R. Scott, and C. E. Southwell. Implicit spectral methods for wave propagation problems. *Journal of Computational Physics*, 97(2):311–336, 1991.
- J. R. Womersley. Method for the calculation of velocity, rate of flow and viscous drag in arteries when the pressure gradient is known. *The Journal of Physiology*, 127(3):553, 1955.
- J. R. Womersley. Oscillatory flow in arteries: the constrained elastic tube as a model of arterial flow and pulse transmission. *Physics in Medicine & Biology*, 2(2):178, 1957.
- Q.-J. Xia, W.-X. Huang, and C.-X. Xu. Direct numerical simulation of turbulent boundary layer over a compliant wall. *Journal of Fluids and Structures*, 71:126–142, 2017.
- F. Xie, X. Zheng, M. S. Triantafyllou, Y. Constantinides, and G. E. Karniadakis. The flow dynamics of the garden-hose instability. *Journal of Fluid Mechanics*, 800:595–612, 2016.
- S. Xu, D. Rempfer, and J. Lumley. Turbulence over a compliant surface: numerical simulation and analysis. *Journal of Fluid Mechanics*, 478:11–34, 2003.
- J. Yang and E. Balaras. An embedded-boundary formulation for large-eddy simulation of turbulent flows interacting with moving boundaries. *Journal of Computational Physics*, 215(1):12–40, 2006.
- R. Yang, W. Mao, and X. Chang. An efficient seismic modeling in viscoelastic isotropic media. *Geophysics*, 80(1):T63–T81, 2015.
- D. M. Yebra, S. Kiil, and K. Dam-Johansen. Antifouling technology—past, present and future steps towards efficient and environmentally friendly antifouling coatings. *Progress in Organic Coatings*, 50(2):75–104, 2004.
- K. Yeo. The hydrodynamic stability of boundary-layer flow over a class of anisotropic compliant walls. *Journal of Fluid Mechanics*, 220:125–160, 1990.
- H. S. Yoon, O. A. El-Samni, and H. H. Chun. Drag reduction in turbulent channel flow with periodically arrayed heating and cooling strips. *Physics of Fluids (1994-present)*, 18(2):025104, 2006.
- M. Zamir. *The physics of pulsatile flow*. Springer, 2000.
- C. Zhang, R. Miorini, and J. Katz. Integrating Mach–Zehnder interferometry with TPIV to measure the time-resolved deformation of a compliant wall along with the 3D velocity field in a turbulent channel flow. *Experiments in Fluids*, 56(11):1–22, 2015.
- C. Zhang, J. Wang, W. Blake, and J. Katz. Deformation of a compliant wall in a turbulent channel flow. *Journal of Fluid Mechanics*, 823:345–390, 2017.

-
- H. Zhao, J. B. Freund, and R. D. Moser. A fixed-mesh method for incompressible flow–structure systems with finite solid deformations. *Journal of Computational Physics*, 227(6):3114–3140, 2008.
- X. Zhou, D. Yu, X. Shao, S. Zhang, and S. Wang. Research and applications of viscoelastic vibration damping materials: A review. *Composite Structures*, 136:460–480, 2016.
- F. Zonta, A. Soldati, and M. Onorato. Growth and spectra of gravity–capillary waves in countercurrent air/water turbulent flow. *Journal of Fluid Mechanics*, 777:245–259, 2015.

Curriculum Vitae



Personalia

Date of birth	25 October 1990
Address	Overboeicop 56, 4145 NR, Schoonrewoerd
E-mail	H.O.G.Benschop@outlook.com

Work

April 2018 – now	Teacher Mechanical Engineering, Avans Hogeschool, 's-Hertogenbosch
Jan 2014 – March 2018	PhD Fluid Dynamics, Delft University of Technology

Education

Sept 2011 – Dec 2013	Master Applied Physics, Delft University of Technology – Research & Development with focus on Physical Transport Phenomena
Sept 2008 – July 2011	Bachelor Applied Physics, Delft University of Technology – Cum laude propaedeutic diploma – Cum laude bachelor – Honours programme
Sept 2002 – July 2008	VWO (preuniversity secondary education), Gomarus Scholengemeenschap, Gorinchem

Research projects

- Sept 2013 – Dec 2013 **Internship**, TNO Delft, Dep. Fluid Dynamics
– Measuring and modelling pressure pulsations generated by reciprocating pump
- Feb 2012 – June 2013 **Master’s final project**, Delft University of Technology, Dep. Clouds, Climate & Air Quality
– Master’s thesis *Validation of Cloud Cover in GPU-resident Atmospheric Large-Eddy Simulations*
- Dec 2010 – July 2011 **Bachelor’s final project**, Delft University of Technology, Dep. Multi-Scale Physics
– Bachelor’s thesis *Computer Simulation of Steady and Incompressible Flow around a Single Tree without Leaves*
– Study prize for the best bachelor’s thesis in the year 2011 of the department Multi-Scale Physics
- Sept 2010 – Jan 2011 **Minor project**, Delft University of Technology
– Design and construction of model sailing yacht

Scientific contributions

Publications

- (1) H. O. G. Benschop and W.-P. Breugem. Drag reduction by herringbone riblet texture in direct numerical simulations of turbulent channel flow. *Journal of Turbulence*, 18(8):717–759, 2017.
- (2) H. O. G. Benschop, A. J. Guerin, A. Brinkmann, M. L. Dale, A. A. Finnie, W.-P. Breugem, A. S. Clare, D. Stübing, C. Price, and K. J. Reynolds. Drag-reducing riblets with fouling-release properties: development and testing. *Biofouling*, pages 1–13, 2018.
- (3) H. O. G. Benschop, A. J. Greidanus, R. Delfos, J. Westerweel, and W.-P. Breugem. Deformation of a linear viscoelastic compliant coating in a turbulent flow. *Journal of Fluid Mechanics*, 2018b, accepted.
- (4) H. O. G. Benschop and W.-P. Breugem. Oscillatory pressure-driven laminar flow coupled to a compliant viscoelastic layer on a rigid base. 2018c, to be submitted.

Conference contributions & training¹

- (1) *European Drag Reduction and Flow Control Meeting (EDRFCM 2015)*, 23 – 26 March 2015, Cambridge, England.
- (2) H. O. G. Benschop and W.-P. Breugem. Direct Numerical Simulations of Drag Reducing Surface Textures. *JMBC² Turbulence Contact Day*, 12 June 2015, Delft, The Netherlands.
- (3) H. O. G. Benschop and W.-P. Breugem. Direct Numerical Simulations of Drag Reduction in Turbulent Channel Flow over Bio-inspired Herringbone Riblet Texture. *15th European Turbulence Conference (ETC15)*, 25 – 28 August 2015, Delft, The Netherlands.

¹The name of the presenting author is underlined.

²The J.M. Burgerscentrum (JMBC) is the Dutch Research School for Fluid Mechanics.

- (4) H. O. G. Benschop and W.-P. Breugem. Turbulent Drag Reduction by Herringbone Riblets. *JMBC Burgers Symposium*, 16 & 17 June 2016, Lunteren, The Netherlands.
- (5) H. O. G. Benschop and W.-P. Breugem. Turbulent Drag Reduction by Herringbone Riblets. *11th European Fluid Mechanics Conference (EFMC11)*, 12 – 16 September 2016, Sevilla, Spain.
- (6) *Joint EM³-JMBC workshop ‘Recent Advances in Fluid-Solid Interaction’*, 11 November 2016, Utrecht, The Netherlands.
- (7) H. O. G. Benschop and W.-P. Breugem. Towards Turbulent Drag Reduction by Compliant Walls: An Analytical Study. *European Drag Reduction and Flow Control Meeting (EDRFCM 2017)*, 3 – 6 April 2017, Monte Porzio Catone (Rome), Italy.
- (8) H. O. G. Benschop and W.-P. Breugem. Turbulent Drag Reduction by Compliant Coatings: An Analytical Study. *16th European Turbulence Conference (ETC16)*, 21 – 24 August 2017, Stockholm, Sweden.
- (9) H. O. G. Benschop, A. J. Greidanus, R. Delfos, J. Westerweel and W.-P. Breugem. Deformation of a viscoelastic wall layer in turbulent flows. *12th European Fluid Mechanics Conference (EFMC12)*, 9 – 13 September 2018, Vienna, Austria.
- (10) W.-P. Breugem and H. O. G. Benschop. Turbulent flow over a herringbone riblet texture. *55th Annual Technical Meeting of the Society of Engineering Science (SES2018)*, 10 – 12 October 2018, Leganés, Madrid, Spain.

Presentations & training in SEAFRONT project

- (1) *Kick-off meeting*, hosted by AkzoNobel, 16 – 17 January 2014, Newcastle upon Tyne, England.
- (2) H. O. G. Benschop and W.-P. Breugem. Drag Reducing Potential of Textured Antifouling Coatings. *First progress meeting*, hosted by Fraunhofer IFAM, 26 – 27 June 2014, Bremen, Germany.
- (3) *Interdisciplinary training on Coating Chemistry*, organized by Sander Kommeren⁴, 10 – 14 November 2014, Eindhoven, The Netherlands.
- (4) H. O. G. Benschop and W.-P. Breugem. Drag Reducing Potential of Riblet Coatings. *Second progress meeting*, hosted by the University of Newcastle, 15 – 16 January 2015, Newcastle upon Tyne, England.

³EM refers to the Dutch Research School for Engineering Mechanics.

⁴Fellow PhD student from the SEAFRONT project.

- (5) H. O. G. Benschop and W.-P. Breugem. Direct Numerical Simulations of Drag Reducing Surface Textures. *Third progress meeting*, hosted by the University of Gothenburg, 2 – 3 July 2015, Gothenburg, Sweden.
- (6) *Interdisciplinary training on Hydrodynamics*, organized by me for Sander Kommeren and Anna Abramova⁴, 19 – 23 October 2015, Delft, The Netherlands.
- (7) H. O. G. Benschop and W.-P. Breugem. Drag Reduction by Herringbone Riblet Texture in Direct Numerical Simulations of Turbulent Channel Flow. *Fourth progress meeting*, hosted by Delft University of Technology, 13 – 15 January 2016, Delft, The Netherlands.
- (8) H. O. G. Benschop and W.-P. Breugem. Turbulent Drag Reduction by Compliant Walls. *Fifth progress meeting*, hosted by Solvay Specialty Polymers, 7 – 9 September 2016, Milan, Italy.
- (9) *Interdisciplinary training on Fouling Biology*, organized by Anna Abramova, 26 – 30 September 2016, Tjärnö and Gothenburg, Sweden.
- (10) H. O. G. Benschop and W.-P. Breugem. Drag Measurements in Cavitation Tunnel & Turbulent Drag Reduction by Compliant Walls. *Sixth progress meeting*, hosted by Biotrend, 1 – 2 February 2017, Coimbra, Portugal.
- (11) H. O. G. Benschop and W.-P. Breugem. Drag-reducing coatings in turbulent flows. *Interdisciplinary training at AkzoNobel*, organized by Kevin Reynolds, 19 – 23 June 2017, Newcastle upon Tyne, England.
- (12) H. O. G. Benschop and W.-P. Breugem. Turbulent Drag Reduction by Compliant Walls. *Seventh progress meeting*, hosted by the University of Bristol, 5 – 6 July 2017, Bristol, England.
- (13) H. O. G. Benschop and W.-P. Breugem. Deformation of a compliant coating in a turbulent flow. *Eighth progress meeting*, hosted by Bio-on, 14 – 15 December 2017, Bologna, Italy.

Internal talks⁵

- (1) H. O. G. Benschop and W.-P. Breugem. Sharks and Birds: Drag Reducing Surface Textures. 3 September 2014.
- (2) H. O. G. Benschop and W.-P. Breugem. Go/No Go Presentation: Drag Reducing Surface Textures. 11 February 2015.
- (3) H. O. G. Benschop and W.-P. Breugem. Drag Reduction by Herringbone Riblets in Direct Numerical Simulations of Turbulent Channel Flow. 2 March 2016.

⁵Mainly for colleagues from the Laboratory for Aero- & Hydrodynamics, and for students of Mechanical Engineering.

- (4) H. O. G. Benschop and W.-P. Breugem. Deformation of a compliant wall in a turbulent channel flow: an analytical study. 13 September 2017.

Blessed be the Lord, Who daily loadeth us with benefits, even the God of our salvation. (Psalm 68:19)

Geloofd zij de Heere; dag bij dag overlaadt Hij ons; die God is onze Zaligheid. (Psalm 68:20)

Acknowledgements / Dankwoord

Een promotietraject van ruim vier jaar wil ik graag afsluiten met een dankwoord. Het spreekt voor zich dat ik dit traject niet alleen heb doorgemaakt. Velen hebben op een directe of indirecte manier bijgedragen aan de totstandkoming van dit proefschrift. Hieronder wil ik een aantal van hen bij name noemen, maar bij voorbaat wil ik alvast hen dankzeggen die ik onbedoeld kan hebben vergeten.

Allereerst wil ik Wim-Paul Breugem, mijn dagelijkse begeleider, hartelijk bedanken. Een betere begeleiding kon ik bijna niet wensen. Je gaf me de mogelijkheid om zelfstandig onderzoek te doen, maar je was ook altijd bereid om me te helpen. Hoogtepunten waren o.a. de gezamenlijke reizen naar het buitenland en jouw verhuizing waarbij ik mocht helpen. Verder ook een woord van waardering voor Jerry Westerweel, mijn eerste promotor. Onze gesprekken waren weinig, maar goed. Ik herinner je als een informele professor die me stimuleerde om buiten de gewone kaders te denken.

Next, I also want to express my thanks towards all colleagues from the SEAFRONT project. A few of them I want to mention specifically. John van Haare and Arie Brouwer coordinated the whole project. The colleagues from Ship Hydrodynamics of Newcastle University (Mehmet, Serkan, Irma and Alessandro) questioned the hydrodynamic aspects of our research. Anders Blomberg organised the training programme for the three PhDs in our project: Anna Abramova, Sander Kommeren and me. Sander arranged a chemistry training in Eindhoven, with Glow as one of the highlights. Anna organised a biology training in Gothenburg with snorkelling and sea food as two highlights. Kevin Reynolds and his colleagues arranged a nice visit to International Paint Ltd in Felling, Gateshead, United Kingdom.

With three partners of the SEAFRONT project we collaborated on the development and testing of a drag-reducing riblet texture with fouling-release properties, which resulted in a nice publication. Dorothea Stübing, Andreas Brinkmann and coworkers (Fraunhofer Institute for Manufacturing Technology and Advanced Materials) delivered many cylinders with either textured or untextured coatings

for drag measurements in the Taylor-Couette setup. Kevin Reynolds, Clayton Price, Alistair Finnie, Marie Dale and colleagues (AkzoNobel, International Paint Ltd.) provided several cylinders with antifouling coatings, and performed fouling-release and panel immersion assays. Andrew Guerin, Tony Clare and coworkers (Newcastle University, school of Natural and Environmental Sciences) characterized the antifouling properties with use of barnacle settlement, and diatom adhesion and ease-of-removal assays.

Mijn collega Arnoud Greidanus heeft op twee manieren aan mijn onderzoek bijgedragen. Hij hielp mij bij de Taylor-Couette metingen, alsook bij de data-verwerking. Daarnaast hebben zijn metingen aan een vervormbare wand in een turbulente stroming geresulteerd in een goede samenwerking en een mooie publicatie. In deze context wil ik ook René Delfos, Jerry Westerweel en Wim-Paul Breugem bedanken voor hun inbreng.

Verschillende onderzoekers, vooral binnen de TU Delft, heb ik benaderd voor advies met betrekking tot het onderzoek aan vervormbare wanden: Gijs Ooms (Fluid Mechanics, 3mE), Willem van de Water (Fluid Mechanics, 3mE), Bendiks Jan Boersma (Process & Energy, 3mE), Matthijs Langelaar (Structural Optimization and Mechanics, 3mE), Koen van Dongen (Imaging Physics, TNW), Sander van Zijl en David Blom (Aerodynamics, LR), Kees Wapenaar en Jan Thorbecke (Applied Geophysics and Petrophysics, CiTG), Kaspar Jansen (Emerging Materials, IO), Arthur Veldman en Henk Seubers (Engineering Mechanics and Numerical Mathematics, Rijksuniversiteit Groningen). Verder heb ik ook twee aangename gesprekken gehad met mijn PhD mentor Wouter Beelaerts van Blokland.

Met genoegen heb ik Sander Bezuijen begeleid, wat heeft geresulteerd in zijn masterscriptie ‘Hydrodynamic drag reduction in turbulent boundary layer flow using riblets’ (Bezuijen, 2017). Sander, bedankt voor alles wat je hebt gedaan. In deze context wil ik ook Otto Salomons en zijn collega’s van Océ Technologies B.V. noemen. Zij hebben een plaat verzorgd met ribbels die zijn geproduceerd met ‘elevated printing’ technologie. In de watertunnel heeft Sander daarmee 5% weerstandsvermindering gemeten, een mooi resultaat! Otto, bedankt.

My colleagues have contributed considerably to a nice time as PhD. Highlights were the coffee at 10 a.m. and the Christmas dinners. The good atmosphere will persist in a pleasant remembrance. All my colleagues I want to thank: Jerry, René, Gerrit, Ruud, Mathieu, Dirk, Daniel, Mark, Willem, Christian, Wim-Paul, Gijs, Aris, Jan, Caroline, Edwin, Jasper R., Guillermo, Mohammad, John, Arati, Özge, Göktürk, Yuk Man, Florian, Andries, Parviz, Arnoud, Ernst Jan, Melika, Maurice, Xu, Ankur, Koen, Greta, Gem, Sören, Marieke, Saad, Mike, Willian, Pedro, Amitosh, Cen, Tariq, Wout, Sita, Jerke, Daniele, Manu, Gosse, Pepijn, Sedat, Jasper T., Norbert, Oleksandr, and everybody that I forgot. Caroline and Rob looked after the administrative and financial matters. Edwin ordered many cylinders for the Taylor-Couette measurements. Pedro often helped me with the use of Fortran and the supercomputer. Regularly I consulted Mathieu or Gerben Roest to solve computer problems. Jerke, Greta, Ankur and Wout shared the office with me. Jerke, de momenten dat jij even buiten ging roken waren voor

jouw gezondheid niet de beste. Toch waren juist die momenten uitermate geschikt om onze gedachten even boven het aardse stof te verheffen. Hartelijk dank voor de waardevolle gesprekken en je bijzondere gastvrijheid. Tot slot wil ik mijn waardering uitspreken voor het werk dat schoonmaker Zoubir heeft verricht. Zijn tevredenheid is voor mij vaak een leerzame spiegel geweest.

De goede tijd in Delft heb ik niet alleen te danken aan mijn collega's. Mijn huis in Delft heb ik gedeeld met Hessel, Adriaan, Bart en Erwin. Het gezamenlijke avondeten was één van de gezelligste doordeweekse momenten. Verder denk ik aan de wekelijkse catechisaties op maandagavond. Meneer Van Bokhoven wil ik dankzeggen voor het leerzame onderwijs, onder andere vanuit Gods Woord en de Institutie van Johannes Calvijn.

Ook buiten Delft heb ik veel steun gehad, direct of indirect. Mijn ouders wil ik bedanken voor hun bijzonder goede zorg en betrokkenheid, die kan ik nooit genoeg waarderen. Het eten stond klaar, de was werd gedraaid en de belangstelling was overvloedig. Ook mijn broers, zus en zwager gaven me elke keer voldoende afleiding om met twee benen op de grond te blijven staan. Verdere familie, vrienden van de studiekring, andere vrienden en bekenden wil ik vooral bedanken voor de vele momenten dat we niet over de inhoud van mijn onderzoek hebben gesproken. Er zijn immers zoveel andere en belangrijker dingen in het leven! Johanna, nog steeds kan ik nauwelijks geloven dat ik jou heb gekregen, dank dat je mij terzijde wilt staan.

Above all I want to express my thanks to the Lord God. He gave me the strength and wisdom to complete a period of four years of research. Through His undeserved grace just the PhD time has become unforgettable. It is therefore my explicit wish that His Name may be glorified. In case something good is to be found in this thesis, forget then my name, but give the honour to God. Soli Deo Gloria.

Bovenal wil ik mijn dank uitspreken aan God de Heere. Hij gaf mij de kracht en de wijsheid om een periode van vier jaar onderzoek af te ronden. Door Zijn onverdiende genade is juist de promotietijd onvergetelijk geworden. Het is daarom mijn nadrukkelijke wens dat Zijn Naam mag worden verheerlijkt. Wanneer er iets goeds in dit proefschrift te vinden is, vergeet dan mijn naam, maar geef God de eer. Soli Deo Gloria.

Blessing, and glory, and wisdom, and thanksgiving, and honour, and power, and might, be unto our God for ever and ever. Amen. (Revelation 7:12)

De lof en de heerlijkheid en de wijsheid en de dankzegging en de eer en de kracht en de sterkte zij onzen God in alle eeuwigheid. Amen. (Openbaring 7:12)